Ollscoil na hÉireann, Corcaigh

National University of Ireland, Cork

Nanomaterial-based Devices for Advanced Energy Storage and Delivery

Thesis presented by

Louise Mc Grath B.Sc. (Hons.)

for the degree of

Doctor of Philosophy

University College Cork

Tyndall National Institute

Supervisor: Dr. James Rohan

Head of Department: Dr. Fatima Gunning

2021

Contents

Declaration

This is to certify that the work I am submitting is my own and has not been submitted for another degree, either at University College Cork or elsewhere. All external references and sources are clearly acknowledged and identified within the contents. I have read and understood the regulations of University College Cork concerning plagiarism.

Louise Mc Grath

Acknowledgements

Over the course of my Ph.D. I have come into contact with many people who deserve to be acknowledged, and I will do my level best to mention them in the following. If I do forget to mention anyone (and I always do!), please know that I do and will always appreciate your help and support throughout my Ph.D. journey.

First and foremost, I would sincerely like to thank my supervisor Dr. James Rohan for affording me the opportunity to conduct my Ph.D. under his supervision. He always made himself available to help me in any way he could, and for that I am truly grateful as I now have knowledge in areas I never would have understood on my own. His support, guidance and encouragement helped me to grow as an individual and gave me the confidence to complete the thesis that you are currently reading.

Next, I would like to thank everyone whom I've had the pleasure to meet within the Electrochemical Materials and Energy group: Lorraine Nagle, Declan Casey, Anita Hamilton, Brian Shanahan, Ricky Anthony, Richard Doyle, Fiona Barry and Ian Seymour, and those within NTG: Niamh Creedon, Caoimhe Robinson, Julia Madden, Pierre Lovera and Colm Barrett. You all helped me in your own way, from chatting to me when I needed it, to helping me solve any problem I needed a hand with. I will forever appreciate it! A special thank you to Anita for taking time out to meet me when you left Tyndall, for inviting me to your wedding, and for sharing many happy moments with you, Iain and the girls: Saidhbh and Fiadh.

Tomás Clancy, and Michael Moore should also be included in the above paragraph, however both deserve a more special mention. Tomás, thanks for all your patience, wisdom and guidance, I think I would still be trying to figure out the Biologics Potentiostat if it wasn't for your help! Michael, I am forever grateful for your support and encouragement throughout the initial years of my Ph.D., you

put up with all my bad moods, and calmed me down when I needed it most. I will forever be grateful for the love and support!

I also extend my gratitude and appreciation to all the support and research staff in Tyndall with whom I have had the pleasure of encountering throughout my journey! Especially those who allowed me into their labs and helped train me I wouldn't be handing this thesis up without you! To John and Mary in Goods-in, you always brightened up my day with your infectious smiles and great chats! You would always help me find the items I needed most, even if it was an empty cardboard box, you are both absolute legends, thank you!

To the outreach officers Karen Twomey (UCC), Alida Zauers and even Caitríona Tyndall, thank you for always supporting my craziness, and for letting me help at outreach events. You have allowed me to find a passion, that I never knew I had! Thanks to Alida in particular for the many coffee breaks to help discuss my rogue outreach events and thank you for the support you have shown me, helping with the nominations for the outreach award that I won! I really appreciate all that you have done for me! You'll never understand the impact you made on my life.

To my friends within Tyndall, where do I even begin? I need to include my actual Ph.D. work in this thesis, so I won't mention all of you by name, but you know who you are! I will instead thank the groups:

To the wonderful people who made/make up the Tea Group, thank you for the countless tea breaks (or water breaks in my case!), breakfasts, and lunches! You gave me the much needed stress relief at the exact moment I needed it, even if it meant meeting up outside of work! Strong friendships were forged, and we have lots of happy memories, so let's hope this will continue for years to come! I warmly thank everyone who was involved in the Tyndall Taggers for allowing me to become part of such a wonderful group of people. I enjoyed the training sessions, and the matches. Thank you for

allowing me to get to know every single one of you, as I really enjoyed playing tag rugby with you, and will always have the medal, to relive such wonderful memories. To all "my" Italians, particularly Francesco, Stefano, Marco and Fabrizio, I really enjoyed my time with each of you, and I hope to maintain contact with you forevermore! A few trips to Italy will be on the cards very soon! To Harry, Ross, Jan and Alessandra, thank you for all the house "parties" and brunches that we had, it was always a wonderful escape for me, especially when the stress levels were through the roof. For those friends who don't fall into either group, thank you for all the chats and pints!

Now I should start thanking those outside of Tyndall who had to endure me whilst I conducted my Ph.D. To my best friends, Michelle, Sinéad and Claire who were patient and understanding, I really appreciate it! You never complained when I had to reschedule plans due to things going wrong in the lab, and when we did meet you took my mind off work. A warm thank you to my other friends who have been wonderful and supportive of me every time we met, here's to many more happy memories in my post-PhD life!

To my friends in Kuk Sool Won, thank you for the support whenever I shared my outreach videos and events with you. Thank you for the numerous fight nights where I could let all my anger and frustration out, and for the tea and biscuits after a hard morning of grading! You are a really unique and special group! Here's to another tough few months to black belt! Thanks especially to Fiona and Matt for allowing me to help out with fundraising by hosting a science/art workshop, it was a great experience!

To my wonderful boyfriend Gökhan, you have been so patient and kind to me, and I don't think I would be able to repay you for all the times you let me vent about things going horribly wrong! You distracted me when I needed to be distracted and pushed me to work when I needed to work. Thanks

for all the junk food Fridays (which always extended into Saturday and Sunday as well!) and for all the holidays we got to experience together!

Last but certainly not least, I would love to thank my family. Over the last few years they have listened to me complain when things haven't gone quite so well for me, and they were happy for me when things worked for me. They were very supportive and even when I was really stressed, they encouraged me to keep trying and told me to never give up! The constant jokes "are you not finished yet?", and "no wonder it's taking you so long to finish you PhD" will now have to come to an end as I am finally finished! Whatever will you joke about now? I don't think I will be able to repay you for all the love and encouragement you have shown me all my life, however at least now I am giving you the opportunity to say you have a doctor in the family, however it is not the most conventional of doctors!

I couldn't have had a more wonderful Ph.D. experience without the love, support and encouragement I received throughout its duration. Thank you to everyone for making my journey a happy one!

Dedicated to my family, both living and departed.

"If we knew what it was we were doing, it would not be called research, would it?"

Dallas Campbell (Science of Stupid)

Abstract

The Internet of Things (IoT) scenario offers benefits such as reduced analysis costs, improved safety and will enable the prediction of future trends due to the multitude of wireless sensors acting as an environmental interface that provides data. Currently, non-rechargeable batteries act as the predominant energy source for today's commercial wireless sensors, however their large sizes often hinders the miniaturisation of IoT sensors, thus reducing the potential application for these sensors. In addition, the high energy and power demands of the sensors dramatically reduce the lifetime of the primary batteries, which then requires their frequent replacement. Therefore, the ultimate challenge facing the mass distribution of wireless sensors is meeting the energy and power requirements to match the lifetime of the microdevices. Advancements towards energy harvester-powered sensors are hindered due to their low efficiency and limitations, therefore the need for hybrid systems comprising a significantly smaller rechargeable energy storage device coupled to energy harvesters are of interest to enable long life autonomous IoT sensors.

Li-ion rechargeable batteries (LiB) are the battery chemistry of choice and have been demonstrated with organic and solid-state electrolytes. LiBs provide high energy density (~270 W kg^{-1}) in conventional organic electrolytes with modest cycle life (500 to 1,000) but are limited to low power densities (<1000 W kg^{-1}) often caused by the presence of inactive binder and conductive additive materials in the anode and cathode, resulting in hampered device operation particularly during the energy intensive periods of sensor measurement and wireless communication. In addition, the utilisation of volatile organic carbonate based electrolytes within the battery raises a safety issue, therefore limiting their potential applications.

In order to circumvent this, solid-state Li microbatteries represent an alternative due to their increased intrinsic safety as no volatile organic components are utilised. In addition, they offer larger potential energy densities due to the removal of inactive binder and conductive additive materials, and in some cases utilisation of Li metal as an anode improves the energy density. They offer a significantly better cycle life when compared to organic electrolyte-based batteries (≥5,000 vs. <1,000). However, their drawbacks have limited their use in commercial systems, for example, the need to maintain thin electrodes (at the micron level) particularly for the low electronic conductivity oxide cathodes typically utilised. In addition, sluggish Li^+ diffusion within the electrolyte and electrodes at room temperature often results in poor power capabilities and a significant potential drop during high current operation.

Based on the time constant (τ) for linear diffusion in a material of dimension L ($\tau = \frac{L^2}{2D}$), where D is the diffusion coefficient, it can be estimated that the time taken for Li^+ to diffuse in typical battery materials of micron dimension will be two to three orders of magnitude slower with a corresponding lower power capability than for a nanoscale (≤100 nm) material. Therefore, a small form factor capable of high current operation is critical in the development of the next-generation hybrid systems. Identification of an appropriate electrolyte which boasts a combination of organic and solid-state properties such as non-volatility, non-flammability and high ionic conductivity at room temperature which can exist in both liquid or solid form is desirable. Identification of such an electrolyte in addition to high power and energy density materials will allow for the realisation of IoT autonomous sensors.

An alternative class of electrolytes have been identified and discussed within this thesis: ionic liquids. They offer the aforementioned favourable properties in addition to large electrochemical windows which enables the use of various anode and cathode materials. Their non-volatility allows for easy

integration into devices, and they offer the opportunity to electrodeposit certain electrode materials such as Ge, which further demonstrates their applicability and suitability as electrolyte materials. These hybrid properties are showcased during a thorough cyclic voltammetry (CV), chronoamperometry (CA) and electrochemical impedance spectroscopy (EIS) analysis. The ability of the ionic liquid to form solid state analogues is demonstrated as a series of polymer gel electrolytes is synthesised using simple synthesis methods. The solid-state polymer gel electrolytes offer comparable ionic conductivities to those of conventional electrolytes (1 M $LiPF_6$ in 1:1 v/v ethylene carbonate (EC):diethyl carbonate (DEC)) (1.9 mS cm^{-1} vs. 7.9 mS cm^{-1}), with their ionic conductivities being up to 600 times greater than typical solid-state electrolytes such as lithium phosphorous oxy-nitride (LiPON).

The utilisation of direct current (D.C.) magnetron sputtering for the deposition of Ge is described, whereby uniform nanoscale thin films (~100 nm) are obtained. The compatibility of the Ge thin films with the ionic liquid electrolyte is demonstrated as typical amorphous CV data is obtained which correlates with the Ge analysed in organic-based electrolytes. Galvanostatic cycling of the Ge electrode in the ionic liquid achieved the highest reported Ge electrode capacities achieved in literature using the pyrrolidinium-based ionic liquid electrolyte. Capacities of ~900 mAh g^{-1} are obtained at 3.5 C (C = C-rate), whereby nanostructured electrodes in literature achieved a maximum capacity of 600 mAh g^{-1} at 1 C using similar electrolyte materials. The addition of carbonate additives such as vinylene carbonate (VC) prevented large scale delamination of the electrode material from the current collector as evidenced by SEM analysis.

The utilisation of electrodeposition to fabricate nanoscale V_2O_5 thin films allows for crystalline or amorphous to be obtained. Both amorphous and crystalline thin films exhibited compatibility with the liquid and polymer gel electrolytes, however, the crystalline V_2O_5 thin films exhibited higher power capabilities due to intercalation pseudocapacitance electrochemical kinetics. Long-term

cycling (~400 cycles) are exhibited with minimal capacity fade (0.4% over 50 cycles at 5 C in the polymer gel electrolyte PG-60) with lithium metal anodes.

To assess the potential use of 1-butyl-1-methylpyrrolidinium bis(trifluoromethylsulfonyl)imide (C_4mpyrTFSI)-based electrolytes with nanostructured electrodes, CV analysis was carried out with inverse opal (IO) TiO_2 electrodes. Similar electrochemical performances to conventional organic electrolyte (1 M $LiPF_6$ in 1:1 v/v EC:DEC) were observed. In addition, identical current densities (organic: -0.04 mA cm^{-2} vs. IL: ~ -0.04 mA cm^{-2} at 0.5 mV s^{-1}) and peak positions were achieved in both solutions. Additive analysis was carried out the mitigate electrode swelling observed in additive-free electrolytes. Finally, polymer gel electrolyte analysis was carried out, whereby high coulombic efficiencies (>90%) were attained.

Prototype ionic liquid-based full cells consisting of V_2O_5 cathodes and Ge anodes are investigated. A reduction in the separator thickness results in more stable cycling across the C-rates as minimal capacity drop is observed in the vinylene carbonate (VC)-containing 260 versus a 900 μm thick electrolyte cell (~0.3 vs. ~1 mAh g^{-1} per cycle at 0.5 C, respectively). Up to 700 cycles was achieved for both VC- and VC-free cells without significant capacity fade or cell failure. These cells are comparable to typical solid-state microbatteries, as capacities of 5.7 and 3.2 μAh at 0.2 C (cycles 11 to 20) and 1 C (cycles 41 to 50) respectively are demonstrated by the prototype, in addition to an average discharge capacity of 1.3 μAh at 5 C for cycles 600 to 650 is attained after significant C-rate analysis (rates from 0.2 C to 10 C utilised).

Table of Acronyms

AFBNNS	Amine functionalised boron nitride nanosheets
AIL	Aprotic ionic liquid
BEPy	N-n-butyl-N-ethylpyrrolidinium
C	C-rate
C_2epyr	Diethylpyrrolidinium
C_2mpyr	N-ethyl-N-methylpyrrolidinium
C_3mpyr	N-propyl-N-methylpyrrolidinium
C_4mpyr	1-butyl-1-methylpyrrolidinium
C_4mpyrTFSI	1-butyl-1-methylpyrrolidinium bis(trifluoromethylsulfonyl)imide
CA	Chronoamperometry
ccnm	carbamoylcyano(nitroso)methanide
CEI	Cathode-electrolyte interphase
CMC	Carboxymethyl cellulose
CNT	Carbon nanotubes
CP	Chronopotentiometry
CPE	Constant phase element
CV	Cyclic voltammetry
D.C.	Direct current
DCA	Dicyanamide
DEC	Diethyl carbonate
DMC	Dimethyl carbonate
DSC	Differential scanning calorimetry
EC	Ethylene carbonate
EDX	Electron-dispersive X-ray spectroscopy
EIS	Electrochemical Impedance Spectroscopy
emim	1-ethyl-3-methylimidazolium
ESW	Electrochemical stability window
FEC	Fluoroethylene carbonate
FSI	Bis(fluorosulfonyl)imide
FT-IR	Fourier-transform infrared spectroscopy
IL	Ionic liquid
IO	Inverse opal
IoT	Internet of Things
LATP	$Li_{1.4}Al_{0.4}Ti_{1.6}(PO_4)_3$
LCO	$LiCoO_2$
LFP	$LiFePO_4$
LiB	Li-ion batteries

LiFSI	Lithium bis(fluorosulfonyl)imide
LiPON	Lithium phosphorous oxy-nitride
LiTFSI	Lithium bis(trifluoromethylsulfonyl)imide
LLZO	$Li_{6.5}La_{2.5}Ba_{0.5}ZrNbO_{12}$
LMO	$LiMn_2O_4$
LTO	$Li_4Ti_5O_{12}$
LTP	$LiTi_2(PO_4)_3$
NCM	$LiNi_{0.3}Mn_{0.3}Co_{0.3}O_2$
NW	Nanowires
OEG	Oligo ethylene glycol
OTf	Triflate
P(DADMA)-TFSI	Poly(diallyldimethylammonium) bis(trifluoromethylsulfonyl)imide
PEC	Poly(ethylene carbonate
PEO	Polyethylene oxide
PG	Polymer gel
PIL	Poly(ionic liquid)
PVD	Physical vapour deposition
PVDF	Polyvinylidene fluoride
PVDF-HFP	Poly(vinylidene fluoride-co-hexafluoropropylene)
$PYR_{1(2o2)}$	1-(2-ethoxyethyl)-1-methylpyrrolidinium
$PYRA_{1(2o1)}$	N-ethyl(methylether)-N-methylpyrrolidinium
R.F.	Radio frequency
R_{ct}	Charge transfer resistance
SEI	Solid-electrolyte interphase
SEM	Scanning electron microscopy
TFSAM	Trifluoromethanesulfonyl-N-cyanoamide
TFSI	Bis(trifluoromethylsulfonyl)imide
TGA	Thermogravimetric analysis
UV	Ultra-violet
VC	Vinylene carbonate
WSN	Wireless sensor nodes
XRD	X-ray diffraction analysis
Z	Warburg diffusion

General Introduction, Objectives & Overview

General Introduction

The Internet of Things (IoT) is a novel paradigm that was first introduced by Kevin Ashton in 1998,[1-2] and since then it has gained significant attention both in academia and industry. This paradigm was conceived due to the huge advancements in the fields of electronics, and the deployment of wireless communication systems, mobile devices and ubiquitous services. In recent years IoT has stepped out of its infancy and has gained traction towards achieving smart environments such as smart cities. This progress has been realised due to the integration of several enabling technologies (energy harvesters, sensors, energy storage) which can create autonomous devices which can then be deployed and forgotten. This opens the gateway for a multitude of applications as shown in figure 1.

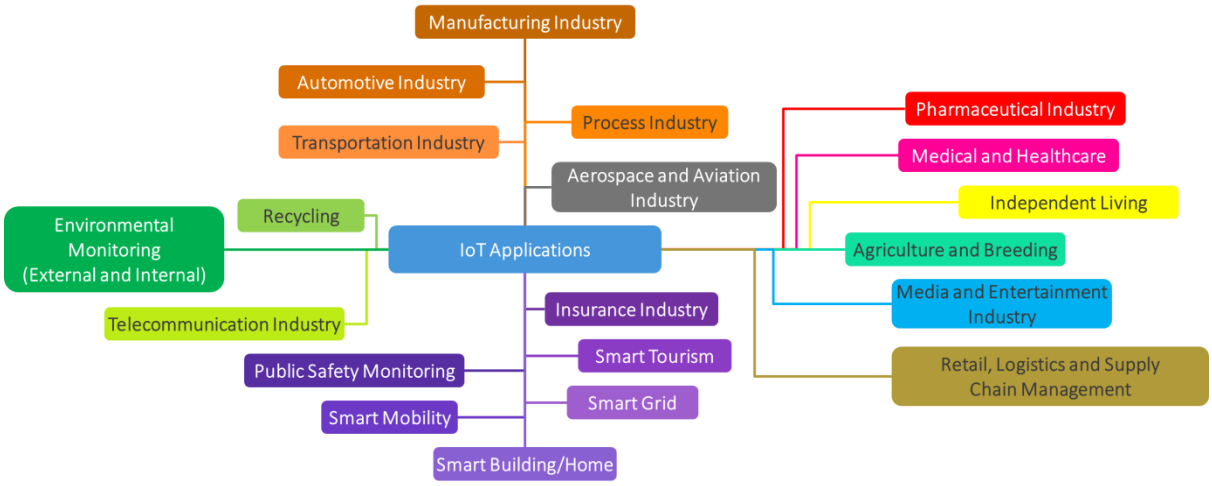

Figure 1: IoT application domains.

Wired sensors are among the most reliable systems as they directly link the sensor to the device that is receiving the input. This means they are the most durable systems which do not need to be replaced often. However, it should be noted that wired systems require a large amount of space and are much

more complicated to maintain. In addition, errors on wired channels are often of permanent nature due to connector or cable failures.[3] Wireless sensor nodes (WSN) are becoming more common for sensor based applications like the IoT. This is due to their low installation costs, and easy maintenance. Wireless sensor networks allow for a greater level of flexibility as the sensor system can easily be adopted to suit the application, thus realisation of IoT is dependent on the WSN. The current trends for interconnected devices show that this realisation is coming to fruition as initial estimates for interconnected devices were 24 billion devices by 2020.[2] However, current trends suggest that actual figures should surpass this estimation as there were 23.14 billion interconnected devices in 2018. Further growth is expected worldwide where 30.73 billion devices should be connected by 2020,[4] and this figure should increase to 75.44 billion by 2025.

One of the main constraints to the deployment of WSNs is the power requirement. A truly autonomous system must be attained in order to successfully 'deploy and forget' WSNs. Many research groups are focusing on energy harvesters and their capabilities in a bid to secure as much power as possible to power the WSN without the use of rechargeable batteries. Possible options for energy harvesting technology include:

1. Photovoltaic cells
2. Thermal energy
3. Radio frequency
4. Mechanical - Vibrational

Each operate using different principles and offer varying levels of power and efficiency. In the case of photovoltaic cells, solar energy is required. In essence one would expect that deployment of solar powered WSN would occur for outdoor applications in regions where sunlight is present almost year round. It is an uncontrollable energy harvester as sunlight is unpredictable. If there is a deficient solar resource the node may harvest insufficient energy which means it will only operate during the day.

During short winter days the node may fail to operate continuously in daylight as the level of solar energy drops further.[5-6] Si solar panels offer efficiencies which are within the range of 8-24%.[7-8] The efficiency is largely dependent on the material: mono-crystalline 15-24%; polycrystalline 14-20.4%; amorphous 8-13.2%. These are capable of producing power ranging from µW to MW depending on its area, for example, a typical value of power density for outdoor use is 15 mW cm^{-2}.[7-8] Power densities of 30 to 90 µW cm^{-2} have been reported for indoor use, where the light intensity is 1000 lux.[9]

Thermal energy harvesters operate based on the Seebeck effect,[10] where thermoelectric transducers depend on spatial variations in temperatures, while pyroelectric transducers depend on temporal variations in temperature.[8] Thermoelectric generators have low efficiency (5-6%). When placed in a stable environment, the thermoelectric system will stop generating power when both plates achieve the same temperature.[11-12] A temperature difference existing between two locations will result in a flow of heat energy from hot to cold in an attempt to develop thermal equilibrium. This heat flow can be exploited to harness useful energy. The efficiency of the thermal energy harvester is dependent on the temperature differential across the thermal electric generator (TEG) and the absolute temperature of the heat sink (cold source). Unless large temperature differentials can be obtained within an environment, other energy harvester technologies could be better suited, as temperatures 100 °C above room temperature would only result in 20% efficiency.[6]

A good alternative for indoor energy harvesting is radio frequency (R.F.) harvesters. They utilise the transmission of radio waves ranging from 3 kHz to 300 GHz, and their subsequent conversion to direct current. This can be accomplished using a single-stage or multistage converter, depending on the requirements of power, voltage, or efficiency. The amount of harvestable power is given by the source power, antenna gain and by the distance from the R.F. source. The conversion efficiency ranges from 50-75%. This high efficiency is due in part to the availability of R.F. sources indoors.[13]

One limitation is the reliance of the signal strength to the distance from the power source which can result in low power levels available for harvesting.[12] In addition, R.F. transmission needs to be directional, or else a large fraction of the transmitted R.F. power is wasted.

A further energy harvester source relies on converting ambient movement or kinetic energy of a device environment into electric energy. This form of mechanical energy harvesting has garnered much attention for use in WSN as it has the ability to function indoors, and there is an abundance of vibrations in most environments. Vibrational harvesting involves the conversion of kinetic energy inherent in mechanical vibrations into electricity. This can be achieved via three pathways: electromagnetic, electrostatic and piezoelectric conversion. The piezoelectric energy harvesters can exploit vibrations from 50 Hz to 50 kHz, induce oscillations between 0.5 μm to over 1 mm, and produce powers that range from tens of μW to over a mW per cm^3.[14-15]

It is clearly evident that despite best efforts to solely power WSN using energy harvesters it will be difficult to achieve without the use of an energy storage system. Coupling of energy harvesters and energy storage technologies enables truly autonomous systems, providing continuous energy. The use of energy storage compensates for the disadvantages associated with energy harvesters. Energy storage describes technology which converts energy from a form that is difficult to store (e.g. electrical energy) to a storable form (e.g. electrochemical). The stored energy can then be converted back into a directly usable form. There are various types of energy storage with different properties such as capacity, power, and charge/discharge rates. In general, energy storage in sensor nodes can be classified into various technologies:[12, 16] (1) supercapacitors, (2) rechargeable batteries and (3) hybrid capacitors which encompass both battery and capacitor properties. Supercapacitors would be best suited for high powered but low energy applications, while batteries tend to suit long lasting and task intensive applications. The energy storage technology can affect the size, cost and lifetime of the node. In order for batteries to be implemented in WSNs, they should fulfil certain requirements:[17]

1. High energy density (to allow for miniaturisation)
2. High current charging/discharging
3. Long cycle life
4. Low impedance if high peak currents required
5. Safe
6. Mechanically and electronically robust

Compared to other battery chemistries, lithium (Li) chemistry provides much higher power and energy densities in both gravimetric (3861 mAh g^{-1})[18] and volumetric (2062 mAh cm^{-3})[19] terms,[20] which are the most important parameters for applications in portable electronics such as smart phones, digital cameras and laptops. In addition, many Li batteries have lower self-discharge rates and hence longer shelf lives. The most common commercial lithium-ion batteries (LiBs) used in the WSN applications are cylindrical, pouch or coin cells. These batteries are generally bulky and large, for instance, the 18650 cylindrical cell is 65.2 mm long and 18.6 mm in diameter.[21] The smallest coin cell (ML421) is about 5 mm in diameter. The rapid development of electronic and information technology towards the directions of multi-functionality, high integration and high power drives the electronic devices towards miniaturization.[22] Li microbatteries are commonly utilised energy storage devices for biological/medical devices,[23] and self-powered microelectronics (miniature transmitters, sensors, actuators, etc.).[24] These devices are sometimes on the millimetre scale or less. In order to achieve miniaturised sensors, there is a need to obtain miniaturised energy storage solutions to replace the generic commercial coin cells still routinely used.

In order to address this, micro-sized Li primary batteries,[25] which address some but not all issues pertaining to the IoT have been developed. As shown in table 1, batteries which are small in size can be obtained with high specific capacity, however, with the advent of the IoT, there is a demand for higher power and energy on a smaller scale.[26]

Company	Model no.	Type	Volume (mm^3)	Max. dimension (mm)	Specific capacity ($Wh\ L^{-1}$)	Chemistry
Panasonic	CR2032	Button	1000	20	675	Li/MnO_2
Panasonic	ML421	Button	38	4.8	95	Li/MnO_2
Panasonic	CG320	Pin-type	192	20	203	–
PNNL	MB306	Pin-type	42	6	528	Li/CF_x
Panasonic	NCR18650	Cylindrical	16700	65	577	Li–cobalt
Thinergy	MEC201	Thin-film	110	25.4	36	$Li/LiCoO_2$
Cymbet	CBC005-BDC	Thin-film	0.75	2.25	27	$Li/LiCoO_2$
Sun *et al.*	Microbattery	3D	0.23	1	1260	$LiFePO_4/Li_4Ti_5O_{12}$
Lai *et al.*	Microbattery	Monolithic porous electrode	6	3	400	$Li/LiCoO_2$
Pikul *et al*.	Microbattery	3D	0.03	–	150	MnO_2/ NiSn

Table 1: Comparison of size and energy density of various lithium-ion batteries. Reprinted with permission from Wang et al.[21]

A crucial hurdle towards the development of feasible microbatteries is that the charge capacity of the battery will usually decrease with decreasing battery size. The decrease in energy originates from the

fact that the capacity of a battery scales linearly with the volume of the electrodes. Therefore the volumetric capacity of the electrode material is more important than the gravimetric capacity.[27-29]

Current investigations into all-solid-state microbatteries are primarily focused on microbatteries containing $LiCoO_2$ (LCO) cathodes in their uncoated state or coated with materials such as $LiNbO_3$,[30-39] Al_2O_3,[40] or $Li_{1.4}Al_{0.4}Ti_{1.6}(PO_4)_3$ (LATP).[41] However, cobalt (Co) is not an abundant material and is only mined in a small number of global locations where the largest share (~50%) is found in the Democratic Republic of Congo.[42] This has led to price instability and a dramatic increase from ~$21,000 per metric tonne in January of 2016 to $95,307 in March of 2018, and $34,500 in February 2020.[43] Therefore researchers are developing cathode materials that either have reduced Co content or are entirely Co-free. Some research groups have investigated hybrid LCO cathode materials which comprise both LCO and $LiMn_2O_4$ (LMO),[44] while other groups have focused their microbattery research on doped LCO films such as $Li(Ni_{0.6}Co_{0.2}Mn_{0.2})O_2$,[45-48] $Li(Ni_{0.3}Co_{0.3}Mn_{0.3})O_2$,[49-52] and $Li(Ni_{0.8}Co_{0.15}Al_{0.05})O_2$,[53-54] where the Co content is lower than for LCO electrodes. Efforts towards Co-free all-solid-state batteries have focused on the utilisation of lithium iron phosphate ($LiFePO_4$),[55-58] $Li_3V_2(PO_4)_3$,[59] and nickel-sulphide carbon nanotubes (NiS-CNT) cathode materials.[60] Further work is being carried out by various research groups[61-65] and companies[66] to further advance the understanding and performance of all-solid-state battery materials, however, high operational temperatures are required for most of the microbatteries without LCO cathodes due to the low ionic conductivity of the compatible electrolyte material, which causes sluggish Li^+ diffusion. Therefore, in order to fully utilise microbatteries without LCO based cathodes, alternative electrolyte materials must be investigated.

Objectives

This work is supported by CONNECT, Science Foundation Ireland's Research Centre for Future Networks and Communications. The goal is to enable increased lifetime and functionality of portable systems with specific Li-ion batteries power capabilities and capacities adapted to the specific applications by varying the electrode and electrolyte materials. Fabrication methods such as electrodeposition and magnetron sputtering allow for fabrication of electrode and electrolyte materials which are compatible with direct Si integration.

In this study, we report on the use of the pyrrolidinium based ionic liquid (IL) 1-butyl-1-methylpyrrolidinium bis(trifluoromethylysulfonyl)imide as an electrolyte for LiBs as an alternative electrolyte material to conventional solid-state and organic electrolytes. A solid-state polymer gel electrolyte containing the IL is developed. The electrochemical properties of both the liquid and polymer gel forms are discussed with various anode and cathode materials. Direct current (D.C.) sputter deposition was utilised to deposit thin-films of Ge, which when utilised with the IL electrolyte demonstrated improved capacity and cycle life compared to literature studies using similar electrolyte materials. The electrodeposition of nanoscale V_2O_5 thin-film electrodes is also reported. The crystalline and amorphous states are analysed with the IL electrolyte demonstrating that crystalline materials are compatible for use in the IL. The results reported are the first of their kind for this particular electrode/electrolyte combination. Finally, full cells are constructed and analysed to determine their viability as LiBs.

The objectives of this work are listed below:

- Assess and compare the electrochemical properties of ionic liquids to conventional organic electrolytes (ionic conductivity and Li-ion mobility) and demonstrate their suitability as alternatives to conventional solid-state electrolytes.

- Fabricate polymer gel electrolytes from the ionic liquid and determine their electrochemical properties.
- Determine the electrochemical performance and properties of D.C. magnetron sputtered nanoscale anode materials.
- Investigate a low-cost plating technique to fabricate nanoscale cathode material for use with IL based electrolytes.
- Construct a preliminary full cell based on the anode, cathode and electrolyte analysis, and assess its capabilities.

Overview

The first chapter discusses a literature review of ionic liquids, particularly those which are applicable to Li-ion battery technology. In the review, pyrrolidinium-based ionic liquids are separated into their respective cations. Both liquid and polymer gel forms of the ionic liquids are discussed. Chapter 2 discusses the fundamental principles of the electrochemical and characterisation techniques used in this study.

In chapter 3, an ionic liquid alternative to conventional solid state and organic electrolytes, which demonstrates favourable electrochemical properties is thoroughly investigated. In addition, a simplified synthesis of the ionic liquid based polymer gels is outlined which can be performed outside of a glovebox at moderate temperatures (50 °C), with no vacuum or external heating required during the drying process, and no further treatment (e.g. soaking in electrolyte, or UV irradiation) once dry. This is contrasted to most methods in the literature which rely on high temperatures during synthesis,[67] or drying of the polymer gels under vacuum or at high temperatures.[68-70]

Chapter 4 discusses the investigation of a high capacity anode, Ge, and its compatibility with the IL electrolyte with and without organic additives vinylene carbonate (VC) and fluoroethylene carbonate (FEC). SEM images before and after cyclic voltammetry (CV) and galvanostatic cycling demonstrate the effect that additives can have to protect the integrity of the electrode material. Similarly, the polymer gel electrolyte synthesised in chapter 3 was used to investigate the compatibility of ionic liquid based polymer gel electrolytes with Ge.

Chapter 5 describes the use of V_2O_5 as an electrode in ionic liquid electrolytes. The effect of the V_2O_5 electrode crystallinity on its electrochemical performance in the IL based electrolytes is discussed, in addition to the effect that thickness can have on the electrode kinetics during CV analysis. Long-term cycling (up to 400 cycles) is demonstrated at various C-rates with minimal capacity fade and coulombic efficiencies >99%.

Chapter 6 discusses the performance of the ionic liquid in its liquid and polymer gel form with a nanostructured inverse opal (IO) TiO_2 anodes. The compatibility of the IO TiO_2 anodes is investigated where the compatibility of the IL is demonstrated, however, the need for further optimisation is required.

Chapter 7 results in a culmination of the previous experimental chapters as a preliminary full cell is constructed utilising the Ge anode, V_2O_5 cathode and IL electrolyte in both its liquid and polymer gel forms. The preliminary steps towards optimisation are outlined with the cells exhibiting an electrochemical performance capable of being competitive with commercial microbatteries provided further optimisation take place.

Lastly, chapter 8 draws conclusion from the conducted work, summarises the achievements and presents an outlook for future work, followed by the appendices.

References

[1] G. Santucci, in *International Conference on Future Trends of the Internet, Vol. 28*, **2009**.

[2] J. Gubbi, R. Buyya, S. Marusic, M. Palaniswami, *Future Generation Computer Systems* **2013**, *29*, 1645-1660 https://doi.org/10.1016/j.future.2013.01.010.

[3] A. Flammini, P. Ferrari, D. Marioli, E. Sisinni, A. Taroni, *Microelectronics Journal* **2009**, *40*, 1322-1336 https://doi.org/10.1016/j.mejo.2008.08.012.

[4] Statista, **2019,** https://www.statista.com/statistics/471264/iot-number-of-connected-devices-worldwide/.

[5] T. Wark, W. Hu, P. Corke, J. Hodge, A. Keto, B. Mackey, G. Foley, P. Sikka, M. Brunig, in *Intelligent Sensors, Sensor Networks and Information Processing, 2008. ISSNIP 2008. International Conference on*, IEEE, **2008**, pp. 599-604.

[6] C. Knight, J. Davidson, S. Behrens, *Sensors* **2008**, *8*, 8037-8066

[7] V. Raghunathan, A. Kansal, J. Hsu, J. Friedman, M. Srivastava, in *Proceedings of the 4th international symposium on Information processing in sensor networks*, IEEE Press, **2005**, p. 64.

[8] M. Prauzek, J. Konecny, M. Borova, K. Janosova, J. Hlavica, P. Musilek, *Sensors* **2018**, *18*, 2446

[9] M. Freitag, J. Teuscher, Y. Saygili, X. Zhang, F. Giordano, P. Liska, J. Hua, S. M. Zakeeruddin, J.-E. Moser, M. Grätzel, A. Hagfeldt, *Nature Photonics* **2017**, *11*, 372-378 10.1038/nphoton.2017.60.

[10] N. Q. Nguyen, K. V. Pochiraju, *Applied Thermal Engineering* **2013**, *51*, 1-9 https://doi.org/10.1016/j.applthermaleng.2012.08.050.

[11] F. K. Shaikh, S. Zeadally, *Renewable and Sustainable Energy Reviews* **2016**, *55*, 1041-1054

[12] F. Akhtar, M. H. Rehmani, *Renewable and Sustainable Energy Reviews* **2015**, *45*, 769-784

[13] P. Kamalinejad, C. Mahapatra, Z. Sheng, S. Mirabbasi, V. C. Leung, Y. L. Guan, *IEEE Communications Magazine* **2015**, *53*, 102-108

[14] J. A. Paradiso, T. Starner, *IEEE Pervasive computing* **2005**, 18-27

[15] A. Hande, R. Bridgelall, B. Zoghi, *Proceedings of the IEEE* **2010**, *98*, 1620-1628 10.1109/JPROC.2010.2050670.

[16] A. Muzaffar, M. B. Ahamed, K. Deshmukh, J. Thirumalai, *Renewable and Sustainable Energy Reviews* **2019**, *101*, 123-145 https://doi.org/10.1016/j.rser.2018.10.026.

[17] J. F. M. Oudenhoven, R. J. M. Vullers, R. Schaijk, *International Journal of Energy Research* **2012**, *36*, 1139-1150 10.1002/er.2949.

[18] A. O. Raji, R. Villegas Salvatierra, N. D. Kim, X. Fan, Y. Li, G. A. L. Silva, J. Sha, J. M. Tour, *ACS Nano* **2017**, *11*, 6362-6369 10.1021/acsnano.7b02731.

[19] Y. Cao, F. Pan, H. Wang, Z. Yang, J. Sun, *Transactions of Tianjin University* **2020**, *26*, 248-255 10.1007/s12209-020-00253-9.

[20] J. M. Tarascon, M. Armand, *Nature* **2001**, *414*, 359-367 10.1038/35104644.

[21] Y. Wang, B. Liu, Q. Li, S. Cartmell, S. Ferrara, Z. D. Deng, J. Xiao, *Journal of Power Sources* **2015**, *286*, 330-345

[22] C. A. Mack, *IEEE Transactions on Semiconductor Manufacturing* **2011**, *24*, 202-207 10.1109/TSM.2010.2096437.

[23] D. C. Bock, A. C. Marschilok, K. J. Takeuchi, E. S. Takeuchi, *Electrochimica Acta* **2012**, *84*, 155-164 10.1016/j.electacta.2012.03.057.

[24] A. Patil, V. Patil, D. Wook Shin, J.-W. Choi, D.-S. Paik, S.-J. Yoon, *Materials Research Bulletin* **2008**, *43*, 1913-1942 10.1016/j.materresbull.2007.08.031.

[25] H. Chen, S. Cartmell, Q. Wang, T. Lozano, Z. D. Deng, H. Li, X. Chen, Y. Yuan, M. E. Gross, T. J. Carlson, J. Xiao, *Scientific Reports* **2014**, *4*, 3790 10.1038/srep03790 https://www.nature.com/articles/srep03790#supplementary-information.

[26] K. A. Cook-Chennault, N. Thambi, A. M. Sastry, *Smart Materials and Structures* **2008**, *17*, 043001 10.1088/0964-1726/17/4/043001.

[27] Y. Gogotsi, P. Simon, *Science* **2011**, *334*, 917-918 https://doi.org/10.1126/science.1213003.

[28] J. Zhu, J. Jiang, Y. Feng, G. Meng, H. Ding, X. Huang, *ACS Applied Materials & Interfaces* **2013**, *5*, 2634-2640 https://doi.org/10.1021/am400055a.

[29] W. Wang, M. Tian, A. Abdulagatov, S. M. George, Y.-C. Lee, R. Yang, *Nano Letters* **2012**, *12*, 655-660 https://doi.org/10.1021/nl203434g.

[30] Z. Zhang, S. Chen, J. Yang, J. Wang, L. Yao, X. Yao, P. Cui, X. Xu, *ACS Applied Materials & Interfaces* **2018**, *10*, 2556-2565 10.1021/acsami.7b16176.

[31] D. Xie, S. Chen, Z. Zhang, J. Ren, L. Yao, L. Wu, X. Yao, X. Xu, *Journal of Power Sources* **2018**, *389*, 140-147 https://doi.org/10.1016/j.jpowsour.2018.04.021.

[32] T. Teranishi, M. Inohara, J. Kano, H. Hayashi, A. Kishimoto, K. Yoda, H. Motobayashi, Y. Tasaki, *Solid State Ionics* **2018**, *314*, 57-60 https://doi.org/10.1016/j.ssi.2017.11.020.

[33] Y. Kato, S. Hori, T. Saito, K. Suzuki, M. Hirayama, A. Mitsui, M. Yonemura, H. Iba, R. Kanno, *Nature Energy* **2016**, *1*, 16030 10.1038/nenergy.2016.30.

[34] Y. Kato, S. Shiotani, K. Morita, K. Suzuki, M. Hirayama, R. Kanno, *The Journal of Physical Chemistry Letters* **2018**, *9*, 607-613 10.1021/acs.jpclett.7b02880.

[35] D. H. Kim, D. Y. Oh, K. H. Park, Y. E. Choi, Y. J. Nam, H. A. Lee, S.-M. Lee, Y. S. Jung, *Nano Letters* **2017**, *17*, 3013-3020 10.1021/acs.nanolett.7b00330.

[36] Y. Ito, A. Sakuda, T. Ohtomo, A. Hayashi, M. Tatsumisago, *Electrochemistry* **2014**, *82*, 591-594 10.5796/electrochemistry.82.591.

[37] M. Kato, T. Hayashi, G. Hasegawa, X. Lu, T. Miyazaki, Y. Matsuda, N. Kuwata, K. Kurihara, J. Kawamura, *Solid State Ionics* **2017**, *308*, 54-60 https://doi.org/10.1016/j.ssi.2017.05.008.

[38] N. Ohta, K. Takada, I. Sakaguchi, L. Zhang, R. Ma, K. Fukuda, M. Osada, T. Sasaki, *Electrochemistry Communications* **2007**, *9*, 1486-1490 https://doi.org/10.1016/j.elecom.2007.02.008.

[39] W. Sun, M. Xie, X. Shi, L. Zhang, *Materials Research Bulletin* **2015**, *61*, 287-291 https://doi.org/10.1016/j.materresbull.2014.10.044.

[40] J. H. Woo, J. E. Trevey, A. S. Cavanagh, Y. S. Choi, S. C. Kim, S. M. George, K. H. Oh, S.-H. Lee, *Journal of The Electrochemical Society* **2012**, *159*, A1120-A1124 10.1149/2.085207jes.

[41] Q. Yang, J. Huang, Y. Li, Y. Wang, J. Qiu, J. Zhang, H. Yu, X. Yu, H. Li, L. Chen, *Journal of Power Sources* **2018**, *388*, 65-70 https://doi.org/10.1016/j.jpowsour.2018.03.076.

[42] P. Barrera, **2019,** https://investingnews.com/daily/resource-investing/battery-metals-investing/cobalt-investing/cobalt-producer-cobalt-reserves/.

[43] T. Economics, **2020,** https://tradingeconomics.com/commodity/cobalt.

[44] S. Cho, S. Kim, W. Kim, S. Kim, S. Ahn, *Polymers* **2018**, *10*, 1364

[45] S.-J. Choi, S.-H. Choi, A. D. Bui, Y.-J. Lee, S.-M. Lee, H.-C. Shin, Y.-C. Ha, *ACS Applied Materials & Interfaces* **2018**, *10*, 31404-31412 10.1021/acsami.8b11244.

[46] Y. J. Nam, D. Y. Oh, S. H. Jung, Y. S. Jung, *Journal of Power Sources* **2018**, *375*, 93-101 https://doi.org/10.1016/j.jpowsour.2017.11.031.

[47] M.-S. Park, Y.-C. Jung, D.-W. Kim, *Solid State Ionics* **2018**, *315*, 65-70 https://doi.org/10.1016/j.ssi.2017.12.007.

[48] T. Ates, M. Keller, J. Kulisch, T. Adermann, S. Passerini, *Energy Storage Materials* **2019**, *17*, 204-210 https://doi.org/10.1016/j.ensm.2018.11.011.

[49] S. Randau, D. A. Weber, O. Kötz, R. Koerver, P. Braun, A. Weber, E. Ivers-Tiffée, T. Adermann, J. Kulisch, W. G. Zeier, F. H. Richter, J. Janek, *Nature Energy* **2020** 10.1038/s41560-020-0565-1.

[50] J. M. Whiteley, J. H. Woo, E. Hu, K.-W. Nam, S.-H. Lee, *Journal of The Electrochemical Society* **2014**, *161*, A1812-A1817 10.1149/2.0501412jes.

[51] M. Yamamoto, Y. Terauchi, A. Sakuda, M. Takahashi, *Scientific Reports* **2018**, *8*, 1212 10.1038/s41598-018-19398-8.

[52] A. Sakuda, K. Kuratani, M. Yamamoto, M. Takahashi, T. Takeuchi, H. Kobayashi, *Journal of The Electrochemical Society* **2017**, *164*, A2474-A2478 10.1149/2.0951712jes.

[53] U. Ulissi, M. Agostini, S. Ito, Y. Aihara, J. Hassoun, *Solid State Ionics* **2016**, *296*, 13-17 https://doi.org/10.1016/j.ssi.2016.08.014.

[54] S. Energy, **2012,** https://www.batteryspace.com/prod-specs/NCR18650B.pdf.

[55] R.-J. Chen, Y.-B. Zhang, T. Liu, B.-Q. Xu, Y.-H. Lin, C.-W. Nan, Y. Shen, *ACS Applied Materials & Interfaces* **2017**, *9*, 9654-9661 10.1021/acsami.6b16304.

[56] P. Hovington, M. Lagacé, A. Guerfi, P. Bouchard, A. Mauger, C. M. Julien, M. Armand, K. Zaghib, *Nano Letters* **2015**, *15*, 2671-2678 10.1021/acs.nanolett.5b00326.

[57] L. Porcarelli, M. A. Aboudzadeh, L. Rubatat, J. R. Nair, A. S. Shaplov, C. Gerbaldi, D. Mecerreyes, *Journal of Power Sources* **2017**, *364*, 191-199 https://doi.org/10.1016/j.jpowsour.2017.08.023.

[58] R. Bouchet, S. Maria, R. Meziane, A. Aboulaich, L. Lienafa, J.-P. Bonnet, T. N. T. Phan, D. Bertin, D. Gigmes, D. Devaux, R. Denoyel, M. Armand, *Nature Materials* **2013**, *12*, 452-457 10.1038/nmat3602.

[59] S. Yu, A. Mertens, H. Tempel, R. Schierholz, H. Kungl, R.-A. Eichel, *ACS Applied Materials & Interfaces* **2018**, *10*, 22264-22277 10.1021/acsami.8b05902.

[60] Q. Zhang, G. Peng, J. P. Mwizerwa, H. Wan, L. Cai, X. Xu, X. Yao, *Journal of Materials Chemistry A* **2018**, *6*, 12098-12105 10.1039/C8TA03449D.

[61] Y. Chen, Z. Wang, X. Li, X. Yao, C. Wang, Y. Li, W. Xue, D. Yu, S. Y. Kim, F. Yang, A. Kushima, G. Zhang, H. Huang, N. Wu, Y.-W. Mai, J. B. Goodenough, J. Li, *Nature* **2020**, *578*, 251-255 10.1038/s41586-020-1972-y.

[62] S.-T. Hsu, B. T. Tran, R. Subramani, H. T. T. Nguyen, A. Rajamani, M.-Y. Lee, S.-S. Hou, Y.-L. Lee, H. Teng, *Journal of Power Sources* **2020**, *449*, 227518 https://doi.org/10.1016/j.jpowsour.2019.227518.

[63] Q. Chen, R. Xu, Z. He, K. Zhao, L. Pan, *Journal of The Electrochemical Society* **2017**, *164*, A1852-A1857 10.1149/2.0651709jes.

[64] Y. Matsuda, N. Kuwata, J. Kawamura, *Solid State Ionics* **2018**, *320*, 38-44 https://doi.org/10.1016/j.ssi.2018.02.024.

[65] Y. Matsuda, N. Kuwata, T. Okawa, A. Dorai, O. Kamishima, J. Kawamura, *Solid State Ionics* **2019**, *335*, 7-14 https://doi.org/10.1016/j.ssi.2019.02.010.

[66] Y.-G. Lee, S. Fujiki, C. Jung, N. Suzuki, N. Yashiro, R. Omoda, D.-S. Ko, T. Shiratsuchi, T. Sugimoto, S. Ryu, J. H. Ku, T. Watanabe, Y. Park, Y. Aihara, D. Im, I. T. Han, *Nature Energy* **2020** 10.1038/s41560-020-0575-z.

[67] Z. Ruisi, C. Yuanfen, R. Montazami, *Materials (1996-1944)* **2015**, *8*, 2735-2748 https://doi.org/10.3390/ma8052735.

[68] H. Ye, J. Huang, J. J. Xu, A. Khalfan, S. G. Greenbaum, *Journal of the Electrochemical Society* **2007**, *154*, A1048-A1057 https://doi.org/10.1149/1.2779962.

[69] P.-L. Kuo, C.-H. Tsao, C.-H. Hsu, S.-T. Chen, H.-M. Hsu, *Journal of Membrane Science* **2016**, *499*, 462-469 https://doi.org/10.1016/j.memsci.2015.11.007.

[70] M. Li, L. Yang, S. Fang, S. Dong, S.-i. Hirano, K. Tachibana, *Polymer International* **2012**, *61*, 259-264 10.1002/pi.3181.

Chapter 1:

Literature Review

The Internet of Things concept requires autonomous wireless sensors to be deployed and ideally forgotten to realise applications such as smart buildings, smart grid and independent living, among others. Through the use of energy harvesters coupled with energy storage systems, these autonomous sensors can be realised. Current microbattery technology utilises an all-solid-state format due to its intrinsic safety when compared to Li-ion batteries containing volatile organic solvents. The utilisation of solid-state electrolytes results in low ionic conductivity electrolytes, which can result in sluggish Li^+ diffusion.[1-4] Therefore in order to improve the electrochemical performance of Li-based microbatteries, alternative electrolyte materials must be determined. One such alternative is ionic liquids (ILs), which are salts in a liquid state at temperatures below 100 °C.[5] They have garnered interest as alternative electrolytes to both organic and solid-state because of their tuneable properties, which results from the cation and anion combination. The cations are typically organic, while the anions can be inorganic or organic.[6]

ILs offer high ionic conductivities with the addition of Li salts such as LiTFSI, for example 1-butyl-1-methylpyrrolidinium bis(trifluoromethylsulfonyl)imide achieves ~3 mS cm^{-1} at room temperature.[7] ILs are often viscous fluids, and a straight channel for diffusion is not provided, as it is complicated by the ever-changing pathways of diffusion caused by the ion pairings.[8-13] . Within energy storage devices, Li^+ can co-ordinate with the IL's anions, causing an increase in the viscosity of the electrolyte, resulting in reduced Li diffusivity. This is evidenced in the literature as higher Li

concentrations leads to increased IL viscosity.[14-17] For these reasons, conventional one-dimensional diffusion as in organic electrolytes cannot be assumed.

As with organic solvents the electrochemical reduction of the IL cation can result in the formation of a solid-electrolyte interphase (SEI) layer, however, the anion can also contribute to its formation. The anion plays a substantial role in the electrochemical stability of the IL, which in turn affects that electrochemical window. For instance, Sun *et al.*[18] investigated the electrochemical stability window (ESW) of 1-ethyl-3-methylimidazolium ($[emim]^+$) based ILs with different aprotic heterocyclic anions, and it is highly dependent on the anion utilised as shown in figure 1.1.

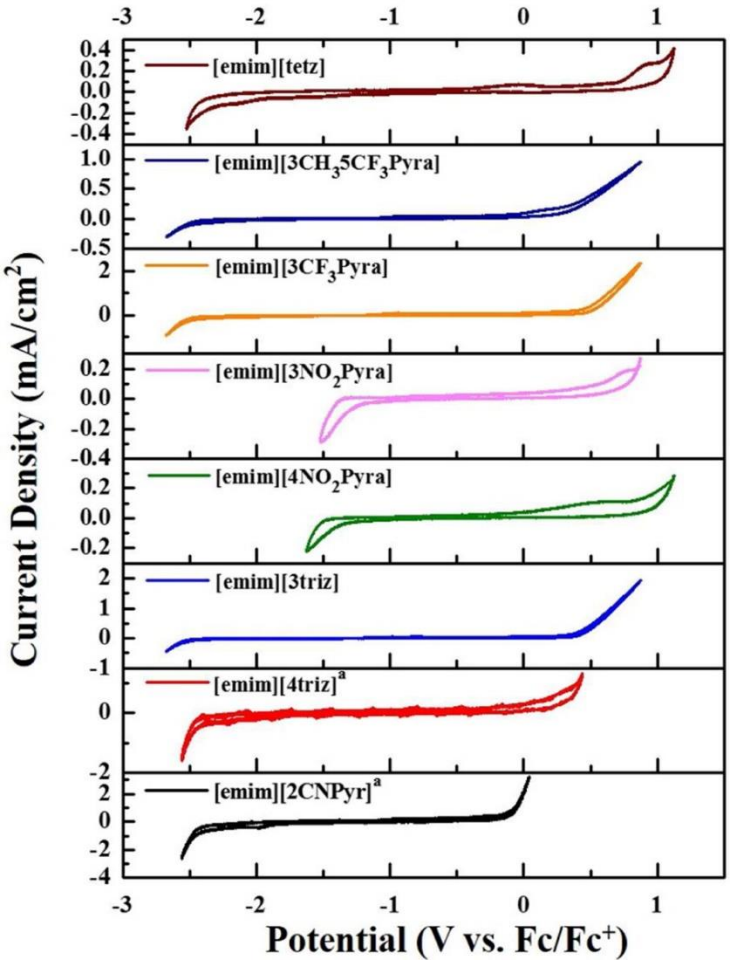

Figure 1.1: Electrochemical windows of [emim]-based ILs measured at ambient temperature at a scanning rate of 100 mV s^{-1} on a glassy carbon working electrode. Reprinted with permission from Sun et al.[18] Copyright 2015 American Chemical Society. [a] Reprinted with permission from Shi et al.[19]

Hayyan *et al.*[20] investigated different cation/anion combinations to determine the effect of the IL structure on its ESW. They determined that certain cations such as phosphonium cations ($P_{14,666}^{+}$) have better reductive stability than others such as pyrrolidinium and imidazolium. Similarly, certain anions (TFSI) offer significantly better oxidative stability than others (e.g. OTf). Understanding the reductive and oxidative limits of cations and anions permits the correct combination to be chosen, in addition to tailoring the combination to suit specific potential needs.

Another parameter to consider is the availability of a "free" proton on the cation of certain ILs. ILs whose cations have this "free" proton are called protic ILs, while those without are referred to as aprotic ILs (AIL) (figure 1.2).[21] Both offer the favourable characteristics associated with ILs such as negligible vapour pressure, non-flammability, and display high chemical and thermal stabilities,[22-24] and some also exhibit high ionic conductivity,[22-24] where AILs are utilised more frequently as electrolytes for LiBs. For more than 10 years, a large number of studies have been dedicated to the use of ILs in LiBs and several types of cations and anions have been used to realize AILs as shown in table 1.1. These cations and anions have been chosen for their favourable properties for LiBs both as the main electrolyte, or as additives in organic electrolytes. In particular, pyrrolidinium-based ILs have demonstrated compatibility with a wide variety of cathode and anode materials.

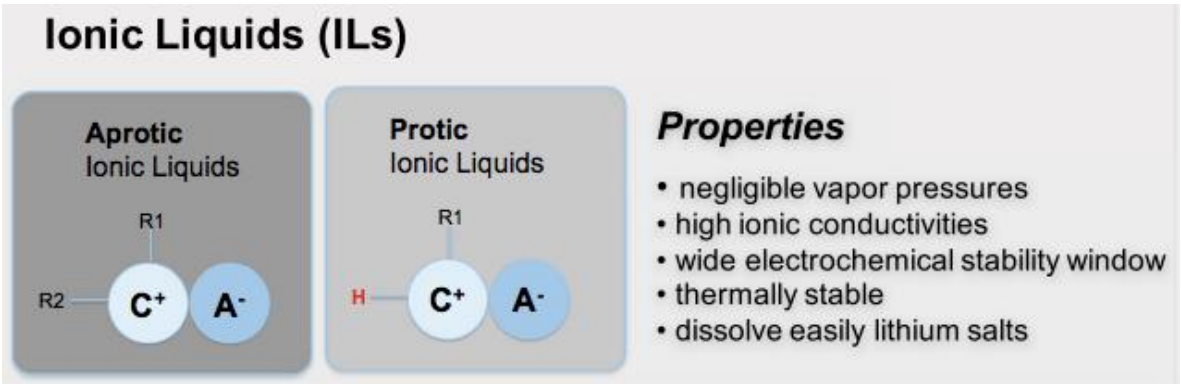

Figure 1.2: Classes and properties of ionic liquids. Reprinted with permission from Balducci et al.[23]

Cation structures	
Parent Structure	Example
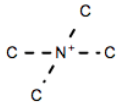 **Ammonium**	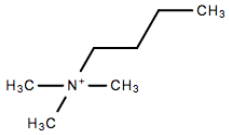 Butyltrimethylammonium
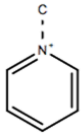 **Pyridinium**	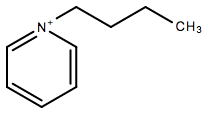 1-butylpyridinium
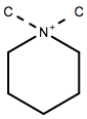 **Piperidinium**	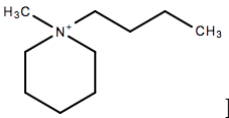 N-butyl, methylpiperidnium
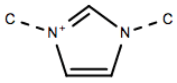 **Imidazolium**	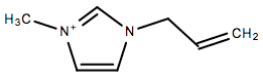 1-allyl-3-methylimidazolium
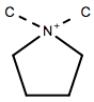 **Pyrrolidinium/Pyrrolidine**	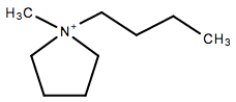 1-butyl-1-methylpyrrolidinium
Anion structures	
Name	Structure
Hexafluorophosphate	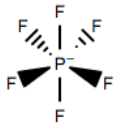
Dicyanamide (DCA)	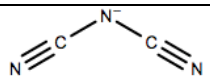
Bis(fluorosulfonyl)imide (FSI / FSA)	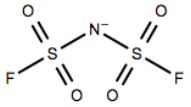
Bis(trifluoromethylsulfonyl)imide (TFSI / TFSA / NTf_2)	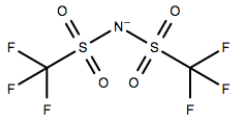

Table 1.1: Structures of aprotic ionic liquid cations and anions typically used in battery applications, where dashed lines in parent structure represent any number of methyl groups.

Pyrrolidinium-based ionic liquids in both liquid and polymer gel forms have demonstrated compatibility with a wide variety of cathode and anode materials for Li-based batteries. The most intensively studied cations are the propyl and butyl types, however, other cations have also been investigated. The cations that will be discussed in the follow sections are outlined in figure 1.3, with their associated abbreviations.

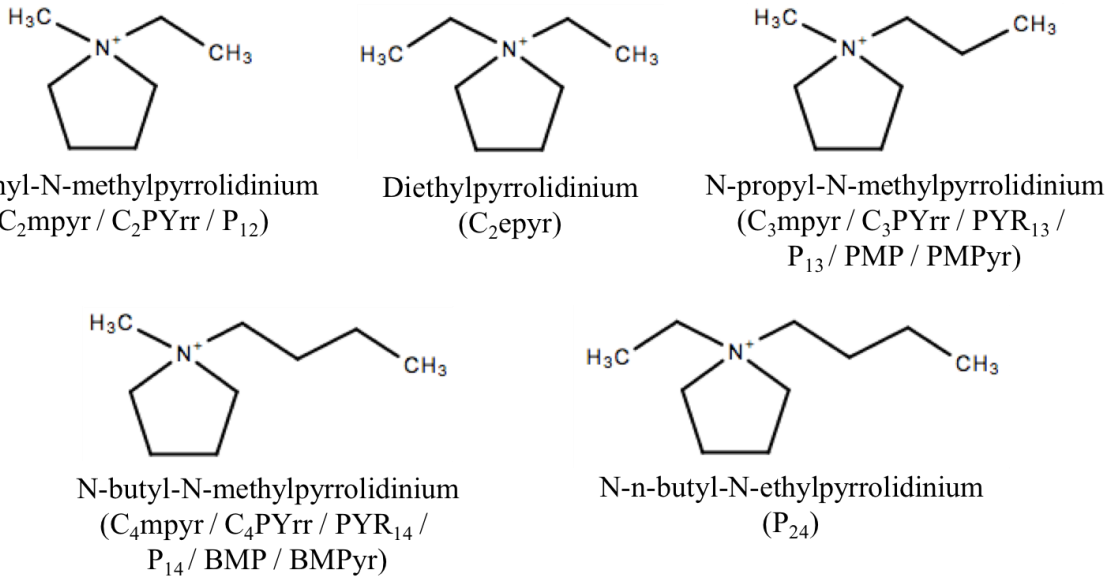

Figure 1.3: Structures and abbreviations of various pyrrolidinium cations.

1.1 N-ethyl-N-methylpyrrolidinium-based ILs

N-ethyl-N-methylpyrrolidinium (C_2mpyr)-based ILs are solids at room temperature.[25] Other ILs consisting of ethyl-based cations have been observed to be solids at room temperature.[26-27] C_2mpyr-based ILs offer distinct structural and transport properties when compared to its longer chain constituents as shorter chains have hindered rotation about the axis which leads to increased viscosity (~9.3 cP vs. ~8.3 cP and ~8.6 cP at 90 ºC) when compared to propyl or butyl side chains, respectively.[25] Many of the electrolytes containing C_2mpyr-cations are polymer gel based rather than liquid. To date, the most commonly used anion for C_2mpyr-based electrolytes is bis(fluorosulfonyl)imide (FSI), with either LiTFSI or LiFSI salt.

Zhou *et al.*[28-29] have investigated polymer gel electrolytes consisting of electrospun PVDF, C_2mpyrFSI and LiFSI salt. In their initial investigation, low LiFSI salt concentrations (1 wt.% to 20 wt.%) were investigated.[28] The optimum LiFSI concentration was determined to be 10 wt.% as it offered a high ionic conductivity (10^{-6} S cm^{-1} vs. 10^{-7} S cm^{-1}), when compared to 1 wt.% LiFSI. The effect of PVDF concentration was also investigated as it interacts on a molecular level with C_2mpyrFSI, which leads to increased molecular disorder.[28] The optimum PVDF content was determined to be 10 wt.% as it provided the best thermal and ionic conductivity properties. Compatibility with Li metal electrodes was determined using a combination of cycling and EIS analysis. The symmetrical Li metal cells were cycled over 500 times at a current density of 0.13 mA cm^{-2} at both room temperature and 50 °C, and the formation of a solid electrolyte interphase (SEI) layer on the Li metal was observed as shown in figure 1.4. For higher LiFSI concentrations, SEI layer formation is continuously observed throughout cycling. Unlike the EIS data in figure 1.4, which shows a reduction in the size of the semi-circle, for higher LiFSI concentrations (>10 wt.%), the semi-circle increased in size, thus highlighting a continuous increase in the interfacial resistance. In both instances, cracks eventually formed on the surface of Li metal, which allowed for the formation of dendrites, however, this occurred after hundreds of cycles which demonstrates that the C_2mpyrFSI-based polymer gel electrolytes are compatible with Li metal electrodes, however, further work is required to mitigate Li dendritic growth to enable long-life cycling of these polymer gels.

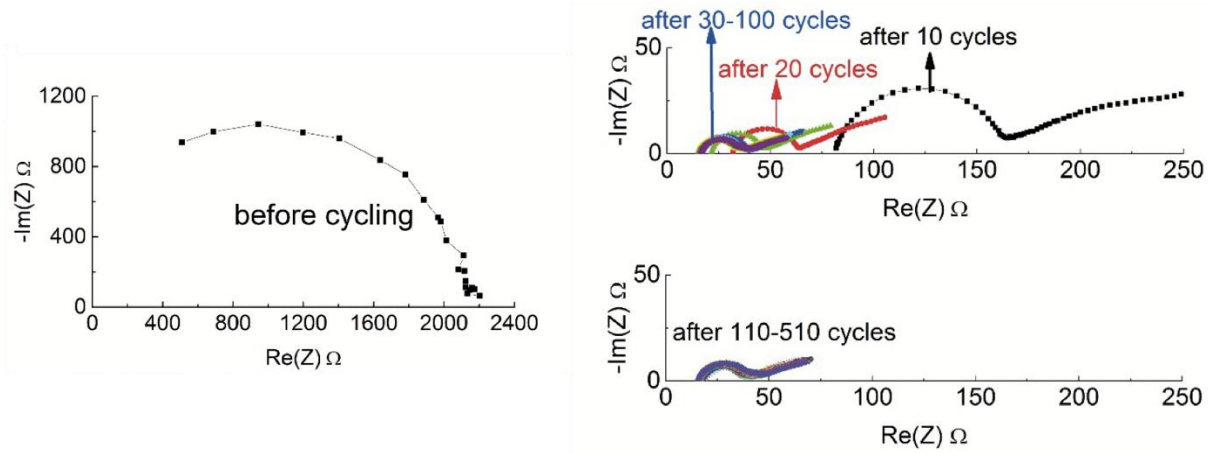

Figure 1.4: Nyquist plots of the Li/C_2mpyrFSI-10 wt.% PVDF-10 wt.% LiFSI /Li symmetric coin cell which was cycled at 0.13 mA cm^{-2} at 50 °C. The impedance was measured every ten cycles. Reproduced from Ref. [28] with permission from the PCCP Owner Societies.

Zhou *et al.*[29] also investigated the compatibility of the C_2mpyrFSI-based polymer gel electrolyte with $LiNi_{0.3}Mn_{0.3}Co_{0.3}O_2$ (NCM). A high cut-off voltage of 4.6 V was utilised to determine the maximum capacity that could be achieved. The initial discharge capacity was ~120 mAh g^{-1} which decreased over 30 cycles, whereby 83% of the initial capacity was obtained (figure 1.5(a)). Comparing these values to a conventional electrolyte (1 M LiPF6 in EC/DEC (1:1) (LP30)), the capacity fade over the 30 cycles is similar as the organic electrolyte yielded a capacity retention of 85% (figure 1.5(b)). The capacity decay in both cases is due to the chemical and structural changes that NCM undergoes at high voltages.[30] Despite the capacity decay, coulombic efficiencies were maintained above 90% over the course of cycling, which demonstrates the potential for this electrolyte in combination with the NCM electrode. A reduction in the cut-off voltage may allow for greater cyclability as the electrolyte demonstrates good rate capabilities, with good capacity recovery (figure 1.5(c)).

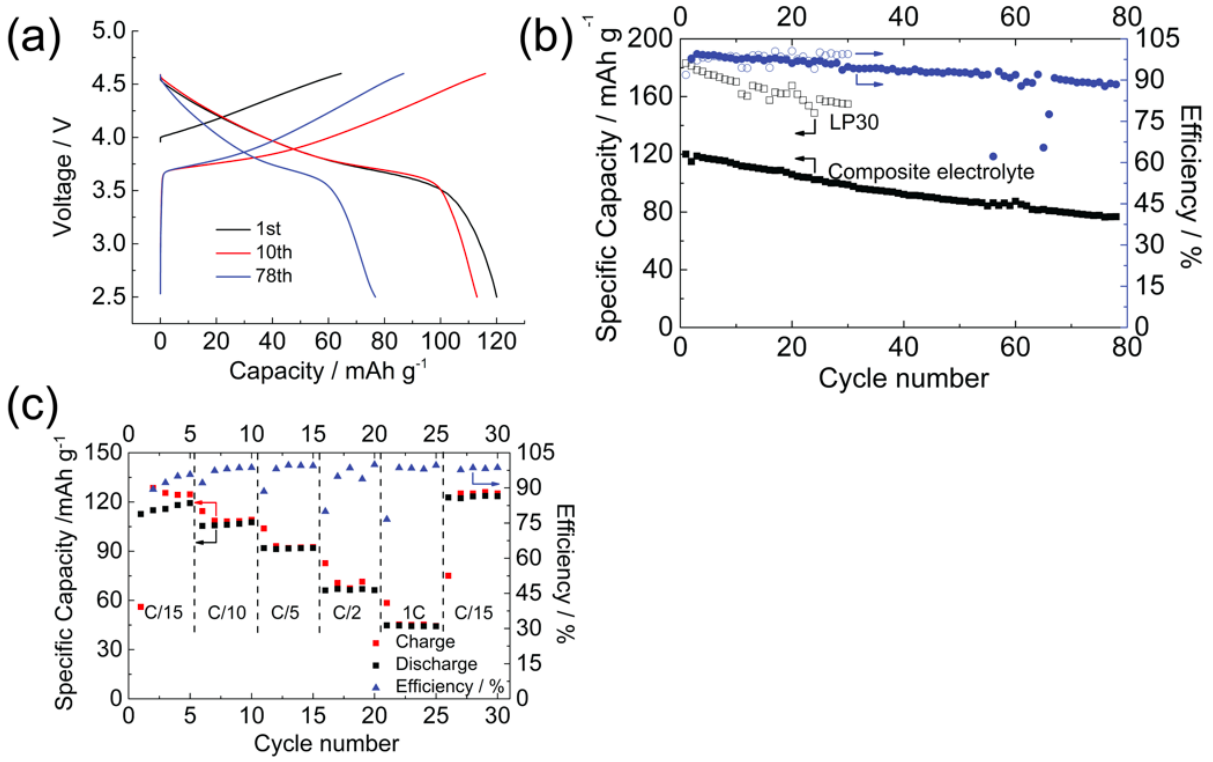

Figure 1.5: NCM electrode with C_2mpyrFSI composite electrolyte cycling at ambient temperature where (a) voltage vs. capacity data, (b) cycling data at C/15 with comparison of NCM with organic electrolyte (LP30) and (c) capacity vs. cycle number at different C-rates. Reprinted with permission from Zhou et al.[29]

Other authors have demonstrated the viability of C_2mpyr-based IL electrolytes when utilising a polymeric ionic liquid (PIL) rather than conventional polymer matrices. Utilisation of PILs should enable higher ionic conductivities in addition to better film forming properties and desirable electrochemical properties.[31-32] Li *et al.*[33] utilised the PIL: poly(diallyldimethylammonium) bis(trifluoromethylsulfonyl)imide (P(DADMA)-TFSI) with C_2mpyrFSI and LiTFSI salt. The salt content was maintained at 20%, while different weight ratios of PIL:C_2mpyrFSI were utilised. Transparent membranes were obtained for weight ratios higher than 40:60. All films exhibited amorphicity as indicated by the absence of endothermic peaks in the XRD data. Thermal stability above 250 °C was exhibited for 50:50, 60:40 and 70:30 gels, with 50:50 gels exhibiting the highest

ionic conductivity of 1.54 x10^{-4} S cm^{-1} at 25 °C. This value is significantly improved when compared the electrospun PVDF-based polymer gel electrolytes by Zhou *et al.*[28-29] Compatibility with Li metal was demonstrated and 1000 cycles achieved in a symmetrical cell without short circuiting. The performance of the electrolyte over a variety of temperatures was investigated with LFP half-cell (figure 1.6(a)). At 0.2 C, the initial discharge capacities and coulombic efficiencies at 25 °C, 40 °C and 80 °C are 122.3 mAh g^{-1} with 77.8%, 150.2 mAh g^{-1} with 89.2% and 163.6 mAh g^{-1} with 97.6%, respectively. All cells maintained their capacity over the course of 150 cycles, with an improvement in the capacity for the cell cycled at 25 °C. Dendrite formation was hindered, however, post-mortem analysis revealed the presence of pits (figure 1.6(b)) on the surface of the Li metal electrode, which may have yielded dendrites upon prolonged cycling.[28]

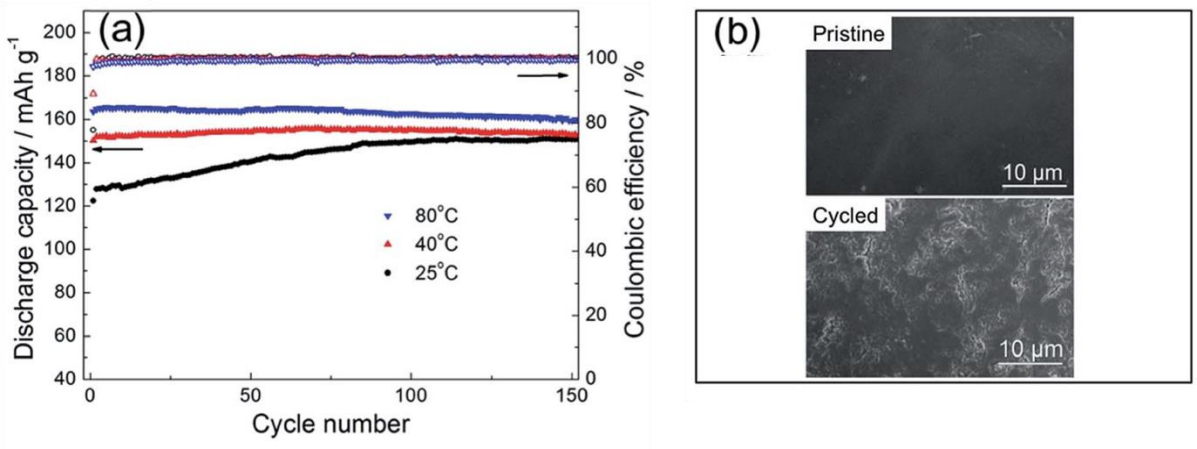

Figure 1.6: (a) discharge capacity and coulombic efficiency versus cycle number at 25 ℃, 40 ℃ and 80 ℃ at a current rate of 0.2 C, (b) SEM images of the pristine lithium and lithium anodes after a rate test Adapted from Ref. [33]with permission from The Royal Society of Chemistry.

The utilisation of C_2mpyr-based ILs is not limited solely to polymer gel electrolytes that are sandwiched between two electrodes as other research groups have investigated the in-situ formation of the ionogel electrolyte within an electrode to ensure encapsulation of the electrode particles.[34] SEM and EDX analysis of the electrodes demonstrate the penetration of the ionogel (green – sulphur

from TFSI) into the electrode as the electrode particles (red) are encapsulated by the ionogel as shown in figure 1.7. This is a viable method for ensuring high surface contact between the gel-based electrolyte and the electrode, particularly where particle or nanostructured materials are utilised.

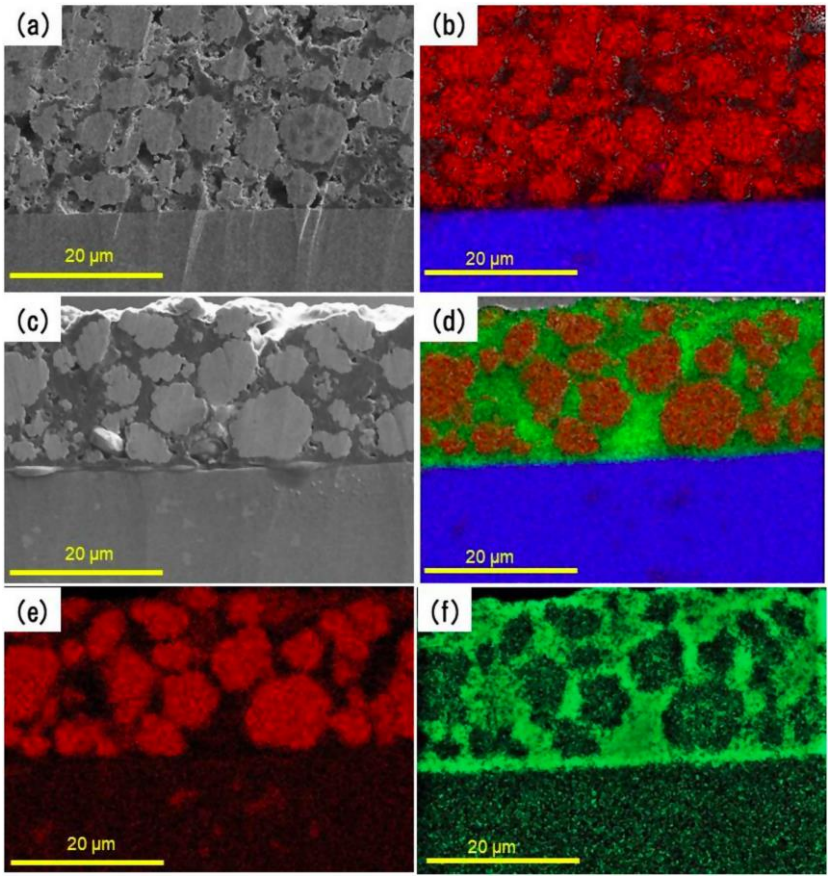

Figure 1.7: SEM and EDX-mapping images of the sectional view of the NMC cathode. (a) and (b) are with no ionogels (control sample) and (c) and (d) are with ionogel respectively. Red, green and blue colours indicate cobalt (NMC), sulphur (ionogels) and aluminium (current collector), respectively. (e) and (f) are EDX-mapping images of cobalt and sulphur extracted from (d). Reprinted with permission from Ogawa et al.[34]

A full cell was assembled by Ogawa *et al.*[34] to demonstrate the enhanced capabilities of the encapsulated cathode and anode particles. The full cell consisted of an LTO anode and NMC cathode. The cell achieved 47% and 65% of the theoretical capacity for 0.05 C and 0.01 C. These results pave

the way for further analysis of polymeric ionic liquid-based electrolytes as they can be synthesised using solvent free processes and have high wettability of the electrode material.

In addition to the utilisation of PILs, further research is being carried out to determine alternative cation-anion combinations of the C_2mpyr-based electrolytes which may yield more favourable properties than typical FSI and TFSI-based ILs. Recently, Yamaguchi *et al.*[35] investigated the effect of various anions on the properties of the IL salt, as it has been reported that FSI-based salts offer higher ionic conductivities (1.23 $x10^{-6}$ S cm^{-1}), than TFSI-based salts.[36] In addition, high ionic conductivities of 1 $x10^{-3}$ S cm^{-1} have been reported for carbamoylcyano(nitroso)methanide (ccnm) anions in combination with C_2mpyr cations.[37] Yamaguchi *et al.*[35] investigated the anions outlined in figure 1.8. From the investigation, it was determined that the ionic radius ratio ($\rho = r_{small\ ion}/r_{large\ ion} < 1$) can have an effect on the ionic conductivities. Lower ρ values exhibited higher ionic conductivities, which is attributed to the size and concentration of vacancies within the crystal,[38-40] therefore, lower ρ values have more voids due to large differences in the ionic radii. This allows for greater tunability of the IL, whereby new battery electrolytes can be considered with anions different to typical FSI or TFSI-based anions. Further work is required before new anions can be realised for battery applications, however, these results demonstrate that favourable thermal and ionic conductivity properties can be attained using unconventional anions.

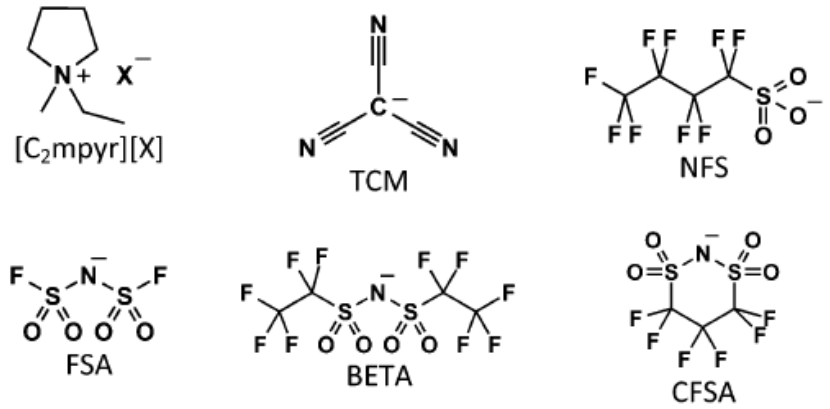

Figure 1.8: Chemical structures of pyrrolidinium cation and various anions investigated by Yamaguchi et al. Reproduced from Ref. Yamaguchi et al.[35] with permission from The Royal Society of Chemistry.

Limited cathode and anode analysis has been carried out as NCM, LFP, LTO and Li metal have demonstrated compatibility with C_2mpyr-based electrolytes. The primary cation/anion combination for C_2mpyr-based electrolytes is C_2mpyrFSI with little literature dedicated to C_2mpyrTFSI-based electrolytes. Further investigations into different C_2mpyr/anion combinations may lead to next generation battery electrolytes, however, in order to realise microbatteries for IoT sensors, other pyrrolidinium-based ILs whose physiochemical properties have been thoroughly characterised need to be investigated.

1.2 N-propyl-N-methylpyrrolidinium-based ILs

Characterisation of N-propyl-N-methylpyrrolidinium (C_3mpyr)-based ILs have been carried out by many research groups to determine the physiochemical properties of the IL with various anions.[41-42] In addition, studies regarding the biodegradability and solubility of C_3mpyr-based ILs, and other pyrrolidinium-based ILs have also been investigated.[43] Thermal stability analysis has been carried out using commercial electrode materials (NCM, LFP, graphite, etc.) with LiFSI salt in C_3mpyrFSI electrolytes.[44] In addition to thermal stability, the total heat generated by the electrode was

determined where the electrodes were at various states of charge.[44] This study also determined that certain cathode and anode materials may undergo exothermic reactions at different temperatures, therefore, demonstrating the need to select the correct electrode material for high temperature applications (figure 1.9).

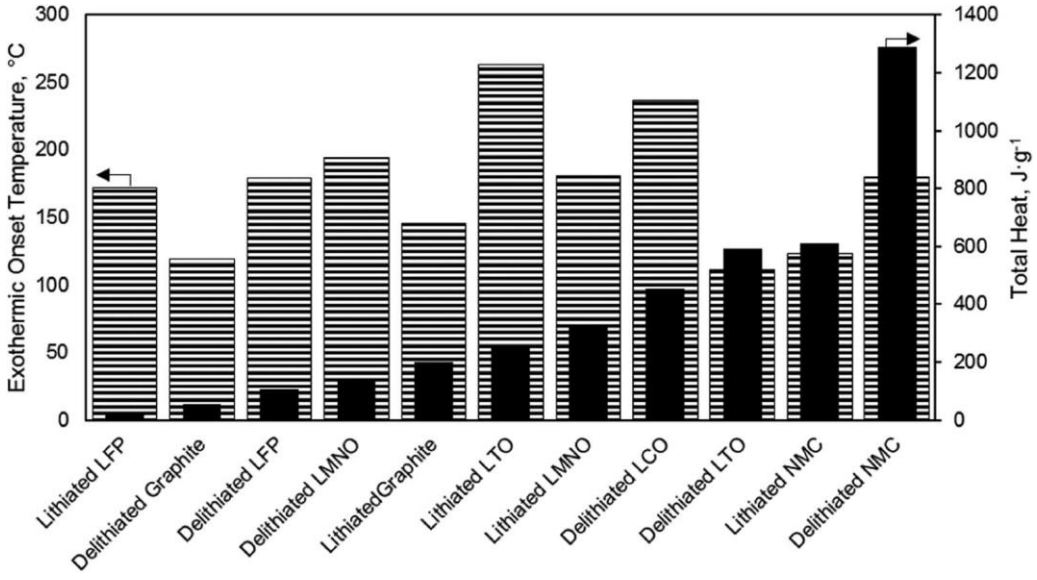

Figure 1.9: Total heat and exothermic onset temperature for cycled electrode from C_3mpyrFSI electrolyte cells. Reprinted with permission from Francis et al.[44]

The characterisation of C_3mpyr-based electrolytes also extends to its compatibility with different types of separators,[45-46] particularly when Li metal anodes are utilised. The long-term cyclability of Li metal based cells is affected by the separator and small pore sizes (~0.06 µm) can prevent short circuits by inhibiting Li dendrites from penetrating the separator.[46] Further information regarding different separator materials can be found in the review by Francis *et al.*[45]

Compatibility with various cathode and anode materials have been demonstrated in C_3mpyr-based electrolytes. In some cases, the C_3mpyr-based electrolytes were utilised as an interlayer,[47] however much of the research has focused on its use as an electrolyte. Two cation/anion combinations have been extensively investigated, namely, C_3mpyrFSI and C_3mpyrTFSI. For the conventional cathode

materials such as lithium nickel manganese cobalt oxide (NMC) and lithium iron phosphate (LFP) electrodes, analysis studies have been carried out primarily with C_3mpyrFSI and either LiTFSI or LiFSI salt. NMC electrodes have demonstrated electrochemical performances comparable to organic electrolytes such as 1.0 M $LiPF_6$ in EC:DEC, (1:1) particularly at low C-rates as shown in figure 1.10(a).[48] Extended cycling at 1 C, demonstrates the overall electrochemical stability of the IL as minimal capacity fade is observed in the IL, while capacity fade is evident for the organic electrolyte (figure 1.10(b)) which is attributed to the formation of a stable SEI layer within the ionic liquid electrolyte.[48]

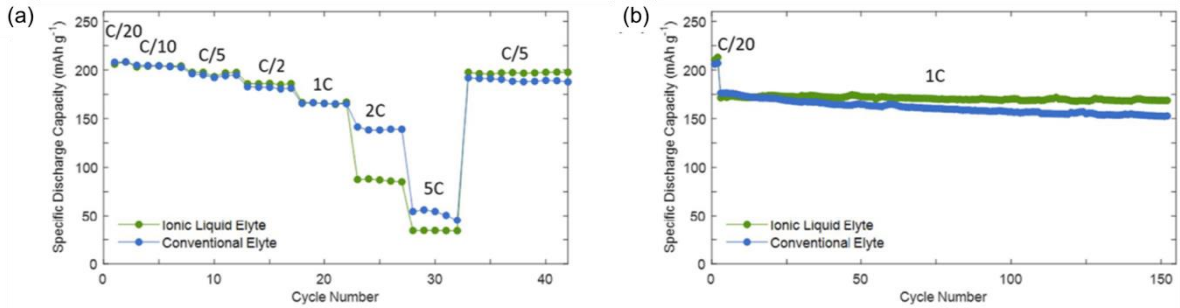

Figure 1.10: (a) NCM-811 rate study comparing IL and organic electrolyte performances, (b) long-term cycling at 1 C. Adapted with permission from Heist et al.[48]

Much like the NMC electrodes, LFP electrodes have also been investigated with C_3mpyrFSI-based electrolytes. For example, Lewandowski *et al.*[49] reported that the combination of C_3mpyrFSI and 0.5 mol kg^{-1} LiTFSI has been shown to work effectively as an electrolyte solution with a metallic lithium anode and LFP cathode. Even at 4 C rate, a discharge capacity of 110 mAh g^{-1} was obtained at 50 ºC, which demonstrates the excellent cyclability of the C_3mpyrFSI electrolyte with the LFP cathode.

Electrolyte mixtures consisting of C_3mpyrTFSI and C_3mpyrFSI have been investigated with NMC and LFP electrodes, whereby different conducting salts were utilised. In the case of NMC, LiTFSI salt was utilised, and the optimum ratio of C_3mpyrTFSI:C_3mpyrFSI was determined to be 3:6.[50]

When LiFSI salt is utilised the optimum ratio of C_3mpyrTFSI:C_3mpyrFSI was determined to be 1:1 when LFP electrodes are utilised.[51] Due to the different properties of the conducting salts, the optimum ratios were chosen based on a compromise between fast ion transport properties, electrochemical/thermal stability, good film forming ability and cost.[50] Huang *et al.*[51] showed that the ternary electrolyte exhibited the best long-term cyclability when compared to its binary analogues: 0.5 M LiFSI in C_3mpyrFSI, 0.5 M LiTFSI in C_3mpyrTFSI and 0.5 M LiFSI in C_3mpyrTFSI at room temperature, and sub-zero temperatures. This paves the way for low-temperature application electrolytes, as most of the research focus is on high-temperature applications. Further work to optimise the ratio of C_3mpyrTFSI to C_3mpyrFSI, could lead to improvements in the electrode capacity obtained at elevated and low temperatures, as binary mixtures such as that tested by Lewandowski *et al.*[49] with higher electrode capacities at higher C-rates (4 C).

The studies described above focused on C_3mpyrFSI-based electrolytes, however analysis of other cathode materials is focused primarily on C_3mpyrTFSI-based electrolytes. The results obtained in this electrolyte are promising as the electrodes exhibit high electrode capacities and coulombic efficiencies. One such example is a composite cathode material: $0.3Li_2MnO_3$-$0.7LiMn_{1.5}Ni_{0.5}O_4$,[52] whereby the IL-based electrolyte exhibited a superior performance when compared to organic based electrolytes, 332 mAh g^{-1} and 310 mAh g^{-1} respectively. Even at high current densities such as 750 mA g^{-1} the IL outperforms the organic electrolyte due to the mitigation of Mn dissolution. This shows that electrode dissolution can be hampered if the correct electrolyte is selected.

Similarly, high capacity cathode materials (>200 mAh g^{-1}) have been investigated with C_3mpyrTFSI ILs. One such material, nickel sulphide, has attracted a lot of attention due to its high theoretical capacity (590 mAh g^{-1} for NiS, and 462 mAh g^{-1} for Ni_3S_2). The NiS-Ni_7S_6 material exhibited the best CV performance when utilised with 1 M LiTFSI in C_3mpyrTFSI as stable cycling was observed

in addition to higher electrode capacities when compared to an organic electrolyte as shown in figure 1.11.

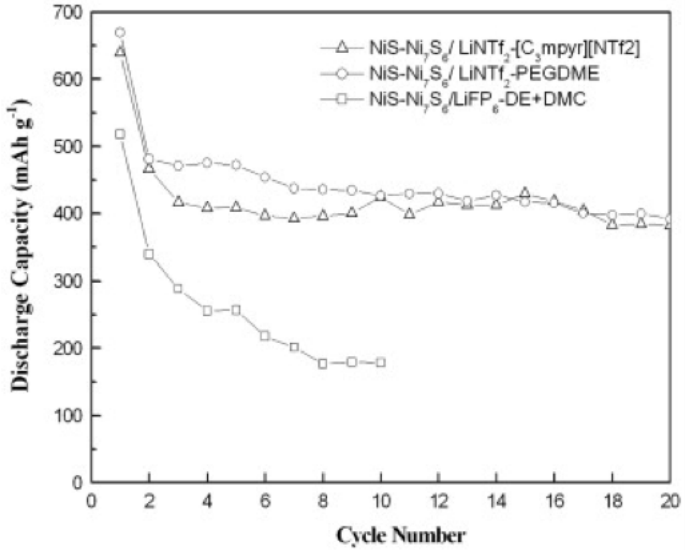

Figure 1.11: Discharge capacities vs. cycle number for NiS-Ni_7S_6 using three different electrolytes. Reprinted with permission from Wang et al.[53]

Studies with vanadium pentoxide (V_2O_5) have also indicated promising electrochemical performances as different morphologies including nanoribbon, nanowire, microflake and commercial powder were investigated with C_3mpyrTFSI.[54] Each morphology yielded greater specific capacity when compared to a conventional organic electrolyte (1 M $LiPF_6$ in EC/DMC (1:1)) as shown in figure 1.12.

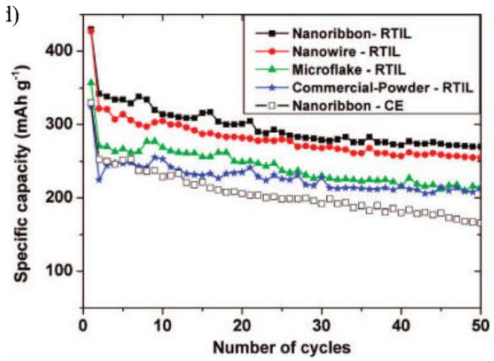

Figure 1.12: Cycle life of V_2O_5 electrodes in C_3mpyrTFSI-based electrolyte (RTIL) and conventional electrolytes (CE) at 25 ºC, where 0.1 C was utilised. Adapted with permission from Chou et al.[54]. Copyright 2008 American Chemical Society.

Similarly for the anode materials, conventional materials such as graphite[50, 55-56] are compatible with the C_3mpyr-based ILs, however, alternative anode materials such as Si have been investigated, and continue to be investigated due to the high gravimetric capacity compared to graphite, and its increased safety when compared to Li metal. More recent research is focused on coated or doped Si films to improve the cyclability of the Si electrodes by buffering or mitigating the expansion and contraction effects upon cycling with Li. Graphene coated Si nanoparticles exhibited superior reversible cycling in C_3mpyrFSI-based electrolyte when compared to the organic electrolytes as shown in figure 1.13.

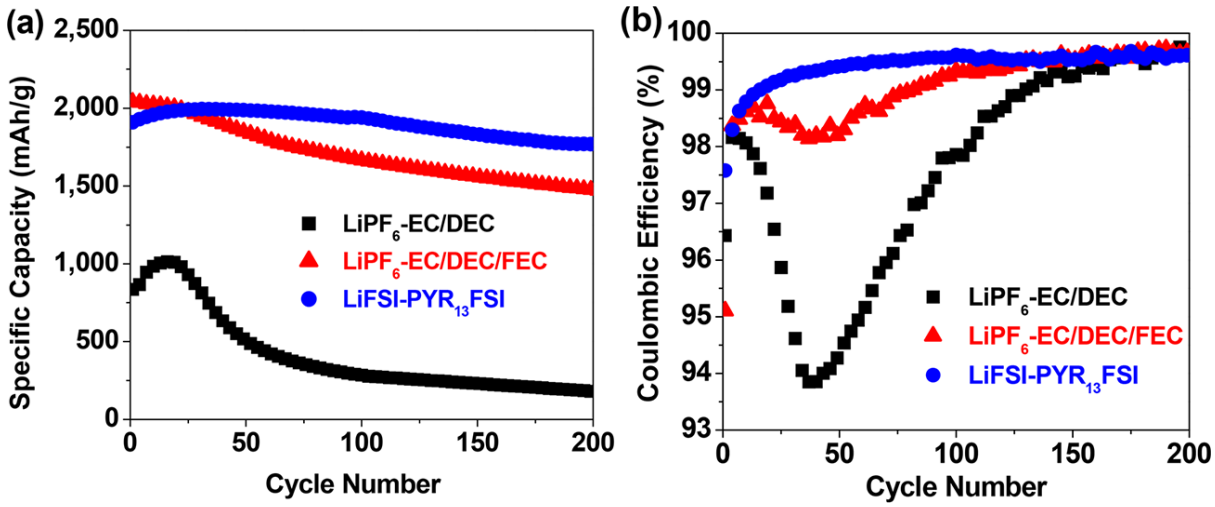

Figure 1.13: Graphene coated Si-NP in various electrolytes (a) The delithiation capacities and (b) Coulombic efficiencies. Reprinted with permission from Park et al.[57] Copyright 2017 American Chemical Society.

Domi *et al.*[58] investigated the effects of doping-Si anodes by comparing doped and undoped Si in 1 M LiFSI and C_3mpyrFSI electrolytes. From their investigation it was determined that P-doping led to reduced vertical electrode expansion during cycling with the IL electrolyte as shown in figure 1.14. Instead of vertical expansion, the films experience horizontal expansion initially, and vertical expansion is noted after the 600th cycle. The expansion rate within organic based electrolytes is faster than for the IL electrolytes, hence the increased cycle numbers observed for the IL electrolytes as over 1400 cycles were reported for the P-doped Si electrodes with 1 M LiFSI and C_3mpyrFSI electrolyte.

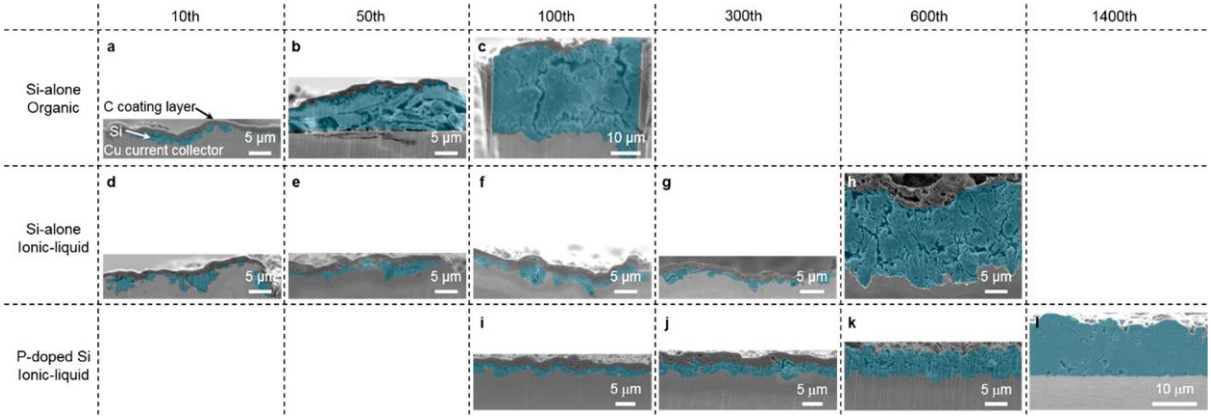

Figure 1.14: Cross-sectional SEM images of lithiated Si active material layers with a charge capacity limit of 1000 mAh g^{-1}. The blue coloured area indicates Si, while the topmost layer is a carbon coating. Reprinted with permission from Domi et al.[58]. Copyright 2019 American Chemical Society.

A comparison of C_3mpyrFSI and C_3mpyrTFSI was investigated to determine the effect of the anion on P-doped Si electrodes. Yodoya *et al.*[59] demonstrated that C_3mpyrFSI-based electrolytes offer better cyclability with phosphorous-doped Si (P-Si) anode than its TFSI-counterpart. As shown in figure 1.15, the C_3mpyrFSI-based electrolytes (Py13-FSA) exhibited stable cycling for over 1400 cycles, with a discharge capacity of 1000 mAh g^{-1}, while the TFSI-counterpart yielded the same discharge capacity for only 600 cycles. The difference in their compatibility with Si anodes is further highlighted when rate capabilities are investigated (figure 1.15(b)). Similar cycling was observed for both ILs, however, at rates above 2 C, the TFSI-based IL experiences a drop in the capacity, while the FSI-based IL maintains 1000 mAh g^{-1} regardless of the rate.

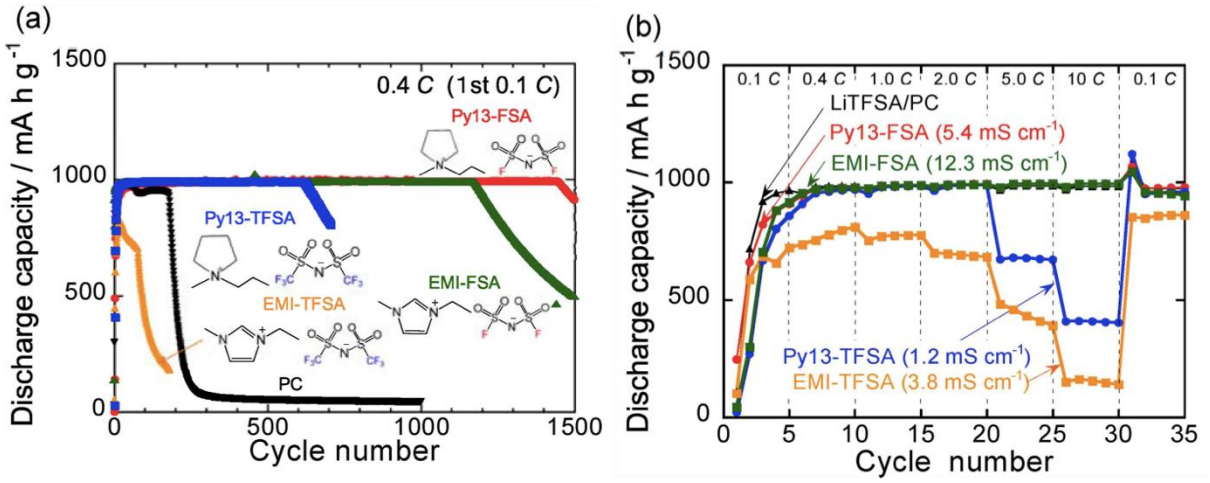

Figure 1.15: (a) Cycling performance and (b) rate capability of P-doped Si electrode in various ionic liquid electrolytes. Reprinted with permission from Yodoya et al.[59]

Further analysis of doped Si films may pave the way for high capacity and long-cycle life anode materials. Nguyen *et al.*[60] investigated Si-Cu anodes with capacities of 1500 mAh g^{-1} over 200 cycles. As Cu is a common current collector material, utilisation of it within the anode material would allow for shorter Li^+ diffusion pathways, and that nanostructuring may be beneficial.

The electrolyte that has been extensively studied with Si is C_3mpyrFSI, this is the same electrolyte that has shown compatibility with NMC and LFP electrodes, therefore, the potential for full cells consisting of Si anodes with either NMC or LFP cathodes can be constructed. However, to date no full cell utilising an Si anode and C_3mpyrFSI electrolyte has been constructed and tested. A full cell containing NMC and graphite has been investigated,[55] where electrochemical impedance analysis was utilised to determine the optimum LiFSI:C_3mpyrFSI ratio. It was determined to be 40:60, as it offered the lowest overall cell resistance, in addition to the highest ionic conductivity. From the impedance analysis it was determined that the maximum cycling rate that could be achieved by the cell is 0.77 C. This analysis is important as it allows researchers to determine the maximum cycling rate of the battery based on cell resistance. This allows for quick analysis of the cells, which highlights the need for improved interfacial contacts between the cathode/electrolyte, anode/electrolyte and

cell/cell, and if optimised could lead to higher C-rate performances. However, to the best of my knowledge no other full cells have been constructed and analysed with C_3mpyr-based electrolytes in their liquid states.

There has been extensive research carried out on C_3mpyr-based polymer gel electrolytes where the two common cathode materials investigated are NMC and LFP. Polymer gel electrolytes that have demonstrated compatibility with NMC electrodes consist of either C_3mpyrFSI or C_3mpyrTFSI. The polymer gel containing C_3mpyrTFSI also contained organic components such as ethylene carbonate (EC), dimethyl carbonate (DMC) and fluoroethylene carbonate (FEC) as shown in figure 1.16.[61] The polymer gel yielded an ionic conductivity of 10^{-4} S cm^{-1} at room temperature, which is one order of magnitude lower than the liquid analogue, which is attributed to the addition of the UV crosslinkers which are inactive components within the gel.[61]

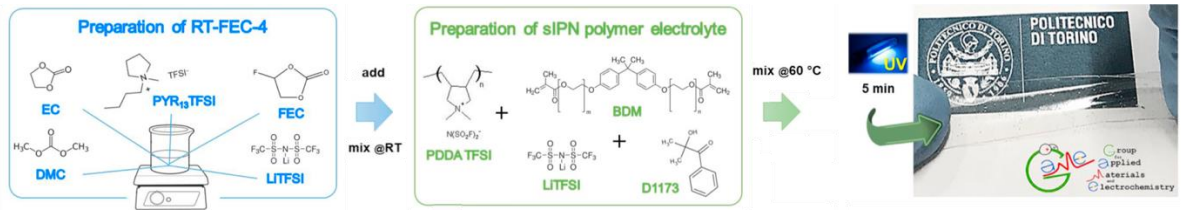

Figure 1.16: Synthesis scheme of crosslinked sIPN polymer electrolyte with photograph. Reprinted with permission from Nair et al.[61]

By utilising alternative polymer materials such as poly(vinylidene fluoride-co-hexafluoropropylene) (PVDF-HFP), polymer gels with high ionic conductivities such as 3.9 x10^{-3} S cm^{-1} at 30 ºC can be obtained as reported by Singh *et al.*[62] In this instance, only PVDF-HFP, 20% wt. LiTFSI and C_3mpyrFSI were utilised, and higher electrode capacities were obtained at C/10 rate, where temperatures of 25 ºC were employed (~180 mAh g^{-1} vs. ~100 mAh g^{-1}) when compared to the cross-linked polymer gel synthesised by Nair *et al.*[61]

These results show that the incorporation of organic electrolytes within the polymer gel electrolyte is not necessary to achieve high ionic conductivities and electrode capacities. Adjusting the polymer matrix from PVDF-HFP to polyethylene oxide (PEO) can lead to significant changes to the electrochemical properties of the gel. For example, Gupta *et al.*[63] utilised a PEO matrix with 20 wt.% LiFSI salt and C_3mpyrFSI, and the highest ionic conductivity of the synthesised polymer gels was 1.14 x10^{-5} S cm^{-1} which is lower than PVDF-HFP-based polymer gels. When tested with LFP electrodes, it was determined that the interfacial kinetics are more favourable with the polymer gel electrolyte when a graphene oxide coat is applied to LFP, thus resulting in higher electrode capacities as shown in figure 1.17.

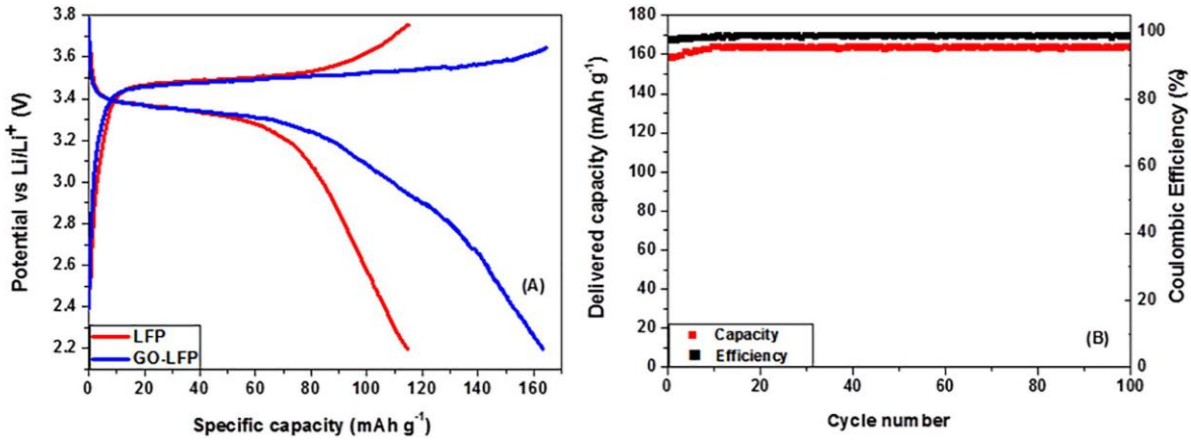

Figure 1.17: (a) Voltage vs. capacity profile of LFP and GO-LFP at 0.1 C-rate. (b) Discharge capacity and Columbic efficiency vs. cycle number of GO-LFP at 0.1 C. Reprinted with permission from Gupta et al.[63]

Guerfi *et al.*[64] immersed LFP and Li metal electrodes in C_3mpyrFSI and 0.7 M LiFSI with 5 wt.% polymer (ether based). Heating the cell under vacuum enables electrolyte penetration of the LFP electrode, which allowed for the formation of a stable SEI layer when cycled with Li. This resulted in capacities that were close to the rated capacity for all rates up to 2 C within an LFP/graphite full cell.

Utilisation of the TFSI anion has proven to be the more popular choice for polymer gel electrolytes when analysed with LFP electrodes. Numerous groups have studied C_3mpyrTFSI-based polymer gel using a variety of methods such as cross-linking[65] and coagulation.[66] Cross-linked polymer gel electrolytes such as that synthesised by Li *et al.*[65] have shown promising results as high electrode capacities and coulombic efficiencies (151.9 mAh g^{-1}, with a coulombic efficiency of 87.9%) are obtained at room temperature. After 80 cycles, an electrode capacity of 131.9 mAh g^{-1} is retained (figure 1.18), which corresponds to a 13% capacity drop over the course of 80 cycles. These figures are impressive as elevated temperatures (>40 ºC) are utilised in the case of other polymer gel electrolytes in order to achieve high electrode capacities.

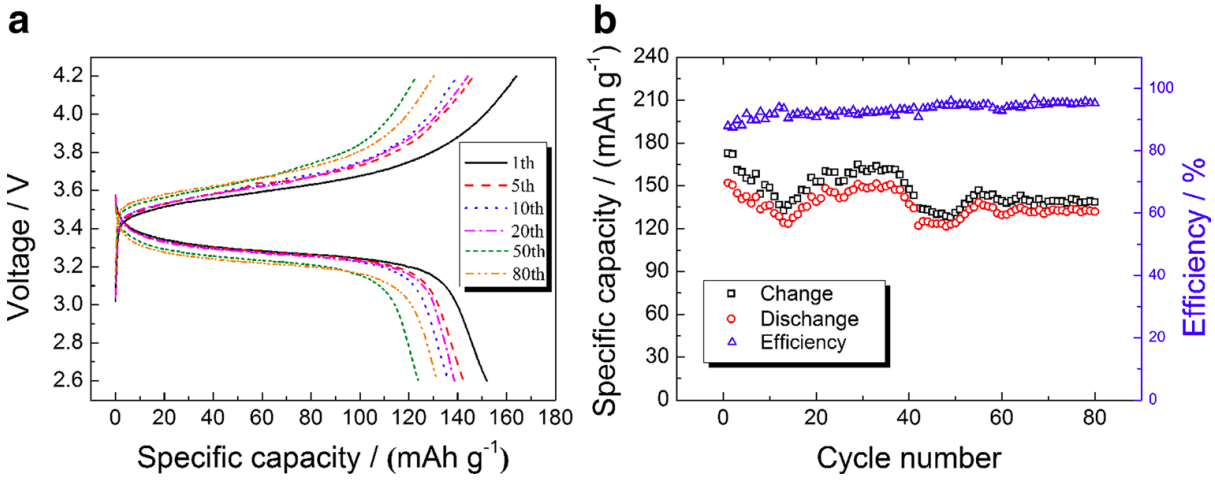

Figure 1.18: Voltage vs. specific capacity curves (a) and specific capacity vs. cycle numbers (b) of the Li/polymer/LFP cells during the charge-discharge process. Reprinted with permission from Li et al.[65]

Coagulation synthesis methods are beneficial for the formation and control of porous membranes as demonstrated by Yang *et al.*[66] By controlling the amount of time spent in the coagulation bath, the porosity of the polymer gel electrolyte can be tailored as shown in figure 1.19. The porosity of the polymer gel greatly affects its ionic conductivity, with the highest values obtained for the polymer gels which spent 5 minutes or less within the coagulation bath (more porous).

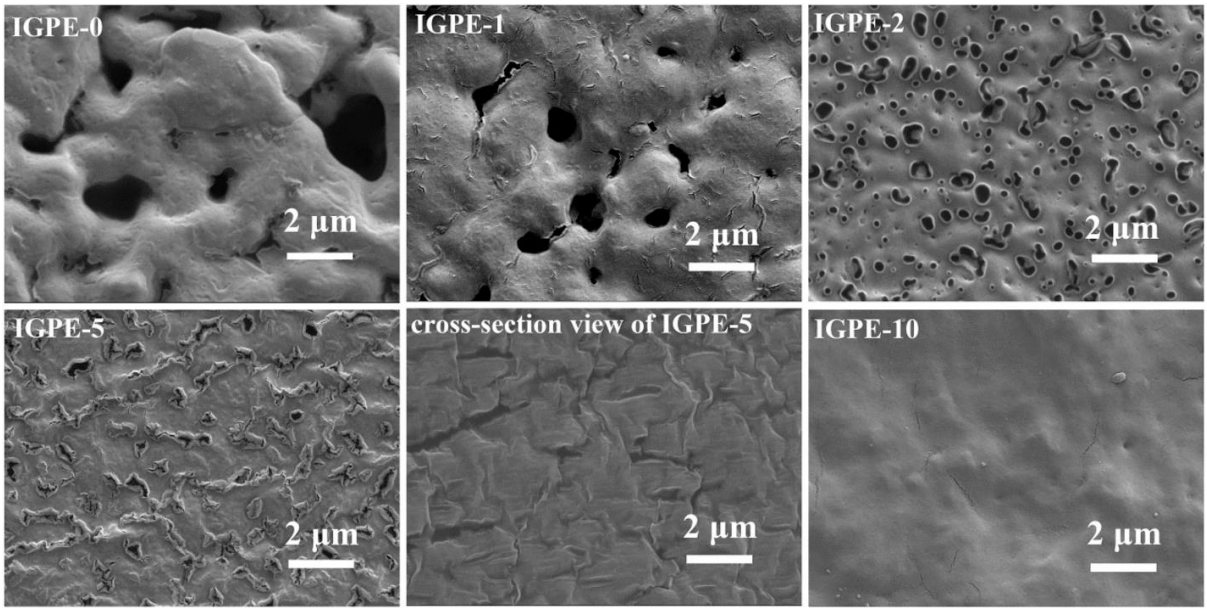

Figure 1.19: SEM images of different IGPE membranes, where the number refers to the length of time (in minutes) the gel spent in the coagulation bath. Reprinted with permission from Yang et al.[66]

The electrochemical tests carried out by Yang *et al.*[66] boasted an improved electrochemical performance when compared to the cross-linked polymer gel synthesised by Li *et al.*[65] as an electrode capacity of ~150 mAh g^{-1} was maintained over the course of 200 cycles with no substantial capacity fade occurring over the course of 200 cycles at room temperature. Electrode capacities above 100 mAh g^{-1} are maintained even at high C-rates such as 3 C (figure 1.20(b)). Elevated temperatures further enhance the electrochemical performance of the cell as electrode capacities higher than 150 mAh g^{-1} are attained, with minimal capacity fade observed over the course of 200 cycles as shown in figure 1.20(c). A similar trend was noted previously with C_3mpyrFSI-based polymer gels, whereby the cross-linked polymer gel yielded poorer electrochemical performances when compared to the PVDF-HFP-based polymer gels.

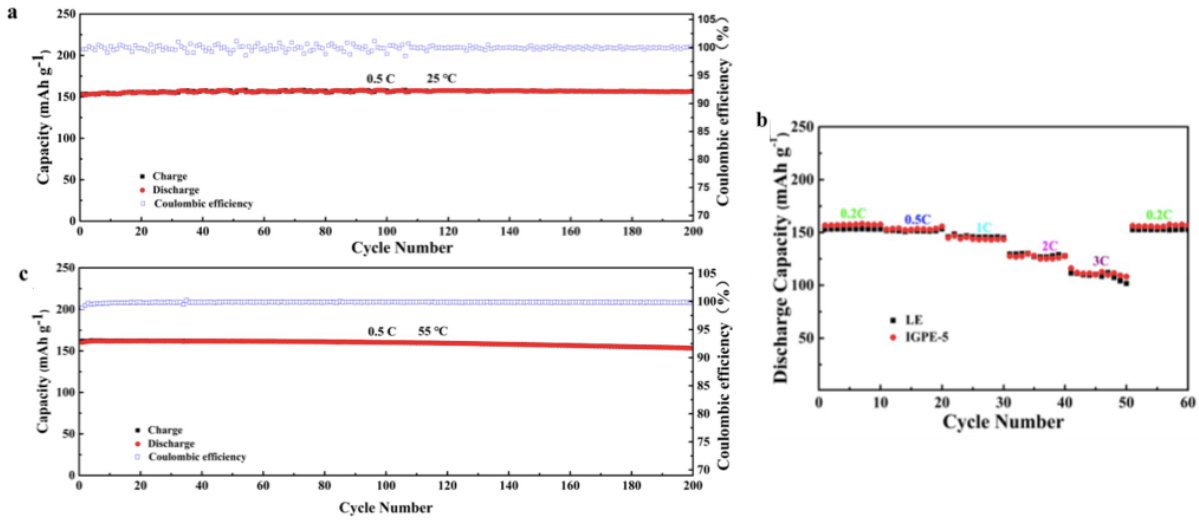

Figure 1.20: (a) Cycle performance of the LFP/IGPE-5/Li cell at 25 ºC, (b) Rate performance of the LFP/IGPE-5/Li and LFP/LE/Li cell at different current densities at 25 ºC. and (c) cycle performance of the LFP/IGPE-5/Li cell at 55 ºC. Reprinted with permission from Yang et al.[66]

The utilisation of inorganic materials within polymer gels have been investigated to enhance the mechanical strength, while improving ion transport properties. Kim *et al.*[67] utilised amine functionalised boron nitride nanosheets (AFBNNS) as an additive within a C_3mpyrTFSI-based polymer gel. The addition of AFBNNS led to an improvement in the mechanical strength and thermal stability, in addition to yielding high Li^+ transference numbers of 0.12 to 0.23, which are comparable to Yang *et al.*[66] The electrochemical performance of LFP with the AFBNNS-based polymer gel electrolyte offers similar performances to Yang *et al.*[66], as high electrode capacities 142.4 mAh g^{-1} and 132.8 mAh g^{-1} were obtained at 0.1 C and 0.2 C respectively as shown in figure 1.21. Without the presence of the AFBNNS, rapid capacity loss is observed over 60 cycles for the liquid and polymer gel electrolytes. Similarly, for NCM and LCO cathode materials, the electrochemical performance is greatly enhanced when AFBNNS-based polymer gel electrolytes are utilised (figure 1.21(b and c)). At elevated temperatures (80 ºC), the LFP cell can deliver a high discharge capacity of 162.1 mAh g^{-1} at 2nd cycle with 91.3% of specific capacity retained after the 50th cycle (figure 1.21(d)).

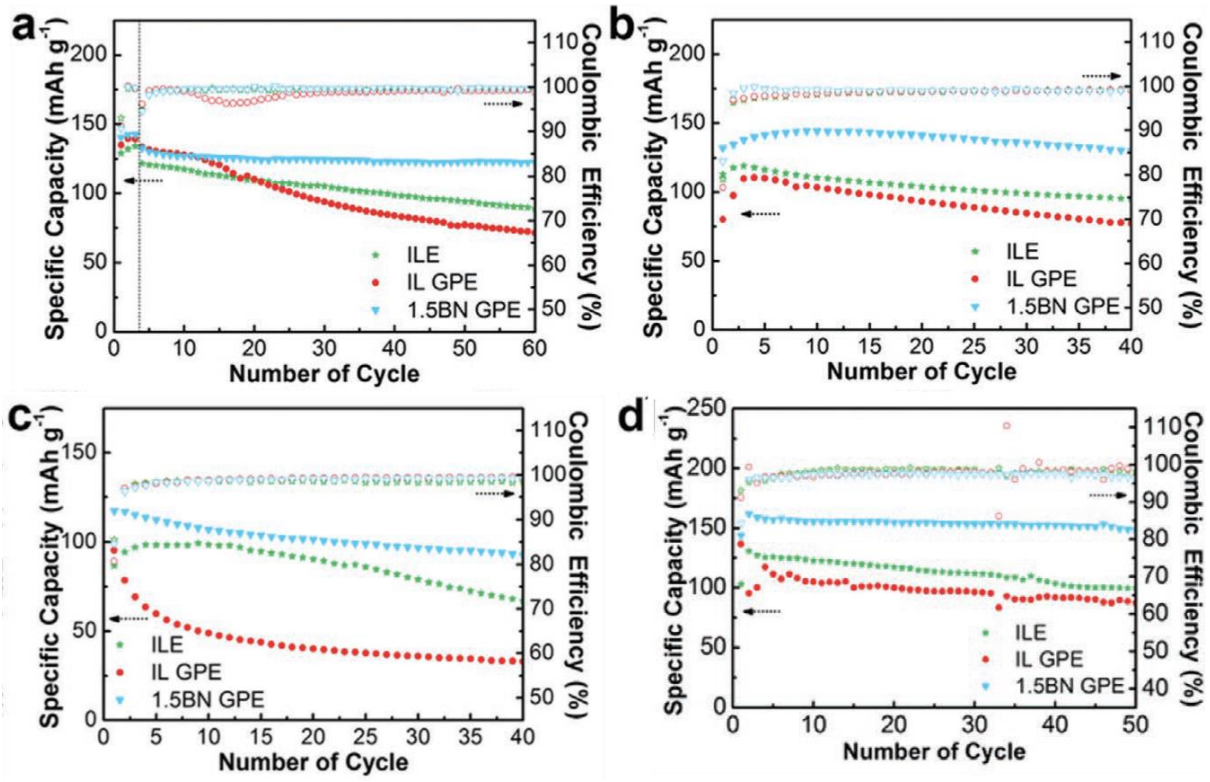

Figure 1.21: Cycling stability at 0.2 C of (a) LFP|Li cell, (b) NCM|Li cell, (c) LCO|Li cell, and (d) cycling stability at 0.5 C of LFP|Li cell at 80 ºC. Adapted with permission from Kim et al.[67]

Another inorganic material that has been utilised for the formation of polymer gel-based electrolytes is Al_2O_3. It has been investigated as a protective agent for Li metal and has mainly been studied from the perspective of surface coating and plating technologies. Wen *et al.*[68] utilised a leaf-like Al_2O_3 skeleton to form a quasi-solid-state electrolyte comprising of 1 M LiTFSI, and C_3mpyrTFSI. In this instance the Al_2O_3 skeleton absorbed the ionic liquid, which allowed for improved ionic conductivity, in addition to promoting the migration of Li^+ both in the bulk and at the interface. When coupled with LFP/Li full cell, the initial discharge capacity obtained was 140.7 mAh g^{-1} of which 95.6% was retained after 100 cycles at 30 ºC and 0.1 C.

C_3mpyr-based electrolytes have been demonstrated to be versatile as they can be utilised as liquid or solid-state electrolytes (polymer gel). The cation/anion combination, C_3mpyrFSI, has proven to be a popular choice among research groups when utilised as a liquid electrolyte as it has compatibility

with high-energy dense materials such as Si, which is beneficial for the miniaturisation of energy storage devices. However, when utilised as a polymer gel, the more popular cation/anion combination is C_3mpyrTFSI. The polymer gel electrolyte analysis has been limited mostly to LFP and Li metal cells, therefore further analysis is required in order to determine the compatibility of C_3mpyrTFSI-based polymer gels with high-energy dense materials, which will realise microbatteries that will satisfy the power requirements for IoT sensors.

1.3 N-butyl-N-methylpyrrolidinium-based ILs

Similarly to C_3mpyr-based ILs, there has been extensive characterisation of 1-butyl-1-methylpyrrolidinium (C_4mpyr)-based ILs,[41] for example, Fernández-Miguez *et al.*[7] investigated high (1.5 M) and low (0.1 M) LiTFSI salt concentrations within C_4mpyrTFSI ILs. It was determined that LiTFSI salt addition leads to higher densities than that of pure IL, but it decreases linearly with increasing temperature. Conductivity values for pure C_4mpyrTFSI and with various LiTFSI salt concentrations (0.1 M, 0.5 M, 1 M and 1.5 M) are investigated. The ionic conductivity decreases with increasing LiTFSI salt concentration, and, the authors determined the conductivity values for each concentration across a range of temperatures. Other characterisation tests carried out have been mentioned in previous pyrrolidinium subsections.[42-43]

One of the more important characterisations carried out recently, is the degradation of C_4mpyrTFSI in the presence of Li metal at room temperature recently studied by Preibisch *et al.*[69] In their study they identified a new degradation product N-butyl-N-methyl-N-but-3-eneamine (figure 1.22). This degradation product was previously unreported and it is suggested that it participates in the formation of an organic layer at the surface of Li metal. This degradation product stems from the C_4mpyr cation, rather than from the anion, which typically dominates in SEI layer formation. The presence of N-butyl-N-methyl-N-but-3-eneamine paves the way to the formation of potentially polymerized species

that could "bind" the inorganic fraction of the decomposition layer and provide elastomeric properties to accommodate changes in the electrode volume. By harnessing the elastomeric properties of N-butyl-N-methyl-N-but-3-eneamine as an additive, the realisation of group IV element anodes could be advanced providing the electrode volume changes can be mitigated due to the "elastic" SEI layer.

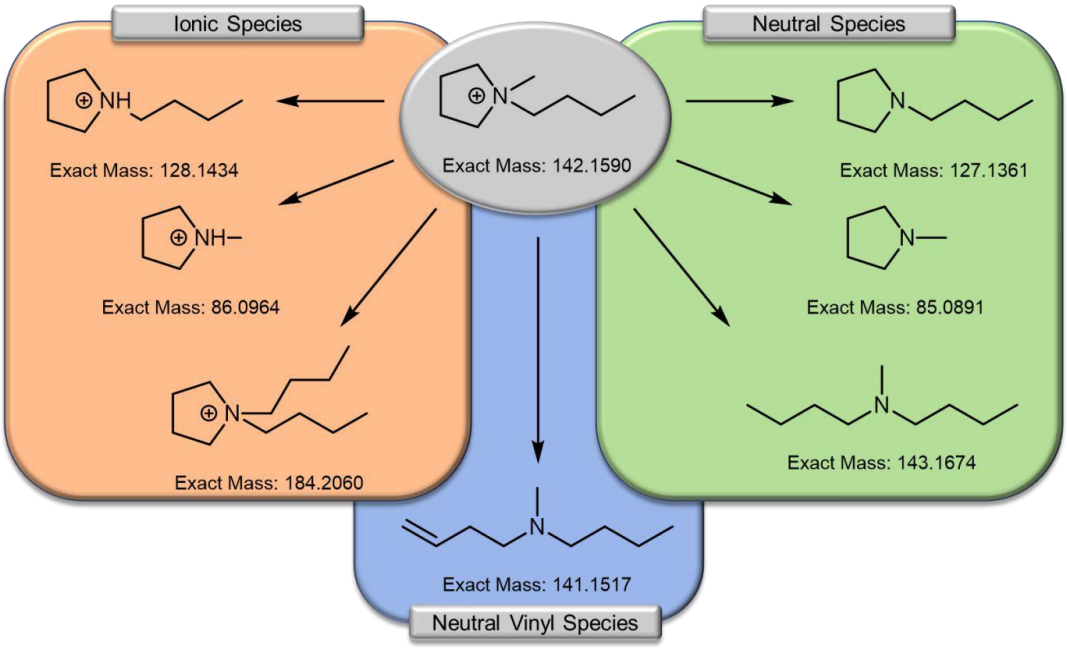

Figure 1.22: Graphical summary of the range of ionic and neutral decomposition species of C_4mpyr-cation. The ionic species (orange box) were identified by Pyschik et al.[70-71] while Kroon et al.[72] confirmed the presence of the neutral species (green box). The neutral vinyl species was identified by Preibisch et al.[69] Reprinted with permission from Preibisch et al.[69]. Copyright 2020 American Chemical Society.

The most commonly studied C_4mpyr-based ILs are based on the TFSI and FSI anions. This is due to their superior film-forming abilities on the surface of Li metal, which enable uniform Li deposition/dissolution with high cycling efficiencies, and no Li dendritic formation as reported by Grande *et al.*[73] This study highlighted the effectiveness of Li^+ mobility within C_4mpyr-based ILs, which is why extensive research has been carried out using C_4mpyr-based electrolytes with those and trifluoromethanesulfonyl-N-cyanoamide (TFSAM) anions (figure 1.23). Recently, TFSAM has been

utilised as an anion due to its ability to inhibit crystallisation over a broader temperature range when compared to TFSI.[74] The asymmetric TFSAM anion, promotes single Li^+ hopping due to higher structural diffusion that occurs as the LiTFSAM salt concentration increases, as reported by Nürnberg *et al.*[74].

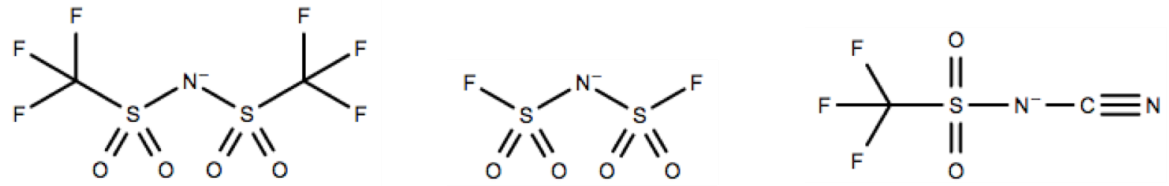

Bis(trifluorosulfonyl)imide (TFSI / TFSA / NTf_2)

Bis(fluorosulfonyl)imide (FSI / FSA)

2,2,2-trifluoromethylsulfonyl-*N*-cyanoamide (TFSAM)

Figure 1.23: Structures of anions utilised with C_4mpyr cations to create battery electrolytes.

Electrolytes containing TFSAM anions, have not been widely investigated, and present a potential area for analysis, however, C_4mpyrTFSAM compatibility with NCM electrodes has been investigated by Hoffknecht *et al.*[75] Cycling at 40 ºC was carried out whereby high cycle efficiencies are obtained from the initial cycle (figure 1.24), as it exhibited a coulombic efficiency of 92.6%. Over 90% of the initial capacity was retained in the 30th cycle, however, the long-term stability of the cell is not outlined, and requires further investigation.

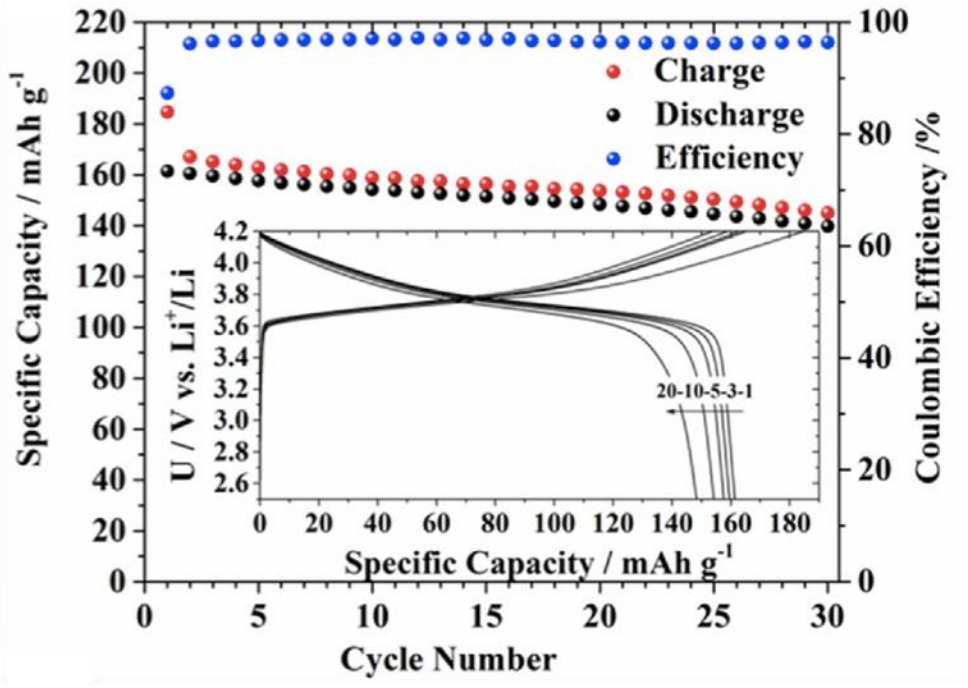

Figure 1.24: Cycling performance of NCM electrodes in 0.4 M LiTFSAM in C_4mpyr TFSAM. Reprinted with permission from Hoffknecht et al.[75]

The cation/anion combinations, C_4mpyrTFSI and C_4mpyrFSI, have been extensively studied, not only as electrolytes, but as electrode binders and interlayers. Liquid interlayers have been investigated at both the anode and cathode sides using C_4mpyrFSI and LiTFSI salt. Pervez *et al.*[76] used it as an interlayer between the $Li_{6.5}La_{2.5}Ba_{0.5}ZrNbO_{12}$ (LLZO) solid-state electrolyte and the electrodes. Due to the liquid-like nature of the IL, it fills the voids between the electrode and electrolytes, thus improving the interfacial properties of LLZO with both the cathode and anode as evidenced by the EIS data shown in figure 1.25. The interfacial resistance between the Li metal and LLZO electrolyte is significantly decreased upon addition of the IL interlayer as shown by the blue line. This allows for the realisation of higher electrode capacities than for cells without the interlayer. Similarly, low interfacial resistance is observed for the IL interlayer in contact with LFP.

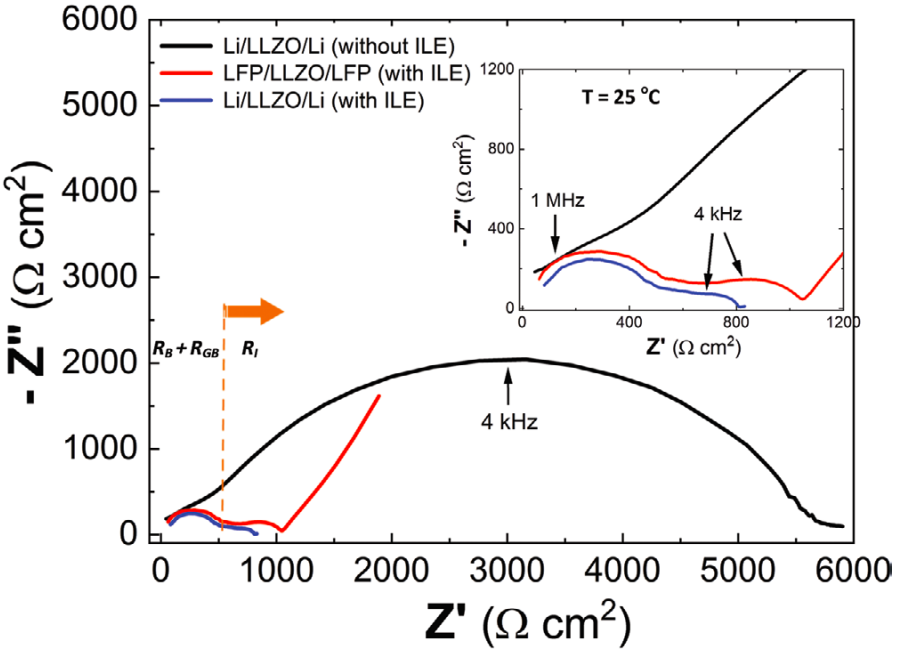

Figure 1.25: EIS data obtained for Li/LLZO/Li with and without ILE, and LFP/LLZO/LFP with ILE cells. The inset shows a magnification of the high frequency part of the plots. All measurements were performed at 25 °C. Reprinted with permission from Pervez et al.[76]

Similarly, improved interfacial kinetics is observed when C_4mpyr-based ILs are used as an electrode binder. In this instance, C_4mpyrTFSI and LiTFSI are confined within a PEO matrix to form a glue-like polymer, which then penetrated sheet-type composite NCM electrodes to act as an ion-conductive binding material which effectively increase the effective contact area between the electrode components as shown in figure 1.26.[77] This resulted in lower overpotentials due to the higher active area, whereby the cell attained 92% of the capacity obtained by NCM electrode in a conventional organic electrolyte.[78]

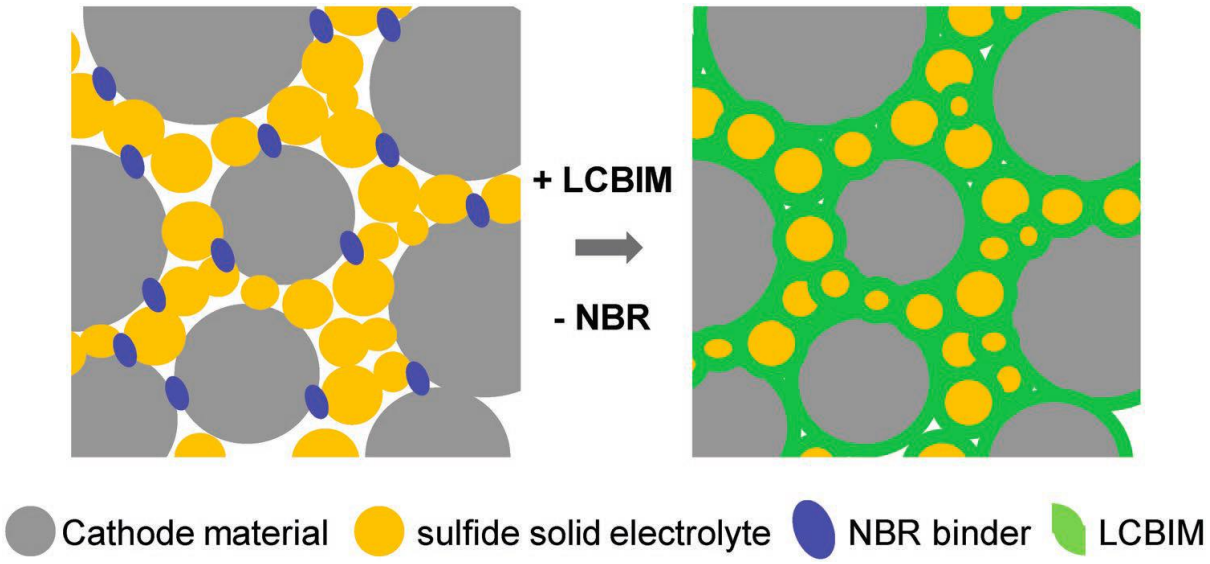

Figure 1.26: Schematic diagram representing the microstructure of the composite electrodes with polymer gel electrolyte (LCBIM), showing that LCBIM improves the interfacial contact area with conductive and adhesive properties. Carbon additives included in the composite electrode are not shown. Reprinted with permission from Cho et al.[77]

C_4mpyrTFSI-based electrolytes have been studied as co-solvents with conventional organic electrolytes. These electrolytes have been studied with anode materials such as graphite and Si. For instance, Balducci *et al.*[79] utilised C_4mpyrTFSI as a co-solvent with LiTFSI salt, and EC/DEC/DMC (1:1:1 w/w), and attained stable cycling over the course of 50 cycles (figure 1.27). The stability of the electrode within the electrolyte is observed as minimal capacity fade is observed across the 50 cycle, in addition, the coulombic efficiency was close to 100% during cycling.

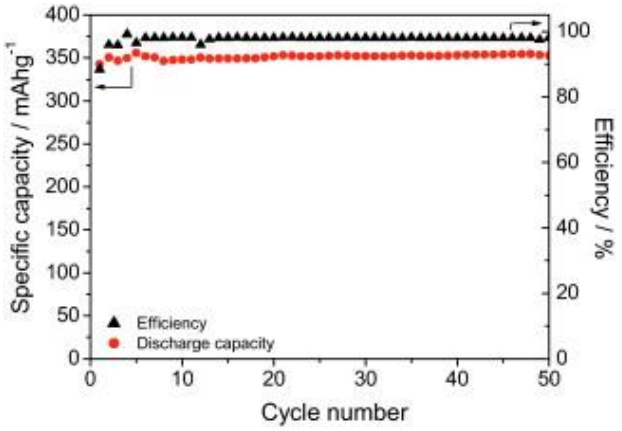

Figure 1.27: Specific discharge capacity and coulombic efficiency of a graphite electrode. The cell was tested between 0.0 V and 1.5 V at the current rate of 0.1 C, after two initial formation cycles carried out at 0.05 C. Reprinted with permission from Balducci et al.[79]

These co-solvent tests showed promising results when utilised with high energy dense materials such as Si, as Balducci *et al.*[79] demonstrated stable discharge capacities of ~550 mAh g^{-1} at 0.1 C, with minimal capacity fade observed across 100 cycles as shown in figure 1.28. The electrolyte used comprised of C_4mpyrTFSI as a co-solvent with EC:DEC:DMC (1:1:1), and LiTFSI salt.

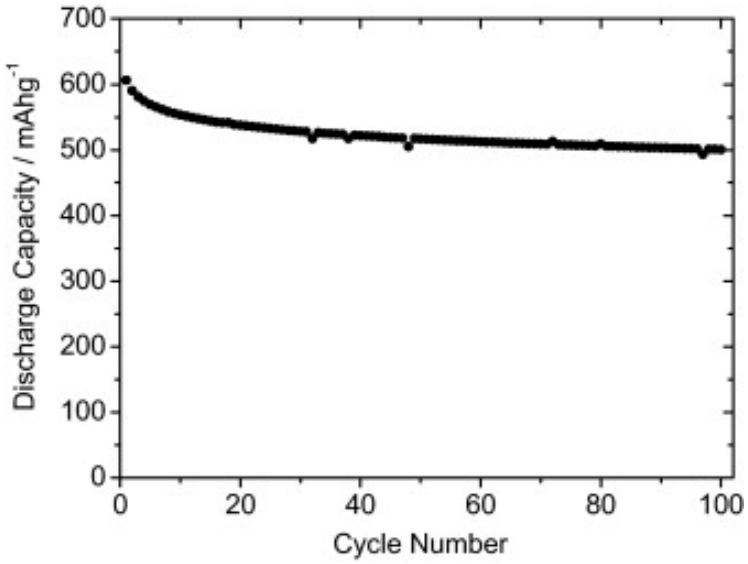

Figure 1.28: Specific discharge capacity of Si-graphite composite electrode tested in an electrolytic solution containing 0.3 M LiTFSI in C_4mpyrTFSI (50%) and (1:1:1 w/w) EC:DEC:DMC. The cell was tested between 0 V and 1.5 V at the current rate of 0.1 C. Reprinted with permission from Balducci et al.[79]

To limit the amount of organic solvents within the electrolyte, C_4mpyr-based ionic liquid electrolytes were investigated. In liquid form, the most commonly studied C_4mpyr-based IL is C_4mpyrTFSI with LiTFSI salt. Utilisation of an ionic liquid electrolyte can lead to lower electrode-wettability and lower Li^+ transport number as observed by Di Lecce *et al.*[80] In their study they investigated the electrochemical performance of the olivine cathode $LiFe_{0.5}Mn_{0.5}PO_4$ and determined that the reversible exchange of 0.6 Li could be obtained in C_4mpyrTFSI which corresponds to an electrode capacity of 100 mAh g^{-1}. In conventional organic electrolytes, Li exchange is significantly higher at 0.7 or greater. However, this is considered a trade-off for the increased intrinsic safety of the IL electrolytes. In addition, utilisation of higher operating temperatures can lead to improved performances as shown in figure 1.29, where the interfacial resistance decreases with increasing temperature. As the temperature increases, the electrode-wettability increases, therefore paving the way for high electrode capacities to be obtained.

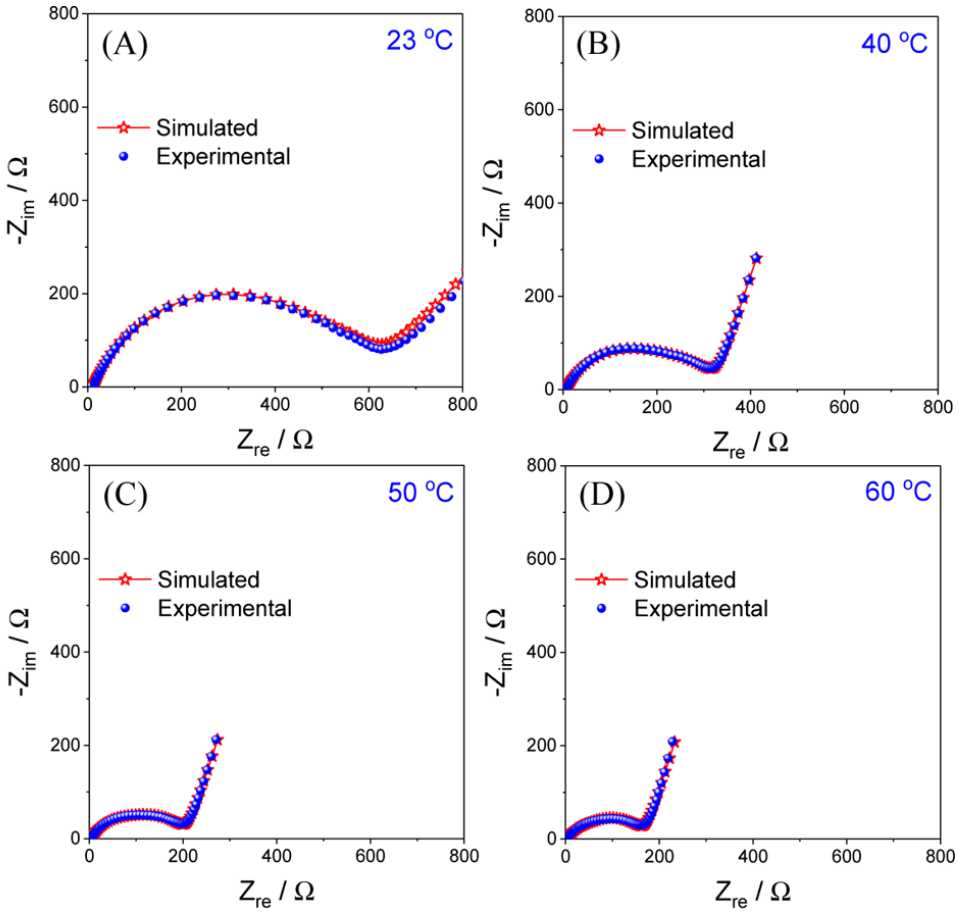

Figure 1.29: Experimental and simulated Nyquist plots related to electrochemical impedance spectra of the Li/C₄mpyrTFSI, LiTFSI 0.1 mol kg^{-1}/LiFe$_{0.5}$Mn$_{0.5}$PO$_4$ cell at (a) 23 °C, (b) 40 °C, (c) 50 °C, and (d) 60 °C. Reprinted with permission from Di Lecce et al.[80]

A comparison of the electrochemical performances of C$_4$mpyrTFSI- and C$_4$mpyrFSI-based electrolytes have been carried out on both anode and cathode materials. Elia *et al.*[81] reported that C$_4$mpyrFSI showed the greatest promise with LFP electrodes as it yielded the highest electrode capacity for charging current densities of 25 mA g^{-1} and 250 mA g^{-1} as shown in figure 1.30. The electrode capacity obtained at 250 mA g^{-1} in C$_4$mpyrFSI is similar to that obtained at 25 mA g^{-1}. The TFSI-based electrolyte by comparison gave poorer rate performance and capacities below 80 mAh g^{-1} were obtained at a current density of at 250 mA g^{-1}.

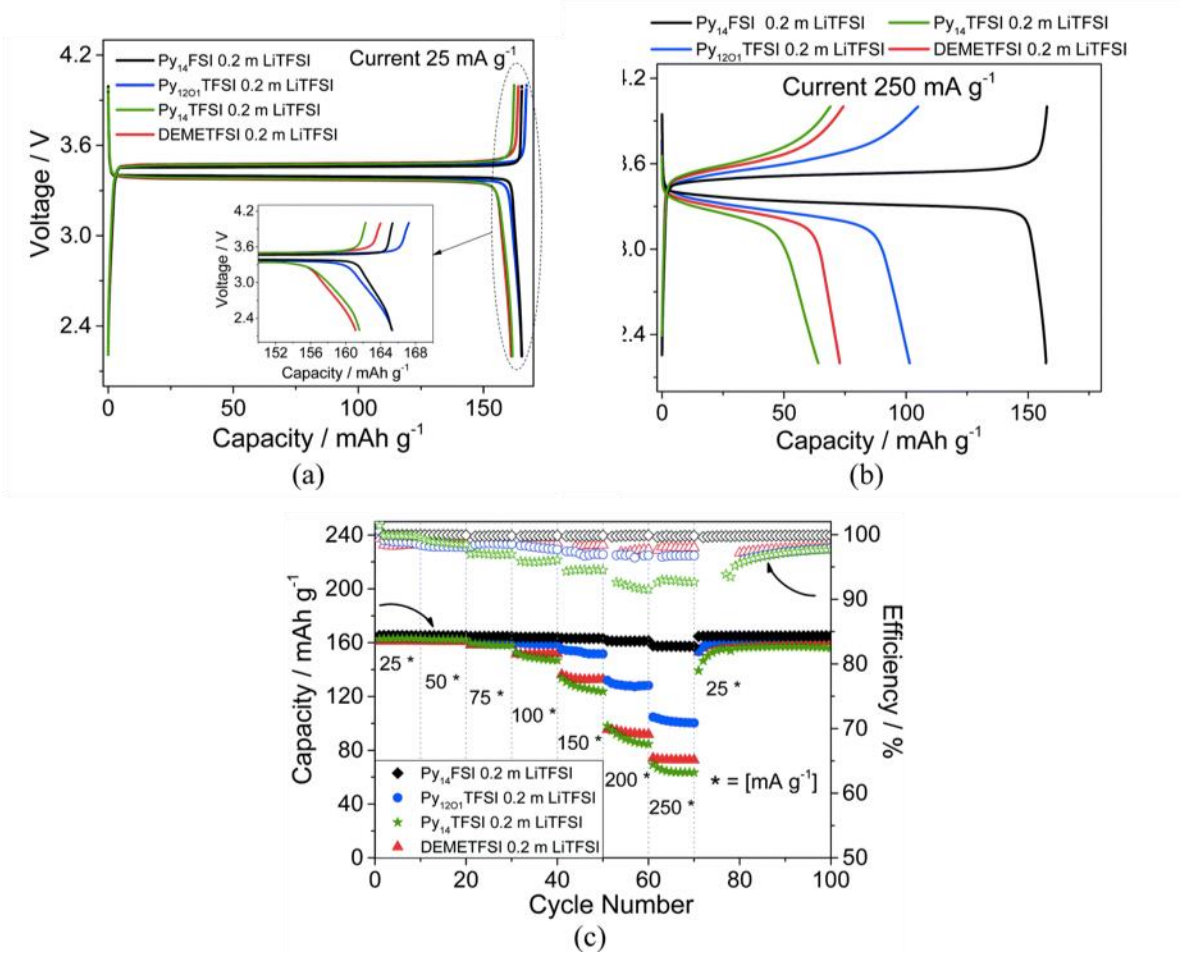

Figure 1.30: Li/IL/LFP cells galvanostatically cycled at (a) 25 mA g^{-1} (0.12 mA cm^{-2}), with inset reporting the magnification of the final part of the curves, and (b) 250 mA g^{-1} (1.2 mA cm^{-2}). (c) Cycling trend and columbic efficiency of the Li/IL/LFP cells at increasing currents. voltage cut-offs were 2.2 and 4 V. Pyr_{14}TFSI–LiTFSI (green), Pyr_{14}FSI–LiTFSI (black), $Pyr_{1(2O1)}$TFSI–LiTFSI (blue), DEME-TFSI–LiTFSI (red). All measurements were performed at 40 °C. Reprinted with permission from Elia et al.[81]

A similar trend was observed for anode materials such as Ge as the lower viscosity, higher ionic conductivity C_4mpyrFSI electrolyte enables higher electrode capacities to be obtained, discharge capacity of 445 mAh g^{-1} vs. 260 mAh g^{-1} for C_4mpyrTFSI. Similar trends were observed with Si electrodes.[82] The difference in the electrochemical performance is attributed to the SEI layer formation on the electrode as the anions undergo different decomposition mechanisms upon

electrochemical reduction at different rates. FSI anions rapidly release F-, forming LiF in the SEI, therefore suggesting the formation of an SEI layer comprised of small inorganic compounds. TFSI anions degrade to form different SEI layer products such as $-SO_2CF_3$ at a much slower rates than FSI counterparts.[83] The composition of the SEI layer can affect the chemical structure and morphology of the SEI layer can critically influence the safety, cycle life, power capability, side reactions and shelf life of Li-ion batteries, hence the difference in the electrochemical performances.

Despite the higher electrochemical performances in liquid form, the use of C_4mpyrFSI electrolytes within polymer matrices is not commonly studied, however, Kerner *et al.*[84] synthesised PIL-based electrolytes, where one set contained C_4mpyrTFSI, and another set contained C_4mpyrFSI. Both electrolytes tested with LFP yielded electrode discharge capacities above 140 mAh g^{-1} at 80 ºC when 0.5 C rate was utilised. The C_4mpyrFSI containing electrolyte yielded higher electrode capacities close to theoretical (~160 mAh g^{-1}) for C-rates up to 0.5 C. A similar trend to the liquid electrolytes is observed as the FSI-containing electrode yields higher electrode capacities, however, high temperatures (80 ºC) are required in order to attain these high electrode capacities. By changing the PIL, Appetecchi *et al.*[85] synthesised films which yielded LFP electrode capacities of 148 mAh g^{-1} (87% of the nominal capacity) at 40 ºC at C/20.

Simple polymer matrices such as PVDF-HFP, poly(ethylene carbonate) (PEC) and CMC have been investigated in addition to polymer gels which consist of PILs. Kimura *et al.*[86] created a polymer consisting of poly(ethylene carbonate) (PEC), LiTFSI, C_4mpyrTFSI and non-woven SiO_2 fibre. It exhibited low ionic conductivity at room temperature (~10^{-7} S cm^{-1}), therefore it is only suited for high temperature applications. At temperatures of 75 ºC, stable cycling was obtained with low electrode polarisation at C/15 rate as shown in figure 1.31, however, improvements to the electrode capacity could be made, in addition to the demonstration of long-term cycling.

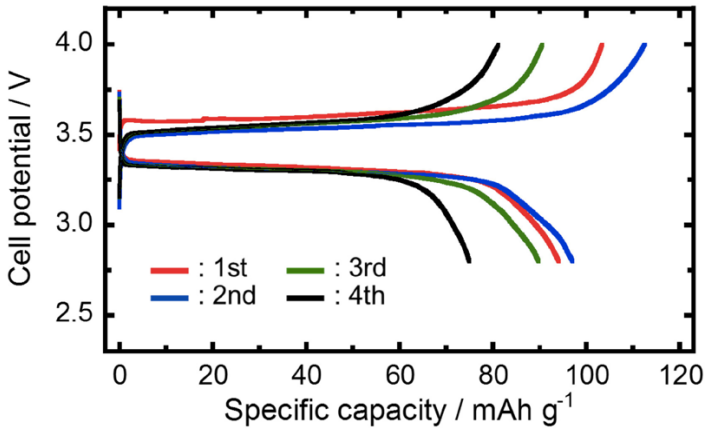

Figure 1.31: Voltage profiles of a galvanostatically cycled LFP half-cell at 75 ºC and C/15 rate. Reprinted with permission from Kimura et al.[86]

The utilisation of PVDF-HFP as a polymer matrix has proven popular for use with cathode and anode materials. Kim *et al.*[87] synthesised an electrospun PVDF-HFP polymer membrane which was then soaked in 1 M LiTFSI and C_4mpyrTFSI. An uptake of 300% was observed, which is significantly higher than that reported for Celgard separators.[88] The soaked membrane exhibited ionic conductivity of the order 10^{-3} at room temperature, with a Li transport number of 0.04. Good reversibility and cyclability is observed at room temperature with LFP electrodes, as shown in figure 1.32. Capacity retention of 92% and 69% is attained for the 0.1 C and 1 C rates after 55 cycles. The increase in electrode polarisation at 1 C suggests that this membrane is better suited to C-rates below 1 C in order to ensure stable, long-term cycling with minimal capacity loss.

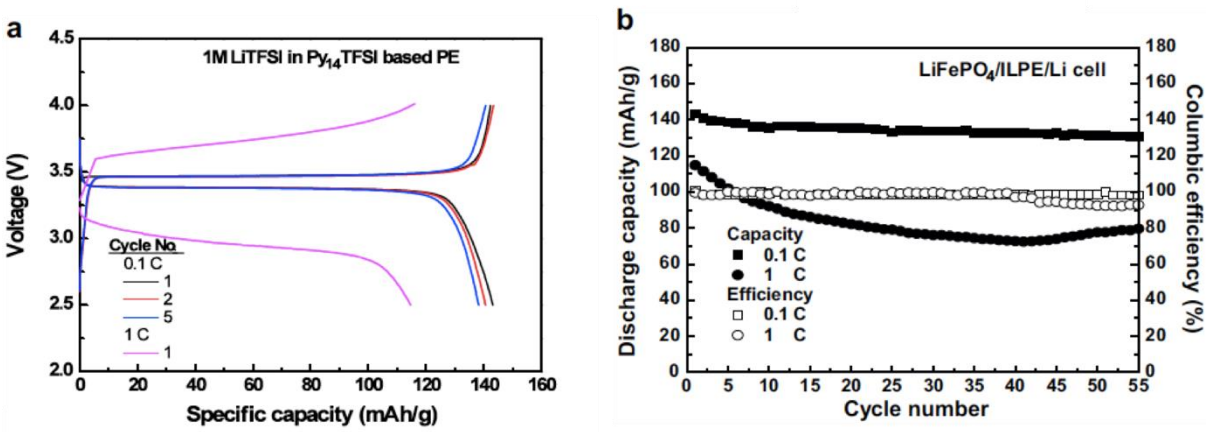

Figure 1.32: (a) First, second, and fifth cycle charge-discharge capacities and (b) cycle performance of a Li/LFP cell with the C4mpyrTFSI-based polymer electrolyte (ILPE) (25 ºC, 0.1 and 1 C-rate, 2.5 V to 4.0 V). Reprinted with permission from Kim et al.[87]

Recently, a polymer gel comprising of PVDF-HFP, C4mpyrTFSI and LiTFSI was reported by McGrath *et al.*[89] The ionic liquid was encapsulated within the membrane and it resulted in free-standing flexible films (figure 1.33) which demonstrated ionic conductivities between the range of 7 $x10^{-5}$ S cm^{-1} and 1.9 x 10^{-3} S cm^{-1}. Galvanostatic cycling analysis with Ge materials achieved average electrode capacities of 800 mAh g^{-1} at 0.2 C, with coulombic efficiencies greater than 99%. Great capacity recovery was observed as the 71^{st} to 80^{th} capacity matched that of the initial capacity at 0.15 C (~900 mAh g^{-1}). Up to 90 cycles was achieved with no capacity fade which indicates a buffering effect of the polymer gel.

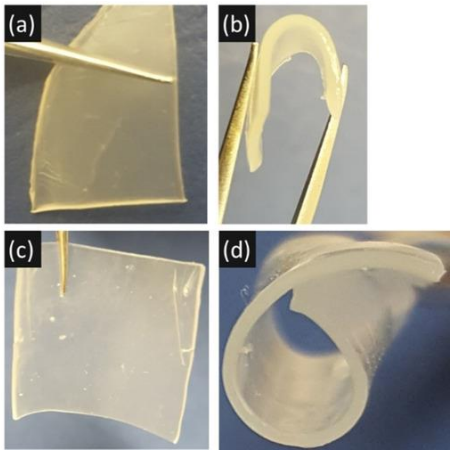

Figure 1.33: Optical images of the polymer gel synthesised by McGrath et al.[89] The films were 400 µm thick where (a and b) have low IL content, and (c and d) have high IL content. Reprinted with permission from McGrath et al.[89]

Other anode materials have been investigated using alternative polymer matrices such as the work of Balducci *et al.*[79] where the conventional PVDF binder was replaced with CMC. The LTO exhibited low electrode polarisation to be achieved during galvanostatic cycling. The electrode capacities obtained were comparable to those exhibited by LTO with PVDF binders in conventional organic electrolytes.

Unlike the previous pyrrolidinium cations, both liquid and polymer gel forms of C_4mpyr-based electrolytes have been utilised in battery prototype tests, where promising results have been obtained. Various cathode and anode materials have compatibility with C_4mpyr-based ILs, and therefore comprehensive full cell tests were carried out with a variety of electrode combinations. Balducci *et al.*[79] investigated Li metal batteries with a polymer gel electrolyte, in addition to a Li-ion batteries utilising LTP and LTO electrodes. Prototype cells were created by stacking 12 to 14 single bipolar cells to achieve a theoretical cell capacity of 0.7 Ah to 0.8 Ah. The electrolyte utilised with the Li-ion battery was a liquid electrolyte: C_4mpyrFSI with LiTFSI salt, while the Li metal battery contained

a cross-linked PEO with C_4mpyrTFSI with LiTFSI salt. The cycling results are shown in figure 1.34. In both instances, 1000 cycles were obtained for each C-rate, with minimal capacity fade observed. The cell capacity for both the Li metal and Li-ion batteries at C/20 is close to theoretical (0.7 Ah to 0.8 Ah). The Li-ion battery shows the best electrochemical performance of the two prototype batteries, however, for low to moderate C-rates, the Li metal performance is comparable to the Li-ion battery. These results demonstrate that the presence of ILs, both solid and liquid, are suitable for use in Li-based batteries. Excellent cycle life is achieved across low to fast C-rates. Nail puncture tests demonstrated increased safety as a voltage drop was observed, however a full short circuit (voltage at 0 V) did not occur. Comparing this to a cell containing organic electrolyte, a full short circuit is achieved under the same conditions. Therefore, not only do the IL-based batteries have desirable electrochemical performances, but enhanced safety is also achieved, thus allowing for the realisation of high performance Li-based batteries.

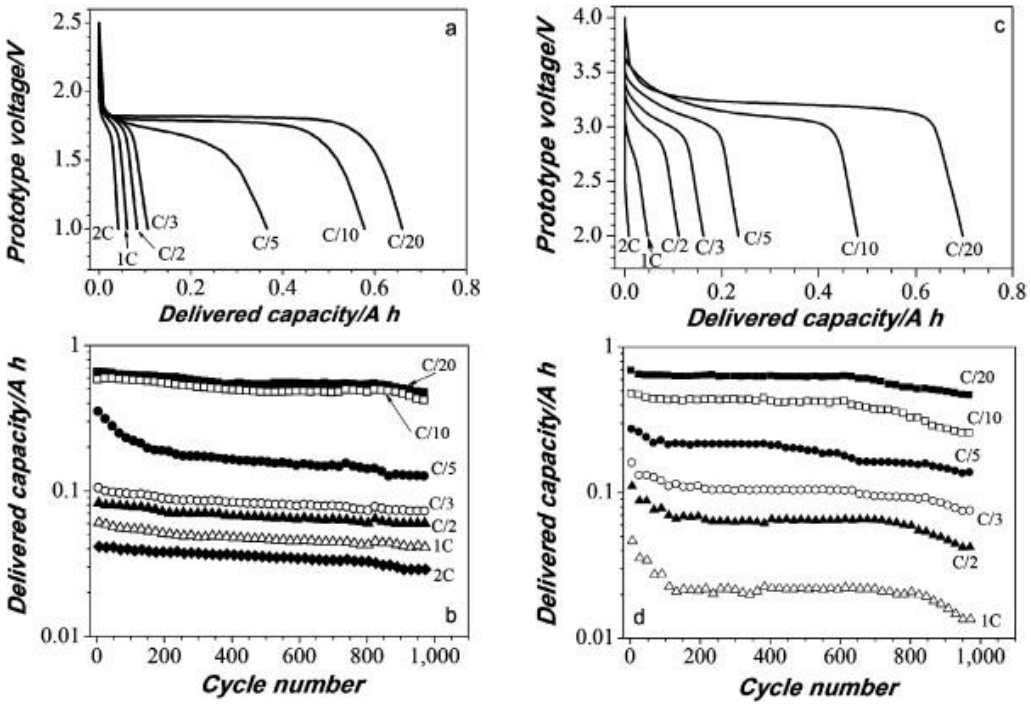

Figure 1.34: (a and c) First discharge voltage profiles and (b and d) capacity vs. cycle number at different discharge current rates of (a and b) Li-ion battery prototype at 20 C and (c and d) Li metal-polymer battery at 40 C. Reprinted with permission from Balducci et al.[79]

Similarly, Kim *et al.*[90] utilised Li/LFP and LTO/LFP cells with PEO-LiTFSI-C_4mpyrFSI, and LiTFSI-C_4mpyrFSI electrolyte, respectively. Their results reflected those obtained by Balducci *et al.*[79] Full cells incorporating group IV elements with promising long-term results have been reported in the literature. Elia *et al.*[81] reported more than 2000 cycles with coulombic efficiency close to 100% for a Sn-C/LFP cell. The results are shown in figure 1.35. From the data, it is evident that the C_4mpyrFSI-based IL allows for good high rate capabilities, as the cell capacity was ~80 mAh g^{-1} at a current density of 500 mA g^{-1}. This was maintained over 2000 cycles, as a capacity retention of 98% was obtained after cycling. The exceptional cycling is due in part to the formation of an SEI layer after 10 cycles, in addition to low interfacial resistances. These results show that long-term cycling can be achieved with minimal capacity fade, or cell failure.

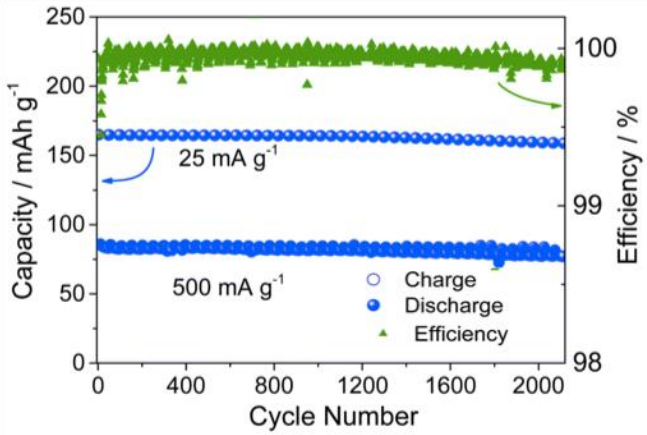

Figure 1.35: Galvanostatic cycling data obtained at different currents for Sn-C/LFP cell at 40 ºC, within the voltage range of 2 V to 3.8 V. Reprinted with permission from Elia et al.[81]

The above results highlight that large Li-ion batteries can be realised with either liquid or polymer gel electrolytes. However, in order to realise the IoT concept, miniaturisation of the battery is required, which may require nanostructured materials in order to obtain high power over a small footprint. C_4mpyr-based ILs may be able to realise nanostructured materials as they have been utilised as electrodeposition media for the electrodeposition of group IV elements: Sn, Ge and Si. Sano *et al*[91]

electrodeposited Sn onto glassy carbon electrodes using C_4mpyrTFSI with 0.5 M C_4mpyr Cl and 10 mM $SnCl_2$. Potentiostatic cathodic reduction at -2.0 V resulted in tubular and granular Sn deposits. Similarly, electrodeposition of Ge has been achieved from a variety of C_4mpyr-based ILs. Wu *et al*.[92] deposited Ge from 1-butyl-1-methylpyrrolidinium dicyanamide (C_4mpyr DCA) using $[GeCl_4(BuIm)_2]$ (BuIm = N-butylimidazole) as a Ge source to create thin films. Ge deposition is also feasible at high temperatures (180 ºC) to produce films.[93] Nanostructured Ge films are also achievable through electrodeposition within C_4mpyr-based ILs. Lahiri *et al.*[94] electrodeposited free-standing Ge nanotubes and core-shell structures, as shown in figure 1.36.

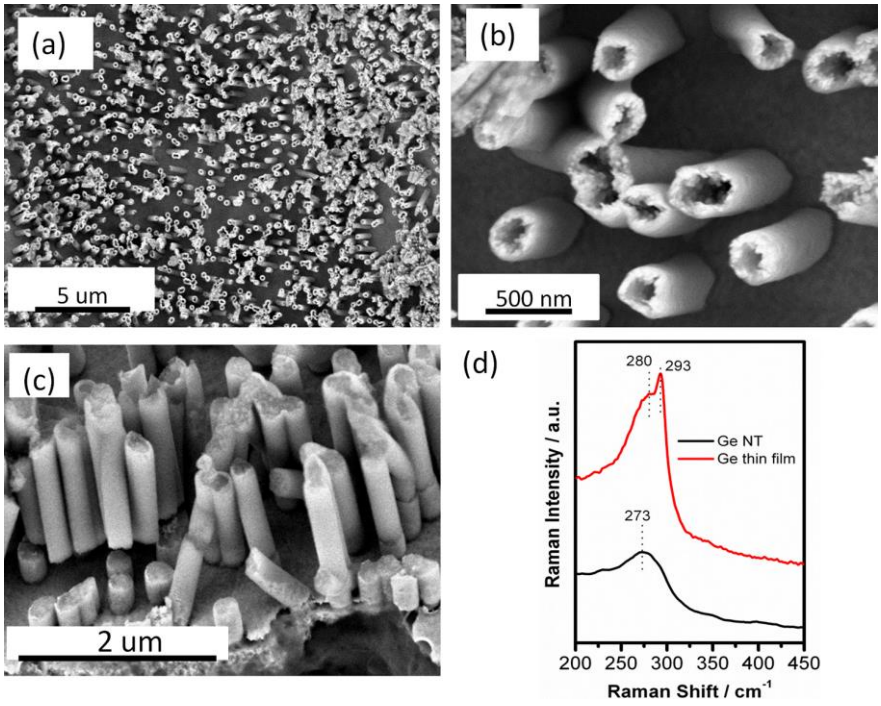

Figure 1.36: (a): Low magnification image of free-standing Ge nanotubes after removal of the template. (b) Higher magnification image of the Ge nanotubes (c) Cross sectional view of the Ge nanotubes. (d) Raman spectra of electrodeposited Ge thin films and nanotubes obtained by exposing the sample to 5 mW, 532 nm laser for 10 seconds. Reprinted with permission from Lahiri et al.[94]

Nanowires (NW) of both Ge and Si have been reported using $GeCl_4$ and $SiCl_4$ as the Ge and Si sources respectively. Both Al-Salman *et al.*[95] and Martineau *et al.*[96] deposited amorphous Si-NW and Ge-NW with homogenous compositions. The capability to electrodeposit the anode material directly from ILs allows for greater electrode wettability, and therefore, more studies should be carried out to determine what materials are compatible for deposition within C_4mpyr-based ILs. Link *et al.*[97] recently investigated the initial stages of Si electrodeposition within C_4mpyrTFSI electrolytes, therefore allowing researchers to better understand the Si nucleation process. By understanding the nucleation process, the deposition of Si and any material can be tailored to yield the required film morphology. This paves the way for new anode material morphologies, which may enable high power Li-based microbatteries.

As discussed, C_4mpyr-based ILs are versatile electrolytes as both their liquid and polymer gel yield promising results when coupled with a variety of cathode (LCO, NCM, LTP), and anode materials (graphite, LTO, Ge, Si, Li metal) in both half-cell and full-cell tests.

1.4 Ether functionalised pyrrolidinium-based ILs

As with other cation types such as ammonium,[15, 81, 98-107] research into ether functionalised ionic liquids are being investigated for pyrrolidinium-based ILs. Various ether functionalised pyrrolidinium ILs have been synthesised and characterised.[42-43, 108] LFP cathodes are commonly analysed with ether functionalised ILs as mentioned in previous sections and it is the cathode material of choice for the electrochemical characterisation of ether functionalised pyrrolidinium-based ILs. Zhang *et al.*[109] designed an ether functionalised IL, 1-(2-ethoxyethyl)-1-methylpyrrolidinium bis(trifluoromethylsulfonyl) imide ($PYR_{1(2o2)}$TFSI) in order to lower viscosity, facilitate the formation of passivation layer and to enhance electrochemical stability. The structure of the synthesised IL cation is shown in figure 1.37.

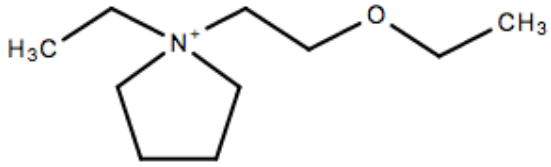

Figure 1.37: Structure of 1-(2-ethoxyethyl)-1-methylpyrrolidinium ($PYR_{1(2o2)}$) cation.

This IL was analysed with LiTFSI salt, and as a co-solvent with DMC and LiTFSI salt. It was determined that the viscosity of the IL was lower than for C_4mpyrTFSI with LiTFSI, which demonstrates that ether functionalisation can reduce the viscosity of the solution. The ionic conductivity of the DMC co-solvent is higher than for the IL only electrolyte (3.02 $x10^{-3}$ S cm^{-1} vs. 1.4 $x10^{-3}$ S cm^{-1}), due to the low viscosity of DMC. The DMC-containing electrolyte yielded the highest electrode capacity, and best rate performance as shown in figure 1.38. Remarkably, the ether functionalised IL electrolyte matched the electrode capacity obtained by the DMC-containing electrolyte at 60 ºC, which indicates that no organic components are required for high temperature applications. The electrochemical analysis demonstrated the superior cycling stability and rate performance of ether functionalised ILs when compared to the non-functionalised counterparts.

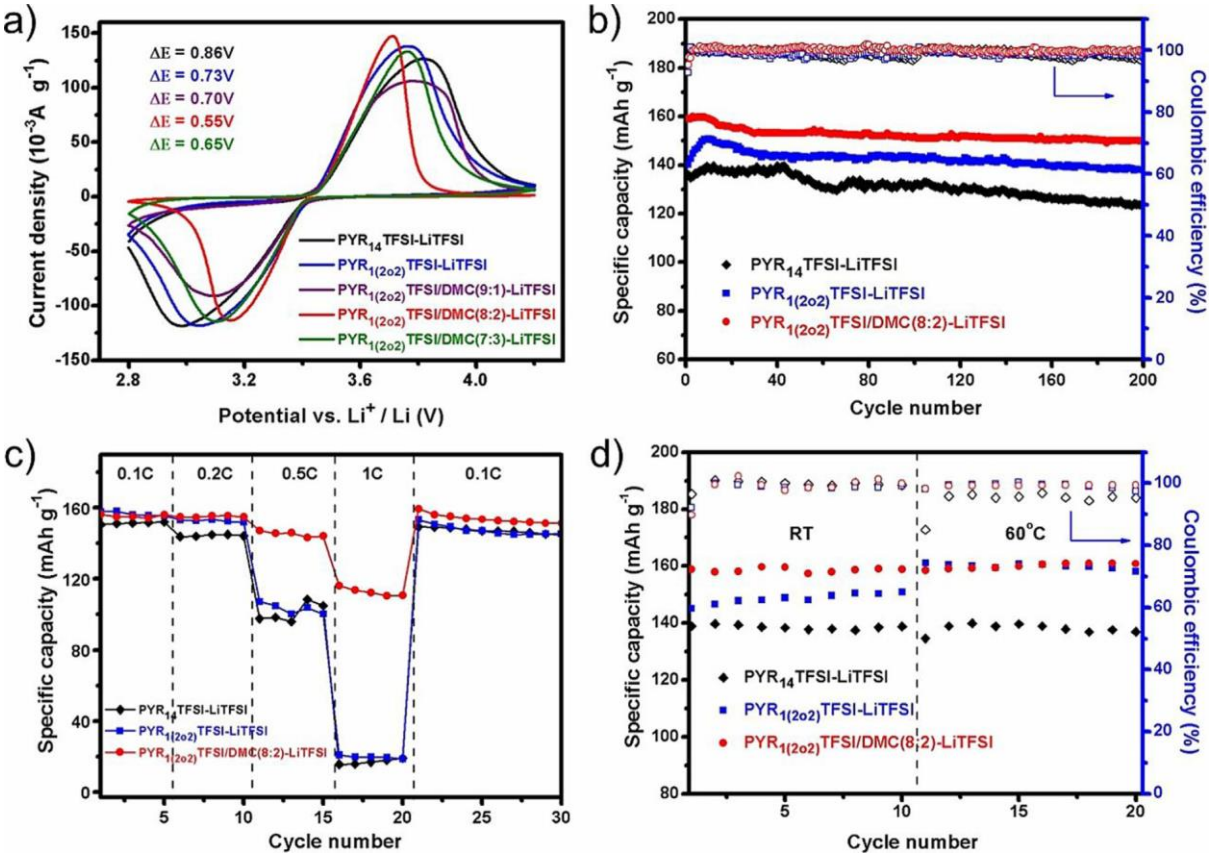

Figure 1.38: (a–c) Performance of various electrolytes at room temperature: (a) CV curves, (b) cycling performance, (c) rate performance, (d) cycling performance of RT and high temperature (60 ºC). Reprinted with permission from Zhang et al.[109]

Dual ether functionalised pyrrolidinium-based ILs, have been reported by Fang *et al.*[110] The data for the electrochemical performances are outlined in the piperidinium section as both piperidinium and pyrrolidinium-based ILs were investigated. The electrode capacities for the dual ether functionalised pyrrolidinium-based ILs are lower than the single functionalised ILs (~130 to 140 mAh g^{-1} vs. ~150 mAh g^{-1}), which demonstrate that over functionalisation of the cations do not yield significant improvements in their electrochemical capabilities.

Polymer gel analogues have been synthesised by Ferrari *et al.*[111] whereby PVDF-HFP/silica composite membranes absorbed a solution of LiTFSI with N-ethyl(methylether)-N-

methylpyrrolidinium trifluoromethanesulfonimide ($PYRA_{1(2o1)}$), whose cation structure is shown in figure 1.39.

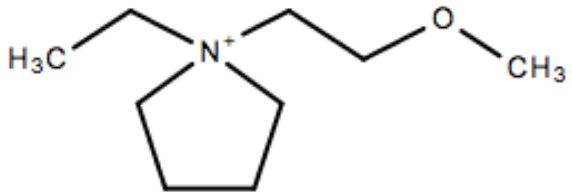

Figure 1.39: Structure of N-ethyl(methylether)-N-methylpyrrolidinium ($PYRA_{1(2o1)}$) cation.

The composite gel electrolyte yields promising capacity retention and reversibility with LFP cathode materials as the average coulombic efficiency of the cell is 99%. The specific capacity obtained for the gel composite is higher than for the liquid analogue over the long-term, as the polymer gel yielded a capacity of 124 mAh g^{-1} after 174 cycles, while the liquid analogue yielded a capacity of only 89 mAh g^{-1} after 14 cycles. The compatibility of the gel composite electrolyte, and lower initial capacities can result in better long-term cycling as the gel composite initially had a lower capacity than its liquid counterpart (139 mAh g^{-1} vs. 156 mAh g^{-1}).

Further work to identify suitable ether functionalised pyrrolidinium-based ILs is required to fully utilise their potential. To the best of my knowledge, the ether functionalised pyrrolidinium-based ILs are the least researched ether functionalised cations of the cation types.

1.5 Other pyrrolidinium-based ILs

There are other pyrrolidinium cation-based ILs which have been investigated by research groups other than the cations mentioned in the previous subsections. N-n-butyl-N-ethylpyrrolidinium bis(trifluoromethylsulfonyl)imide (BEPyTFSI), whose structure is shown in figure 1.40, was investigated in the early 2000s in both its liquid and polymer gel forms.[112-114]

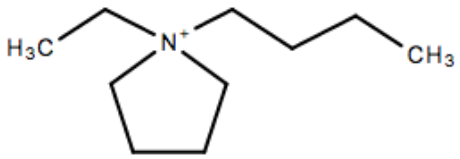

Figure 1.40: Structure of N-n-butyl-N-ethylpyrrolidinium (BEPy) cation

More recently, focus has been placed on dicationic ionic liquids which consist of an anion and a doubly charged cation as head groups linked by a variable length of alkyl or oligo ethylene glycol (OEG) chain as a rigid or flexible spacer. Mei e*t al.*[115] synthesised a variety of dicationic-based ionic liquids and characterised their physiochemical properties. No analysis was carried out to determine their suitability for battery applications, however, they exhibited high ionic conductivities of the order 10^{-3} S cm^{-1}, which are comparable to the single cation-based ILs.

Symmetrical cations are also being investigated such as diethylpyrrolidinium (C_2epyr), whose structure was shown at the start of the section. Al-Masri *et al.*[116] synthesised a quasi-solid-state electrolyte containing 90 mol% LiFSI salt and C_2epyrFSI, which exhibited an ionic conductivity of ~2 x10^{-4} S cm^{-1} at 30 ºC. This value is an improvement on those outlined in section 1.3.5.1, as ionic conductivities of ~10^{-6} S cm^{-1} were obtained for C_2mpyr-based electrolytes. In addition, high Li^+ transference numbers were obtained, and stable lithium plating and stripping behaviour was reported, supported by a reduction in dendrite formation on the lithium surface compared to a liquid electrolyte. These results pave the way for the development of high salt content quasi-solid-state electrolytes utilising symmetrical pyrrolidinium cations.

Conclusion

In summary, an array of ionic liquid-based electrolytes are available for use in lithium metal and lithium-ion batteries. ILs have been utilised as interlayers, additives, co-solvents, a component in mixed IL electrolytes, the sole electrolyte, and as polymer gels. Their versatility is clearly highlighted in the preceding section, with each cation offering unique properties. The most promising pyrrolidinium-based IL is C_4mpyrTFSI due to its favourable properties such as wide electrochemical window, high thermal stability, and its ability to be utilised as a polymer gel electrolyte. This IL in particular is a potential replacement for conventional solid-state electrolytes in lithium-based microbatteries due to its compatibility with a wide range of materials with high energy densities, and its ability to form polymer gels.

References

[1] R.-J. Chen, Y.-B. Zhang, T. Liu, B.-Q. Xu, Y.-H. Lin, C.-W. Nan, Y. Shen, *ACS Applied Materials & Interfaces* **2017**, *9*, 9654-9661 10.1021/acsami.6b16304.

[2] P. Hovington, M. Lagacé, A. Guerfi, P. Bouchard, A. Mauger, C. M. Julien, M. Armand, K. Zaghib, *Nano Letters* **2015**, *15*, 2671-2678 10.1021/acs.nanolett.5b00326.

[3] L. Porcarelli, M. A. Aboudzadeh, L. Rubatat, J. R. Nair, A. S. Shaplov, C. Gerbaldi, D. Mecerreyes, *Journal of Power Sources* **2017**, *364*, 191-199 https://doi.org/10.1016/j.jpowsour.2017.08.023.

[4] R. Bouchet, S. Maria, R. Meziane, A. Aboulaich, L. Lienafa, J.-P. Bonnet, T. N. T. Phan, D. Bertin, D. Gigmes, D. Devaux, R. Denoyel, M. Armand, *Nature Materials* **2013**, *12*, 452-457 10.1038/nmat3602.

[5] S. Zhang, X. Lu, Q. Zhou, X. Li, X. Zhang, S. Li, *Ionic Liquids: Physicochemical Properties*, Elsevier Science, **2009**.

[6] A. Eftekhari, Y. Liu, P. Chen, *Journal of Power Sources* **2016**, *334*, 221-239 https://doi.org/10.1016/j.jpowsour.2016.10.025.

[7] L. Fernández-Miguez, P. Vallet, L. C. Tasende-Rodríguez, A. Doval, M. Villanueva, Ó. Cabeza, L. M. Varela, J. Salgado, J. J. Parajó, *Proceedings* **2019**, *41*, 57

[8] F. Endres, O. Höfft, N. Borisenko, L. H. Gasparotto, A. Prowald, R. Al-Salman, T. Carstens, R. Atkin, A. Bund, S. Zein El Abedin, *Physical Chemistry Chemical Physics* **2010**, *12*, 1724-1732 10.1039/B923527M.

[9] O. Hollóczki, F. Malberg, T. Welton, B. Kirchner, *Physical Chemistry Chemical Physics* **2014**, *16*, 16880-16890 10.1039/C4CP01177E.

[10] S. Katsuta, K. Imai, Y. Kudo, Y. Takeda, H. Seki, M. Nakakoshi, *Journal of Chemical & Engineering Data* **2008**, *53*, 1528-1532 10.1021/je800152d.

[11] B. Kirchner, F. Malberg, D. S. Firaha, O. Hollóczki, *Journal of Physics: Condensed Matter* **2015**, *27*, 463002 10.1088/0953-8984/27/46/463002.

[12] K. Ma, J. Forsman, C. E. Woodward, *The Journal of Chemical Physics* **2015**, *142*, 174704 10.1063/1.4919314.

[13] W. Zhao, F. Leroy, B. Heggen, S. Zahn, B. Kirchner, S. Balasubramanian, F. Müller-Plathe, *Journal of the American Chemical Society* **2009**, *131*, 15825-15833 10.1021/ja906337p.

[14] N.-W. Li, Y.-X. Yin, J.-Y. Li, C.-H. Zhang, Y.-G. Guo, *Advanced Science* **2017**, *4*, 1600400-n/a 10.1002/advs.201600400.

[15] A. Hofmann, M. Schulz, T. Hanemann, *International Journal of Electrochemical Science* **2013**, *8*, 10170-10189

[16] S. Drvarič Talian, M. Bešter-Rogač, R. Dominko, *Electrochimica Acta* **2017**, *252*, 147-153 https://doi.org/10.1016/j.electacta.2017.08.168.

[17] E. Karpierz, L. Niedzicki, T. Trzeciak, M. Zawadzki, M. Dranka, J. Zachara, G. Z. Żukowska, A. Bitner-Michalska, W. Wieczorek, *Scientific reports* **2016**, *6*, 35587 10.1038/srep35587.

[18] L. Sun, O. Morales-Collazo, H. Xia, J. F. Brennecke, *The Journal of Physical Chemistry B* **2015**, *119*, 15030-15039 10.1021/acs.jpcb.5b09175.

[19] C. Shi, M. Quiroz-Guzman, A. DeSilva, J. F. Brennecke, *Journal of The Electrochemical Society* **2013**, *160*, A1604-A1610 10.1149/2.116309jes.

[20] M. Hayyan, F. S. Mjalli, M. A. Hashim, I. M. AlNashef, T. X. Mei, *Journal of Industrial and Engineering Chemistry* **2013**, *19*, 106-112 https://doi.org/10.1016/j.jiec.2012.07.011.

[21] G. G. Eshetu, S. Grugeon, S. Laruelle, S. Boyanov, A. Lecocq, J.-P. Bertrand, G. Marlair, *Physical Chemistry Chemical Physics* **2013**, *15*, 9145-9155 10.1039/C3CP51315G.

[22] P Wasserscheid, T. Welton, in *Ionic Liquids in Synthesis*, *Vol. 1*, **2008**, pp. 348-355.

[23] A. Balducci, *Topics in Current Chemistry* **2017**, *375*, 20 10.1007/s41061-017-0109-8.

[24] B. Kirchner, P. J. di Dio, J. Hutter, in *Multiscale Molecular Methods in Applied Chemistry* (Eds.: B. Kirchner, J. Vrabec), Springer Berlin Heidelberg, Berlin, Heidelberg, **2012**, pp. 109-153.

[25] A. M. Fleshman, N. A. Mauro, *Journal of Molecular Liquids* **2019**, *279*, 23-31 https://doi.org/10.1016/j.molliq.2019.01.108.

[26] K. Kim, Y. H. Cho, H. C. Shin, *Journal of Power Sources* **2013**, *225*, 113-118 10.1016/j.jpowsour.2012.10.038.

[27] U. Domańska, M. Królikowska, K. Paduszyński, *Fluid Phase Equilibria* **2011**, *303*, 1-9 https://doi.org/10.1016/j.fluid.2010.12.008.

[28] Y. Zhou, X. Wang, H. Zhu, M. Armand, M. Forsyth, G. W. Greene, J. M. Pringle, P. C. Howlett, *Physical Chemistry Chemical Physics* **2017**, *19*, 2225-2234 10.1039/C6CP07415D.

[29] Y. Zhou, X. Wang, H. Zhu, M. Yoshizawa-Fujita, Y. Miyachi, M. Armand, M. Forsyth, G. W. Greene, J. M. Pringle, P. C. Howlett, *ChemSusChem* **2017**, *10*, 3135-3145 10.1002/cssc.201700691.

[30] J. Choi, A. Manthiram, *Journal of The Electrochemical Society* **2005**, *152*, A1714 10.1149/1.1954927.

[31] H. Ohno, K. Ito, *Chemistry Letters* **1998**, *27*, 751-752 10.1246/cl.1998.751.

[32] A. S. Shaplov, R. Marcilla, D. Mecerreyes, *Electrochimica Acta* **2015**, *175*, 18-34 https://doi.org/10.1016/j.electacta.2015.03.038.

[33] X. W. Li, Z. X. Zhang, S. J. Li, K. H. Yang, L. Yang, *Journal of Materials Chemistry A* **2017**, *5*, 21362-21369 10.1039/c7ta04204c.

[34] H. Ogawa, H. Mori, *Polymer* **2019**, *178*, 121614 https://doi.org/10.1016/j.polymer.2019.121614.

[35] S. Yamaguchi, H. Yamada, Y. Takeoka, M. Rikukawa, M. Yoshizawa-Fujita, *New Journal of Chemistry* **2019**, *43*, 4008-4012 10.1039/C8NJ05127E.

[36] M. Yoshizawa-Fujita, E. Kishi, M. Suematsu, T. Takekawa, M. Rikukawa, *Chemistry Letters* **2014**, *43*, 1909-1911 10.1246/cl.140833.

[37] J. Janikowski, M. R. Razali, C. M. Forsyth, K. M. Nairn, S. R. Batten, D. R. MacFarlane, J. M. Pringle, *ChemPlusChem* **2013**, *78*, 486-497 10.1002/cplu.201300068.

[38] A. J. Hill, J. Huang, J. Efthimiadis, P. Meakin, M. Forsyth, D. R. MacFarlane, *Solid State Ionics* **2002**, *154-155*, 119-124 https://doi.org/10.1016/S0167-2738(02)00472-1.

[39] D. R. MacFarlane, P. Meakin, N. Amini, M. Forsyth, *Journal of Physics: Condensed Matter* **2001**, *13*, 8257-8267 10.1088/0953-8984/13/36/303.

[40] S. J. Pas, J. Huang, M. Forsyth, D. R. MacFarlane, A. J. Hill, *The Journal of Chemical Physics* **2005**, *122*, 064704 10.1063/1.1845397.

[41] S. Asha, K. P. Vijayalakshmi, B. K. George, *International Journal of Quantum Chemistry* **2019**, *119*, 12 10.1002/qua.26014.

[42] S. Pandian, K. S. Hariharan, S. P. Adiga, S. M. Kolake, *Journal of The Electrochemical Society* **2020**, *167*, 070550 10.1149/1945-7111/ab8061.

[43] G. G. Eshetu, S. Jeong, P. Pandard, A. Lecocq, G. Marlair, S. Passerini, *ChemSusChem* **2017**, *10*, 3146-3159 10.1002/cssc.201701006.

[44] C. Francis, R. Louey, K. Sammut, A. S. Best, *Journal of The Electrochemical Society* **2018**, *165*, A1204-A1221 10.1149/2.0281807jes.

[45] C. F. J. Francis, I. L. Kyratzis, A. S. Best, *Advanced Materials* **2020**, *n/a*, 1904205 10.1002/adma.201904205.

[46] M. Eftekharnia, M. Hasanpoor, M. Forsyth, R. Kerr, P. C. Howlett, *ACS Applied Energy Materials* **2019**, *2*, 6655-6663 10.1021/acsaem.9b01175.

[47] B. Z. Zheng, J. P. Zhu, H. C. Wang, M. Feng, E. Umeshbabu, Y. X. Li, Q. H. Wu, Y. Yang, *ACS Applied Materials & Interfaces* **2018**, *10*, 25473-25482 10.1021/acsami.8b08860.

[48] A. Heist, S. Hafner, S. H. Lee, *Journal of The Electrochemical Society* **2019**, *166*, A873-A879 10.1149/2.0071906jes.

[49] A. P. Lewandowski, A. F. Hollenkamp, S. W. Donne, A. S. Best, *Journal of Power Sources* **2010**, *195*, 2029-2035 https://doi.org/10.1016/j.jpowsour.2009.10.059.

[50] M. Moreno, E. Simonetti, G. B. Appetecchi, M. Carewska, M. Montanino, G. T. Kim, N. Loeffler, S. Passerini, *Journal of The Electrochemical Society* **2016**, *164*, A6026-A6031 10.1149/2.0051701jes.

[51] Q. W. Huang, Y. Y. Lee, B. Gurkan, *Industrial & Engineering Chemistry Research* **2019**, *58*, 22587-22597 10.1021/acs.iecr.9b03202.

[52] P. P. Dahiya, J. Patra, J. K. Chang, K. Sahoo, S. B. Majumder, S. Basu, *Journal of the Taiwan Institute of Chemical Engineers* **2019**, *95*, 195-201 10.1016/j.jtice.2018.06.038.

[53] J.-Z. Wang, S.-L. Chou, S.-Y. Chew, J.-Z. Sun, M. Forsyth, D. R. MacFarlane, H.-K. Liu, *Solid State Ionics* **2008**, *179*, 2379-2382 https://doi.org/10.1016/j.ssi.2008.09.007.

[54] S.-L. Chou, J.-Z. Wang, J.-Z. Sun, D. Wexler, M. Forsyth, H.-K. Liu, D. R. MacFarlane, S.-X. Dou, *Chemistry of Materials* **2008**, *20*, 7044-7051 10.1021/cm801468q.

[55] F. Sälzer, L. Pateras Pescara, F. Franke, C. Müller, J. Winkler, M. Schwalm, B. Roling, *Batteries & Supercaps* **2020**, *3*, 117-125 10.1002/batt.201900111.

[56] S. Seki, Y. Kobayashi, H. Miyashiro, Y. Ohno, Y. Mita, N. Terada, P. Charest, A. Guerfi, K. Zaghib, *The Journal of Physical Chemistry C* **2008**, *112*, 16708-16713 10.1021/jp805403e.

[57] J. H. Park, J. Moon, S. Han, S. Park, J. W. Lim, D. J. Yun, D. Y. Kim, K. Park, I. H. Son, *Journal of Physical Chemistry C* **2017**, *121*, 26155-26162 10.1021/acs.jpcc.7b05876.

[58] Y. Domi, H. Usui, K. Yamaguchi, S. Yodoya, H. Sakaguchi, *ACS Applied Materials & Interfaces* **2019**, *11*, 2950-2960 10.1021/acsami.8b17123.

[59] S. Yodoya, Y. Domi, H. Usui, H. Sakaguchi, *ChemistrySelect* **2019**, *4*, 1375-1378 10.1002/slct.201803282.

[60] C. C. Nguyen, S.-W. Song, *Electrochemistry Communications* **2010**, *12*, 1593-1595 https://doi.org/10.1016/j.elecom.2010.09.003.

[61] J. R. Nair, F. Colò, A. Kazzazi, M. Moreno, D. Bresser, R. Lin, F. Bella, G. Meligrana, S. Fantini, E. Simonetti, G. B. Appetecchi, S. Passerini, C. Gerbaldi, *Journal of Power Sources* **2019**, *412*, 398-407 https://doi.org/10.1016/j.jpowsour.2018.11.061.

[62] S. K. Singh, D. Dutta, R. K. Singh, *Electrochimica Acta* **2020**, *343*, 136122 https://doi.org/10.1016/j.electacta.2020.136122.

[63] H. Gupta, S. Kataria, L. Balo, V. K. Singh, S. K. Singh, A. K. Tripathi, Y. L. Verma, R. K. Singh, *Solid State Ionics* **2018**, *320*, 186-192 https://doi.org/10.1016/j.ssi.2018.03.008.

[64] A. Guerfi, M. Dontigny, Y. Kobayashi, A. Vijh, K. Zaghib, *Journal of Solid State Electrochemistry* **2008**, *13*, 1003 10.1007/s10008-008-0697-x.

[65] L. B. Li, X. Y. Yang, J. S. Li, Y. P. Xu, *Ionics* **2018**, *24*, 735-741 10.1007/s11581-017-2254-z.

[66] Y. Yang, Q. Wu, D. Wang, C. Ma, Z. Chen, C. Zhu, Y. Gao, C. Li, *Journal of Membrane Science* **2020**, *595*, 117549 https://doi.org/10.1016/j.memsci.2019.117549.

[67] D. Kim, X. Liu, B. Yu, S. Mateti, L. A. O'Dell, Q. Rong, Y. Chen, *Advanced Functional Materials* **2020**, *30*, 1910813 10.1002/adfm.201910813.

[68] Z. Wen, Y. Li, Z. Zhao, W. Qu, N. Chen, Y. Xing, Y. Ma, L. Li, F. Wu, R. Chen, *Journal of Materials Chemistry A* **2020** 10.1039/D0TA02098B.

[69] Y. Preibisch, F. Horsthemke, M. Winter, S. Nowak, A. S. Best, *Chemistry of Materials* **2020**, *32*, 2389-2398 10.1021/acs.chemmater.9b04827.

[70] M. Pyschik, C. Schultz, S. Passerini, M. Winter, S. Nowak, *Electrochimica Acta* **2015**, *176*, 1143-1152 https://doi.org/10.1016/j.electacta.2015.07.168.

[71] M. Pyschik, M. Winter, S. Nowak, *Journal of Chromatography A* **2017**, *1485*, 131-141 https://doi.org/10.1016/j.chroma.2017.01.034.

[72] M. C. Kroon, W. Buijs, C. J. Peters, G.-J. Witkamp, *Green Chemistry* **2006**, *8*, 241-245 10.1039/B512724F.

[73] L. Grande, J. von Zamory, S. L. Koch, J. Kalhoff, E. Paillard, S. Passerini, *ACS Applied Materials & Interfaces* **2015**, *7*, 5950-5958 10.1021/acsami.5b00209.

[74] P. Nürnberg, E. I. Lozinskaya, A. S. Shaplov, M. Schönhoff, *The Journal of Physical Chemistry B* **2020**, *124*, 861-870 10.1021/acs.jpcb.9b11051.

[75] J. P. Hoffknecht, M. Drews, X. He, E. Paillard, *Electrochimica Acta* **2017**, *250*, 25-34 10.1016/j.electacta.2017.08.020.

[76] S. A. Pervez, G. Kim, B. P. Vinayan, M. A. Cambaz, M. Kuenzel, M. Hekmatfar, M. Fichtner, S. Passerini, *Small* **2020**, *16*, 2000279 10.1002/smll.202000279.

[77] W. Cho, J. Park, K. Kim, J. S. Yu, G. Jeong, *Small*, 7 10.1002/smll.201902138.

[78] J. Li, L. E. Downie, L. Ma, W. Qiu, J. R. Dahn, *Journal of The Electrochemical Society* **2015**, *162*, A1401-A1408 10.1149/2.1011507jes.

[79] A. Balducci, S. S. Jeong, G. T. Kim, S. Passerini, M. Winter, M. Schmuck, G. B. Appetecchi, R. Marcilla, D. Mecerreyes, V. Barsukov, V. Khomenko, I. Cantero, I. De

Meatza, M. Holzapfel, N. Tran, *Journal of Power Sources* **2011**, *196*, 9719-9730 https://doi.org/10.1016/j.jpowsour.2011.07.058.

[80] D. Di Lecce, J. Hassoun, *Acs Omega* **2018**, *3*, 8583-8588 10.1021/acsomega.8b01328.

[81] G. A. Elia, U. Ulissi, S. Jeong, S. Passerini, J. Hassoun, *Energy & Environmental Science* **2016**, *9*, 3210-3220 10.1039/C6EE01295G.

[82] N. Sanchez-Ramirez, B. D. Assresahegn, R. M. Torresi, D. Bélanger, *Energy Storage Materials* **2020**, *25*, 477-486 https://doi.org/10.1016/j.ensm.2019.09.035.

[83] D. M. Piper, T. Evans, K. Leung, T. Watkins, J. Olson, S. C. Kim, S. S. Han, V. Bhat, K. H. Oh, D. A. Buttry, S.-H. Lee, *Nature Communications* **2015**, *6*, 6230 10.1038/ncomms7230.

[84] M. Kerner, P. Johansson, *Batteries-Basel* **2018**, *4*, 12 10.3390/batteries4010010.

[85] G. B. Appetecchi, G. T. Kim, M. Montanino, M. Carewska, R. Marcilla, D. Mecerreyes, I. De Meatza, **2010**, *195*, 3668-3675 10.1016/j.jpowsour.2009.11.146.

[86] K. Kimura, H. Matsumoto, J. Hassoun, S. Panero, B. Scrosati, Y. Tominaga, *Electrochimica Acta* **2015**, *175*, 134-140 https://doi.org/10.1016/j.electacta.2015.03.117.

[87] J.-K. Kim, L. Niedzicki, J. Scheers, C.-R. Shin, D.-H. Lim, W. Wieczorek, P. Johansson, J.-H. Ahn, A. Matic, P. Jacobsson, *Journal of Power Sources* **2013**, *224*, 93-98 https://doi.org/10.1016/j.jpowsour.2012.09.029.

[88] S. W. Choi, S. M. Jo, W. S. Lee, Y.-R. Kim, *Advanced Materials* **2003**, *15*, 2027-2032 10.1002/adma.200304617.

[89] L. M. McGrath, J. Jones, E. Carey, J. F. Rohan, in *ChemistryOpen, Vol. 8*, **2019**, pp. 1429-1436.

[90] G. T. Kim, S. S. Jeong, M. Z. Xue, A. Balducci, M. Winter, S. Passerini, F. Alessandrini, G. B. Appetecchi, *Journal of Power Sources* **2012**, *199*, 239-246 https://doi.org/10.1016/j.jpowsour.2011.10.036.

[91] M. Sano, N. Tachikawa, K. Yoshii, N. Serizawa, Y. Katayama, *Electrochemistry* **2018**, *86*, 260-264 10.5796/electrochemistry.18-00033.

[92] M. Wu, N. R. Brooks, S. Schaltin, K. Binnemans, J. Fransaer, *Physical Chemistry Chemical Physics* **2013**, *15*, 4955-4964 10.1039/C3CP44554B.

[93] M. Wu, G. Vanhoutte, N. R. Brooks, K. Binnemans, J. Fransaer, *Physical Chemistry Chemical Physics* **2015**, *17*, 12080-12089 10.1039/C4CP06076H.

[94] A. Lahiri, A. Willert, S. Z. E. Abedin, F. Endres, *Electrochimica Acta* **2014**, *121*, 154-158 https://doi.org/10.1016/j.electacta.2013.12.084.

[95] R. Al-Salman, J. Mallet, M. Molinari, P. Fricoteaux, F. Martineau, M. Troyon, S. Z. El Abedin, F. Endres, *Physical Chemistry Chemical Physics* **2008**, *10*, 6233-6237 10.1039/B809075K.

[96] F. Martineau, K. Namur, J. Mallet, F. Delavoie, F. Endres, M. Troyon, M. Molinari, *IOP Conference Series: Materials Science and Engineering* **2009**, *6*, 012012 10.1088/1757-899x/6/1/012012.

[97] S. Link, S. Ivanov, A. Dimitrova, S. Krischok, A. Bund, *Journal of Crystal Growth* **2020**, *531*, 125346 https://doi.org/10.1016/j.jcrysgro.2019.125346.

[98] N.-S. Choi, Y. Lee, S.-S. Kim, S.-C. Shin, Y.-M. Kang, *Journal of Power Sources* **2010**, *195*, 2368-2371 https://doi.org/10.1016/j.jpowsour.2009.10.063.

[99] W. Lu, A. Goering, L. Qu, L. Dai, *Physical Chemistry Chemical Physics* **2012**, *14*, 12099-12104 10.1039/C2CP40726D.

[100] X. Gao, F. Wu, A. Mariani, S. Passerini, *ChemSusChem* **2019**, *12*, 4185-4193 10.1002/cssc.201901739.

[101] M. Li, B. Yang, L. Wang, Y. Zhang, Z. Zhang, S. Fang, Z. Zhang, *Journal of Membrane Science* **2013**, *447*, 222-227 https://doi.org/10.1016/j.memsci.2013.07.007.

[102] M. Li, L. Wang, B. Yang, T. Du, Y. Zhang, *Electrochimica Acta* **2014**, *123*, 296-302 https://doi.org/10.1016/j.electacta.2013.12.179.

[103] N. Zhou, Y. Wang, Y. Zhou, J. Shen, Y. Zhou, Y. Yang, *Electrochimica Acta* **2019**, *301*, 284-293 https://doi.org/10.1016/j.electacta.2019.01.143.

[104] T. Sato, S. Marukane, T. Narutomi, T. Akao, *Journal of Power Sources* **2007**, *164*, 390-396 https://doi.org/10.1016/j.jpowsour.2006.10.048.

[105] S. Fang, L. Qu, D. Luo, S. Shen, L. Yang, S.-i. Hirano, *RSC Advances* **2015**, *5*, 33897-33904 10.1039/C5RA01713K.

[106] H.-B. Han, K. Liu, S.-W. Feng, S.-S. Zhou, W.-F. Feng, J. Nie, H. Li, X.-J. Huang, H. Matsumoto, M. Armand, Z.-B. Zhou, *Electrochimica Acta* **2010**, *55*, 7134-7144 https://doi.org/10.1016/j.electacta.2010.06.063.

[107] S. Fang, Y. Jin, L. Yang, S.-i. Hirano, K. Tachibana, S. Katayama, *Electrochimica Acta* **2011**, *56*, 4663-4671 https://doi.org/10.1016/j.electacta.2011.02.107.

[108] X. Y. Mei, Z. Yue, J. Tufts, H. Dunya, B. K. Mandal, *Journal of Fluorine Chemistry* **2018**, *212*, 26-37 10.1016/j.jfluchem.2018.05.008.

[109] S. Zhang, J. Li, N. Jiang, X. Li, S. Pasupath, Y. Fang, Q. Liu, D. Dang, *Chemistry – An Asian Journal* **2019**, *14*, 2810-2814 10.1002/asia.201900581.

[110] S. Fang, Z. Zhang, Y. Jin, L. Yang, S.-i. Hirano, K. Tachibana, S. Katayama, *Journal of Power Sources* **2011**, *196*, 5637-5644 https://doi.org/10.1016/j.jpowsour.2011.02.047.

[111] S. Ferrari, E. Quartarone, P. Mustarelli, A. Magistris, M. Fagnoni, S. Protti, C. Gerbaldi, A. Spinella, *Journal of Power Sources* **2010**, *195*, 559-566 https://doi.org/10.1016/j.jpowsour.2009.08.015.

[112] C. Sirisopanaporn, A. Fernicola, B. Scrosati, *Journal of Power Sources* **2009**, *186*, 490-495 https://doi.org/10.1016/j.jpowsour.2008.10.036.

[113] A. Fernicola, F. C. Weise, S. G. Greenbaum, J. Kagimoto, B. Scrosati, A. Soleto, *Journal of The Electrochemical Society* **2009**, *156*, A514-A520

[114] A. Fernicola, F. Croce, B. Scrosati, T. Watanabe, H. Ohno, *Journal of Power Sources* **2007**, *174*, 342-348 https://doi.org/10.1016/j.jpowsour.2007.09.013.

[115] X. Y. Mei, Z. Yue, Q. Ma, H. Dunya, B. K. Mandal, *Journal of Molecular Liquids* **2018**, *272*, 1001-1018 10.1016/j.molliq.2018.10.085.

[116] D. Al-Masri, R. Yunis, H. J. Zhu, L. Y. Jin, P. Bruce, A. F. Hollenkamp, J. M. Pringle, *Journal of Materials Chemistry A* **2019**, *7*, 25389-25398 10.1039/c9ta11175a.

Chapter 2:

Electrochemical and Physical Characterisation Techniques

2.1 Electrochemical Techniques

2.1.1 Cyclic Voltammetry

Cyclic voltammetry (CV) is a widely used technique, which acquires qualitative information about electrochemical reactions. It stems from a set of techniques known as potential sweep methods which apply a continuously time varying potential to the working electrode. This results in the occurrence of oxidation or reduction reactions of electroactive species in solution (faradaic reactions), the possible adsorption of species according to the potential and a capacitive current due to double layer charging.[1] The principle use of CV has been to diagnose electrochemical reaction mechanisms, for the detection and identification of species present in solution and for the semi quantitative analysis of reaction rates.[2-3] It consists of scanning linearly, the potential of a stationary working electrode, using a triangular waveform as shown in figure 2.1.

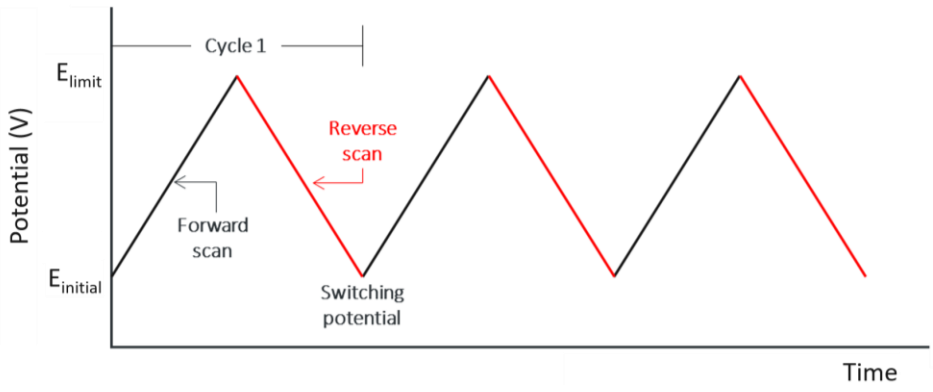

Figure 2.1: Potential-time excitation signal in CV experiment.

The potential, measured as a difference between the reference and working electrodes, is scanned from an initial value to a set potential, and then reversed to the initial potential or a specified final potential. As the potential is scanned, the resulting current between the working electrode and the counter electrode is measured and displayed as a voltammogram. The initial potential is chosen such that no Faradaic processes occur, as this allows for direct comparison of the forward and reverse scans. Depending on the information sought, single or multiple cycles can be used, where equilibrium potentials (E_{eq}) can be determined, electron transfer kinetics can be quantified and chemical reactions prior to/or following electrochemical reactions can be detected.

For example, in a solution which contains the reduced form of a redox couple, the initial potential is chosen to be sufficiently negative relative to the E_{eq} of the redox couple and is scanned in the anodic direction. At the initial potential, the bulk solution contains only the reduced form of the redox couple, and results in a background current reading. As the potential is scanned, and approaches the E_{eq} of the redox couple, the reduced form is converted into its oxidised form, which results in an increase in the net anodic current which increases exponentially with the potential. Concentration gradients are set up for both the oxidised and reduced species, and diffusion of the electroactive species occurs across these gradients. The corresponding peak currents indicate that the overpotential (the difference between the theoretical cell potential and the actual potential that is necessary to cause a reaction) is positive enough to instantly convert any reduced species that reach the electrode's surface into its oxidised form. The subsequent current is dependent on the rate of mass transfer to the electrode surface. When the scan is reversed for a reversible redox couple, the reaction slows down, the current approaches zero on the current axis, i.e. E_{eq}. at this point a net reduction of the oxidised species to its reduced form occurs, which results in an increase in the cathodic current. As the oxidised species reach the electrode surface they instantly reduce, which is indicated by the resultant peak in the example shown in figure 2.2.

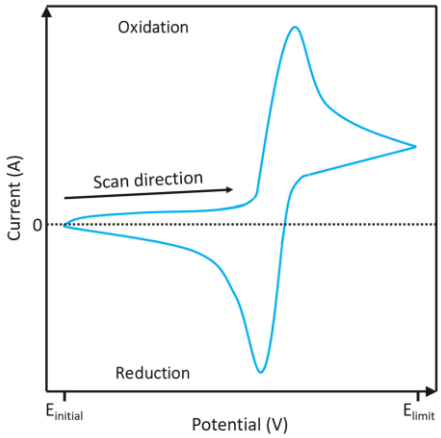

Figure 2.2: Typical CV for a reversible R - ne$^-$ ↔ O redox process.

The surface area under the current profile is proportional to the charge in the reaction as the potential of a CV is changed at a constant scan rate. By applying CV to analyse the electrochemical performance of Li-ion battery electrodes, the electrode capacity can be determined from the Li^+ insertion/de-insertion peaks. The cathodic current values indicate Li insertion into the working electrode, or surface reactions such as SEI layer formation. The anodic current values indicate Li^+ extraction from the working electrode or oxidation of the electrolyte.

2.1.2 Chronoamperometry

Although CV can provide qualitative information, it is less helpful for kinetic studies due to its continuous potential change during the experiment. Perturbing the system, with a potential or current step results in an instantaneous alteration to the electrochemical system, and analysis of the system after this perturbation permits deductions about electrode reactions and their rates.[1] The study of the variation of the current response with time under potentiostatic control is known as chronoamperometry (CA). CA is used to study various processes such as the kinetics of diffusion processes, chemical reactions, adsorptions and provide quantitative information about electrochemical nucleation and growth processes. The potential is stepped from one where no

electrode reaction occurs to one where faradaic reactions occur. This potential is maintained at this value for a specific amount of time, and results in a current response, such as those shown in figure 2.3. This current is the faradaic current, I_f, since it is due only to a faradaic electrode process (only electron transfer). However, when the potential is changed, the double layer has to be charged, giving rise to a capacitive current, I_c.

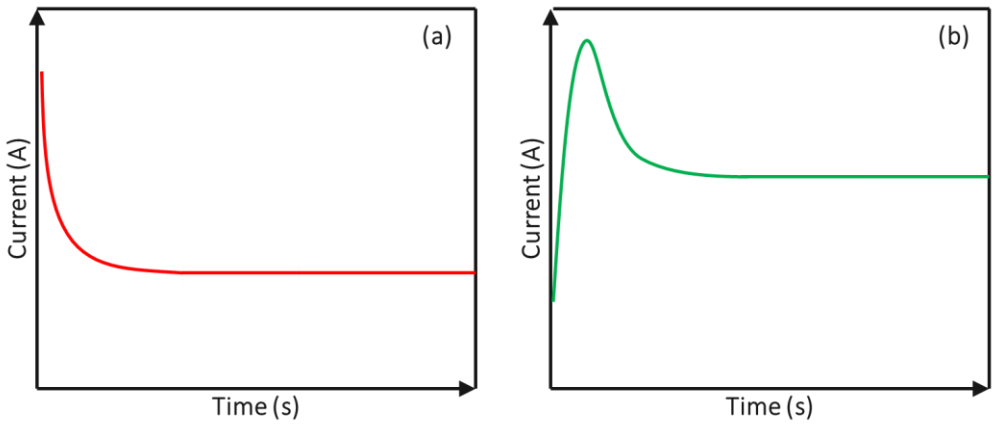

Figure 2.3: Examples of CA current profiles that can be obtained for various processes such as (a) redox couple and (b) metal deposition processes.

For a redox couple, where both the oxidised (O) and reduced (R) forms are soluble in the electrolyte, assuming the electrode potential is poised at an initial potential more positive than redox couple potential (E_{redox}) and by applying a potential step more negative than E_{redox} will create a response that is significantly lower, thus resulting in rapid reduction of the oxidised species when it reaches the electrode surface. A diffusion layer results at the electrode surface, where the concentration of the electroactive species becomes gradually lower near the electrode surface. This in turn creates a concentration gradient between the electrode and the bulk of the solution. The diffusion layer grows and extends into the bulk of the solution as a function of time, and results in a decrease in current over time.

In contrast, for metal deposition, the reduced form is not soluble in solution. Assuming the oxidised form is present in solution, applying a negative potential below E_{eq} will allow for the insoluble reduced form to initially form nuclei, which grow independently (figure 2.4). Initially, the current response increases due to the nucleation and growth of the metal deposit. When the nuclei are deposited, they can be grown to create either a 2D or 3D structure which results in an increase in the surface area and consequentially the current response. A diffusion layer forms around these nuclei, initially these diffusion layers are isolated and grow independently. As the nuclei grow and get close to either other nuclei or growth sites, the diffusion layers begin to overlap and combine. This results in a planar flux,[4-5] and reduced surface area in comparison to the initial 3D nuclei as shown in figure 2.4.

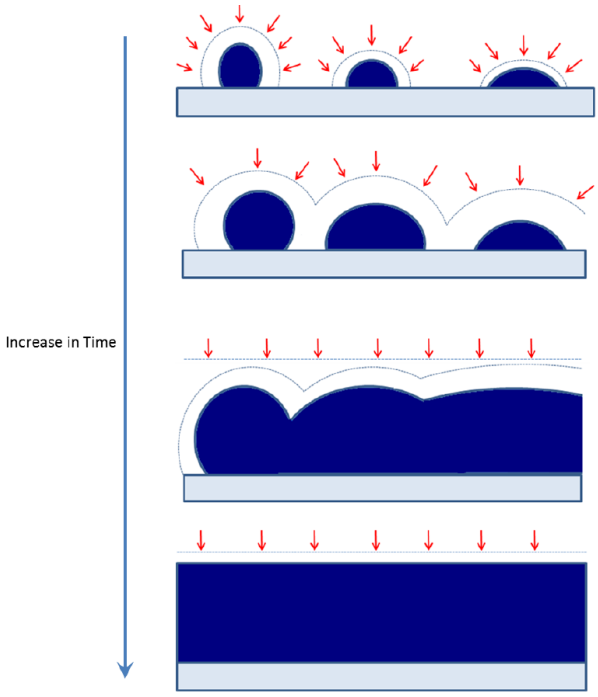

Figure 2.4: Time dependent behaviour of the flux of the electroactive material during electrodeposition on a foreign substrate.

The transition from the formation of the 3D nuclei to the planar diffusion is reflected in the current response – initial rise to the eventual drop in current. The diffusion controlled growth of metal

deposits have been theoretically modelled with models based on planar diffusion flux.[6-8] The experimental currents tend to deviate positively with respect to the theoretical current as convection develops at prolonged hold times due to density gradients that form from electrolysis products.

2.1.3 Chronopotentiometry

Chronopotentiometry (CP) is similar to CA, however it involves applying a constant current, and the resultant potential is measured until it reaches a set potential, or for a defined length of time. It is useful for investigating reactions which occur at the working electrode but with the advantage that the reaction rate is fixed. The corresponding potential is measured and is the result of both kinetic and thermodynamic reactions. The ohmic drop is also constant since it is equal to both the current and solution resistance. CP is also known as charge-discharge or galvanostatic cycling and plot potential against time (figure 2.5).

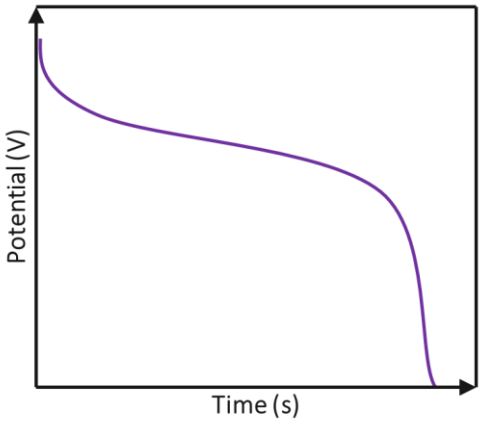

Figure 2.5: Example of CP profile.

For battery materials, these plots can also represent the capacity of the electrode (mAh g^{-1}) versus the potential. The capacity (mAh g^{-1}) of the electrode is the amount of charge that can be stored/released per gram of electrode material. Information which can be obtained from these plots include:

1. Capacity at a given potential
2. Average cell potential

3. Specific energy (Wh g^{-1})
4. Formation of redox species – indicated by plateau in curve
5. Polarisation – difference in plateau potentials of charge and discharge profiles

The disadvantages associated with CP, particularly when planar electrodes are utilised, are convection at long times and complications by charging current contributions to the overall current.[9] Convective effects can be minimized by choosing current densities such that transition times are no longer than 30–60 s. Double layer charging that occurs throughout the CP experiment, can be problematic as the current that flows to charge the double-layer means that the faradaic current differs from the applied current, thus introducing inaccuracies in the measurement of transition times. Coupling short transition times with large capacitance electrodes, and low concentration contribute to higher fraction of the applied current, which can lead to less accurate determinations of electrochemical processes such as diffusion coefficients.

2.1.4 Electrochemical Impedance Spectroscopy

For impedance measurements, the cell is perturbed with an alternating signal of a small magnitude, and the response to the perturbation at the steady state is observed.[10] It is capable of high precision and is frequently used for the evaluation of heterogeneous charge transfer parameters and for studies of the double layer structure. To understand the concept of impedance, an understanding of electronic circuits is essential, and will be outlined in the following.

Ohm's Law outlines the fundamental relationship between voltage, current and resistance. Ohm's law states that the electric current that flows through a conductor, I, is directly proportional to the voltage applied to the conductor, V. The ratio of voltage to current is called the resistance, R.

$$R = \frac{V}{I} \qquad \text{Equation 2.1}$$

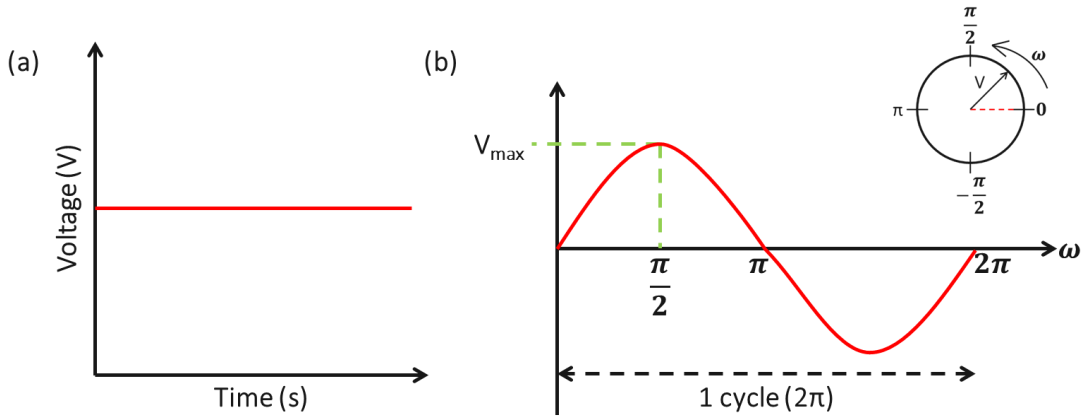

Figure 2.6: Graphs of voltage versus time for (a) direct current, and (b) alternating current.

Alternating current (AC) circuits are not purely resistive and require a modification to Ohm's Law in order for it to be applicable. The modification requires the effect of capacitance and inductance to be considered. This leads to the formation of equation 2.2, where Z is the impedance of the circuit, V and I are the root mean squared values of the voltage and current.

$$Z = \frac{V}{I} \qquad \text{Equation 2.2}$$

When a sine wave is applied to a circuit, the resulting sinusoidal current will have the same frequency, however, it may have a phase difference. This can be represented using waveform and phasor diagrams, and clearly illustrates the differences between the various elements that can be measured with impedance.

For a purely resistive circuit, the current and voltage have the same behaviour for both alternating and direct voltage. This results in a sinusoidal current with the same frequency, which passes through zero at the same time as the voltage. They are considered to be in-phase even though the magnitude of the current value may vary by comparison to the sinusoidal voltage (figure 2.7).

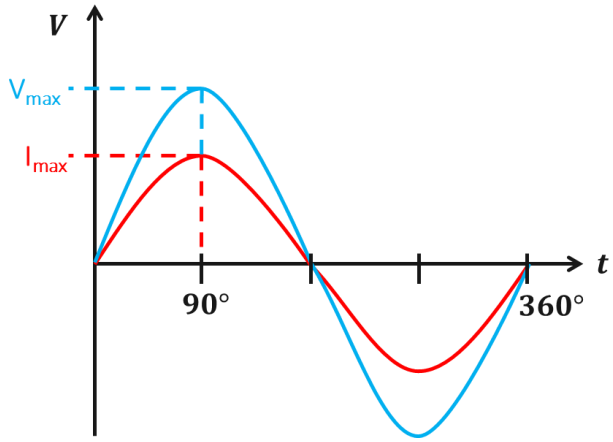

Figure 2.7: Waveform illustrating a purely resistive circuit, where both voltage and current are in phase.

This can be represented as a phasor diagram, where it yields information regarding complex impedance. Impedance consists of imaginary and real parts, where the x-axis represents the real part of the system, and the y-axis represents the imaginary components of the system. As the voltage and current are in-phase, then the phase angle is zero ($\theta = 0°$), and so the system does not contain an imaginary component (figure 2.8).

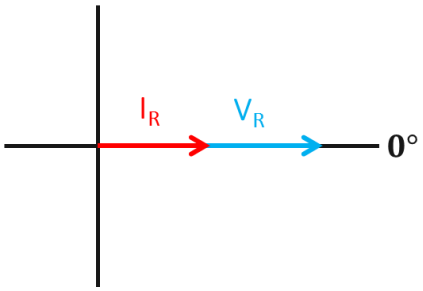

Figure 2.8: Phasor diagram for a purely resistive circuit where $\theta = 0$.

AC circuits often have other elements such as capacitance and inductance which are collectively known as reactance. Electrical reactance is the opposition of a circuit element to a change in current or voltage due to the element's inductance or capacitance. The total reactance of the system is the sum of its capacitive reactance (X_C) and its inductive reactance ($-X_L$):

$$X = X_C + X_L \qquad \text{Equation 2.3}$$

Ideal capacitors and inductors store energy rather than dissipating it, unlike resistors, and hence they contribute to the imaginary part of the impedance:

$$Z = R + jX \qquad \text{Equation 2.4}$$

where Z is the complex impedance, R is the resistance, j is the imaginary component (where $j^2 = -1$), and X is the circuit reactance. The presence of either ideal capacitors or inductors within a circuit induces a phase shift between the current and the voltage, which are considered out of phase, when the phase angle is 90°.

It is understood that the capacitive reactance is inversely proportional to the frequency, while the inductive reactance is proportional. Therefore, with increasing AC frequency, the capacitive reactance decreases, whereas the inductive reactance increases. For an ideal capacitor, the voltage lags behind the current by a 90° phase shift, where the voltage wave is -90° "out of phase" with the current wave. The reactance of an ideal capacitor is therefore it's impedance and is negative for all frequency and capacity values as shown in figure 2.9.

$$Z = X_C = \frac{1}{\omega C} \qquad \text{Equation 2.5}$$

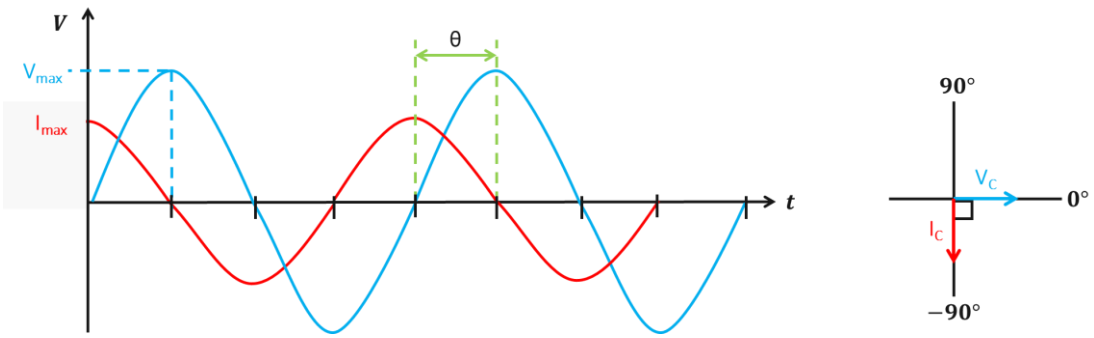

Figure 2.9: Sinusoidal waveform (left) and phasor diagram (right) for a pure capacitor with the voltage as the reference phasor (θ = -90°).

For an ideal inductor, the voltage leads the current by a 90° phase shift, where the voltage wave is +90° "out of phase" with the current wave. The reactance of an ideal inductor is therefore its impedance and is negative for all frequency and capacity values as shown in figure 2.10.

$$Z = X_L = \omega L \qquad \text{Equation 2.5}$$

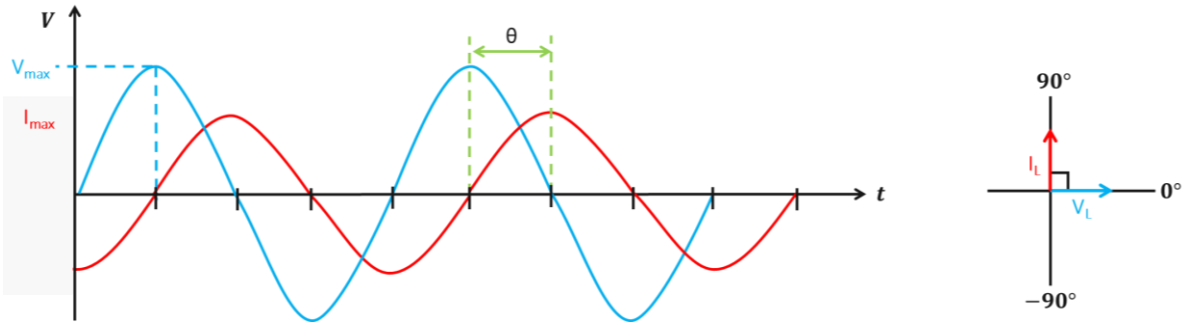

Figure 2.10: Sinusoidal waveform (left) and phasor diagram (right) for a pure inductor with the voltage as the reference phasor ($\theta = +90°$).

The above theory is based on the existence of ideal elements, however purely resistive, capacitive and inductive elements do not exist and the phase angle will be somewhere between 0° and 90° for real systems.

Equivalent circuits must be applied to the experimental data in order to try understand the complex reactions being measured. The circuit that provides the best fit can be used to ascertain the reactions that may be occurring such as electrode modifications, or reactions occurring at the electrode/electrolyte interface. Some circuits despite having different circuit elements or configuration can fit the experimental data, therefore, it is important to understand which circuit elements are present within the cell. For example, Warburg diffusion (W) occurs when ions diffuse within the system, it is generally observed in the low frequency region (< 100 Hz) as the diffusion distance has increased, and reactants must diffuse farther to the electrode. Depending on the cell voltage utilised, other reactions can be observed. For example, utilising cell voltages corresponding

to a cell reaction will allow for charge transfer resistance (R_{ct}) to be observed as shown in a typical Nyquist plot (figure 2.11(a)). The Nyquist plot obtained is the response to the imposition of varying frequencies, where typical frequency ranges used in the literature are approximately 150 kHz to 10 Hz,[11] where figure 2.11(b) shows which regions of the plot are typically associated with kHz, Hz and mHz frequencies. These include electrochemical charge transfer between the solution and the electrode and the diffusion of metal ions in the electrolyte, via oxidation and reduction processes. It is usually observed in Nyquist plots as a semi-circle as shown in figure 2.11, and it arises from internal cell resistance. The formation of a solid-electrolyte interphase (SEI) layer during cycling of battery materials can often result in the formation of a second semi-circle within the Nyquist plot.

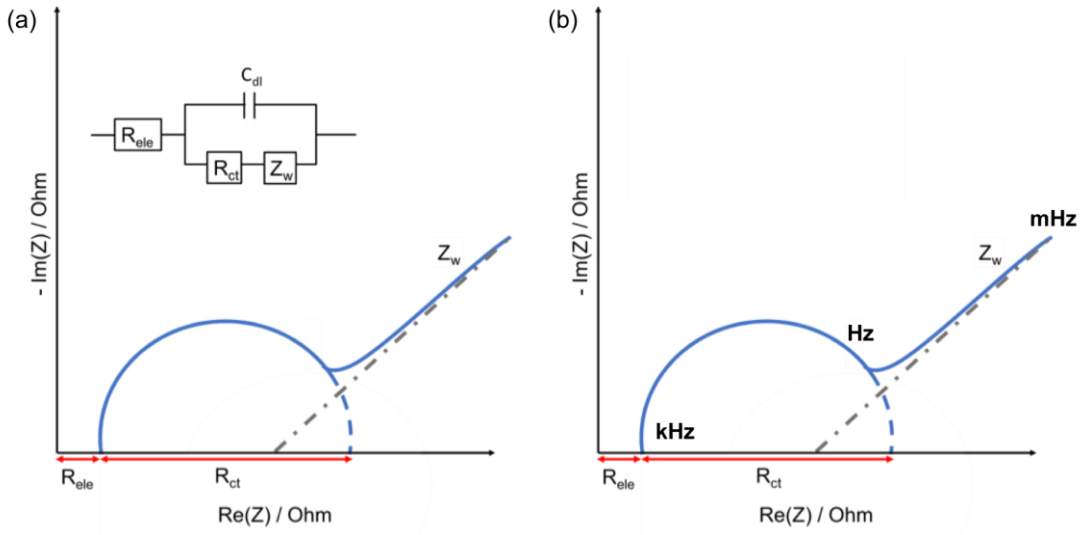

Figure 2.11: Typical Nyquist plot for cell containing electrolyte resistance (R_{ele}), charge-transfer resistance (R_{ct}), Warburg impedance (Z_W) and double layer capacitance (C_{dl}). Inset is equivalent circuit.

EIS is useful in determining the conductivity of the electrolyte, analysing the electrode/electrolyte interface e.g. SEI layer formation, among other factors which will determine the performance of battery materials.

2.2 Physical Characterisation and Deposition

2.2.1 Scanning Electron Microscope and Energy Dispersive X-ray Spectrometry

Scanning electron microscopy (SEM) utilises electrons rather than light photons to form an image and can be used to observe and characterise materials at the nanometre to micron scale. It comprises of various parts such as the electron gun, condenser lens, scanning coil, objective lens, among others (figure 2.12).

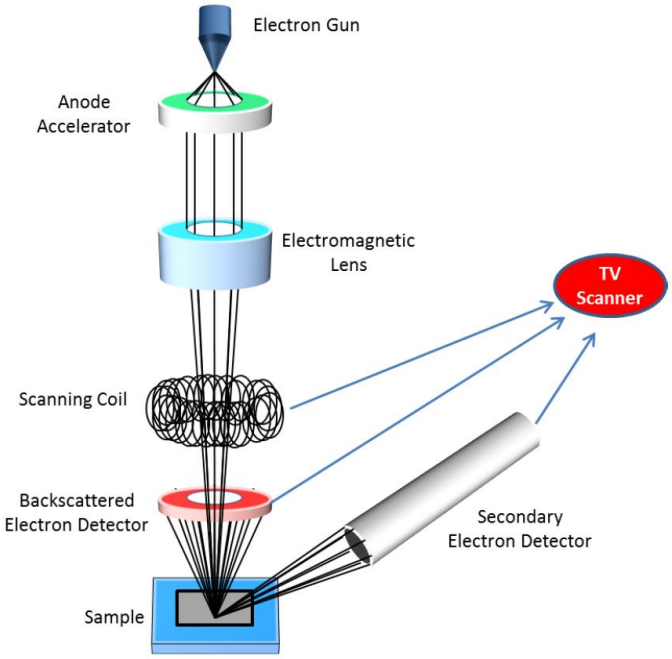

Figure 2.12: Schematic illustration of the working principle of SEM. Adapted from Goldstein et. al.[12]

The electron gun produces a highly energised electron beam which is then rastered across the sample surface. There are three types of electron gun:

1. Field-emission
2. Schottky-emission
3. Thermionic emission

For the thermionic emission electron gun, it comprises a filament which is typically made of tungsten. From this filament (cathode) thermoelectrons are emitted. The thermoelectrons are focused with electron lenses to form a beam when the filament is heated at high temperatures. In order to accelerate the electron beam, a negative voltage is required which will repel and accelerate the negatively charged electrons. This is achieved through the use of the Wehnelt electrode. Once the beam passes through the anode, it is accelerated through a column which contains various condenser and objective lenses (figure 2.13).

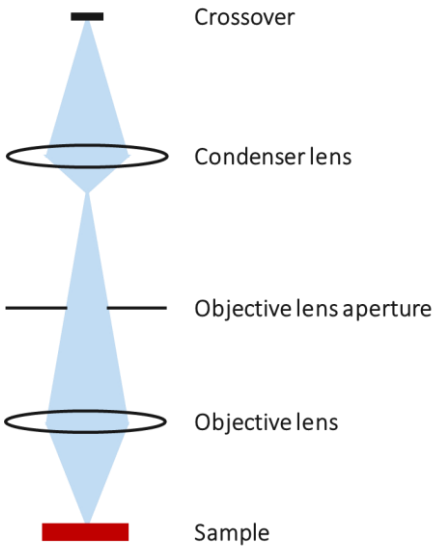

Figure 2.13: Schematic illustrating the formation of the electron probe using the various lenses.

These lenses allow the electron beam to be focused onto the sample by producing a small electron probe. The focused beam will then hit the sample surface and penetrate into the sample. The depth of penetration depends on the beam energy, the atomic number of the atoms in the molecule and finally the density of the constituent atoms. The electron beam interacts with the sample to produce various scattering effects which are collected by a detector. These scattering effects can be elastic or inelastic, and produces backscattered and secondary electrons, respectively.

Secondary electrons are utilised for imaging as they can be used to provide contrast within an image. This is achieved as secondary electrons have very small energies, and those produced within the

sample will be quickly absorbed, while those generated at the top surface of the sample will be emitted. This translates into regions of dark and bright which show changes in elevation or pitch within a sample.

In order to view the sample in the greatest detail, the electron probe must be finely focused. The diameter of the electron probe must be smaller or similar in size to the feature being examined. The beam current, accelerating voltage and convergence angle must be optimised in order to ensure high detail can be obtained. Utilisation of a small probe diameter requires large beam currents, which in turn can result in less surface details. Striking the perfect balance between the aforementioned parameters will ensure that highly resolved features can be imaged.

The electron beam interacts with the sample to produce backscattered and secondary electrons. The secondary electrons are utilised for imaging, while the backscattered electrons can be used for energy dispersive x-ray spectrometry (EDX). Backscattered electrons possess higher energy than secondary electrons and contain information from deep regions of the sample. They are sensitive to the composition of the specimen, and so can be used to determine the sample composition. Primary and backscattered electrons can cause ionisation of the sample's atoms, and upon relaxation of these ions, x-rays are emitted. These x-rays are characteristic of individual elements and can be used to characterise the material's composition. The x-rays detected by the detector, are then compared to a material database, which ensures accurate identification of the elements present.

2.2.2 Raman Spectroscopy

Raman spectroscopy is a non-destructive analytical technique that can be used on materials to determine their physical form and chemical structure from their characteristic spectral pattern. It is a spectroscopic technique which is based on inelastic scattering of monochromatic light. When light is shone on the sample, the photons are either absorbed, scattered or have no interaction, i.e. pass

through. When the energy gap between the ground state and excited state of the molecule is met, then a photon is absorbed, and the molecule promoted to the higher energy excited state. After it is absorbed, the photon is reemitted, whereby the frequency is shifted up or down in comparison to the original monochromatic frequency. This frequency shift provides information about vibrational, rotational and other low frequency transitions in molecules.

It is possible for a photon to interact with material and scatter from it, where its energy does not match the energy gap of the molecule. In this case the scattered photons can be observed by collecting light at an angle to the incident beam. These are dependent on the wavelength of the incident beam, and are proportional to the fourth power of the frequency[13] as shown in equation 2.6.

$$I \propto \frac{1}{\lambda^4} \qquad \text{Equation 2.6}$$

There are two scattering processes that are detected in vibrational spectroscopy: elastic and inelastic scattering. Elastic scattering is a dominant process which occurs when photons are scattered and is often referred to as Rayleigh scattering. If nuclear motion is induced during the scattering process then energy will be transferred either from the molecule to the scattered photon or from the incident photon to the molecule. This is regarded as inelastic scattering and the energy of the scattered photon is different from that of the incident photon by one vibrational unit. It is a weak process whereby only one in every 10^6-10^8 photons which scatter is Raman scattered.[13] Raman scattering can be further subdivided into Stokes and Anti-Stokes scattering. Stokes scattering occurs when the molecule absorbs energy in the ground vibrational state (m) and is promoted to a higher energy excited vibrational state (n) as shown in figure 2.14. The photon loses energy to the molecule and results in a lower frequency to the incident beam. For Anti-Stokes scattering, some molecules may be present in an excited state (such as n) due to thermal energy. In this instance, the molecule loses energy to the photon, and results in the photon having a higher frequency than the incident beam. Usually Stokes

scattering is measured for Raman, but for some materials where there is fluorescence interference, it would be preferable to measure Anti-Stokes.

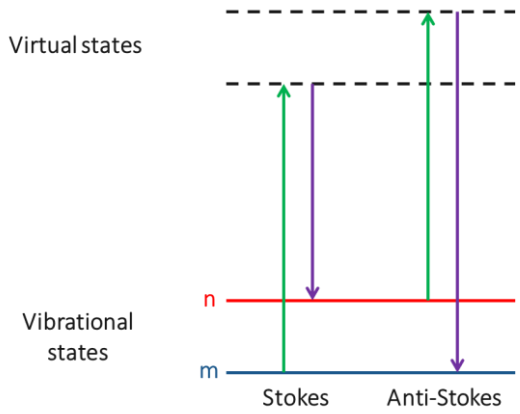

Figure 2.14: Diagram of Raman scattering processes. The lowest energy vibrational state (m) is the ground vibrational state, and n is the excited state due to thermal energy.

There are rules which govern whether a molecule will be Raman or IR active, as changes in dipole moments are considered IR active, while changes in polarizability are considered Raman active. In general, a molecule can be both IR and Raman active (figure 2.15), however, according to the mutual exclusion rule, the vibrational mode of centrosymmetric molecules, e.g. CS_2, may be either IR active or Raman active but not both.

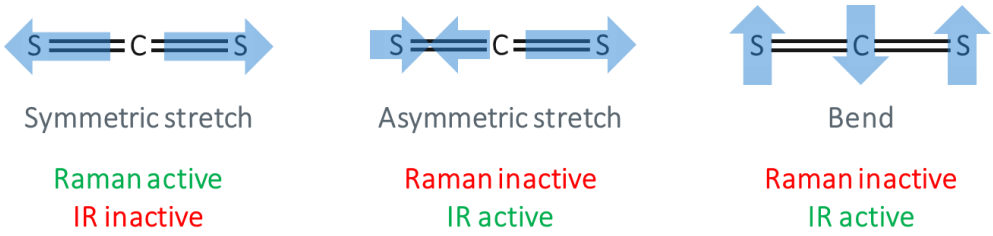

Figure 2.15: Raman and IR active vibrational modes of CS_2 depicting the mutual exclusion rule.

2.2.3 Infrared Spectroscopy

Infrared spectroscopy (IR) is also a non-destructive analytical technique. It can determine the presence of molecules regardless of the sample's form. Gases, liquids, pastes, powders and many

other sample forms can be analysed with IR. The technique is based on the vibrations of the atoms of a molecule. Typically, infrared radiation is passed through a sample (figure 2.16), and the fraction of incident radiation that is absorbed at a particular energy is determined. The energy at which a peak in an absorption spectrum appears corresponds to the frequency of a vibration of a part of a sample molecule.[14]

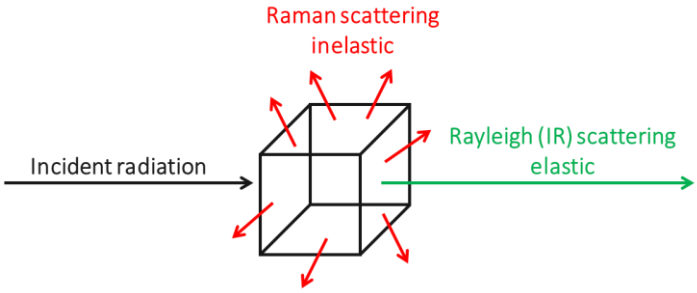

Figure 2.16: Schematic depicting how Raman and IR absorption processes occur.

For a molecule to show IR absorptions, an electric dipole moment must change during the vibration of a molecule. This is regarded as the selection rule, and it differentiates IR from Raman. For most analysis, the mid-IR range is sufficient as it covers 4000 cm^{-1} to 400 cm^{-1}, and most bond vibrations fall within this range (figure 2.17).

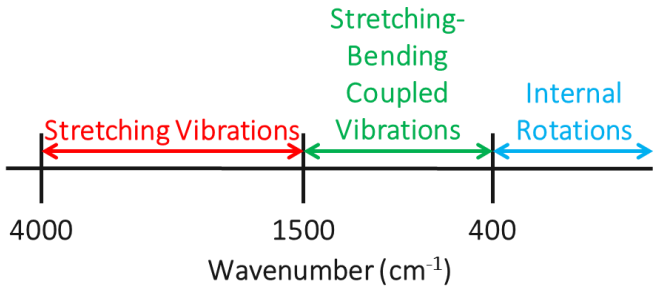

Figure 2.17: General regions for stretching and bending vibrations.

Bond vibrations occur at quantised frequencies as only certain vibrational energy levels are allowed. The frequencies are determined by various factors such as bond strengths, molecular geometry and the masses of the connecting atoms.[15] The stronger the bond, the greater its vibrational frequency,

and the wavelength associated with it will be shorter. Understanding this can help differentiate the various bonds within the molecule, for example the C=O bond, is stronger than for C-O, and infrared radiation is absorbed at different wavelengths: 1870-1540 cm^{-1} for C=O, and 1370-1000 cm^{-1} for C-O.

The use of IR is quite advantageous as it is quite sensitive, fast and relatively inexpensive technique that provides information rich spectra. It often provides complementary information to Raman spectra, and so combining both methods to analyse materials is often beneficial.

2.2.4 Surface Profilometer

A profilometer is an instrument used to measure the surface profile of films, such as surface height and roughness. A contact profilometer utilises a diamond stylus that is in physical contact with the sample surface. This stylus is then mechanically and laterally moved over the surface of the film at a specific distance with a specific contact force. As the surface film is being scanned, a feedback loop is used to monitor the force pushed up against the stylus. An image of the surface film can be reconstructed as the stylus is held by an arm that is set at a specific amount of torque, and changes in the z-axis are monitored as shown in figure 2.18.

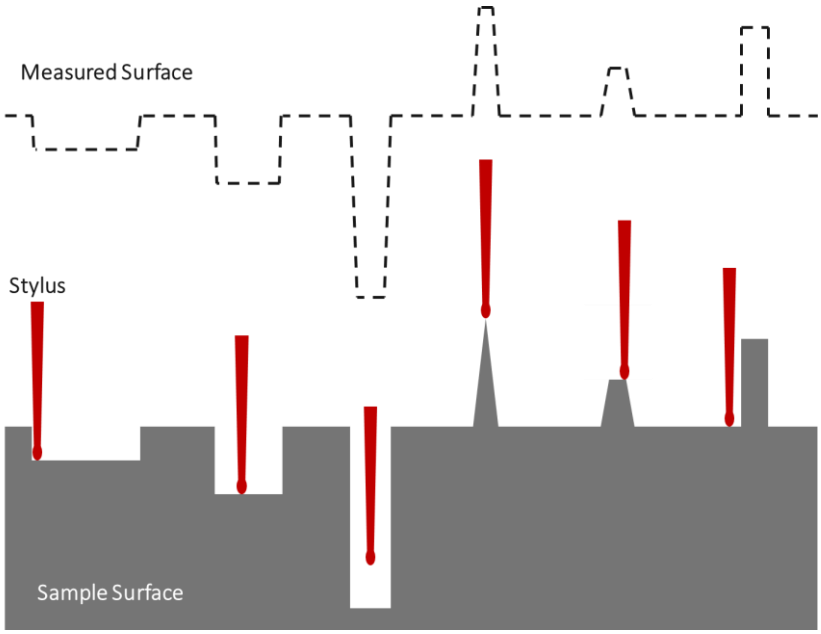

Figure 2.18: Schematic of the working principle of a contact surface profilometer.

As the stylus is in direct contact with the surface, it is a highly sensitive technique; however, its resolution is highly dependent on the shape and radius of the stylus as shown in figure 2.19.

Figure 2.19: Effect of stylus tip angle and radius on the surface film reconstruction (trace).

One disadvantage of contact profilometry is its direct contact with the sample surface, and this can be quite destructive for softer surfaces.

Surface profilometry is ideal for determining the thickness of deposited layers, and the quality of the surface films such as smoothness and roughness. Careful consideration of the type of profilometer must be undertaken to ensure accurate analysis of the substrate films, which can then be used to accurately determine the electrode capacity as outlined in the following chapters.

2.2.4 Differential Scanning Calorimetry

Differential scanning calorimetry (DSC) is a technique for measuring the energy necessary to establish a near-zero temperature difference between a substance and an inert reference material. Both specimens are subjected to identical temperature regimes in an environment heated or cooled at a controlled rate. Two types of DSC are commonly used:

1. Power compensation DSC (also known as heat flux DSC due to its direct measurement of heat flow)
2. Heat-flux DSC

For power-compensation DSC, the temperatures of the sample and reference are controlled independently. This is achieved through the use of separate and identical furnaces. In heat-flux DSC, the sample and reference are connected by a metal disc (low resistance heat-flow path) in a single furnace. For both versions of DSC, enthalpy or heat capacity changes are recorded in the sample relative to the reference.

DSC is beneficial for the analysis of polymers as it can be used to determine a variety of properties such as the glass transition region, the melting region, and the crystallisation behaviour. The glass transition region can characterise amorphous polymers, blend or even the amorphous region of a crystalline sample. From the plot of heat flow rate versus temperature, the degree of crystallinity within a polymer can be determined from the step height. Analysis of the melting points of a polymer can determine the various components of the polymer, as each component will have its own characteristic melting point. Utilisation of this can help distinguish the various polymorphs of polymers, as solid-solid phase transitions can be observed.

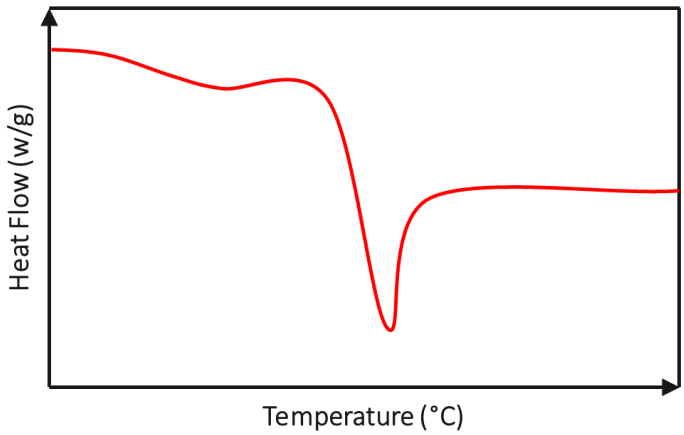

Figure 2.20: Example of a DSC trace.

Overall DSC is a useful technique for the analysis of various materials, especially with regards to polymers. Utilisation of DSC in conjunction with thermogravimetric analysis can yield a comprehensive analysis of polymers.

2.2.5 Thermogravimetric Analysis

Thermogravimetric analysis (TGA) monitors the change in the mass of a sample as a function of temperature or time. The sample is subjected to a controlled temperature programme in a controlled atmosphere.[16-17] A purge gas is utilised during analysis which can create an inert, oxidising or reducing atmosphere. The mass loss from a sample can be categorised[17] as volatile components generally evaporate between ambient and 300 °C, reaction products generally form between 100 °C and 250 °C, while the generation of volatile degradation products could require temperatures between 200 °C and 800 °C. Mass loss processes can be characterised using TGA, where it can yield information regarding the sample's composition, extent of cure and thermal stability.

Typically for polymer analysis, the pyrolysis of the polymer at a constant heating rate is carried out. Utilisation of an inert environment for this process can allow for direct comparison with other polymers.

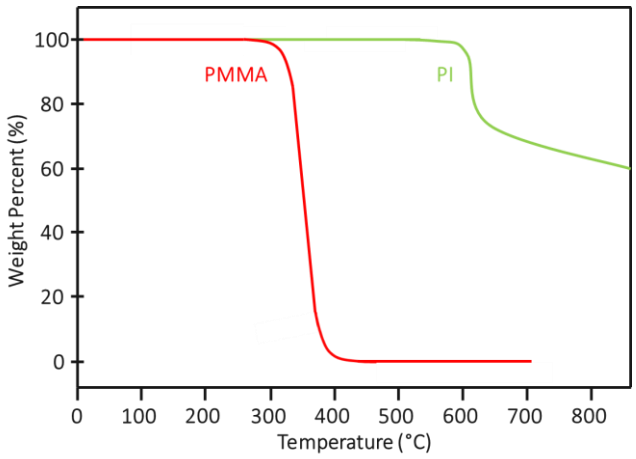

Figure 2.21: Example depicting how TGA analysis can be used to compare the service temperatures of polymer materials. PMMA refers to poly(methyl methacrylate), while PI refers to polyimide.

The polymer materials generally degrade by free-radical processes initiated by bond dissociation at the pyrolysis temperature. The specific pathway of degradation is dependent on the bond strengths, and polymer structure. This allows for the polymer to be easily characterised.

2.2.6 Sputter Deposition

Physical vapour deposition (PVD) encompasses a variety of techniques which involve the physical vaporisation of atoms from a surface by momentum transfer from bombarding energetic atomic-sized particles. Sputter deposition is one such technique, whereby thin films of elemental or compound materials can be deposited. The technique is called sputter deposition as the surface being sputtered is the source of the deposited material.

For direct current (D.C.) magnetron sputtering, a D.C. power supply is used to supply a voltage between the cathode (material target) and the anode. The substrate to be sputtered is placed on the anode as shown in figure 2.22.

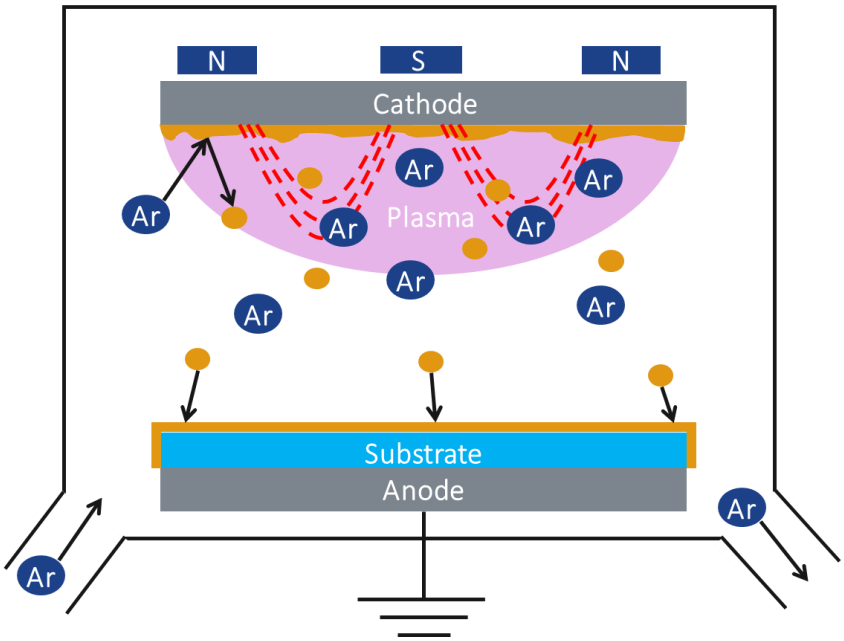

Figure 2.22: Schematic illustrating the operation principle of sputter deposition under Ar.

When a voltage is applied between the cathode and the anode, an ionised gas is generated from the sputtering gas. This forms a hot gas-like phase consisting of ions and electrons and is commonly known as plasma. The charged gas atoms bombard the cathode and releases atoms from the cathode. These travel across the vacuum and inert gas environment where they condense on the cooler surface of the substrate to form a thin film. Electrons that are formed in the plasma accelerate in the opposite direction to the ions, where they collide with gas atoms resulting in the formation of more free ions and electrons and ensures the continuation of the plasma. However, if the pressure chosen for the process is too low, there will not be enough collisions between atoms and electrons in order to sustain the plasma. Too high a pressure will result in too many collisions and reduce the electron's energy thus inhibiting its ability to ionise the atoms.

Utilisation of a planar magnetron is the addition of a magnetic field which is parallel to the target surface. This interacts with the electrons and deflects them to stay near the target surface. Depending on the arrangement of the magnets, the electrons can be circulated on a closed path on the target

surface. This increases the electron flux, and produces high-density plasma, which increases the ionisation efficiency and deposition rate, while lowering the heating effect subjected at the substrate.

One disadvantage of planar magnetron sputtering is the non-uniformity of the plasma over the target surface, and the deposition pattern is dependent on the position of the substrate with respect to the target. It leads to only 10-30% utilisation of the target material before the target must be recycled, however despite this, magnetron sputter deposition is a widely used technique for material deposition.

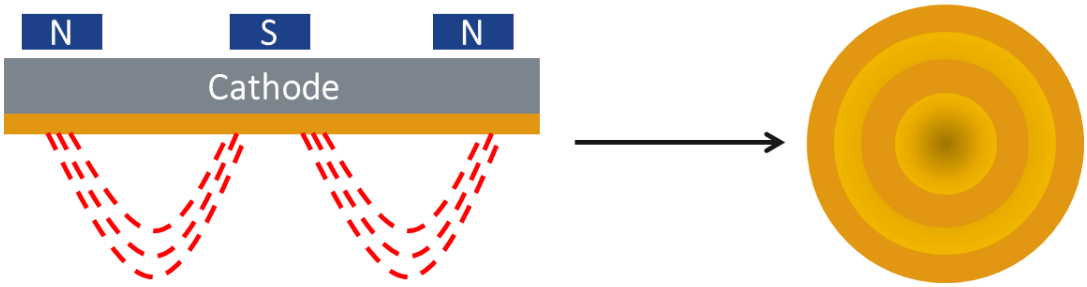

Figure 2.23: Illustration depicting how the planar magnetron affects the target through prolonged use. The lighter rings are the utilised area during sputter deposition, while the darker areas are the unused material.

Both elemental and compound based conductive materials can be sputtered using D.C. sputtering, and so this technique is appropriate for the fabrication of both cathode and anode electrode materials.

References

[1] C. M. Brett, A. M. O. Brett, *Electrochemistry: principles, methods, and applications, Vol. 4*, Oxford University Press Oxford, **1993**.

[2] D. D. Macdonald, *Transient techniques in electrochemistry*, Plenum press New York, **1977**.

[3] P. T. Kissinger, W. R. Heineman, *Journal of Chemical Education* **1983**, *60*, 702 10.1021/ed060p702.

[4] G. Gunawardena, G. Hills, I. Montenegro, B. Scharifker, *Journal of Electroanalytical Chemistry and Interfacial Electrochemistry* **1982**, *138*, 255-271 https://doi.org/10.1016/0022-0728(82)85082-1.

[5] B. Scharifker, G. Hills, *Electrochimica Acta* **1983**, *28*, 879-889 https://doi.org/10.1016/0013-4686(83)85163-9.

[6] L. Heerman, A. Tarallo, *Electrochemistry Communications* **2000**, *2*, 85-89 https://doi.org/10.1016/S1388-2481(99)00144-7.

[7] L. Heerman, A. Tarallo, *Journal of Electroanalytical Chemistry* **1999**, *470*, 70-76 https://doi.org/10.1016/S0022-0728(99)00221-1.

[8] E. Matthijs, S. Langerock, E. Michailova, L. Heerman, *Journal of Electroanalytical Chemistry* **2004**, *570*, 123-133 https://doi.org/10.1016/j.jelechem.2004.03.024.

[9] J. E. Baur, in *Handbook of Electrochemistry* (Ed.: C. G. Zoski), Elsevier, Amsterdam, **2007**, pp. 829-848.

[10] A. J. Bard, L. R. Faulkner, *Electrochemical Methods: Fundamentals and Applications*, Wiley, **2000**.

[11] L. M. McGrath, J. Jones, E. Carey, J. F. Rohan, in *ChemistryOpen, Vol. 8*, **2019**, pp. 1429-1436.

[12] J. Goldstein, J. I. Goldstein, Y. Goldshtain, D. E. Newbury, D. C. Joy, P. Echlin, C. E. Lyman, E. Lifshin, L. Sawyer, O. R. N. L. D. S. D. E. M. F. D. C. Joy, *Scanning Electron Microscopy and X-Ray Microanalysis: Third Edition*, Springer US, **2003**.

[13] E. Smith, G. Dent, *Modern Raman Spectroscopy: A Practical Approach*, **2005**

[14] B. H. Stuart, *Infrared Spectroscopy: Fundamentals and Applications*, Wiley, **2004**.

[15] J. M. Thompson, *Infrared Spectroscopy*, Pan Stanford Publishing, **2018**.

[16] C. M. Earnest, *Compositional analysis by thermogravimetry, Vol. 997*, ASTM International, **1988**.

[17] J. D. Menczel, R. B. Prime, *Thermal Analysis of Polymers: Fundamentals and Applications*, Wiley, **2014**.

Chapter 3:

Ionic Liquid Electrolyte Analysis

3.1 Abstract

The ionic liquid 1-butyl-1-methylpyrrolidinium bis(trifluoromethylsulfonyl)imide (C_4mpyrTFSI) was investigated to determine if its electrochemical properties were favourable for Li-ion battery applications. It was determined that it offers good Li-ion mobility as evidenced by the highly stable Li deposition and stripping onto the electrode surface at potentials beyond the blank ionic liquid's reductive potential. In addition, it exhibits ionic conductivities of the same magnitude as conventional organic electrolytes, 500 times greater than conventional solid-state electrolytes (1.5 mS cm^{-1} versus 3 $x10^{-3}$ mS cm^{-1}).

Thermally stable, flexible polymer gel electrolytes with high ionic conductivity were prepared by mixing the C_4mpyrTFSI, LiTFSI salt and poly(vinylidene difluoride-co-hexafluoropropylene (PVDF-HFP). FT-IR and Raman spectroscopy show that an amorphous film was obtained for high (60 wt.%) C_4mpyrTFSI contents. Thermogravimetric analysis (TGA) confirmed that the polymer gels are stable below ~300 °C in both nitrogen and air environments. Ionic conductivity of 1.9 $x10^{-3}$ S cm^{-1} at room temperature was achieved for the 60 % ionic liquid loaded gel.

3.2 Introduction

Conventional Li microbatteries utilise solid state electrolytes[1] such as LiPON which have intrinsic safety benefits when compared to volatile organic electrolytes. Due to the slower reactivity of solid state electrolytes compared to liquids, there is an expectation of longer device lifetimes.[2] Solid-state

batteries have been shown to operate for more than 10,000 cycles,[3] however scalability has yet to be proven. Some disadvantages associated with solid-state electrolytes that have hindered their use include low ionic conductivity and poor interfacial contact. Typically, organic electrolytes offer ionic conductivities >7 mS cm^{-1}, which is approximately 2,000 times greater than ionic conductivities obtained for typical solid-state electrolytes such as LiPON (3×10^{-3} mS cm^{-1}).[4-5] The interfacial issues stem from the instability of the interface in terms of composition and structure. Oftentimes the interfacial composition and structure that forms between the solid electrolytes and electrode materials exhibit major deviations from those of the bulk materials. Another issue faced by solid-state electrolytes is the requirement for physical contact with the electrode materials,[6] whereby ionic diffusion relies on contact to solid particles. These point contacts can be sensitive to stresses which occur during electrochemical cycling, and can lead to the formation and propagation of cracks,[7-8] as well as interfacial delamination.[9]

Finding an alternative electrolyte solution, which embodies the advantages of organic solvents such as high ionic conductivity, and those of solid-state such as long cycle life and safety would assist with energy storage for the Internet of Things (IoT) and other applications. Ionic liquid based electrolytes offer many favourable properties. For example, C_4mpyrTFSI (figure 3.1) boasts a large electrochemical window,[10] low volatility, non-flammability, wide operation temperatures[11] and high ionic conductivities.

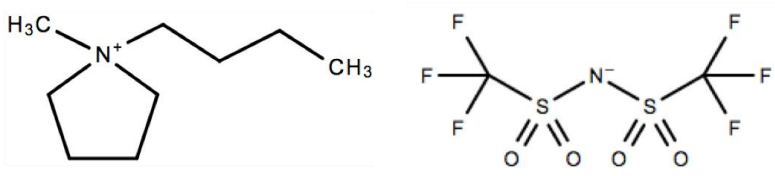

Figure 3.1: Structure of C_4mpyrTFSI ionic liquid.

The ionic liquid properties are highly dependent on the chosen cation/anion combination, which is advantageous as it allows electrolyte properties to be tailored to suit the application. Xue *et al.*[12]

reviewed ionic liquids with fluorine containing anions detailing their various properties including the tunability of the electrolytes. Hayes *et al.*[13] provide a comprehensive insight into ionic liquids and investigates various properties such as self-assembly control in the bulk and at the solid interface. Investigators have shown the compatibility of ionic liquids with numerous Li-ion battery electrodes.[14-17] Ionic liquids appropriate for battery applications have been reviewed by MacFarlane *et al.*[11]

Some ionic liquids can be used to form polymer gels.[18] The preservation of favourable properties, in addition to the encapsulation of a liquid electrolyte within a polymer matrix provides a further alternative to the conventional solid-state electrolytes. Polymer gel electrolytes derived from ionic liquids can offer varying degrees of flexibility and higher ionic conductivities than solid-state electrolytes[19-21] in addition to good thermal, interfacial and electrochemical stabilities. Specifically, Pont *et al.*[22] investigated the properties of pyrrolidinium-based polymeric ionic liquids as polymer electrolytes. Their work highlighted that mechanically stable polymer gels with high ionic conductivities (10^{-4} S cm^{-1}) and large electrochemical windows (~7 V) can be obtained. Ferrari *et al.*[23] demonstrated improved cycling behaviour of $LiFePO_4$ electrodes over 180 cycles with N-methoxyethyl-N-methylpyrrolidinium-based polymer gel electrolytes when compared to their liquid counterparts. Sirisopanaporn *et al.*[24] demonstrated the safety of ionic liquid based polymer gels, as it was observed that a protective solid-electrolyte interface (SEI) layer forms on the surface of lithium metal anodes, with no electrolyte leakage after 4 months of storage. A combination of PVDF-HFP with C_4mpyrTFSI has been investigated by Kim *et al.*[25] using a two-step process where a fibrous PVDF-HFP membrane was synthesised via electrospinning methods. The formed membranes were then soaked in 1 M LiTFSI/C_4mpyrTFSI to create an ionic liquid-based polymer gel electrolyte. The polymer gel composition and the resultant properties such as ionic conductivity, thermal and electrochemical stability can be more easily tailored using the single step solvent casting method

described in this work. The improved characteristics are attributed to changes in the crystalline structure of the polymer gel due to the quantity of C_4mpyrTFSI utilised.

This work describes an alternative electrolyte to conventional solid state and organic electrolytes, which demonstrates favourable electrochemical properties. In addition, a simplified synthesis of the ionic liquid based polymer gels is outlined, whereby most methods in the literature rely on high temperatures during synthesis,[19] or drying of the polymer gels under vacuum or at high temperatures.[20, 26-27] Our method can be performed outside of a glovebox at moderate temperatures (50 °C), with no vacuum or external heating required during the drying process, and no further treatment (e.g. soaking in electrolyte, or UV irradiation) once dry to produce polymer gel electrolytes with favourable electrochemical properties.

3.3 Experimental

3.3.1 Ionic liquid analysis

The organic electrolyte ethylene carbonate (EC) and diethyl carbonate (DEC) in a solution 1:1 v/v with 1 M $LiPF_6$ salt was used as the baseline lithium electrolyte. Ionic liquids trihexyltetradecylphosphonium bis(trifluoromethylsulfonyl)imide ($P_{14,666}$TFSI) and 1-butyl-1-methylpyrrolidinium bis(trifluoromethylsulfonyl)imide (C_4mpyrTFSI) were investigated to determine their electrochemical window. A three-electrode set up was utilised where a 100 µm Ni microelectrode was used as the working electrode, while the reference and counter electrodes were Li metal.

Cyclic voltammetry (CV) analysis was carried out on C_4mpyrTFSI with various LiTFSI salt concentrations over the potential range of -0.7 V to 2.5 V with scan rates of 50 and 100 mV s^{-1} to determine the effect of LiTFSI salt concentration on the deposition and stripping of Li on the surface

of the Ni microelectrode. A three-electrode set up was utilised where a 10 µm and 100 µm Ni microelectrode were used as the working electrode, while the reference and the counter electrode were Li metal, unless otherwise stated. The deposition and stripping efficiency was determined using chronoamperometry. The second cell set up consisted of a microdisc array, where ten 20 µm Au microdiscs were modified with Ni and utilised as the working electrode with on-chip Pt reference and counter electrodes.

A Bio-Logic VSP multi-channel potentiostat was used for electrochemical impedance spectroscopy (EIS). A two electrode set up, where two stainless steel electrodes was utilised for EIS tests. The distance between the two electrodes was maintained at 0.1 cm, while the both electrodes were 0.658 cm^2. The cell was calibrated using 0.1 M KCl solution. The tests were carried out using a 1 MHz to 10 Hz with 10 mV amplitude. The ionic conductivity was calculated using equation 3.1.

$$\sigma = \frac{A.R}{l} \qquad \text{Equation 3.1}$$

where A is the area of the electrode, R is the resistance measured and l is the distance between the electrodes.

3.3.2 Ionic liquid polymer gel electrolyte synthesis and characterisation

1-butyl-1-methylpyrrolidinium bis(trifluoromethylsulfonyl)imide(C_4mpyrTFSI) was obtained from Solvionic (>99% purity). Li bis(trifluoromethylsulfonyl) imide (LiTFSI) and PVDF-HFP were obtained from Sigma Aldrich (>99% purity). All chemicals were stored under argon atmosphere and used as received.

The polymer gels were synthesised by dissolving PVDF-HFP in molecular-sieve dried acetone at 50 °C with stirring for 30 minutes. Once dissolved, the LiTFSI was added and stirred for a further 30

minutes. Finally, C_4mpyrTFSI was added and the mixture was stirred for 1 hour. The solution was solvent cast into petri dishes and the acetone evaporated.

FT-IR data was recorded using a Perkin Elmer Spotlight for mid-IR wavelengths (4,000 to 400 cm^{-1}). Raman spectra of the polymer gels were recorded on a Horiba Raman Spectrometer with dual wavelengths (532 nm and 785 nm). Analysis was carried out using a 785 nm wavelength to avoid fluorescence emitted at lower wavelengths. Thermogravimetric analysis (TGA) was carried out using a TA Instruments, model TA Q50 and platinum pans. The temperature ramp was varied (20, 40 and 60 °C per minute (min^{-1})) to obtain temperature profiles over the temperature range 30 °C to 800 °C. The polymer gels were analysed under N_2 and air. Differential scanning calorimetry (DSC) was carried out using a TA Instruments Q2000 with attached refrigerated cooling system. The samples were cooled to -40 °C and using temperature ramps of 20, 40 and 60 °C min^{-1}, the temperature was increased to 180 °C. The purge gas used was nitrogen with a flow rate of 10 ml min^{-1}.

The ionic conductivity of the polymer gels was determined over a frequency range of 150 kHz to 10 Hz, with an amplitude of 10 mV and using the equation 3.1 previously mentioned in section 3.3.1. In this instance, A is the area of the polymer gel, R is the resistance measured and l is the thickness of the polymer gel sample. The thicknesses of the polymer gels were determined using a micrometer, and this value was used in equation 3.1. The polymer gels were then sandwiched between two stainless steel electrodes and the measurements were carried out at open circuit potential.

3.4 Results and discussion

3.4.1 Ionic liquid electrolyte

To determine the viability of ionic liquids as Li-ion battery electrolytes, their oxidative and reductive windows were determined and compared to conventional organic electrolytes such as 1:1 v/v EC:DEC. The electrochemical windows were determined by the onset of oxidative and reductive peaks by CV analysis as shown in figure 3.2. The blank figure 3.2(a) (without Li salt) organic electrolyte starts to undergo oxidative and reductive processes at approximately 4 V and 0.5 V, respectively. Data for $P_{14,666}$TFSI and C_4mpyrTFSI are shown in figure 3.2(b) and (c) respectively. $P_{14,666}$TFSI yields an electrochemical window of approximately 4 V, while C_4mpyrTFSI yields a 5 V electrochemical window. The difference in the electrochemical windows can be attributed to the cation/anion combination present in the ionic liquids. Oxidative stability is attributed to the anion, and both ionic liquids offer similar oxidative decomposition potentials[10] (figure 3.2(d)), while a stark contrast exists in the reductive decomposition potentials which has been attributed to the cations present in the ionic liquids.[28-31] It has been noted that both $P_{14,666}^+$ and C_4mpyr^+ cations have similar reductive decomposition potentials, however, Rogers *et al.*[32] have shown that the breakdown potentials for $P_{14,666}^+$ and C_4mpyr^+ cations are -3.117 V and -3.191 V versus Fc/Fc^+, respectively, at a current density of 250 μA cm^2, where the TFSI anion was coupled with both. Similar results were observed in figure 3.2(d) as the C_4mpyrTFSI exhibited better reductive stability when compared to $P_{14,666}$TFSI. It is evident that C_4mpyrTFSI offers the largest electrochemical window of the three blank electrolytes, and this is maintained even with the addition of 0.2 M LiTFSI salt (figure 3.2(e)). The addition of the LiTFSI salt exhibits a stabilisation effect as pushing the potential (-1 V) beyond the reductive decomposition potential of the blank electrolyte (-0.3 V) does not yield any negative effects and the electrochemical window is maintained at 5 V. Li deposition and stripping occurs when

the potential is pushed to such negative potentials, and despite this reaction occurring, there is no effect on the stability of the electrochemical window.

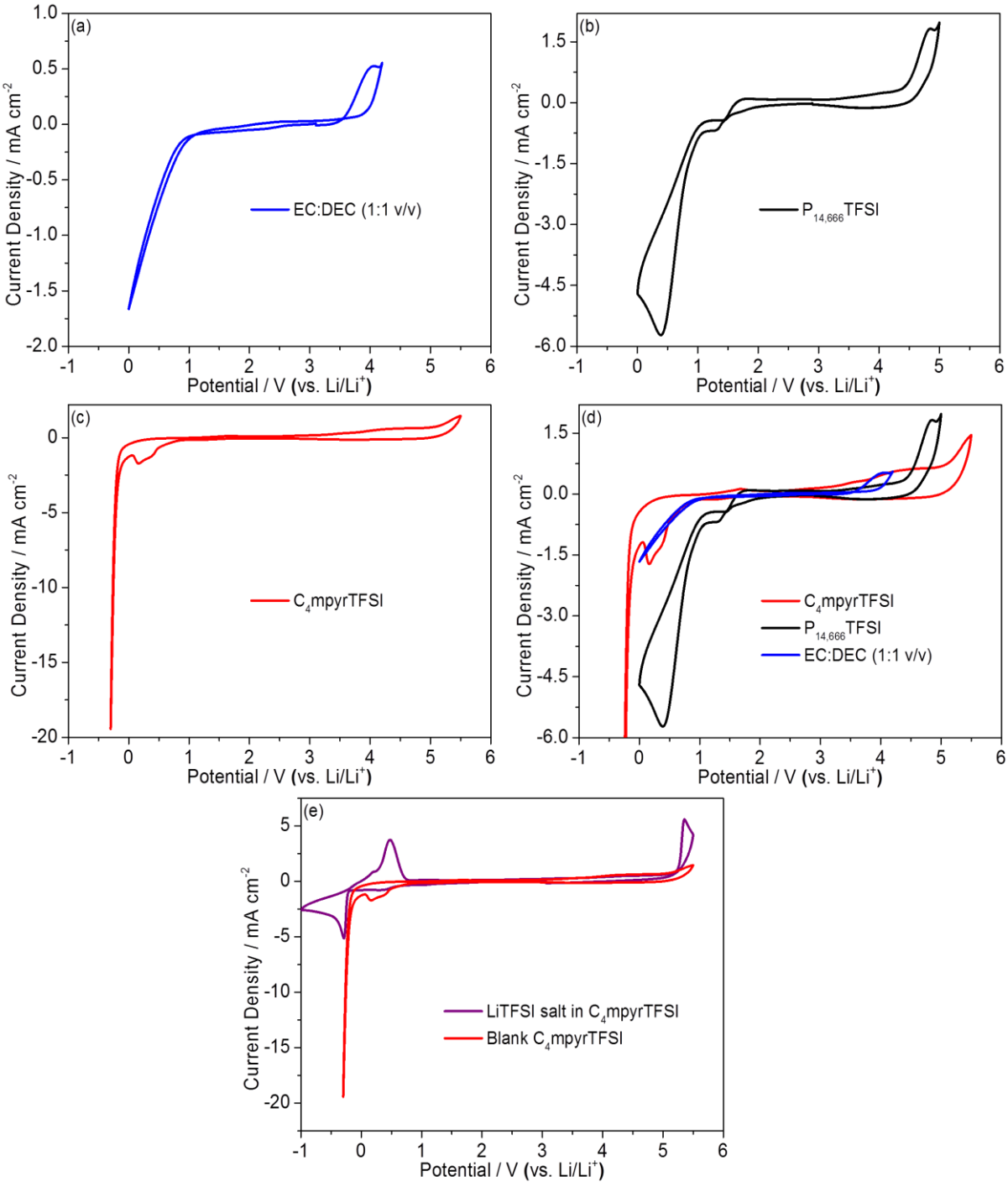

Figure 3.2: Electrochemical analysis at 50 mV s^{-1} using a 100 µm Ni microelectrode for (a) EC:DEC (1:1 v/v), (b) $P_{14,666}$TFSI, (c) C_4mpyrTFSI, (d) superimposed data for (a to c) and (e) C_4mpyrTFSI and 0.2M LiTFSI salt in C_4mpyrTFSI.

C_4mpyrTFSI was further investigated whereby Li conducting salt LiTFSI was added to the ionic liquid (IL) to investigate Li-ion mobility within the ionic liquid and determine an optimum concentration. This was carried out in a two-fold investigation, CV and EIS to determine the optimum LiTFSI salt content for C_4mpyrTFSI electrolytes. Initially CV analysis was carried out to determine the lithium deposition and stripping mechanisms within the ionic liquid. From figure 3.3, it can be seen that LiTFSI salt is compatible with the C_4mpyrTFSI electrolyte as stable cycling was obtained at both 50 and 100 mV s^{-1}. Similar Li deposition and stripping trends were observed at both scan rates, whereby increased LiTFSI salt concentrations led to thicker Li deposits, therefore demonstrating good Li-ion mobility.

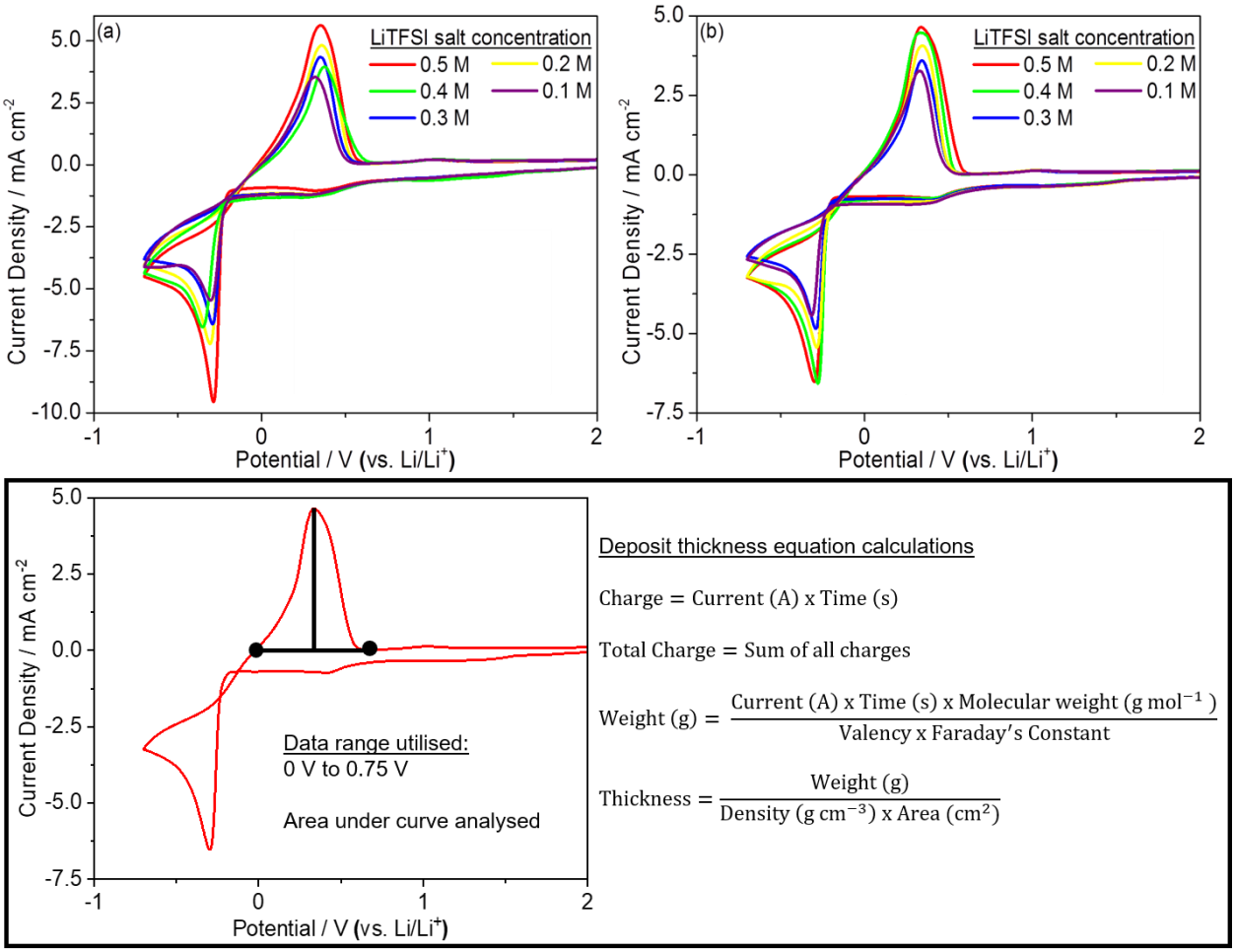

Figure 3.3: CV for C_4mpyrTFSI at a 100 µm Ni microelectrode between 2.0 V and -0.7 V at (a) 100 and (b) 50 mV s^{-1}. Black box indicates the region and potential range utilised and the equations used to estimate deposit thickness.

However, if compared to a typical organic electrolyte such as 1 M $LiPF_6$ in (1:1 v/v) EC:DEC (< 2 cP at 25 °C)[33] (figure 3.4), it is evident that the higher viscosity of the salt in ionic liquid (~ 100 cP at 25 °C)[34] hinders Li-ion mobility as the current density obtained is approximately 31 times less than that for 1 M $LiPF_6$ in (1:1 v/v) EC:DEC (5 mA cm^{-2} versus 155 mA cm^{-2}). The deposition/stripping current should ideally cross the potential scale at 0 V, which is observed for both the organic electrolyte (figure 3.4(a)), and ionic liquid which indicates that Li deposition/stripping processes are not hindered in the ionic liquid despite the higher viscosity. The approximate Li deposit

thickness value from the organic electrolyte was 1673 nm at a scan rate of 50 mV s^{-1} with a potential limit of -0.5 V versus Li/Li^+, while the 0.5 M LiTFSI in IL solution deposited only 26 nm under the same conditions. Different Li salts were utilised which may impart an effect on the deposition and stripping processes, however, it is evident that the Li-ion mobility is hindered when compared to typical organic electrolytes due to Li co-ordination with the anion as observed previously in the literature.[35-38]

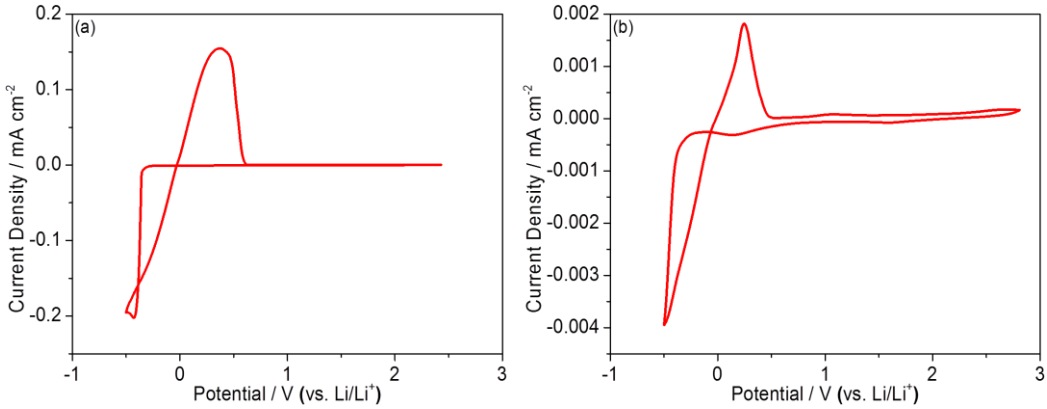

Figure 3.4: Comparison of (a) organic electrolyte: 1 M $LiPF_6$ in (1:1 v/v) EC:DEC and (b) ionic liquid electrolyte: 0.5 M LiTFSI in C_4mpyrTFSI at 100 µm Ni microelectrode. Scan rate of 50 mV s^{-1} was utilised.

The efficiency of the deposition/stripping processes was investigated using CA techniques, and it was determined that an efficiency of ~49% was achieved at a singular Ni microelectrode (figure 3.5 insets). A microdisc array was also investigated to determine an averaged efficiency across multiple electrodes. Depending on the chosen deposition and dissolution potentials, efficiencies from 49% to 78% were achieved at the microdisc array. Figure 3.5 shows the CA data for the microdisc array electrodes where an efficiency of 78% was obtained.

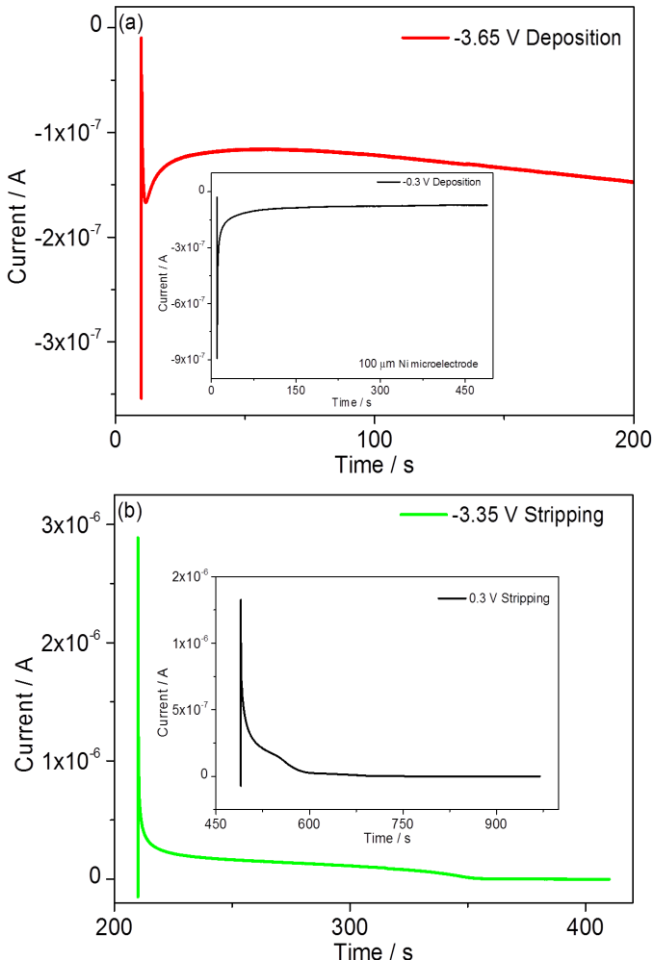

Figure 3.5: Chronoamperometric Li deposition and stripping at ten 20 µm diameter Ni modified Au microdisc electrodes, (Pt pseudo-reference was used), where insets refer to experiments carried out using a single 100 µm diameter Ni microelectrode (Li metal reference was used).

This CV and CA data for the LiTFSI salt in C_4mpyrTFSI has shown that Li deposition and stripping can be obtained from the 0.5 M salt concentration, however it has been observed[36, 38] that increasing salt concentrations (0.1 M to 0.5 M, etc.) in ionic liquids can result in the reduction of its ionic conductivity. In order to determine the optimum salt concentration, the ionic conductivity of the salt in IL must be determined.

The ionic conductivity was obtained using the cell shown in figure 3.6. Using stainless steel electrodes, side reactions are minimised, as the stainless steel is chemically inert. The measurements were carried

out at open circuit voltage (OCV). If a potential bias was applied, reactions other than ion diffusion could complicate the data analysis. For this cell set-up, the equivalent circuit consisted of electrolyte resistance (R), Warburg impedance (W) and a constant phase element (CPE) (figure 3.6(b)). This was determined as the electrolyte imparts a resistance (R), the bare electrode in the electrolyte acts as a capacitor (Q), and Warburg impedance (W) refers to Li-ion diffusion.

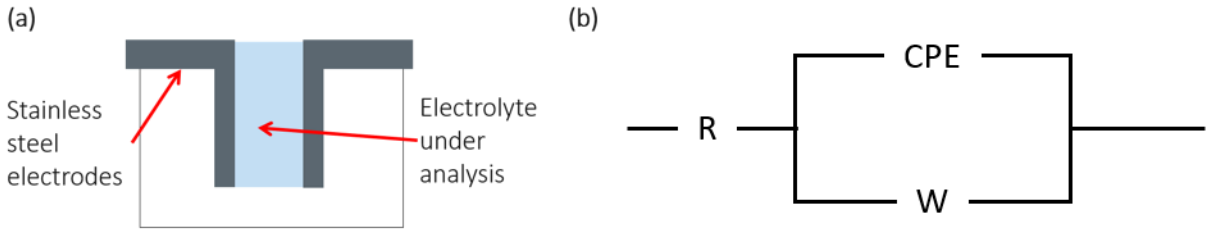

Figure 3.6: (a) Experimental cell used for EIS measurement and (b) its equivalent circuit model.

Initially the blank ionic liquid was investigated, and this was compared to the salt in ionic liquid data. From the data in figure 3.7, it is clear the equivalent circuit that has been applied to fit the experimental data is in good agreement with both the blank and salt in C_4mpyrTFSI solutions. Slight deviations between the fit and experimental data are observed in figure 3.7(a) and (b). The deviations occur at low frequencies, where Warburg diffusion is recorded. As Warburg diffusion assumes all diffusion within the cell is semi-infinite, deviations can occur as real systems often have finite diffusion. Figure 3.7(g) shows a comparison of the EIS data obtained. It is obvious from the data that the real impedance (Re(Z)) increases with increasing salt concentration. This trend has been observed for other ionic liquid solutions,[35-38] and is attributed to the increasing viscosity of the ionic liquid.

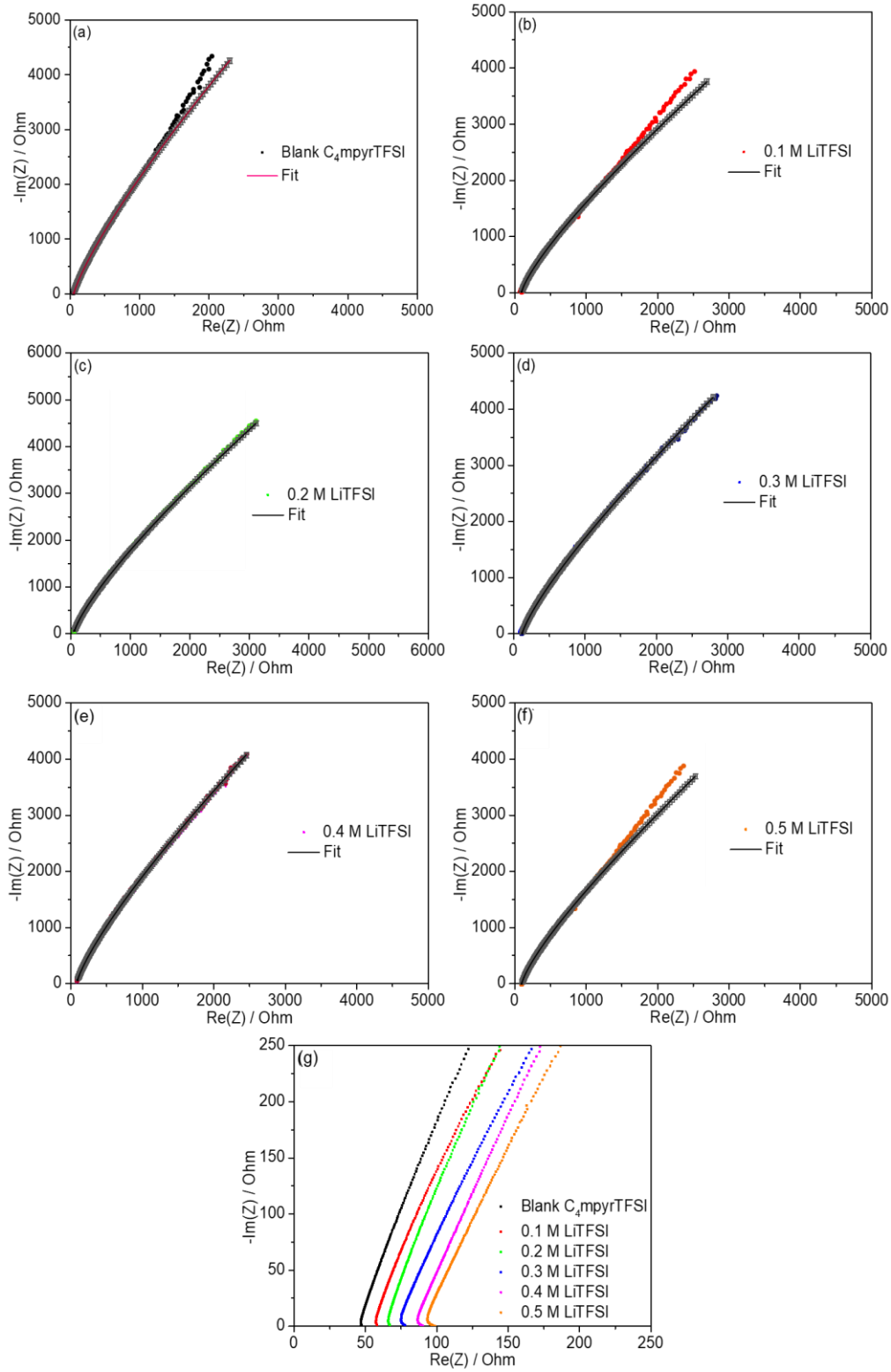

Figure 3.7: EIS experimental and fit data for (a) blank C4mpyr TFSI, (b) 0.1 M, (c) 0.2 M, (d) 0.3 M, (e) 0.4 M, (f) 0.5 M LiTFSI salt in C4mpyr TFSI and (g) comparison of the high frequency EIS data. Frequency and fit range used (unless otherwise stated): 150 kHz to 10 Hz.

As the resistance increases, the ionic liquid conductivity decreases due to the inverse relationship between resistance and conductivity, therefore the ionic conductivity for the 0.5 M LiTFSI in C_4mpyrTFSI is lower than that of the 0.1 M LiTFSI in C_4mpyrTFSI solution. By utilising equation 3.1 mentioned in section 3.3.1, the ionic conductivity values were obtained and are shown in table 3.1 which confirms that ionic conductivities decrease with increasing salt concentration, however, all salt concentrations yield ionic conductivities of the same magnitude as 1 M $LiPF_6$ in (1:1 v/v) EC:DEC, whose ionic conductivity is 7.9 mS cm^{-1} under the same conditions.[39] As the electrolytes are being investigated for Li-ion microbatteries, their ionic conductivity is also compared to solid state electrolytes such as LiPON for which an ionic conductivity of 3 $x10^{-3}$ mS cm^{-1} under the same conditions is observed,[4-5] which is 500 times less than that of 0.5 M LiTFSI in C_4mpyrTFSI.

	Blank C4mpyrTFSI	**0.1 M LiTFSI**	**0.2 M LiTFSI**	**0.3 M LiTFSI**	**0.4 M LiTFSI**	**0.5 M LiTFSI**
Conductivity (mS cm^{-1})	3.2	2.6	2.3	2.0	1.7	1.5
99% CI	±0.14	±0.17	±0.17	±0.05	±0.05	±0.11

Table 3.1: Comparison of ionic conductivities of blank and LiTFSI C_4mpyrTFSI solution with 99% confidence interval (CI).

The relationship between the salt concentration and the ionic conductivity is linear as shown by the high R^2 value in figure 3.8.

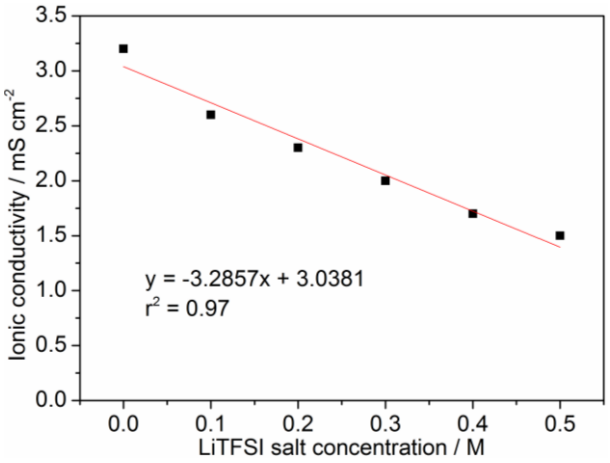

Figure 3.8: Relationship between ionic conductivity and the LiTFSI salt concentration in C_4mpyrTFSI solutions.

Based on the above results, it has been demonstrated that utilisation of ionic liquid based electrolytes is a viable alternative to conventional solid state electrolytes due to its superior ionic conductivity, and therefore better Li-ion mobility. C_4mpyrTFSI demonstrates favourable properties as a liquid electrolyte and can also be used to create polymer gel electrolytes as outlined in the following section.

3.4.2 Ionic liquid polymer gel electrolyte

A series of polymer gels were synthesized, where the C_4mpyrTFSI content was varied between 10 wt.% and 60 wt.%. They were labelled as PG-X where X denoted the C_4mpyrTFSI content. For example, gels with 10 wt.% and 60 wt.% C_4mpyrTFSI are called PG-10 and PG-60, respectively. Gels that contained more than 60 wt.% C_4mpyrTFSI resulted in pastes rather than films. For comparison films consisting of PVDF-HFP, and PVDF-HFP with LiTFSI were also synthesised. Figure 3.9 displays the flexible polymer gels with the lowest and highest C_4mpyrTFSI content, PG-10 and PG-60.

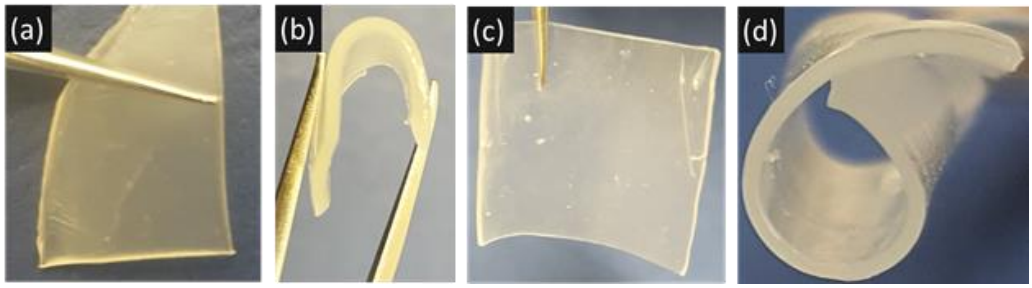

Figure 3.9: Optical images of synthesised 400 μm thick polymer gel electrolytes (a and b) PG-10, and (c and d) PG-60.

The degree of flexibility is attributed to the PVDF-HFP content, as less rigid films are obtained with higher C_4mpyrTFSI. In order to further determine the effect of LiTFSI salt and C_4mpyrTFSI on the morphology of the films, SEM analysis was conducted on films containing PVDF-HFP only, PVDF-HFP and LiTFSI, PG-10 and PG-60 (figure 3.10). The pure PVDF-HFP film exhibits a flake-like surface (figure 3.10(a)); however, upon addition of LiTFSI there is a distinct change to a more smooth surface morphology of the film (figure 3.10(b)). When 10 wt.% C_4mpyrTFSI is introduced to the polymer gel the porosity of the polymer gel increases (figure 3.10(c)). Despite the increased porosity the morphology of the films in 3.10(b) and (c) remain similar. The surface morphology for PG-60 (figure 3.10(d)) is significantly rougher which suggests that addition of LiTFSI and C_4mpyrTFSI can lead to differences in the polymer's structure.

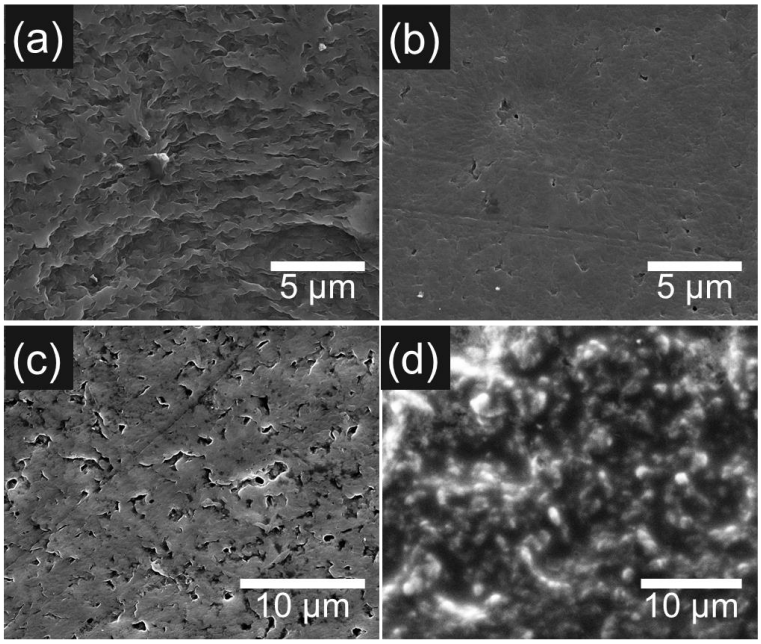

Figure 3.10: SEM micrographs of (a) PVDF-HFP, (b) PVDF-HFP with LiTFSI, (c) PG-10, (d) PG-60 films.

To elucidate the change in surface morphology, the crystallinity of the polymer gels was investigated using FT-IR and Raman spectroscopy. It is well understood that PVDF-HFP can exhibit different crystalline phases [40] (α, β, γ, δ) where the non-polar α-phase is the common crystalline state observed under normal conditions. The structures of the α-, β- and γ-phase are shown in figure 3.11.

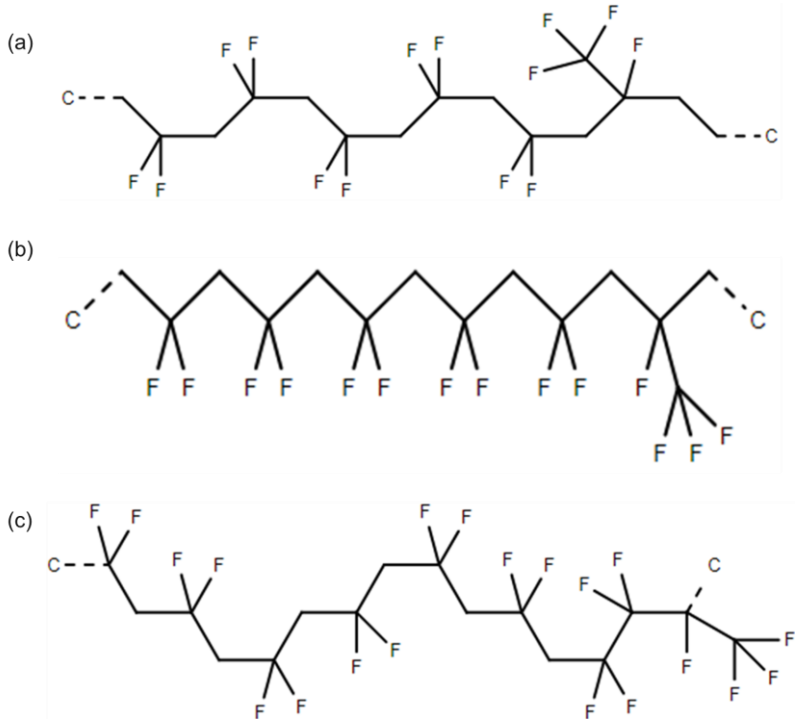

Figure 3.11: Structures of PVDF-HFP where (a) α-phase, (b) β-phase, and (c) γ-phase.

Different crystalline phases can be obtained if the polymer undergoes stress, such as stretching or straining. Each crystalline state yields distinctive peaks when analysed using IR. The IR spectrum obtained for pure PVDF-HFP is shown in Figures 3.12(a) and (b). There are several notable peaks obtained including at: 762 cm^{-1} ($C-F_2$ bending mode, α-phase),[41-47] 796 cm^{-1} ($C-F_3$ stretching mode, α-phase),[41, 43, 45-46] 855 cm^{-1} (α-phase),[41] 872 cm^{-1} ($C-H_2$ wagging of vinylidene, amorphous HFP),[42, 47] 974 cm^{-1} (out of plane C-H bending or twisting, α-phase),[41-43, 46] 1058 cm^{-1} (symmetric stretching of $C-F_3$, amorphous HFP),[42] 1178 cm^{-1} (asymmetric C-F stretching),[42, 48] 1383 cm^{-1} ($C-H_2$ wagging vibration),[42-43, 48] and 1404 cm^{-1} ($C-H_2$ scissoring vibration).[42-43, 48]

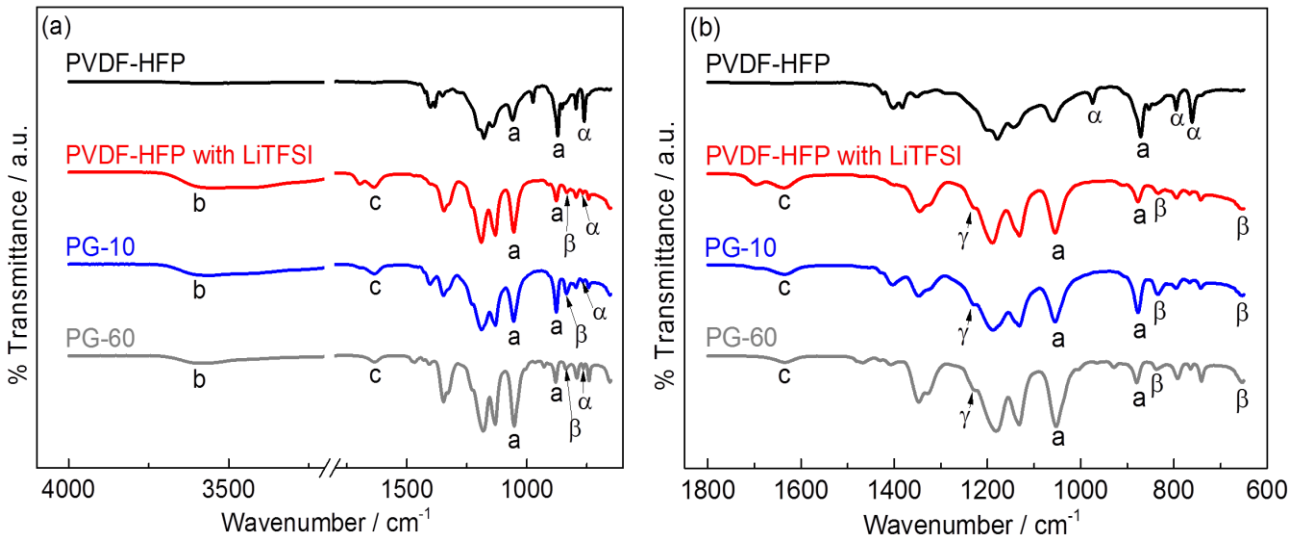

Figure 3.12: Room temperature FT-IR spectra of PVDF-HFP, PVDF-HFP with LiTFSI, PG-10 and PG-60, (a) displaying the range 4000 to 650 cm^{-1}, (b) displaying the range 1800 to 650 cm^{-1}.

Only α-phase peaks are observed in the pure PVDF-HFP film, however upon addition of the LiTFSI salt there are notable changes in the IR spectrum. In the first instance, there is an additional peak observed at 658 cm^{-1} which can be attributed to the β-phase of PVDF-HFP.[48] A weak peak at 811 cm^{-1} is also observed which can be attributed to the γ-phase. The appearance of these two peaks signifies that the addition of LiTFSI salt stresses the polymer matrix and changes the crystalline phase formed. A broad peak within the region of 3700 cm^{-1} to 3050 cm^{-1} (peak b) can be attributed to the $TFSI^-$ anion. A peak at 1640 cm^{-1} (peak c) is ascribed to the complexation of the LiTFSI salt with the polymer backbone.[21] The intensity of this peak decreases with increasing C_4mpyrTFSI content as the combination of LiTFSI and C_4mpyrTFSI reduces the tendency to form complexes.[25] This phenomenon could explain why different surface morphologies were obtained, as the LiTFSI is complexed with the polymer backbone and subsequently non-complexed when the C_4mpyrTFSI content is increased. For both PG-10 and PG-60 the FT-IR spectra are similar to the spectra for PVDF-HFP with LiTFSI, whereby peaks for amorphous (peak a), β- and γ-phases are observed. This trend is observed across the polymer gel series (figure 3.13). For PG-60, the β- and γ-phase peaks are less

intense than those for PG-10 (figure 3.13), however, the peaks denoting amorphicity yield higher intensities, which suggest that it adopts a more amorphous structure than PG-10 (figure 3.13).

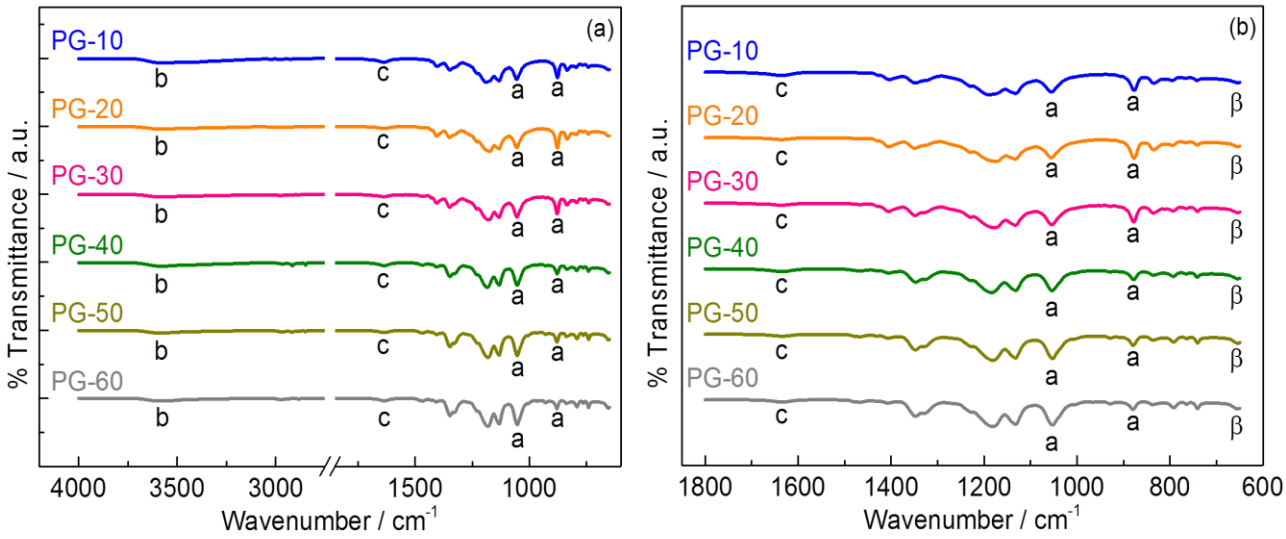

Figure 3.13: FT-IR data for the polymer gel series where the C_4mpyrTFSI content was increased from 10 wt.% to 60 wt.% (a) 4000 to 650 cm^{-1} range and (b) 1800 to 650 cm^{-1}. Similar crystalline states were observed for the series of polymer gels, where amorphous, α-phase, and β-phase were all observed.

Figure 3.14 shows the Raman data obtained for the films, where the same films were analysed in order to obtain further structural information. For the PVDF-HFP film, the strong peak obtained at 793 cm^{-1} can be attributed to C-H_2 rocking and C-F_2 stretching modes, which is indicative of α-phase PVDF-HFP. Similarly, peaks at 873 cm^{-1} and 1426 cm^{-1} are due to a combination of C-C symmetric stretching and C-C-C skeletal bonding modes, C-H_2 scissoring and C-H_2 wagging modes respectively [49-50] which indicate that our pure PVDF-HFP films exists in the α-phase.

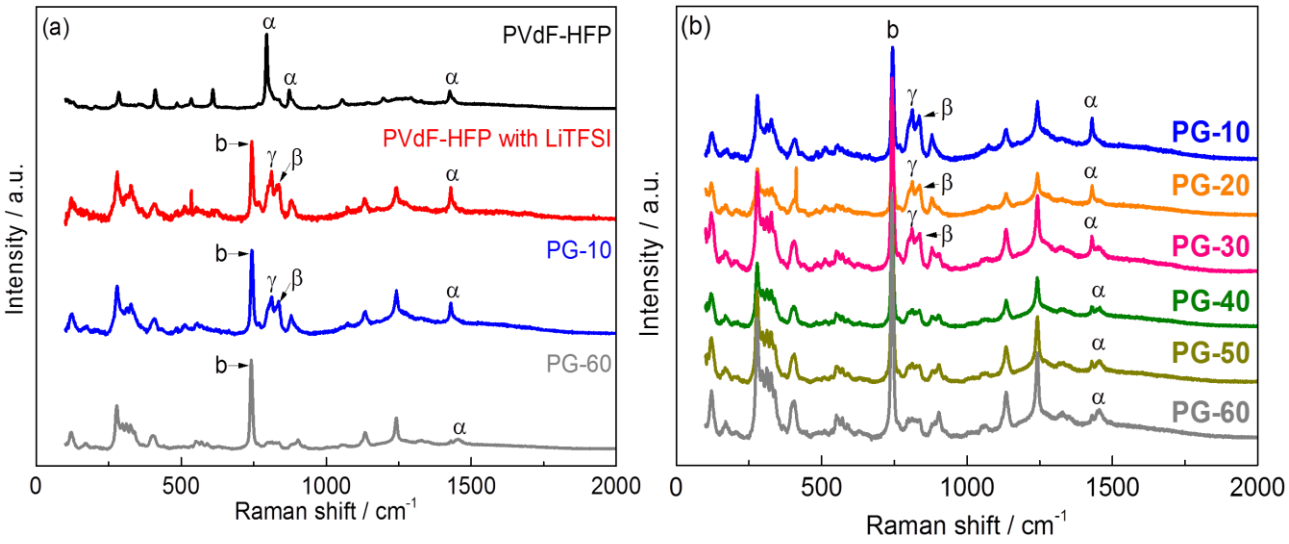

Figure 3.14: (a) Room temperature Raman spectra of PVDF-HFP, PVDF-HFP with LiTFSI, PG-10 and PG-60, (b) Raman data for the polymer gel series where the C_4mpyrTFSI content was increased from 10 wt.% to 60 wt.%.

Upon addition of LiTFSI some of the previously observed peaks are dampened, whereby the peak at 793 cm^{-1} is no longer observed but rather a doublet peak at 811 cm^{-1} and 836 cm^{-1}. This is observed as the crystalline state of the PVDF-HFP film changes from α-phase to a mixture of β- (836 cm^{-1}) [49] and γ-phase (811 cm^{-1}).[50] Furthermore, the peak observed at 873 cm^{-1} in the PVDF-HFP data, shifts to 878 cm^{-1} which is indicative of a shift from α-phase to γ-phase. [50] This follows a similar trend noted in the IR data where peaks for both crystalline states were observed, while peaks pertaining to α-phase were dampened or not observed. A weak peak at 743 cm^{-1} (peak b) is attributed to the $TFSI^-$ anion [25, 50-51] and this peak yields information regarding the conformational state of the anion. A peak observed at 747 cm^{-1} would suggest that the anion is co-ordinated to Li cation,[25] which would reduce ionic conductivity and mobility. Peaks obtained at 739 cm^{-1} and 743 cm^{-1} suggest that the anion is not co-ordinated to the Li cation, and adopts a cisoid and transoid conformational state.[52] A peak at 743 cm^{-1} is observed which suggests that the $TFSI^-$ anion adopts a transoid conformation where the CF_3 groups are on opposite sides of the S-N-S plane. When 10 wt.% C_4mpyrTFSI is added to the gel, the intensity of this peak increases due to the higher concentrations of $TFSI^-$ anions present. This

trend is observed across a series of polymer gels where the C_4mpyrTFSI content was increased. The PG-10 film data is similar to that obtained for PVDF-HFP with LiTFSI, however the intensities of the peaks increases as seen for the peaks between 250 cm^{-1} and 440 cm^{-1} which are attributed to C-C aliphatic chains. The pyrrolidinium ring is considered to be aliphatic as it does not contain C=C bonds, hence increasing the content of C_4mpyrTFSI leads to increased intensities observed in Raman spectra (figure 3.14(a and b)). The peaks corresponding to both β- (836 cm^{-1}) and γ-phase (811 cm^{-1}) are observed for PG-10, which suggests that its structure is similar to PVDF-HFP with LiTFSI. The Raman data obtained for PG-60 show these peaks with similar intensities as PVDF-HFP with LiTFSI, though the gels have different crystal structures. There are no prominent α-phase peaks observed but rather a weak peak at 1429 cm^{-1}. This suggests that PG-60 adopts a predominantly amorphous structure with some crystallinity due to the presence of PVDF.

The effect of crystallinity on the melting point and thermal stability of the polymer gels were investigated by both DSC and TGA, where the DSC plots obtained for pure PVDF-HFP, PVDF-HFP with LiTFSI, PG-10, and PG-60 are shown in figure 3.15. From this data, the large exothermic peak obtained is attributed to the melting point of the polymers. Pure PVDF-HFP has a melting point of 149 °C, which decreases slightly to 147 °C upon addition of LiTFSI salt. Similar trends are observed when C_4mpyrTFSI is added to the polymer gel, as the melting points for PG-10 and PG-60 are 146 °C and 120 °C, respectively. The decrease in the melting temperature is attributed to phase changes within the polymer gel. As the amorphicity is increased the melting temperature decreases as observed by Kim *et al.*[25] Similarly, the degree of crystallinity was determined from the DSC data, using equation 3.2: [25]

$$X_C(\%) = \frac{\Delta H_m}{\Delta H_{m.ref}}\ x\ 100 \qquad \text{Equation 3.2}$$

Upon addition of LiTFSI salt and C_4mpyrTFSI the degree of crystallinity decreased from 34% for PG-10 to 11% for PG-60. This demonstrates that PG-60 adopts an amorphous structure. This data is

in good agreement with the FT-IR and Raman data, with the crystallinity of the films decreasing upon addition of the LiTFSI salt and C_4mpyrTFSI and for which the PG-60 film shows the highest degree of amorphicity.

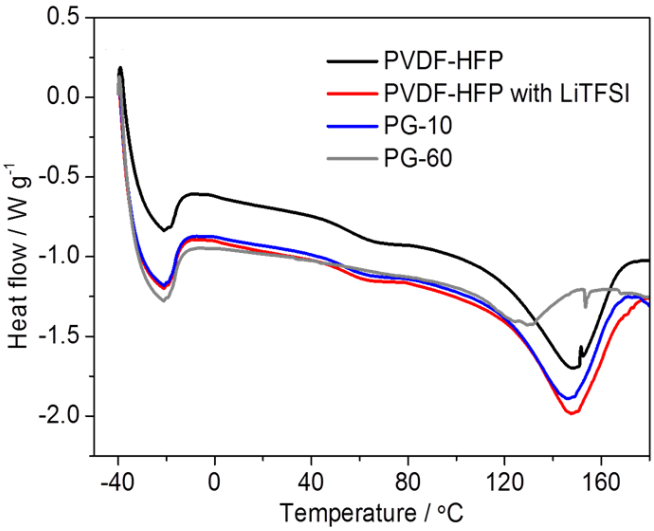

Figure 3.15: DSC traces of pure PVDF-HFP, PVDF-HFP with LiTFSI, PG-10, and PG-60

The TGA plots of pure PVDF-HFP, PVDF-HFP with LiTFSI, PG-10, and PG-60 in N_2 are shown in figure. 3.16(a). PVDF-HFP degrades in two steps, where the first step occurs between 100 °C to 300 °C and the other at ~450 °C. The weight loss observed between 100 °C and 300 °C is attributed to the loss of residual acetone from the film synthesis trapped within the PVDF-HFP matrix.[53-54] The degradation at ~450 °C is attributed to the decomposition of PVDF-HFP.[25] From the data it is clear that the PVDF-HFP has not degraded completely with more than 30% weight remaining. This results from the formation of a char, which is characteristic of linear aromatic and cyclic structures on degradation in nitrogen.[54] Upon addition of the LiTFSI salt, the thermal stability of the polymer gel decreases, whereby the onset of thermal degradation occurs at ~300 °C. This change in the thermal stability is attributed to the change in the crystallinity of the films described above.

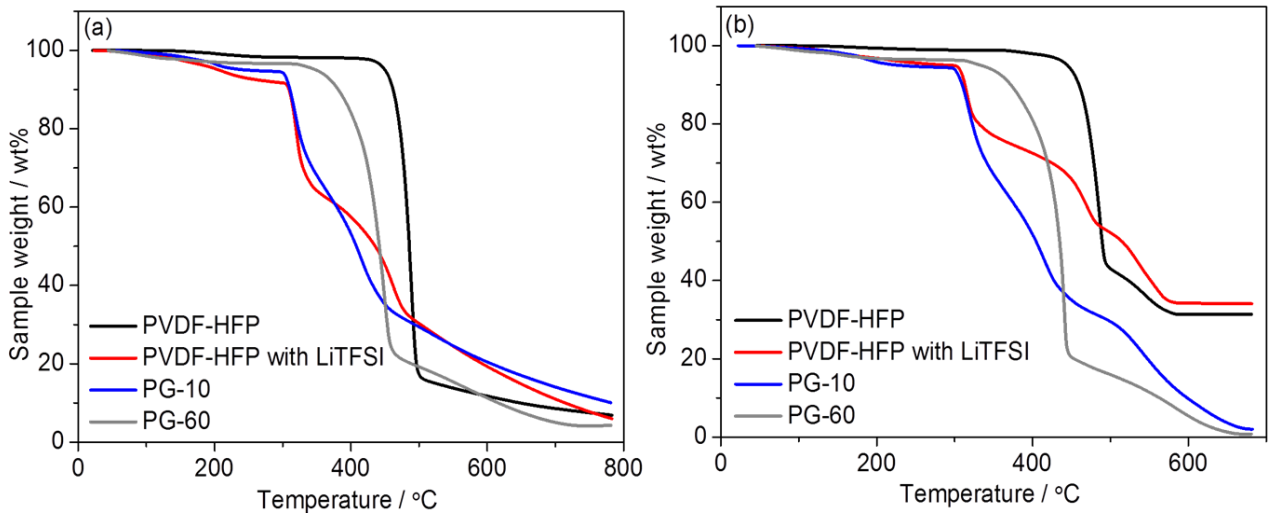

Figure 3.16: TGA plots obtained under (a) N_2 and (b) air, where the N_2 flow rate was 10 ml min^{-1}.

The addition of the LiTFSI salt to PVDF-HFP causes stress, which leads to the observation of other crystalline forms. This stress is caused by LiTFSI salt complexing with the PVDF-HFP backbone which has been observed previously by Shalu *et al.*[21] Similarly when a small amount of C_4mpyrTFSI is added to the polymer gel, a low thermal stability is noted with decomposition at ~300 °C. This result is expected as PVDF-HFP with LiTFSI and PG-10 yield similar crystal structures. When a higher amount of C_4mpyrTFSI is present in the gel, the thermal stability of the polymer increases and is closer to that observed for pure PVDF-HFP films. This is attributed to the change in crystalline structure as the polymer gel exhibits a predominantly amorphous and α-phase structure similar to that of pure PVDF-HFP. The onset of thermal degradation at ~350 °C is due to the C_4mpyrTFSI, with subsequent degradation from PVDF-HFP.[25] Both the PG-10 and PG-60 exhibit a large operating temperature range which is advantageous for battery applications.

TGA analysis on the polymer gels was carried out in air to determine if the packaging environment of the battery would affect the operational temperature of the polymer gel. Similar results are obtained where the degradation of the polymer gels follow the same mechanisms. Both polymer gels with C_4mpyrTFSI exhibit thermal stability up to ~300 °C in air. This is further observed when the

temperature ramp rates are varied as there is no significant change in the thermal degradation onset temperature (figure 3.17).

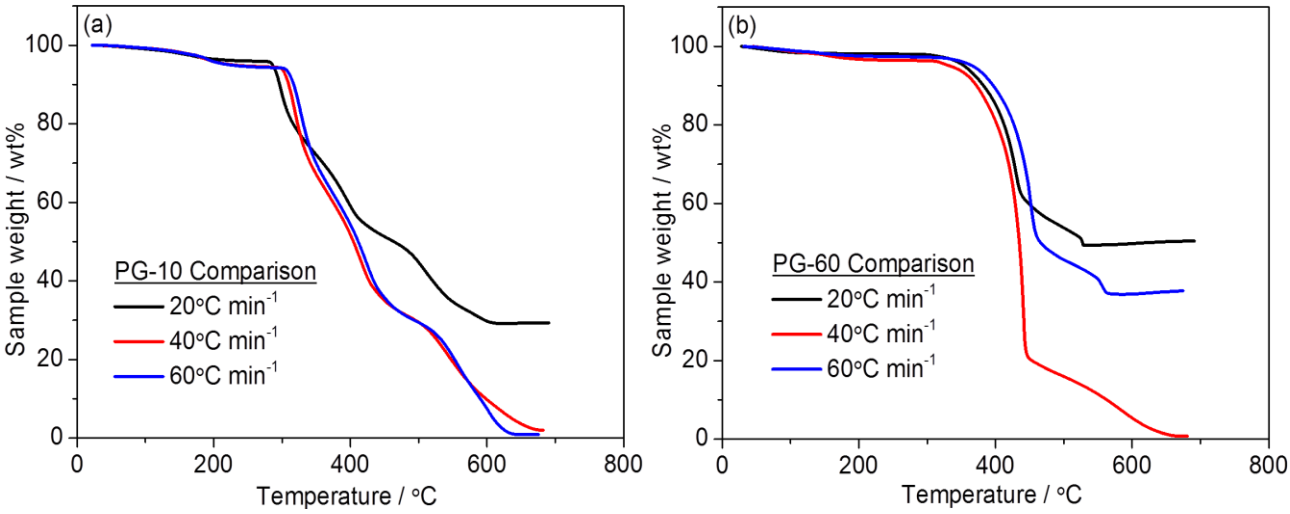

Figure 3.17: TGA data where PG-10 and PG-60 were analysed in air. The temperature was ramped by 20 °C min^{-1}, 40 °C min^{-1} and 60 °C min^{-1}.

The onset of decomposition for the polymer gels in air varies by less than 4 °C by comparison with those assessed under N_2 (figure 3.18). However, unlike under N_2 where char formation was observed, full decomposition of PG-60 and PG-10 occurred in air. This suggests that at elevated temperatures, storing or operating the polymer gel in air would have a greater effect on its performance and stability. At temperatures less than 400 °C, the polymer gel reacts similarly in air and N_2 environments.

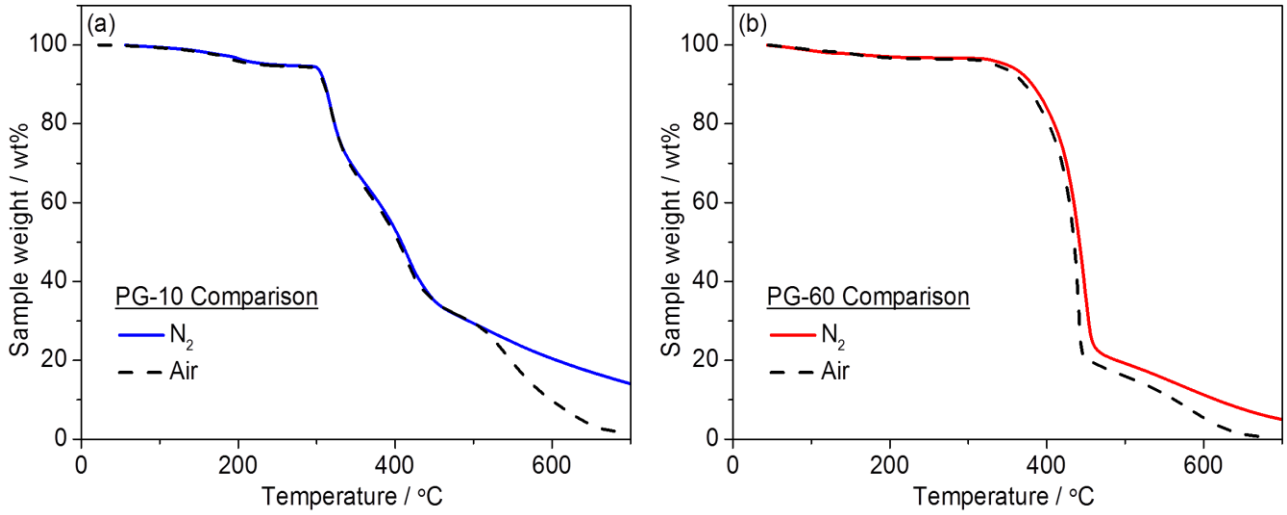

Figure 3.18: comparison of TGA plots for (a) PG-10 and (b) PG-60 obtained under N_2 and air.

The crystallinity of the polymer gels leads to differences in their surface morphology and thermal stability. To determine the effects of crystallinity on the electrochemical properties, the ionic conductivity of the polymer gel films was determined using EIS at room temperature. It is known that the crystalline regions of polymers are responsible for the mechanical stability, while the amorphous regions are responsible for ionic conduction.[21] The addition of LiTFSI salt and C_4mpyrTFSI to the PVDF-HFP matrix is responsible for viable ionic conductivities. The PG-X conductivity values were determined from the EIS data shown in figure 3.19. There is a significant decrease in the resistivity of the polymer gel, as the real impedance (Re(Z)) values decrease with increasing amounts of C_4mpyrTFSI. As the ionic conductivities were obtained at OCV, the main influential circuit element was the Warburg co-efficient. The addition of C_4mpyrTFSI to the PVDF-HFP and LiTFSI matrix led to decreased imaginary impedance (-Im(Z)) values, which demonstrates that its addition leads to decreased resistance to ionic diffusion within the polymer gels. The fit data shown in figure 3.19 tends to deviate at low frequencies where Warburg diffusion occurs, this is due to a deviation from semi-infinite diffusion, which was observed for the liquid IL electrolyte in figure 3.7. Figure 3.19(a) exhibits a response tending towards resistive-like behaviour, while figure 3.19 (b), (c), (d) and (f) exhibit a capacitive-like behaviour at low frequencies.

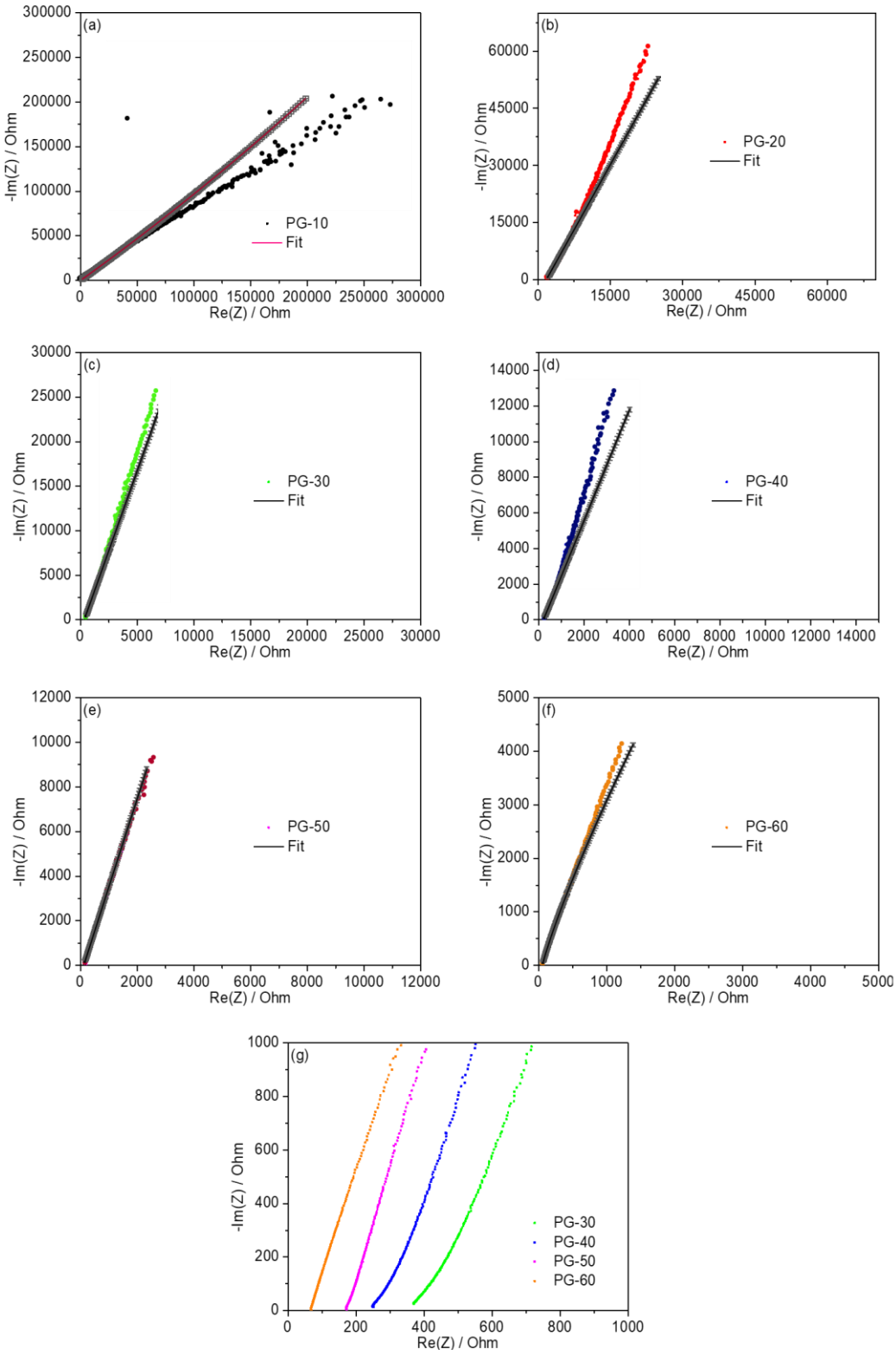

Figure 3.19: EIS data obtained at OCV at 25 °C for (a) PG-10, (b) PG-20, (c) PG-30, (d) PG-40, (e) PG-50, (f) PG-60 and (g) comparison of PG-30 to PG-60, PG-10 and PG-20 not included due to higher resistances. Frequency and fit range used (unless otherwise stated): 150 kHz to 10 Hz.

Table 3.2 shows the ionic conductivities for a typical solid-state[4] and organic electrolyte[39] in addition to the experimental values obtained for the polymer gels. From this table it can be seen that all versions of the polymer gel offer significantly higher ionic conductivities than solid-state LiPON.[5] This trend is observed across the series of polymer gels (table 3.2).

	LiPON	**PG-10**	**PG-20**	**PG-30**	**PG-40**	**PG-50**	**PG-60**	**1 M $LiPF_6$ in EC:DEC**
Conductivity (mS cm^{-1})	3 x 10^{-3}	7 x10^{-2}	7 x10^{-2}	0.2	0.4	0.8	1.9	7.9
99% CI	N/A	±0.005	±0.005	±0.054	±0.060	±0.148	±0.391	N/A

Table 3.2: Comparison of ionic conductivities of solid state,[4-5] polymer gel and organic solvent electrolytes,[39] with 99% confidence interval (CI) where applicable.

The polymer gel containing 60 wt.% C_4mpyrTFSI is almost 600 times more conductive than LiPON, while the polymer gel containing 10 wt.% C_4mpyrTFSI is 23 times greater. Comparing their ionic conductivities to that of 1 M $LiPF_6$ in EC:DEC (1:1 v/v) it is evident that the polymer gels are comparable to standard organic solvents. The ionic conductivity of the ionic liquid C_4mpyrTFSI with 0.5 M LiTFSI salt (~1.5 mS cm^{-1}) mentioned in section 3.3.1, is lower than that for polymer gel PG-60.

Thus, both liquid and polymer gel forms of C_4mpyrTFSI offer favourable properties with respect to ionic conductivity. Their compatibility with anode and cathode materials is described in the subsequent chapters.

3.5 Conclusion

In this chapter an ionic liquid electrolyte was investigated to determine if its properties were suitable for Li-ion batteries by investigating its electrochemical window, its Li-ion mobility and its ionic conductivity. It has been demonstrated that C_4mpyrTFSI offers favourable properties as it has a 5 V electrochemical window, demonstrates Li deposition and stripping at both a singular microelectrode and at a microdisc array, where efficiencies were 49% and 78% respectively. The low efficiencies are attributed to the higher viscosity of the salt in ionic liquid which hinders Li-ion mobility as the current density obtained is approximately 31 times less than that for 1 M $LiPF_6$ in (1:1 v/v) EC:DEC (5 mA cm^{-2} versus 155 mA cm^{-2}).

A linear trend was identified in the EIS data whereby the ionic conductivity of the ionic liquid decreased linearly with increasing salt concentrations, however, even at a 0.5 M LiTFSI salt concentration, the ionic liquid demonstrated an ionic conductivity (1.5 mS cm^{-1}) of the same magnitude as that for conventional organic electrolytes. (7.9 mS cm^{-1}). This ionic conductivity is 500 times greater than that for solid-state electrolytes such as LiPON.

Flexible polymer gel electrolytes containing PVDF-HFP, C_4mpyrTFSI and LiTFSI salt were synthesised in a one-pot synthesis outside of a glovebox at moderate temperatures (50 °C), with no vacuum or external heating required during the drying process, and no further treatment (e.g. soaking in electrolyte, or UV irradiation) once dry to produce polymer gel electrolytes with favourable electrochemical properties. The C_4mpyrTFSI content within the gel yields differences in the crystallinity, surface morphology, thermal stability and ionic conductivity. Despite this, both 10 wt.% and 60 wt.% C_4mpyrTFSI content polymer gels exhibited thermal stability up to 300 °C and ionic conductivities 23 and 600 times greater, respectively, than that of typical solid-state electrolytes.

These gel electrolytes are, therefore, alternatives to the standard solid state electrolytes as they offer separator and electrolyte features in a relatively high conductivity, stable electrolyte.

References

[1] B. Laïk, I. Ressejac, C. Venet, J.-P. Pereira-Ramos, *Thin Solid Films* **2018**, *649*, 69-74 https://doi.org/10.1016/j.tsf.2018.01.033.

[2] T. Famprikis, P. Canepa, J. A. Dawson, M. S. Islam, C. Masquelier, *Nature Materials* **2019**, *18*, 1278-1291 10.1038/s41563-019-0431-3.

[3] J. Li, C. Ma, M. Chi, C. Liang, N. J. Dudney, *Advanced Energy Materials* **2015**, *5*, 1401408 10.1002/aenm.201401408.

[4] J. F. Oudenhoven, L. Baggetto, P. H. Notten, *Advanced Energy Materials* **2011**, *1*, 10-33

[5] J. F. Ribeiro, R. Sousa, J. P. Carmo, L. M. Gonçalves, M. F. Silva, M. M. Silva, J. H. Correia, *Thin Solid Films* **2012**, *522*, 85-89 https://doi.org/10.1016/j.tsf.2012.09.007.

[6] W. Zhang, D. Schröder, T. Arlt, I. Manke, R. Koerver, R. Pinedo, D. A. Weber, J. Sann, W. G. Zeier, J. Janek, *Journal of Materials Chemistry A* **2017**, *5*, 9929-9936 10.1039/C7TA02730C.

[7] R. Koerver, W. Zhang, L. de Biasi, S. Schweidler, A. O. Kondrakov, S. Kolling, T. Brezesinski, P. Hartmann, W. G. Zeier, J. Janek, *Energy & Environmental Science* **2018**, *11*, 2142-2158 10.1039/C8EE00907D.

[8] R. Koerver, I. Aygün, T. Leichtweiß, C. Dietrich, W. Zhang, J. O. Binder, P. Hartmann, W. G. Zeier, J. Janek, *Chemistry of Materials* **2017**, *29*, 5574-5582 10.1021/acs.chemmater.7b00931.

[9] G. Bucci, B. Talamini, A. Renuka Balakrishna, Y.-M. Chiang, W. C. Carter, *Physical Review Materials* **2018**, *2*, 105407 10.1103/PhysRevMaterials.2.105407.

[10] M. Hayyan, F. S. Mjalli, M. A. Hashim, I. M. AlNashef, T. X. Mei, *Journal of Industrial and Engineering Chemistry* **2013**, *19*, 106-112

[11] D. R. MacFarlane, N. Tachikawa, M. Forsyth, J. M. Pringle, P. C. Howlett, G. D. Elliott, J. H. Davis, M. Watanabe, P. Simon, C. A. Angell, *Energy & Environmental Science* **2014**, *7*, 232-250 https://doi.org/10.1039/C3EE42099J.

[12] H. Xue, R. Verma, J. n. M. Shreeve, *Journal of Fluorine Chemistry* **2006**, *127*, 159-176 10.1016/j.jfluchem.2005.11.007.

[13] R. Hayes, G. G. Warr, R. Atkin, *Chem Rev* **2015**, *115*, 6357-6426 10.1021/cr500411q.

[14] M. Kerner, N. Plylahan, J. Scheers, P. Johansson, *Physical Chemistry Chemical Physics* **2015**, *17*, 19569-19581 10.1039/C5CP01891A.

[15] M. Holzapfel, C. Jost, P. Novak, *Chem Commun (Camb)* **2004**, 2098-2099 10.1039/b407526a.

[16] N. Wongittharom, T.-C. Lee, C.-H. Hsu, G. Ting-Kuo Fey, K.-P. Huang, J.-K. Chang, *Journal of Power Sources* **2013**, *240*, 676-682 https://doi.org/10.1016/j.jpowsour.2013.05.014.

[17] J. Saint, A. S. Best, A. F. Hollenkamp, J. Kerr, J. H. Shin, M. M. Doeff, *Journal of the Electrochemical Society* **2008**, *155*, A172 10.1149/1.2820627.

[18] D. R. MacFarlane, M. Forsyth, P. C. Howlett, M. Kar, S. Passerini, J. M. Pringle, H. Ohno, M. Watanabe, F. Yan, W. Zheng, S. Zhang, J. Zhang, *Nature Reviews Materials* **2016**, *1*, 15005 10.1038/natrevmats.2015.5.

[19] Z. Ruisi, C. Yuanfen, R. Montazami, *Materials (1996-1944)* **2015**, *8*, 2735-2748 10.3390/ma8052735.

[20] P.-L. Kuo, C.-H. Tsao, C.-H. Hsu, S.-T. Chen, H.-M. Hsu, *Journal of Membrane Science* **2016**, *499*, 462-469 http://dx.doi.org/10.1016/j.memsci.2015.11.007.

[21] V. K. S. Shalu, R. K. Singh, *Journal of Materials Chemistry C* **2015**, *3*, 7305-7318 https://doi.org/10.1039/c5tc00940e.

[22] A.-L. Pont, R. Marcilla, I. De Meatza, H. Grande, D. Mecerreyes, *Journal of Power Sources* **2009**, *188*, 558-563 https://doi.org/10.1016/j.jpowsour.2008.11.115.

[23] S. Ferrari, E. Quartarone, P. Mustarelli, A. Magistris, M. Fagnoni, S. Protti, C. Gerbaldi, A. Spinella, *Journal of Power Sources* **2010**, *195*, 559-566 https://doi.org/10.1016/j.jpowsour.2009.08.015.

[24] C. Sirisopanaporn, A. Fernicola, B. Scrosati, *Journal of Power Sources* **2009**, *186*, 490-495 https://doi.org/10.1016/j.jpowsour.2008.10.036.

[25] J.-K. Kim, L. Niedzicki, J. Scheers, C.-R. Shin, D.-H. Lim, W. Wieczorek, P. Johansson, J.-H. Ahn, A. Matic, P. Jacobsson, *Journal of Power Sources* **2013**, *224*, 93-98 https://doi.org/10.1016/j.jpowsour.2012.09.029.

[26] H. Ye, J. Huang, J. J. Xu, A. Khalfan, S. G. Greenbaum, *Journal of the Electrochemical Society* **2007**, *154*, A1048-A1057 https://doi.org/10.1149/1.2779962.

[27] M. Li, L. Yang, S. Fang, S. Dong, S.-i. Hirano, K. Tachibana, *Polymer International* **2012**, *61*, 259-264 10.1002/pi.3181.

[28] M. Hayyan, F. S. Mjalli, M. A. Hashim, I. M. AlNashef, X. M. Tan, K. L. Chooi, *Journal of Applied Sciences* **2010**, *10*, 1176-1180 10.3923/jas.2010.1176.1180.

[29] M. Hayyan, F. S. Mjalli, M. A. Hashim, I. M. Alnashef, S. M. Al-Zahrani, K. L. Chooi, *Journal of Molecular Liquids* **2012**, *167*, 28-33 10.1016/j.molliq.2011.12.005.

[30] M. Hayyan, F. S. Mjalli, I. M. AlNashef, M. A. Hashim, *Journal of Fluorine Chemistry* **2012**, *142*, 83-89 10.1016/j.jfluchem.2012.06.028.

[31] M. Hayyan, F. S. Mjalli, M. A. Hashim, I. M. Alnashef, X. M. Tan, *Journal of Electroanalytical Chemistry* **2011**, *657*, 150-157 10.1016/j.jelechem.2011.04.008.

[32] E. I. Rogers, B. Šljukić, C. Hardacre, R. G. Compton, *Journal of Chemical & Engineering Data* **2009**, *54*, 2049-2053 10.1021/je800898z.

[33] B. Flamme, G. Rodriguez Garcia, M. Weil, M. Haddad, P. Phansavath, V. Ratovelomanana-Vidal, A. Chagnes, *Green Chemistry* **2017**, *19*, 1828-1849 10.1039/C7GC00252A.

[34] T. Vogl, S. Menne, R.-S. Kühnel, A. Balducci, *Journal of Materials Chemistry A* **2014**, *2*, 8258-8265 10.1039/C3TA15224C.

[35] N.-W. Li, Y.-X. Yin, J.-Y. Li, C.-H. Zhang, Y.-G. Guo, *Advanced Science* **2017**, *4*, 1600400-n/a 10.1002/advs.201600400.

[36] A. Hofmann, M. Schulz, T. Hanemann, *International Journal of electrochemical science* **2013**, *8*, 10170-10189

[37] S. Drvarič Talian, M. Bešter-Rogač, R. Dominko, *Electrochimica Acta* **2017**, *252*, 147-153 https://doi.org/10.1016/j.electacta.2017.08.168.

[38] E. Karpierz, L. Niedzicki, T. Trzeciak, M. Zawadzki, M. Dranka, J. Zachara, G. Z. Żukowska, A. Bitner-Michalska, W. Wieczorek, *Scientific reports* **2016**, *6*, 35587 10.1038/srep35587.

[39] K. Hayashi, Y. Nemoto, S.-i. Tobishima, J.-i. Yamaki, *Electrochimica Acta* **1999**, *44*, 2337-2344

[40] J.-H. Cao, B.-K. Zhu, Y.-Y. Xu, *Journal of Membrane Science* **2006**, *281*, 446-453 https://doi.org/10.1016/j.memsci.2006.04.013.

[41] P. Martins, A. C. Lopes, S. Lanceros-Mendez, *Progress in Polymer Science* **2014**, *39*, 683-706 https://doi.org/10.1016/j.progpolymsci.2013.07.006.

[42] S. Ramesh, O. P. Ling, *Polymer Chemistry* **2010**, *1*, 702-707 https://doi.org/10.1039/B9PY00244H.

[43] M. A. Gebreyesus, Y. Purushotham, J. S. Kumar, *Heliyon* **2016**, *2*, e00134 https://doi.org/10.1016/j.heliyon.2016.e00134.

[44] S. Abbrent, J. Plestil, D. Hlavata, J. Lindgren, J. Tegenfeldt, Å. Wendsjö, *Polymer* **2001**, *42*, 1407-1416 https://doi.org/10.1016/S0032-3861(00)00517-6.

[45] L. Ruan, X. Yao, Y. Chang, L. Zhou, G. Qin, X. Zhang, *Polymers* **2018**, *10*, 228 https://doi.org/10.3390/polym10030228.

[46] D. Yuan, Z. Li, W. Thitsartarn, X. Fan, J. Sun, H. Li, C. He, *Journal of Materials Chemistry C* **2015**, *3*, 3708-3713 https://doi.org/10.1039/C5TC00005J.

[47] L. N. Sim, S. R. Majid, A. K. Arof, *Vibrational Spectroscopy* **2012**, *58*, 57-66 https://doi.org/10.1016/j.vibspec.2011.11.005.

[48] A. Daneshkhah, S. Shrestha, A. Siegel, K. Varahramyan, M. Agarwal, *Sensors* **2017**, *17*, 595 https://doi.org/10.3390/s17030595.

[49] J. Pitawala, M. A. Navarra, B. Scrosati, P. Jacobsson, A. Matic, *Journal of Power Sources* **2014**, *245*, 830-835 https://doi.org/10.1016/j.jpowsour.2013.07.045.

[50] S. Das, A. Ghosh, T. J. M., A. M., *Journal of Applied Physics* **2016**, *119*, 095101 https://doi.org/10.1063/1.4942658.

[51] L. J. Hardwick, M. Holzapfel, A. Wokaun, P. Novák, *Journal of Raman Spectroscopy* **2007**, *38*, 110-112 https://doi.org/10.1002/jrs.1632.

[52] M. Herstedt, M. Smirnov, P. Johansson, M. Chami, J. Grondin, L. Servant, J. C. Lassègues, *Journal of Raman Spectroscopy* **2005**, *36*, 762-770 https://doi.org/10.1002/jrs.1347.

[53] W. Liu, X. K. Zhang, F. Wu, Y. Xiang, *IOP Conference Series: Materials Science and Engineering* **2017**, *213*, 012036

[54] J. D. Menczel, R. B. Prime, *Thermal Analysis of Polymers: Fundamentals and Applications*, Wiley, **2014**.

Chapter 4:

Evaluation of Ge Anodes with Ionic Liquid Based Electrolytes

4.1 Abstract

Ge compatibility with C_4mpyrTFSI-based electrolytes is investigated, whereby compatibility is demonstrated with 0.5 M LiTFSI in C_4mpyrTFSI, 3% VC in 0.5 M LiTFSI in C_4mpyrTFSI, and the polymer gel analogue PG-60. The compatibility of the electrolytes is demonstrated by CV and galvanostatic cycling techniques. Results comparable to other C_4mpyr-based ILs in the literature are demonstrated.

4.2 Introduction

Due to the emergence of the Internet of Things (IoT) with in excess of 75 billion connected devices expected by 2025,[1] there is an increased focus on miniaturised wireless sensors. Coupling energy harvesters with microbatteries is an option to power the miniaturised sensors. Efficient power management systems will also be required to enable long-life IoT sensors. Metallic Li offers one of the largest gravimetric capacities for anode materials[2] and has been utilised in commercial microbatteries. However, for microbatteries, volume or area is more important than weight.[3-5] Li metal with a theoretical volumetric capacity of 2,062 mA h cm^{-3} is surpassed by Ge and Si for which the capacities are 8,650 and 9783 mAh cm^{-3}, respectively.[6]

Si and Ge have similar physical and chemical properties and both can theoretically hold up to 4.4 Li^+ ions per atom ($Li_{22}M_5$, M = Si, Ge) resulting in high gravimetric capacities of 4,200 and 1,623 mAh g^{-1}, respectively. Ge is more expensive than Si, however, its electronic conductivity is 10,000 times greater and its Li^+ ion diffusion coefficient is 400 times faster.[7-8] Ge thin films have been used to demonstrate high rate capability,[7, 9] due to high lithium diffusivity,[7] and thin native oxide layer by comparison to Si leads to a lower irreversible capacity during the first cycle.[10]

Both materials undergo volume expansion up to 300%, which hinders their commercial application due to mechanical instability. This results in low cycle life in the bulk state due to structural disintegration and delamination from the current collector.[11-13] Volumetric expansion differs during lithium alloying for these materials. Si experiences anisotropic expansion, while isotropic expansion occurs in Ge upon lithiation. Anisotropic expansion in Si during lithiation leads to significant differences in the expansion rate along the <110> and <111> directions. This causes stress to build up, which eventually causes cracking and pulverisation of the electrode.[14] The isotropic volume expansion exhibited by Ge makes it more resistant to cracking and pulverisation as there is no contribution to the overall stress in the film from non-uniform expansion.[15]

In this work, the utilisation of polymer gel electrolytes to alleviate the expansion effects experienced by Ge during cycling were investigated. Polymer gel electrolyte materials have shown buffering capabilities in both capacitor[16] and battery[17-19] applications whereby a polymer gel buffered the expansion effects experienced by the electrode and maintained the electrode's integrity. Mechanically, this is attributed to the polymer gel's high viscosity and elasticity, which prevents active electrode material separation from the current collector.

This work describes the investigation of Ge anodes for use with ionic liquid based electrolytes developed in chapter 3. The influence of additives is investigated to determine their effect on the electrochemical performance of planar Ge electrodes.

4.3 Experimental

A stack of Ti (10 nm) and Cu (250 nm) was deposited on a 4" diameter silicon wafer using metal sputter targets (Kurt J. Lesker) in a D.C. magnetron (Quorum Q300T D) dual sputter coating system. The Ti layer acted as an adhesion layer between the SiO_2 substrate and Cu current collector. Planar 100 nm Ge samples were created by direct current (D.C.) sputter deposition in an Ar environment using a 99.99% pure Ge target (Kurt J. Lesker) at a pressure and current of 1 $x10^{-2}$ mBar and 90 mA, respectively. A punched Cu foil template was placed over the samples during sputtering to control the size of the active electrode area (0.64 cm^2).

The sample thickness was controlled by a film thickness monitor (FTM), which measures the coating thickness on a quartz crystal monitor within the chamber. Once the samples were prepared their thicknesses were verified by profilometer measurements.

The structure and the morphology of the samples were analysed using a Zeiss Supra 40 SEM coupled with energy dispersive X-ray spectroscopy (EDX). Raman spectroscopy was performed on a Renishaw Invia, with 514 nm laser.

Electrochemical measurements of the Li^+ capacity were assessed by CV and galvanostatic cycling with potential limitation (GCPL) using a Bio-logic VSP potentiostat at various scan rates and discharge/charge currents, respectively. For both techniques, a three-electrode pouch cell setup was utilised where 0.25 mm thick lithium foil (Sigma Aldrich) acted as counter and reference electrode. 0.64 cm^2 of the anode was exposed as the working electrode to the electrolyte solutions as mentioned

in chapter 3. The potential of the Ge anode was measured versus the Li metal reference electrode in both CV and GCPL analysis, where the potential range utilised was 1.5 V to 0 V. The current was imposed on the Ge electrode during GCPL analysis. Cell assembly was carried out in an argon-filled glove box (M. Braun LABstar Glove Box) with O_2 and H_2O maintained below 0.1 ppm.

4.4 Results and discussion

The Ge films were investigated initially using Raman analysis to determine the crystallinity of films obtained when sputter deposited onto a Si substrate. Characteristic amorphous Ge Raman peaks were obtained (figure 4.1) as evidenced by the peak at 279 cm^{-1}.[20] This is in agreement with previous studies[21-23] of D.C. and radio frequency (R.F.) magnetron sputtered thin films whereby the broad peak is attributed to the first order transverse optical phonon mode of Ge and is indicative of an amorphous Ge film. Crystalline films of Ge yield a peak at ~291 cm^{-1} which corresponds to the Raman active first order transverse optical phonon mode of crystalline Ge.[24] Investigation with SEM and EDX analysis yielded the expected results where Ge was detected in addition to the Cu current collector and Si substrate. As shown in figure 4.1(b), no discernible features were noted for the Ge film, which demonstrates that smooth planar films were obtained.

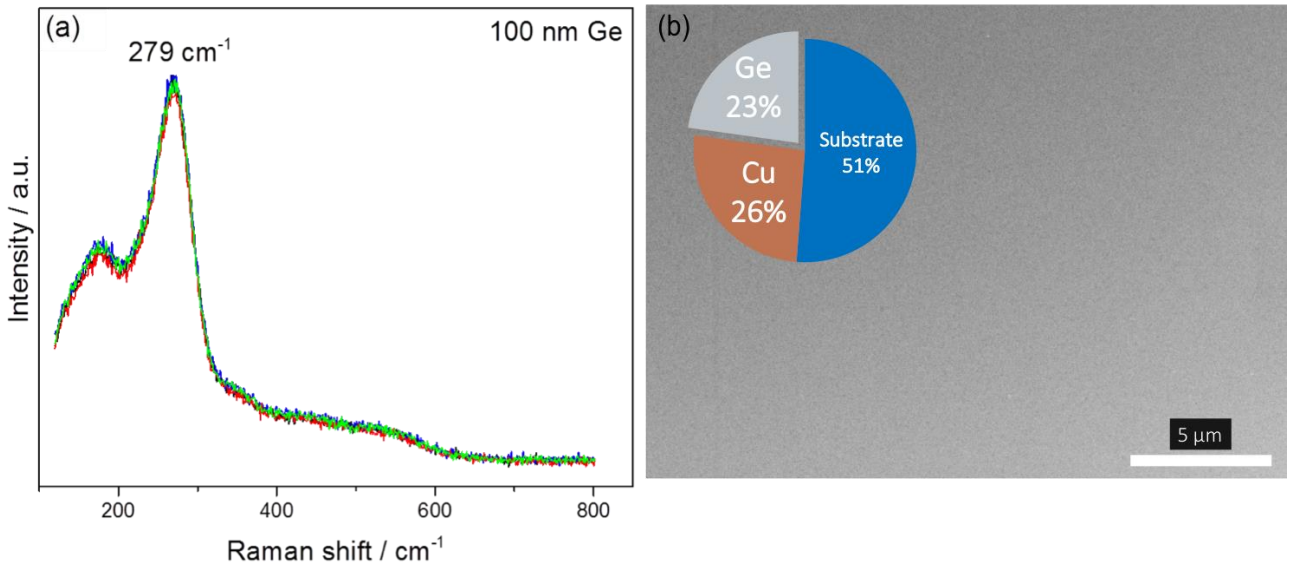

Figure 4.1: Raman spectra of (a) 100 nm Ge and (c) SEM micrograph of planar Ge film with EDX inset.

Initially, CV analysis was carried out to determine the compatibility of Ge anodes with C_4mpyrTFSI-based electrolytes. Their performance was compared to Ge anodes within a conventional organic electrolyte (1 M $LiPF_6$ in 1:1 v/v EC:DEC), with both CVs shown in figure 4.2. It can be seen that the characteristic CV data for amorphous Ge electrodes is observed for Ge films within organic and IL electrolytes. Peaks at 0.54 V (I), 0.29 V (II) and 0.05 V (III) are attributed to Li-Ge alloying with a broad anodic peak at 0.47 V (VI) which indicates delithiation of amorphous Li_xGe at a scan rate of 0.05 mV s^{-1}. The 0.05 mV s^{-1} CV data for both electrolytes is similar in shape, therefore demonstrating compatibility of C_4mpyrTFSI electrolytes with Ge as similar diffusion kinetics are occurring for both electrolytes. At higher scan rates, deviations in the CV shapes are observed as shallow, broad peaks for both electrolytes, suggesting that the sweep rate is almost too high for the electrode to fully alloy and dealloy Li, thus leading to reduced capacity values as shown in table 4.1. The CVs for both electrolytes overlap which demonstrates that a stable SEI layer has formed on the surface of the Ge anode, which allows for reproducible currents to be obtained for each scan rate. Without the formation of the SEI layer, changes in the current density would be observed, and the CV data would not overlap.

The current densities obtained by the 100 nm Ge in organic electrolyte in figure 4.2 are in agreement with literature values as current densities of 0.05 mA cm^{-2} (delithiation) and -0.06 mA cm^{-2} (lithiation) are observed for 400 nm p-doped Ge thin film electrodes where typical amorphous CV data is observed.[25] In addition, 225 nm n-doped Ge films synthesised under similar conditions (D.C. sputtering) have exhibited current densities of ~0.05 mA cm^{-2} (delithiation) and approximately -0.04 mA cm^{-2} (lithiation) at 0.05 mV s^{-1},[26] with the same organic electrolyte (1 M $LiPF_6$ in 1:1 v/v EC:DEC), which demonstrates that the current densities obtained for the organic electrolyte in figure 4.2(a) match those obtained in the literature. Lower electrode current densities within the organic electrolyte may be attributed to the SEI layer that forms on the electrode surface. Organic electrolytes typically breakdown into inorganic compounds such as Li_2CO_3, and organic compounds such as $Li(CH_2)_2OCO_2Li$ (EC containing electrolytes).[27] Organic components within the SEI layer have been shown to significantly decrease Li^+ transport within the SEI layer which increases the charge transfer resistance of the cell.[28] SEI layers formed on Ge electrodes in C_4mpyrTFSI with LiTFSI salt electrolytes have been demonstrated to be comprised mainly of inorganic compounds such as Li_2CO_3, Li_2O, Li_2S, LiF, $LiOH/Li_2O_2$ as demonstrated by Lahiri *et al.*[29] Thus higher Li transport would be observed and higher current densities.

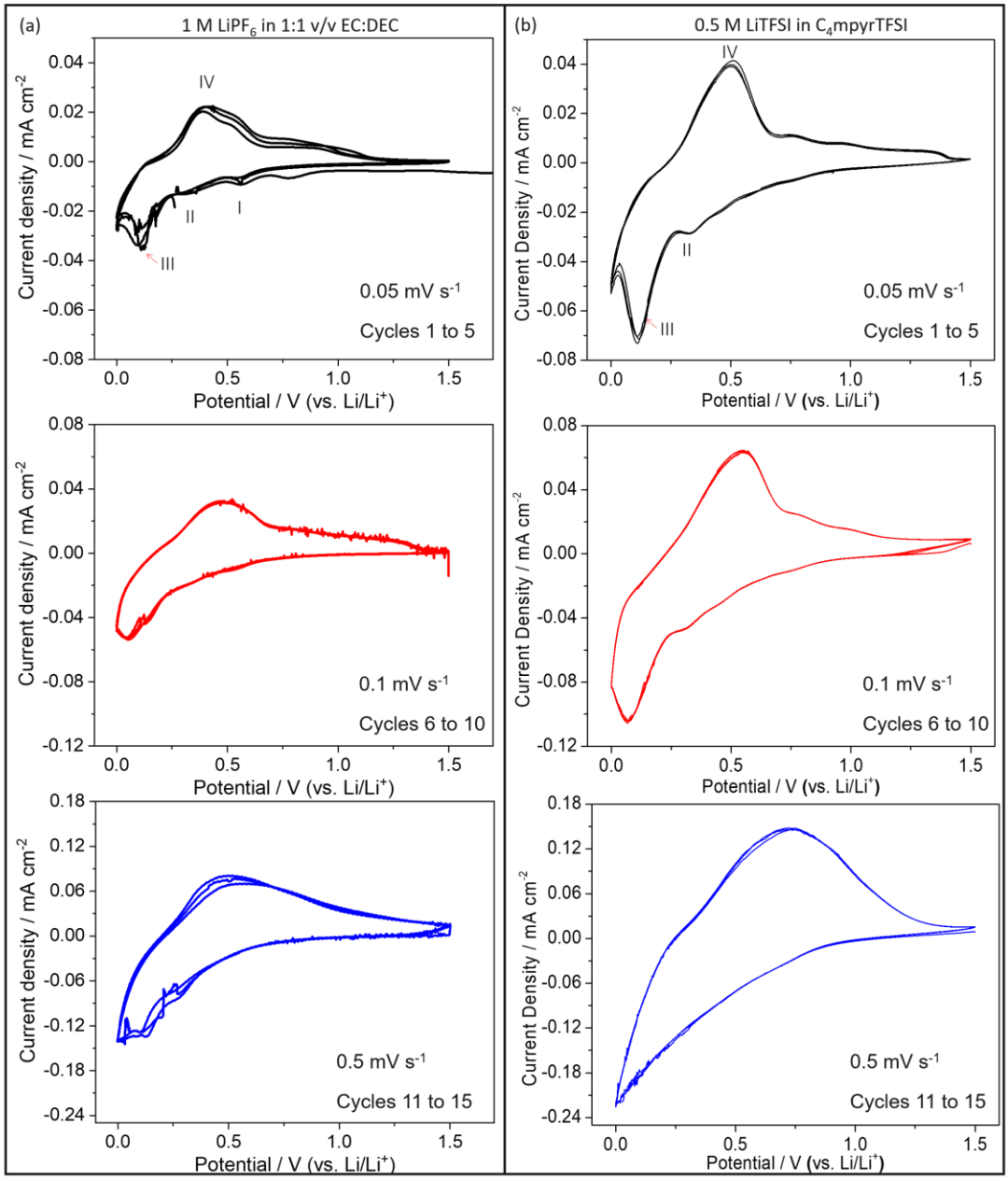

Figure 4.2: Comparison of the electrochemical performance of 100 nm Ge in (a) 1 M $LiPF_6$ in 1:1 v/v EC DEC and (b) 0.5 M LiTFSI in C_4mpyrTFSI.

The SEI layer formation occurs more readily within the organic electrolyte than for C_4mpyrTFSI as electrolyte breakdown occurs more rapidly within organic electrolytes owing to their narrower electrochemical window (reductive limit is 0.5 V vs. Li/Li^+) as demonstrated in section 3.4.1. By comparison, the IL exhibits high reductive stability with electrolyte breakdown occurring beyond 0

V vs. Li/Li^+. In chapter 3, the analysis was carried out at a Ni microelectrode where fast scan rates were utilised (1 mV s^{-1} up to 100 mV s^{-1}). From this analysis, the breakdown of the IL is unclear as quick experimental timescales are utilised, and thus is was determined that the IL does not readily provide breakdown products for SEI layer formation at these faster scan rates. This suggests that SEI layer formation within the IL is a sluggish process and is seen more clearly at the slow scan rates utilised with Ge analysis as higher than theoretical capacities were obtained in the initial cycles (0.05 mV s^{-1}) as shown in table 4.1. In addition, the organic electrolyte boasts higher coulombic efficiencies across all scan rates (70% to 98%), which is indicative of the formation of a stable SEI layer, while the maximum coulombic efficiency obtained by the IL was 88% at 0.5 mV s^{-1}. However, despite the inability of the IL to rapidly form an SEI layer on Ge, it yields higher electrode charge and discharge capacities than the organic electrolyte as shown in table 4.1. The capacity retention for both electrolytes is similar, as values of 98% vs. 99% and 59% vs. 61% were obtained for the organic and IL electrolyte at 0.1 mV s^{-1} and 0.5 mV s^{-1} respectively. This demonstrates that the higher viscosity, and thus lower ionic conductivity of the IL, has little effect on its electrochemical performance with Ge anodes.

Electrolyte	1 M $LiPF_6$ in 1:1 v/v EC:DEC	0.5 M LiTFSI in C_4mpyrTFSI	Scan rate (mV s^{-1})
Average lithiation capacity (mAh g^{-1})	1510	1874	0.05
	995	1440	0.1
	590	733	0.5
Average delithiation capacity (mAh g^{-1})	982	1054	0.05
	967	1045	0.1
	577	641	0.5
Average coulombic efficiency (%)	70	56	0.05
	97	73	0.1
	98	88	0.5

Table 4.1: Comparison of coulombic efficiency, lithiation and delithiation capacities obtained during CV analysis of Ge in 1 M $LiPF_6$ in 1:1 v/v EC/DEC and 0.5 M LiTFSI in C_4mpyrTFSI. Average of 5 cycles obtained at each scan rate.

The above results demonstrate the compatibility of C_4mpyrTFSI as it offers similar electrochemical performances to organic electrolytes. Capacity values obtained at various scan rates are shown in figure 4.3. In this instance, the formation of an SEI layer is surmised in the initial cycles as the lithiation capacity is not observed for the initial scan rates of 0.05 mV s^{-1} (average: 2896 mAh g^{-1}) as they exceed the theoretical capacity of Ge (1624 mAh g^{-1}). This demonstrates slow SEI layer formation occurs within the IL electrolyte when coupled with Ge. Once a stable SEI layer forms, stable cycling is observed for the subsequent cycles as evidenced in figure 4.3. After scanning at fast scan rates (0.5 mV s^{-1}), the capacity recovers quickly when slower scan rates are employed. In the case of 0.05 mV s^{-1} (blue), the capacity improves after cycling at faster scan rates when compared to its initial capacity values. In addition, the coulombic efficiency also improves (~65% vs. ~60%) after

cycling at fast scan rates which demonstrates that a more stable SEI layer has formed. This data coupled with the comparable electrochemical performances with organic electrolytes demonstrate that Ge is compatible with C_4mpyrTFSI.

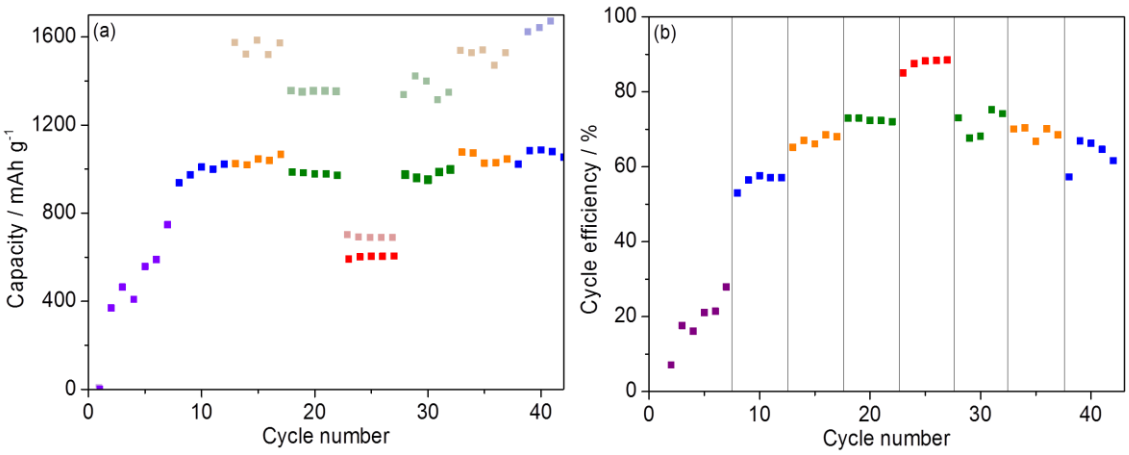

Figure 4.3: (a) Capacity data obtained from 100 nm Ge where (b) refers to the respective coulombic efficiencies. The scan rates utilised are 0.025 mV s^{-1}(purple), 0.05 mV s^{-1}(blue), 0.075 mV s^{-1}(orange), 0.1 mV s^{-1}(green), and 0.5 mV s^{-1}(red). Pale colours refer to lithiation, while darker colour refers to delithiation. Same for subsequent graphs.

The coulombic efficiencies for C_4mpyrTFSI are considerably lower than those obtained in organic electrolytes. In order to improve the coulombic efficiency, the addition of VC and FEC additives was investigated (figure 4.4).

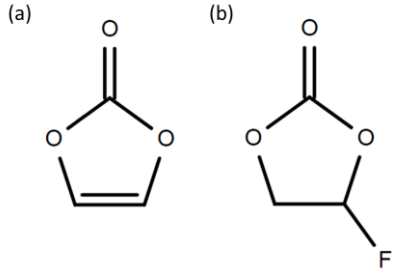

Figure 4.4: Chemical structures of (a) VC and (b) FEC

To the best of our knowledge, the use of Ge anodes with additives such as VC and FEC in C_4mpyrTFSI has not been previously investigated, therefore initially EIS was carried out to determine

if the addition of the carbonate additives affects the ionic conductivity of the ionic liquid electrolyte. Figure 4.5(b and c) shows the experimental data for FEC- and VC-containing electrolytes, where good agreement between the experimental and fit data is observed. The EIS data is similar to that obtained for 0.5 M LiTFSI in C_4mpyrTFSI (figure 4.5(a)) and this is reflected in the ionic conductivity as similar ionic conductivities were obtained for 0.5 M LiTFSI in C_4mpyrTFSI, 3 wt.% FEC in 0.5 M LiTFSI in C_4mpyrTFSI and 3 wt.% VC in 0.5 M LiTFSI in C_4mpyrTFSI. (1.5 mS cm^{-1}, 1.45 mS cm^{-1} and 1.54 mS cm^{-1} respectively).

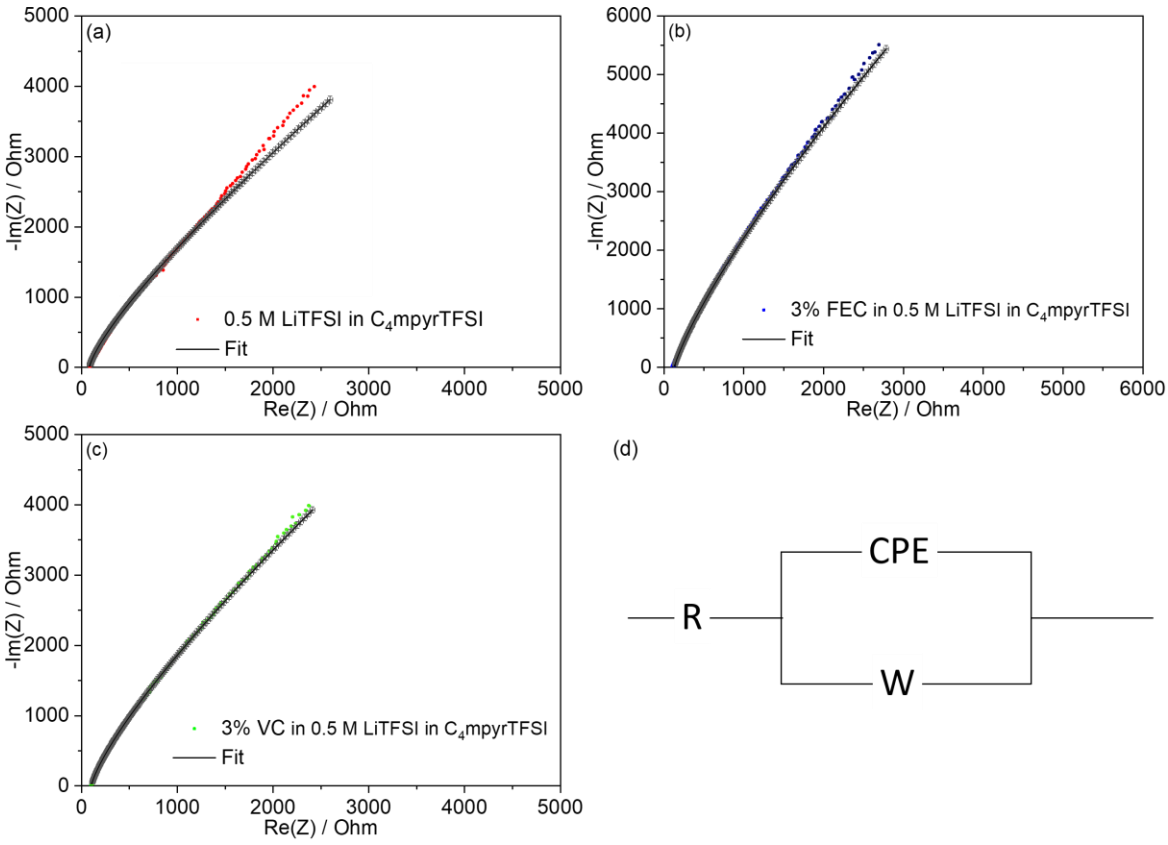

Figure 4.5: (a, b, c) EIS and fit data for various C_4mpyrTFSI electrolytes and (d) equivalent circuit used for fit data. Frequency range of 150 kHz to 10 Hz at open circuit voltage (OCV), with an amplitude of 5 mV at room temperature.

CV analysis is required to determine if stable SEI layers form at the electrolyte/Ge interface. These carbonate additives have been chosen due to their reduced electrochemical stability (breakdown occurs at potentials higher than 0 V vs. Li/Li^+) when compared to C_4mpyrTFSI (stable at potentials beyond 0 V vs. Li/Li^+). The formation of an SEI layer within IL electrolytes is sluggish when compared to the organic carbonate containing electrolytes. Therefore, the utilisation of carbonate based additives whose breakdown occurs at potentials higher than 0 V vs. Li/Li^+, will allow for faster SEI layer formation within the IL electrolyte. This should enable stable electrode capacities, and higher coulombic efficiencies in the IL electrolytes than without additives. Their performance with similar anode materials (Sn, Si and Ge) have been investigated in a variety of typical organic electrolytes such as 1 M lithium $LiPF_6$ in a 1:1 (v/v) EC:DMC,[30-34] therefore demonstrating their viability as effective additives for use with group IV materials. Their primary function is to enable the formation of SEI layers, and as mentioned they have been proven to be effective with group IV elements such as Ge. Therefore, the investigation of the SEI formed and its stability with the IL is carried out to further the understanding of the SEI/IL interphase which will enable high coulombic efficiencies and higher electrode capacities to be obtained.

The initial CV data obtained for 3 wt.% VC and 3 wt.% FEC are shown in figure 4.6, where similar CV shapes are observed when compared to the additive-free electrolyte (figure 4.2), which demonstrates that similar electrode kinetics. The 3 wt.% VC-based IL electrolyte shows an evolution of the CV data, which is indicative of electrolyte breakdown to enable the formation of an SEI layer. In the initial cycles, a large reductive peak is observed which suggests that electrolyte breakdown was occurring, in this case the decomposition of VC. From cycle 3 onwards, the characteristic Ge CV data is observed with well-defined lithiation and delithiation peaks which overlap for each subsequent cycle. Similar overlap is observed with the increased scan rates as observed in figure 4.7.

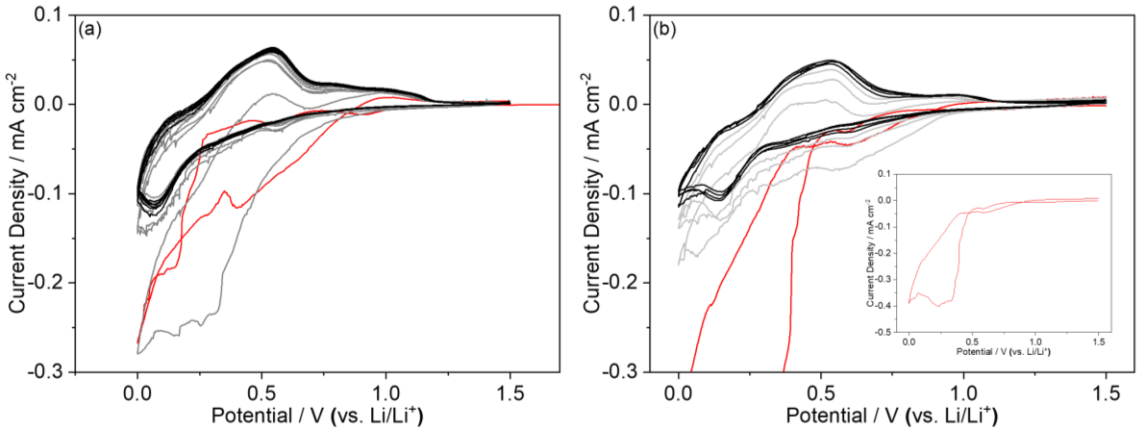

Figure 4.6: Ge CV data (cycles 1 to 15) at 0.05 mV s^{-1} in 0.5 M LiTFSI in C4mpyrTFSI with (a) 3 wt.% VC and (b) 3 wt.% FEC. Inset: initial 3 wt.% FEC cycle.

The current densities in the CV data for Ge with the 3 wt.% VC electrolyte are higher than those obtained in 0.5 M LiTFSI in C_4mpyrTFSI (0.06 mA cm^{-2} vs. 0.04 mA cm^{-2} at 0.05 mV s^{-1}), which could be attributed to the electrolyte breakdown to form an SEI layer. This explains why electrode capacities greater than theoretical are obtained for 0.05 mV s^{-1} and 0.1 mV s^{-1} scan rates as shown in table 4.2 (e.g. 1656 mAh g^{-1} vs. 1624 mAh g^{-1} at 0.1 mV s^{-1}). The lower coulombic efficiency (table 4.2) obtained with the presence of 3 wt.% VC is attributed to the breakdown of VC to form an SEI layer, however, at higher scan rates, an improvement in the coulombic efficiency is observed when compared to the additive free electrolyte (77% vs. 73% at 0.1 mV s^{-1}).

Electrolyte	With 3 wt.% VC	Without 3 wt.% VC	Scan rate ($mV\ s^{-1}$)
Average lithiation capacity ($mAh\ g^{-1}$)	4558	1874	0.05
	1656	1440	0.1
	685	733	0.5
Average delithiation capacity ($mAh\ g^{-1}$)	1718	1054	0.05
	1278	1045	0.1
	613	641	0.5
Average coulombic efficiency (%)	47	56	0.05
	77	73	0.1
	90	88	0.5

Table 4.2: Comparison of average coulombic efficiency, lithiation and delithiation capacities obtained during CV analysis of Ge in 0.5 M LiTFSI in C_4mpyrTFSI with and without 3 wt.% VC additive.

The 3 wt.% FEC yields similar CV data as the 3 wt.% VC as demonstrated in figure 4.6(b), however, the lithiation electrode capacities on average are 2.6 times higher than for 3 wt.% VC-based electrolyte as shown in table 4.3, due to the initial large reductive peak attributed to electrolyte breakdown. In addition, the coulombic efficiencies were half those attained by the VC containing electrolyte. This demonstrates that the Ge is more compatible with the VC additive than the FEC when Ge thicknesses are ~100 nm as less electrolyte breakdown is required to form a stable SEI layer, thus demonstrating faster stabilisation of the cell.

Electrolyte	Average lithiation capacity (mAh g^{-1})	Average delithiation capacity (mAh g^{-1})	Average coulombic efficiency (%)
3 wt.% VC	4558	1718	47
3 wt.% FEC	11640	1625	21

Table 4.3: Comparison of average coulombic efficiency, lithiation and delithiation capacities obtained during CV analysis of Ge in 0.5 M LiTFSI in C_4mpyrTFSI with a 3 wt.% VC or 3 wt.% FEC additive at 0.05 mV s^{-1}.

The difference in electrochemical performance could be attributed to the SEI layer products formed during VC and FEC decomposition. It has been suggested in the literature that similar reduction products are formed during FEC and VC breakdown, however, the quantities of the various components (Li_2CO_3, $Li_2C_2O_4$, and HCO_2Li) differ.[35] This difference in SEI layer formation may contribute to the difference in electrochemical performance of Ge with the additives. Therefore, longer term cycling (up to 100 cycles) was carried out with Ge in 3 wt.% VC, where the 0.1 mV s^{-1} and 0.5 mV s^{-1} CV data is shown in figure 4.7 where overlap is noted which demonstrates that the cell has stabilised. Figure 4.7(c) shows the capacity data obtained from CV analysis, it can be seen that high lithiation capacities (>1400 mAh g^{-1}) are obtained at 0.1 mV s^{-1} scan rates, in addition to high delithiation capacities (>1200 mAh g^{-1}). As the scan rate is increased by a factor of 5 (0.5 mV s^{-1}), the capacity is maintained above 600 mAh g^{-1}, which is higher than other anode materials. As previously observed in 0.5 M LiTFSI in C_4mpyrTFSI, the 0.5 mV s^{-1} scan rate appears to be too quick to allow for full Li^+ alloying and dealloying as the typical diffusion controlled peaks are not observed, which results in lower electrode capacity. Stable coulombic efficiencies of 90% are achieved at this scan rate, with an improvement in electrode capacity across 20 cycles as the initial capacity was 598 mAh g^{-1}, while after 20 cycles, the capacity was 620 mAh g^{-1}. Capacity loss would be expected due to the expansion and contraction effects experienced by Ge upon lithiation and delithiation which

leads to the formation of cracks and eventual delamination of the electrode from the current collector. A similar trend is observed for the subsequent 0.1 mV s^{-1} cycles. In the final 0.05 mV s^{-1} data, the electrode capacity is higher than theoretical which suggests that cracks formed within the electrode, which leads to continued SEI layer formation, and thus higher than theoretical electrode capacities. It must be noted that there are limitations to the data as slow scan rates were not employed to allow for the stabilisation of the SEI layer which limits the attainable electrode capacities.

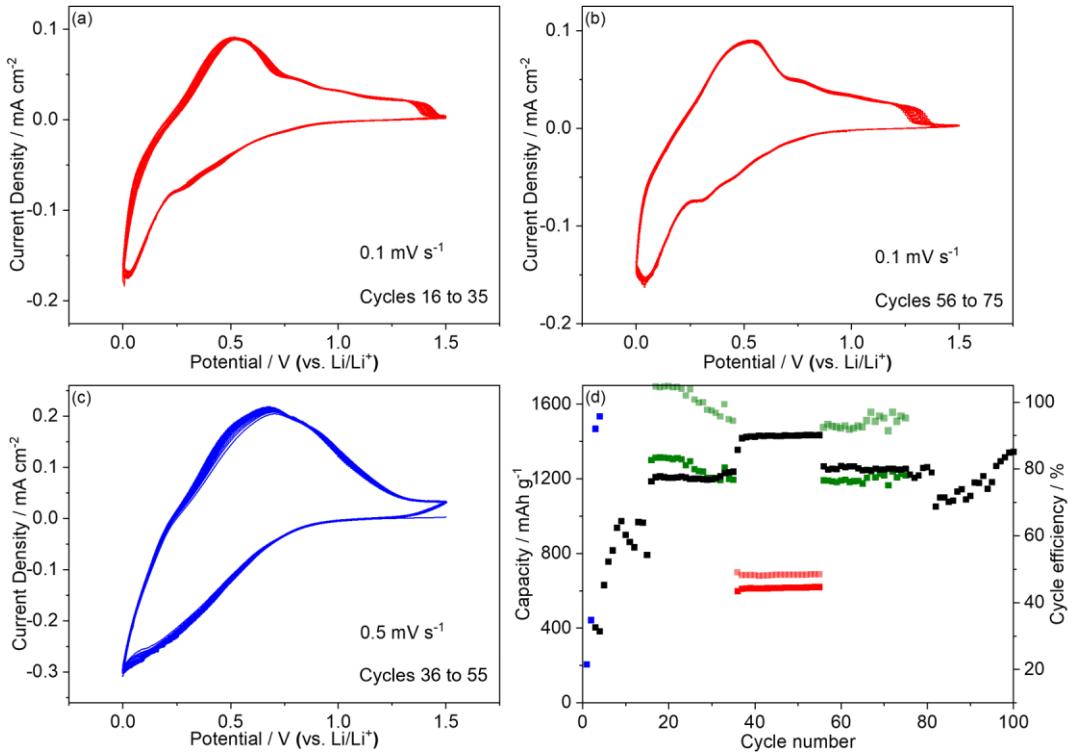

Figure 4.7: CV analysis of Ge electrodes where 3 wt.% VC was added to 0.5 M LiTFSI in C_4mpyrTFSI where scan rates utilised were (a and b) 0.1 mV s^{-1}, (c) 0.5 mV s^{-1}, (d) capacity data obtained at various scan rates: 0.05 mV s^{-1} (blue), 0.1 mV s^{-1} (green) and 0.5 mV s^{-1} (red).

SEM analysis after 100 cycles with various scan rates in the IL-based electrolytes was carried out to determine if a change in the morphological features occurred. The SEM data for pristine, and cycled electrodes are shown in figure 4.8. All three electrodes experienced delamination from the current collector as evidenced by the EDX data. The Ge electrode in 0.5 M LiTFSI in C_4mpyrTFSI yielded

the least amount of delamination as large patches of Ge electrode were visible on the current collector after cycling as shown in figure 4.8(a). By comparison Ge islands are observed after 100 cycles in 3 wt.% VC in 0.5 M LiTFSI in C_4mpyrTFSI (figure 4.8(b)), which verifies that continued SEI layer formation was occurring as observed in the above CV data (figure 4.7) due to microcracks within the film. This demonstrates why the capacities for the VC-containing and additive free electrolytes were similar at all scan rates, as the continuous cracking of the Ge electrode required continuous SEI layer formation to cover the freshly exposed Ge. The Ge electrode utilised with FEC containing electrolytes yielded the highest level of delamination, as large areas of substrate were observed, with a few chunks of Ge scattered upon the current collector, such as that shown in figure 4.8(c). This demonstrates that FEC as an additive is incompatible for use with Ge with C_4mpyrTFSI electrolytes as it does not prevent or slow down the rate of Ge delamination from the current collector.

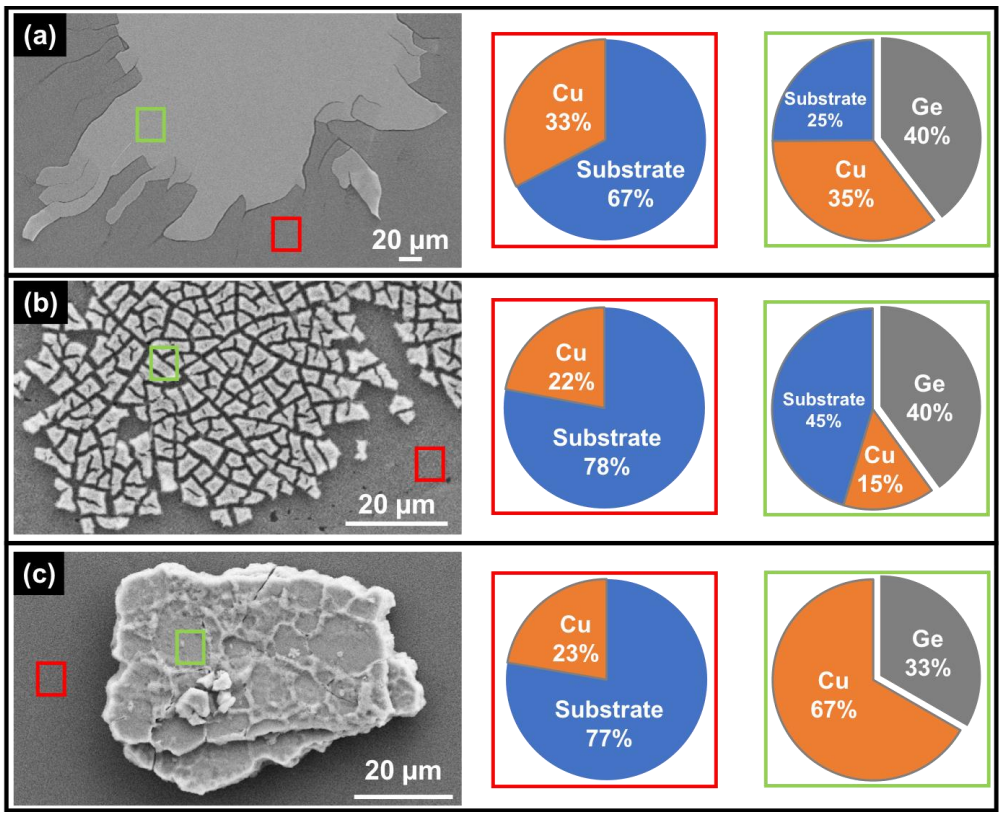

Figure 4.8: SEM and EDX data for cycled Ge electrodes in (a) 0.5 M LiTFSI in C_4mpyrTFSI, (b) 3 wt.% VC in 0.5 M LiTFSI in C_4mpyrTFSI, and (c) 3 wt.% FEC in 0.5 M LiTFSI in C_4mpyrTFSI.

Despite the addition of SEI layer forming additives to the IL electrolyte, the appearance of cracks due to expansion and contraction effects are still observed, which causes electrode delamination as evidenced in the above SEM images (figure 4.8). Utilisation of a polymer gel electrolyte has been suggested as a potential solution to mitigate these expansion and contraction effects, thus ensuring good adherence to the current collector.[16] The polymer gel PG-60 synthesised in chapter 3, was utilised and the electrochemical performance of Ge with PG-60 is shown in figure 4.9. The initial scans with Ge are shown in figure 4.9(a), where a scan rate of 0.025 mV s^{-1} was utilized. The CV shows the characteristic CV data for amorphous Ge, with a pronounced reduction peak at 1 V. This peak has been attributed to the electrolyte reduction reactions and it does not appear in subsequent cycles. This peak has not been observed previously with the liquid based electrolytes, thus demonstrating that an electrolyte reaction with the substrate is occurring, rather than a large reductive peak associated with electrolyte breakdown as observed in figures 4.6. The peak current observed is larger than what has been previously observed and the reduction layer products formed allow a stable system to be obtained after 3 cycles as evidenced by the overlapping data. This overlapping is observed at all scan rates, even in the latter half of the cycling as shown in figure. 4.9(b). Furthermore, the coulombic efficiency is greater than 95% after 90 cycles which demonstrates the cyclability of PG-60 with Ge. In addition, the capacity retention was maintained at an average of 86% across the various scan rates.

Similar results were obtained with a PG-60 thickness of 42 µm, whereby higher capacities were obtained due to the reduction in electrolyte volume (Figure. 4.9(d)), allowing a shorter Li^+ diffusion pathway through the electrolyte. The average cycling efficiency over 50 cycles was 82%, which is lower than that for the 400 µm thick PG-60 (95% over 90 cycles), however, the thinner electrode maintained capacity values close to the theoretical capacity of Ge at 0.05 mV s^{-1} and 0.1 mV s^{-1} as shown in figure 4.9(d). Cycling at 0.5 mV s^{-1} yields higher capacity values (~850 mAh g^{-1}) than for

the 400 µm PG-60 (~500 mAh g^{-1}) which demonstrates that the thinner electrolyte allows for higher specific capacities to be obtained due to shorter diffusion pathways. Further work is required to improve capacity retention, as 78% of the initial 0.1 mV s^{-1} capacity was obtained for the final 0.1 mV s^{-1}, however, these initial results demonstrate that thin films of PG-60 are viable for use as a solid state electrolyte. Both figure 4.9(c) and 4.9(d) indicate that both the 400 µm and 42 µm PG-60 are capable of buffering the volumetric expansion effects experienced by Ge upon cycling with Li. The results demonstrate that Ge is compatible with the C_4mpyrTFSI based polymer gel electrolyte, in addition to the liquid counterparts.

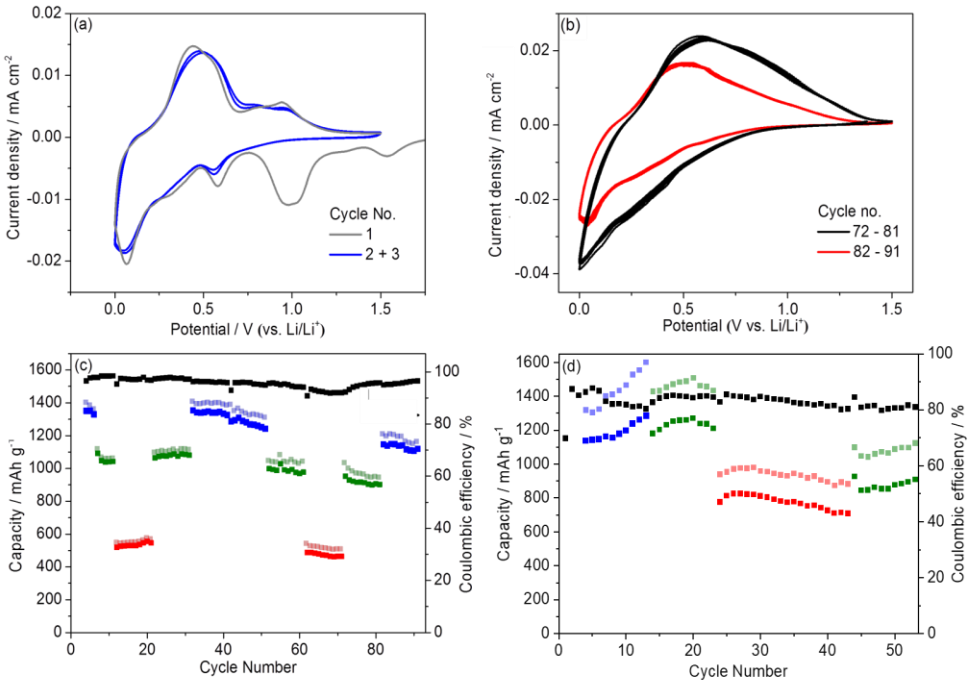

Figure 4.9: CV data obtained for 100 nm Ge with 400 µm thick PG-60, (a) initial 3 cycles obtained at 0.025 mV s^{-1} scan rate, (b) final cycles obtained at 0.05 mV s^{-1} (red) and 0.1 mV s^{-1} (black), (c) and (d) capacity values obtained for each scan rate: 0.05 mV s^{-1} (blue), 0.1 mV s^{-1} (green), and 0.5 mV s^{-1} (red), the coulombic efficiency (black) is indicated on the right hand. Reprinted with permission from McGrath et al.[36]

Galvanostatic cycling analysis was then carried out on the liquid and polymer gel electrolytes. Galvanostatic cycling replicates the charging and discharging cycling that would occur in batteries, either via constant current or constant voltage. Literature analysis of Ge with similar IL electrolytes (1 M LiTFSI in C_4mpyrTFSI and 1 M LiTFSI in C_4mpyrFSI) and an electrodeposited Ge electrode exhibited a maximum electrode capacity of 600 mAh g^{-1} at 1 C.[37] In organic based electrolytes (1 M $LiPF_6$ in 1:1:2 v/v/v of ethylene carbonate (EC):propylene carbonate (PC):diethyl carbonate (DEC) with 10 wt.% FEC) nanoarchitectured Ge-based anodes achieved electrode capacities of ~1200 mAh g^{-1} at 1 C.[38] In both instances, lithiation referred to the sweep from 1.5 V to 0 V, while delithiation is from 0 V to 1.5 V.[29]

The galvanostatic profiles are shown in figure 4.10 for 0.5 M LiTFSI in C_4mpyrTFSI and 3 wt.% VC in 0.5 M LiTFSI in C_4mpyrTFSI. For both electrolytes, electrolyte breakdown is prevalent in the initial C-rates utilised as the lithiation profile does not tend towards 0 V, but rather sustains at potentials between 0.1 V and 0.5 V (figure 4.10(a) and (c)). At these C-rates, very little lithiation is occurring due to the need to form an SEI layer on the surface of the Ge electrode. The cell containing 3 wt.% VC showed less electrolyte breakdown than for the VC-free electrolytes, which results in the potential drop towards 0 V, and thus a higher percentage of the response is attributed to lithiation.

The 0.5 M LiTFSI in C_4mpyrTFSI galvanostatic cycling data, corresponds with the initial CV data in 0.5 M LiTFSI in C_4mpyrTFSI whereby lithiation capacities above theoretical (1874 mAh g^{-1} vs. 1624 mAh g^{-1}) were obtained (table 4.2). The stabilisation of electrode capacity, in addition to an increase in coulombic efficiency is observed in later cycles, which suggests that the SEI layer formed on the surface of Ge, therefore, allowing for just lithiation and delithiation processes to occur. At 2 C, the delithiation capacity stabilises at ~1000 mAh g^{-1}, while the lithiation capacity drops to ~1300 mAh g^{-1}. High coulombic efficiencies are obtained (>95%) for fast C-rates of 3.5 C and 5 C, however the electrode capacities are only 17% and 4% of theoretical, and therefore, would be unsuitable C-rates

to use with Ge electrodes. This low capacity can be attributed to two things, firstly continued crack formation observed within the Ge film as shown in the SEM images (figure 4.11), which led to delamination of the electrode material from the current collector with continued cycling. As less active material is present, the electrode capacity is diminished, thus resulting in low electrode capacities at 3.5 C and 5 C. This diminished active material is evidenced when the electrode capacities for the initial and final 0.15 C rates are compared. In both instances a combination of electrolyte breakdown and lithiation is observed, whereby the initial 0.15 C lithiation capacity was close to theoretical (~1624 mAh g^{-1}), while the final 0.15 C data yielded a decreased lithiation capacity of ~1580 mAh g^{-1}, thus demonstrating that less active material is present in the latter half of cycling. Secondly, the CV data demonstrated that at higher scan rates (0.5 mV s^{-1}) the CV shapes observed yielded shallow, broad peaks (figure 4.2) which were indicative that the sweep rate is too high for the electrode to fully alloy and dealloy Li, thus leading to reduced capacity values. Converting 0.5 mV s^{-1} to its equivalent C-rate of 1.2 C, it is evident to see 3.5 C and 5 C would lead to low capacities as the timescale for Li lithiation and delithiation is too short. Therefore, the limit for high C-rates is 2 C, as it offers an appreciable electrode capacity, however, further work is required to improve the coulombic efficiency.

A significant improvement was observed when 3 wt.% VC was added to 0.5 M LiTFSI in C_4mpyrTFSI. The galvanostatic cycling data shown in figure 4.10(c) tend towards 0 V for C-rates where electrolyte breakdown was occurring in 0.5 M LiTFSI in C_4mpyrTFSI (0.4 C, 0.9 C and 1 C). This highlights the benefits of adding VC to the electrolyte as it allows for quicker formation of an SEI layer, as evidenced by the higher coulombic efficiencies (~60% vs. ~30%) and higher delithiation capacities (>940 mAh g^{-1} vs. 67 mAh g^{-1}) obtained after 20 cycles. This correlates with the CV data (figure 4.6), as higher electrode capacities were attained when VC was added to the electrolyte. In addition, at high C-rates of 3.5 C and 5 C, there is a less significant drop in the capacity, as ~58% and

~26% of the theoretical capacity is maintained versus 17% and 4% for the respective C-rates in 0.5 M LiTFSI in C_4mpyrTFSI. When 0.15 C is applied after 5 C, the lithiation capacity recovers to the initial lithiation capacity, and the delithiation capacity improves to 800 mAh g^{-1}. The Ge anode in 3 wt.% VC in 0.5 M LiTFSI in C_4mpyrTFSI yields a substantial electrochemical improvement, therefore demonstrating the SEI layer improvements that can be achieved when VC is utilised with Ge anodes, whereby faster C-rates yield coulombic efficiencies up to 98%.

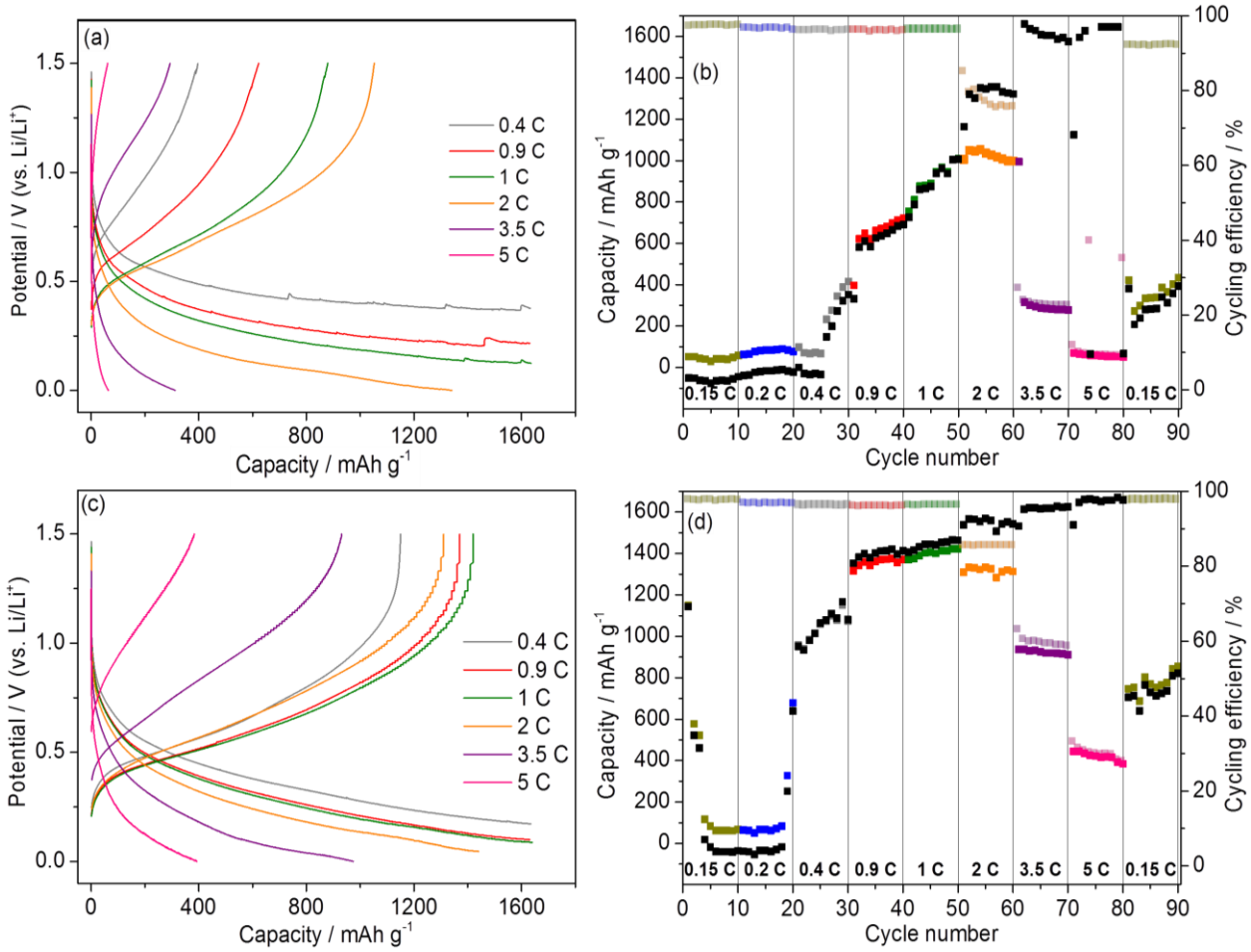

Figure 4.10: Galvanostatic cycling profiles for Ge in (a and b) 0.5 M LiTFSI in C_4mpyrTFSI, (c and d) 3% VC in 0.5 M LiTFSI in C_4mpyrTFSI electrolytes. 0.15 C and 0.2 C are not shown for data clarity as electrolyte degradation was prevalent at these C-rates.

These 3 wt.% VC in 0.5 M LiTFSI in C_4mpyrTFSI results have demonstrated better electrochemical rate performances than those in the literature where similar IL electrolytes were used: 1 M LiTFSI in

C_4mpyrTFSI and 1 M LiTFSI in C_4mpyrFSI. In this case, the Ge was electrodeposited, and the maximum electrode capacities did not exceed 600 mAh g^{-1} at 1 C.[37] At the same C-rate delithiation electrode capacities were double the literature data (~1300 mAh g^{-1}). These results are comparable to nanoarchitectured Ge-based anodes in organic electrolytes as capacities of <1200 mAh g^{-1} have been demonstrated at 1 C in 1 M $LiPF_6$ in 1:1:2 v/v/v of ethylene carbonate (EC):propylene carbonate (PC):diethyl carbonate (DEC) with 10 wt.% FEC.[38]

After cycling, post-mortem analysis was carried out using SEM to determine if Ge delamination occurred. As shown in figure 4.11, regions of heavy delamination (no Ge detected by EDX, figure 4.11(b)) are observed on the surface of the 0.5 M LiTFSI in C_4mpyrTFSI cycled electrode, with other regions exhibiting cracks (figure 4.11(a)). These results are in direct correlation with the galvanostatic data (figure 4.10(a and b)), as continued electrolyte breakdown was observed in the initial C-rates to form an SEI layer on the surface of the Ge electrode. The continuous formation of cracks within the film, and delamination of the film from the current collector would expose fresh Ge to the electrolyte, therefore requiring further electrolyte breakdown to form an SEI layer. By comparison, the 3 wt.% VC cycled Ge anode does not exhibit large regions of delamination, but rather microcracks (figure 4.11(c)), therefore demonstrating the superior film forming abilities afforded by VC.

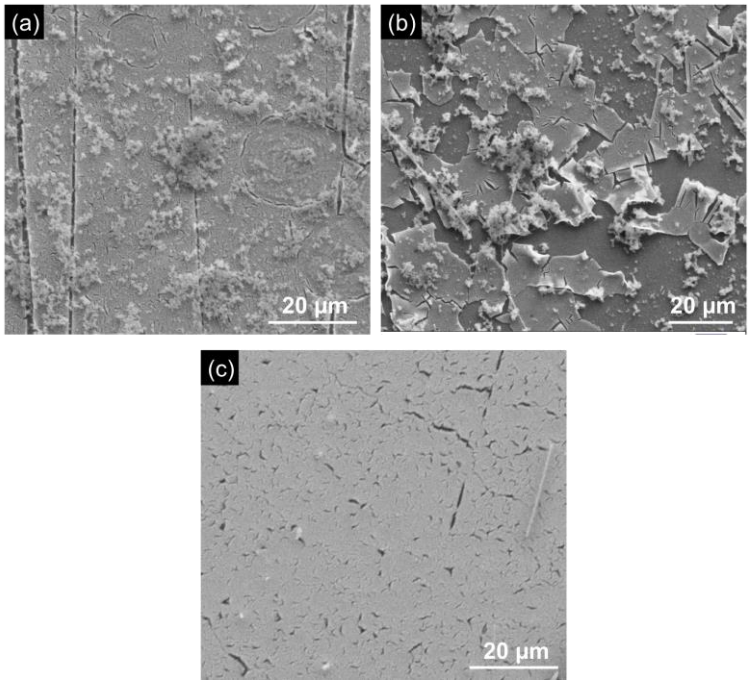

Figure 4.11: SEM micrographs of galvanostatically cycled Ge anodes after 90 cycles at various C-rates, (a and b) 0.5 M LiTFSI in C_4mpyrTFSI and (c) 3 wt.% in 0.5 M LiTFSI in C_4mpyrTFSI.

Galvanostatic cycling was carried out using a polymer gel electrolyte (PG-60) to determine if the use of a polymer gel will mitigate/buffer the expansion and contraction effects experienced by Ge upon cycling with Li, as has been suggested in the literature for other materials[17-19] such as MnO_2 based nanowire capacitors.[16] PG-60 is a polymer gel electrolyte consisting of PVDF-HFP, LiTFSI salt and C_4mpyrTFSI, where the 60 wt.% of the polymer is attributed to C_4mpyrTFSI. The polymer gel was created by drop casting the polymer as outlined in chapter 3. This process resulted in a film with a thickness of 320 µm, and the galvanostatic cycling data is shown in figure 4.12. Various C-rates were employed to determine the cyclability of the Ge with PG-60 at fast and slow rates. Figure 4.12(a) shows the initial cycles obtained for 0.15 C. No evidence of SEI layer formation is observed in the initial cycles as the potentials tend towards 0 V. This data does not correspond with the CV data obtained in figure 4.9 where a large peak corresponding to SEI layer formation is observed. During delithiation, large electrode capacities (1694 and 1809 mAh g^{-1}) are obtained in cycles 2 and 3 respectively, which suggests that a side reaction is occurring within the cell, which stabilises after the

4th cycle. This response may be attributed to a side reaction between PVDF-HFP-containing polymer gel electrolyte and Li due to the imposition of a constant current as no corresponding reaction was observed during CV analysis. During constant current analysis, the Li may co-ordinate with the polymer electrolyte, potentially to the uncoordinated TFSI anions. The co-ordination of Li with TFSI anions has been previously observed within the literature.[39] This would cause a phase transition to occur within the polymer gel electrolyte in addition to reduced Li diffusivity and lower electrode capacities in the subsequent cycles. At 0.5 mV s^{-1} (equivalent to ~1 C) electrode capacities greater than 500 mAh g^{-1} were obtained during CV analysis (figure 4.9(c)), while capacities of ~200 mAh g^{-1} are obtained at 0.9 C for galvanostatic analysis (figure 4.12 (d)). In-situ FT-IR and Raman analysis of this reaction may enable a more accurate characterisation of the reaction occurring within the cell.

From cycle 4, the system stabilises and the lithiation/delithiation profiles overlap as shown in figure. 4.12(a), suggesting the cell has stabilised. The lithiation and delithiation capacities remain stable around 900 and 850 mAh g^{-1} respectively. The average coulombic efficiency for cycles 4 to 10 is 96%. Similar stability is seen at increased C-rates as shown in figure. 4.12(b). The 0.2 C data in figure. 4.12(b), yields charge and discharge capacities of 756 and 750 mAh g^{-1} respectively, with a coulombic efficiency of 99.3%. This is further evidence that the SEI layer formed in the initial cycles has led to a stable system as demonstrated in subsequent cycles at 0.4 C and 0.9 C data as high coulombic efficiencies are observed, 99.9% and 99.7% respectively. The specific capacities decrease to approximately 210 to 220 mAh g^{-1} for both lithiation and delithiation cycles at the 0.9 C rate, and this corresponds to 13 to 14% of the theoretical capacity of Ge. This suggests that slower charge times may be suited for polymer gels of this thickness as higher capacities are obtained at 0.15 C and 0.2 C. Despite this, faster C-rates were investigated (1.8 C, 3.5 C and 5 C) followed immediately by scans at 0.15 C as shown in figure 4.12(d). The final 0.15 C cycling data is shown in figure 4.12(c). From this data, the system stability is demonstrated as there is good overlap between the initial and final

0.15 C data. Similarly, the lithiation and delithiation capacities obtained are 1094 and 890 mAh g^{-1} respectively, with an average coulombic efficiency of 83%. The lithiation/delithiation cycles demonstrate that PG-60 is capable of buffering the volumetric expansion effects experienced by Ge upon cycling with Li as high electrode capacities are recovered even after fast charge/discharge times as shown in figure 4.12(d).

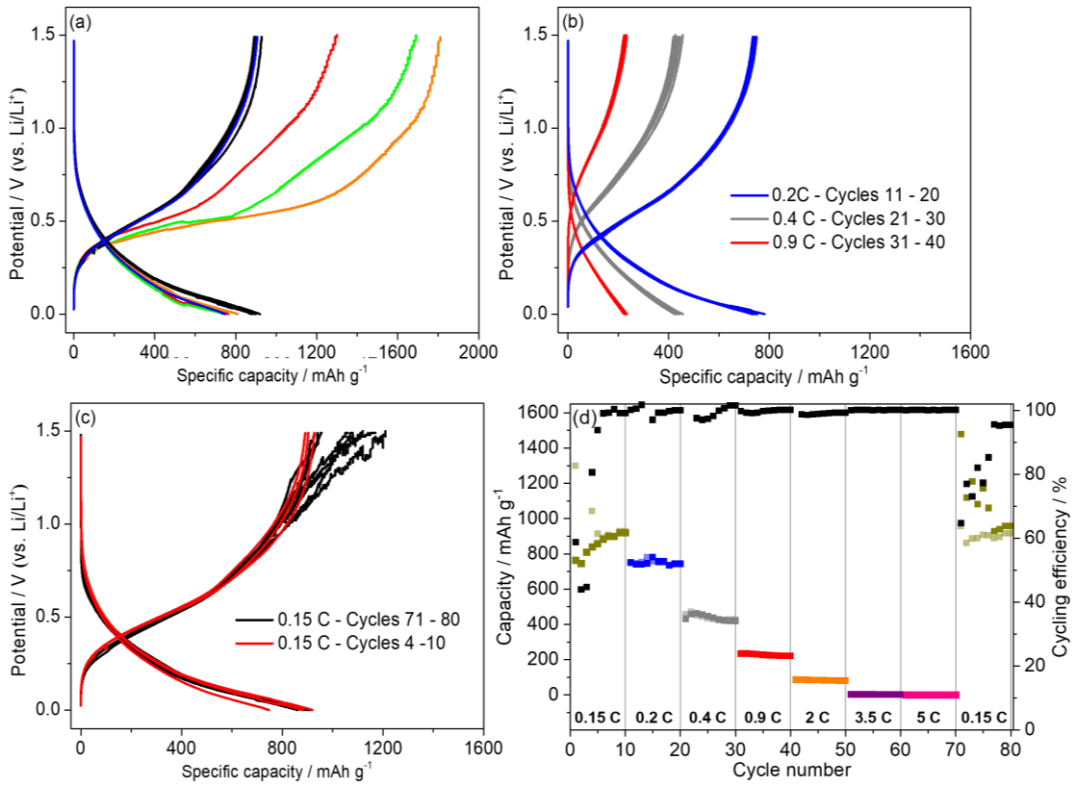

Figure 4.12: Galvanostatic cycling data obtained for 100 nm Ge with 320 µm thick PG-60, (a) initial charge/discharge cycles obtained at 0.15 C, where the red data corresponds to cycle 1, green to cycle 2, orange to cycle 3, black for cycles 4 to 9 and blue for cycle 10, (b) subsequent cycles obtained at 0.2 C (blue), 0.4 C (grey) and 0.9 C (red), (c) comparison of initial (red) and final (black) charge/discharge cycles obtained at 0.15 C, (d) capacity data at various C-rates. Reprinted with permission from McGrath et al.[36]

The Ge anode demonstrates compatibility with C_4mpyrTFSI electrolytes, whereby the polymer gel electrolyte PG-60 exhibited stable cycling with coulombic efficiencies of greater than 99% achieved

at various C-rates as shown in figure 4.12. The Ge anode in liquid based electrolyte solutions yielded varying performances, where the 3 wt.% VC in 0.5 M LiTFSI in C_4mpyrTFSI yielded the best results as high lithiation and delithiation capacities were obtained (>1200 mAh g^{-1}), where coulombic efficiencies of 97% were obtained. Based on the galvanostatic cycling data, the optimal electrolyte additive combination for the battery containing Ge anodes and C_4mpyrTFSI-based ILs can be identified as 3 wt.% VC in 0.5 M LiTFSI in C_4mpyrTFSI which is capable of fast charging and discharging, while Ge anodes with PG-60 electrolytes would be better suited for slower charging and discharging applications.

4.5 Conclusion

The ionic liquid C_4mpyrTFSI demonstrated compatibility with planar Ge electrodes as stable CV data with high electrode capacities were obtained (>600 mAh g^{-1} at 0.5 mV s^{-1}). The current densities obtained in C_4mpyrTFSI-based electrolytes were higher than those obtained within conventional organic electrolytes due to the presence of SEI layer components (Li_2CO_3, Li_2O, Li_2S, LiF, LiOH/Li_2O_2) which do not hinder Li^+ transport within the SEI layer, thus resulting in higher electrode capacities. Ge delamination from the Cu current collector was observed during SEM analysis in all liquid electrolytes, thus demonstrating the need for a polymer gel analogue. PG-60 which was synthesised and characterised in chapter 3, demonstrated exhibited electrochemical stability with a Ge electrode, whereby coulombic efficiencies greater than 95% were maintained over 90 cycles.

Galvanostatic analysis was carried out using the liquid and polymer gel forms of C_4mpyrTFSI. It was determined that the addition of 3 wt.% VC greatly improves the electrochemical performance of the Ge anode when compared to a Ge anode in 0.5 M LiTFSI in C_4mpyrTFSI as higher electrode capacities at various C-rates, for example, at 3.5 C the VC containing electrolyte achieved a discharge capacity of ~1000 mAh g^{-1} versus ~300 mAh g^{-1} for the additive-free electrolyte. These results have

been proven to be comparable to those obtained in literature by Lahiri *et al.*[37] where C_4mpyr-based IL electrolytes have been used. To the best of my knowledge, no other Ge analysis was carried out in C_4mpyr-based IL electrolytes. In addition, the results obtained are comparable to nanostructured Ge electrodes cycled in organic electrolytes[38] which demonstrates the promise of this Ge/IL combination. Galvanostatic cycling with PG-60 further demonstrated its compatibility with Ge, as coulombic efficiencies of >99% were obtained at various C-rates. Therefore, this polymer gel electrolyte is capable of buffering the expansion effects experienced by Ge and is suitable for use as a flexible, high conductivity, thermally stable electrolyte for application in Li-ion microbatteries.

References

[1] Statista, **2016,** https://www.statista.com/statistics/471264/iot-number-of-connected-devices-worldwide/.

[2] B. Laïk, I. Ressejac, C. Venet, J.-P. Pereira-Ramos, *Thin Solid Films* **2018**, *649*, 69-74 https://doi.org/10.1016/j.tsf.2018.01.033.

[3] J. Zhu, J. Jiang, Y. Feng, G. Meng, H. Ding, X. Huang, *ACS Applied Materials & Interfaces* **2013**, *5*, 2634-2640 https://doi.org/10.1021/am400055a.

[4] W. Wang, M. Tian, A. Abdulagatov, S. M. George, Y.-C. Lee, R. Yang, *Nano Letters* **2012**, *12*, 655-660 https://doi.org/10.1021/nl203434g.

[5] Y. Gogotsi, P. Simon, *Science* **2011**, *334*, 917-918 https://doi.org/10.1126/science.1213003.

[6] X. L. Wu, Y. G. Guo, L. J. Wan, *Chemistry - An Asian Journal* **2013**, *8*, 1948 https://doi.org/10.1002/asia.201300279.

[7] J. Graetz, C. C. Ahn, R. Yazami, B. Fultz, *Journal of the Electrochemical Society* **2004**, *151*, A698-A702 10.1149/1.1697412.

[8] D. Wang, Y.-L. Chang, Q. Wang, J. Cao, D. B. Farmer, R. G. Gordon, H. Dai, *Journal of the American Chemical Society* **2004**, *126*, 11602-11611 10.1021/ja047435x.

[9] L. Baggetto, R. A. H. Niessen, F. Roozeboom, P. H. L. Notten, *Advanced Functional Materials* **2008**, *18*, 1057-1066 10.1002/adfm.200701245.

[10] C.-M. Hwang, J.-W. Park, *Thin Solid Films* **2010**, *518*, 6590-6597 https://doi.org/10.1016/j.tsf.2010.03.045.

[11] C. K. Chan, X. F. Zhang, Y. Cui, *Nano Letters* **2008**, *8*, 307-309 10.1021/nl0727157.

[12] C. K. Chan, H. Peng, G. Liu, K. McIlwrath, X. F. Zhang, R. A. Huggins, Y. Cui, *Nat Nanotechnol* **2008**, *3*, 31-35 10.1038/nnano.2007.411.

[13] L. Pan, H. Wang, D. Gao, S. Chen, L. Tan, L. Li, *Chemical communications* **2014**, *50*, 5878-5880 10.1039/C4CC01728E.

[14] X. H. Liu, J. W. Wang, S. Huang, F. Fan, X. Huang, Y. Liu, S. Krylyuk, J. Yoo, S. A. Dayeh, A. V. Davydov, S. X. Mao, S. T. Picraux, S. Zhang, J. Li, T. Zhu, J. Y. Huang, *Nat Nanotechnol* **2012**, *7*, 749-756 10.1038/nnano.2012.170.

[15] W. Liang, H. Yang, F. Fan, Y. Liu, X. H. Liu, J. Y. Huang, T. Zhu, S. Zhang, *ACS Nano* **2013**, *7*, 3427-3433 10.1021/nn400330h.

[16] M. Le Thai, G. T. Chandran, R. K. Dutta, X. Li, R. M. Penner, *ACS Energy Letters* **2016**, *1*, 57-63 https://doi.org/10.1021/acsenergylett.6b00029.

[17] P. Dou, Z. Cao, J. Zheng, C. Wang, X. Xu, *Journal of Alloys and Compounds* **2016**, *685*, 690-698 https://doi.org/10.1016/j.jallcom.2016.05.218.

[18] Q. Huang, J. Song, Y. Gao, D. Wang, S. Liu, S. Peng, C. Usher, A. Goliaszewski, D. Wang, *Nature Communications* **2019**, *10*, 5586 10.1038/s41467-019-13434-5.

[19] T. Ma, X. Yu, X. Cheng, H. Li, W. Zhu, X. Qiu, *ACS Applied Materials & Interfaces* **2017**, *9*, 13247-13254 10.1021/acsami.7b03046.

[20] D. V. Sheglov, E. B. Gorokhov, V. A. Volodin, K. N. Astankova, A. V. Latyshev, *Nanotechnology* **2008**, *19*, 245302 10.1088/0957-4484/19/24/245302.

[21] C.-Y. Tsao, J. Wong, J. Huang, P. Campbell, D. Song, M. A. Green, *Applied Physics A* **2011**, *102*, 689-694 10.1007/s00339-010-5957-9.

[22] T. Halenkovič, J. Gutwirth, P. Němec, E. Baudet, M. Specht, Y. Gueguen, J.-C. Sangleboeuf, V. Nazabal, *Journal of the American Ceramic Society* **2018**, *101*, 2877-2887 10.1111/jace.15453.

[23] K. Järrendahl, I. Ivanov, J. E. Sundgren, G. Radnóczi, Z. Czigány, J. Greene, *Journal of Materials Research* **1997**, *12*, 1806-1815 10.1557/JMR.1997.0249.

[24] V. Ho, W. Choi, C. Heng, V. Ng, *Materials Physics and Mechanics* **2001**, *4*, 42-45

[25] B. Laforge, L. Levan-Jodin, R. Salot, A. Billard, *Journal of The Electrochemical Society* **2008**, *155*, A181 10.1149/1.2820666.

[26] T. Clancy, University College Cork (https://cora.ucc.ie/handle/10468/8074), **2019**.

[27] A. Wang, S. Kadam, H. Li, S. Shi, Y. Qi, *npj Computational Materials* **2018**, *4*, 15 10.1038/s41524-018-0064-0.

[28] X.-B. Cheng, R. Zhang, C.-Z. Zhao, F. Wei, J.-G. Zhang, Q. Zhang, *Advanced Science* **2015**, *3*, 1500213-1500213 10.1002/advs.201500213.

[29] A. Lahiri, N. Borisenko, A. Borodin, M. Olschewski, F. Endres, *Physical Chemistry Chemical Physics* **2016**, *18*, 5630-5637 10.1039/C5CP06184A.

[30] L. Chen, K. Wang, X. Xie, J. Xie, *Journal of Power Sources* **2007**, *174*, 538-543 10.1016/j.jpowsour.2007.06.149.

[31] K. Stokes, University of Limerick **2018**.

[32] K. Schroder, J. Alvarado, T. A. Yersak, J. Li, N. Dudney, L. J. Webb, Y. S. Meng, K. J. Stevenson, *Chemistry of Materials* **2015**, *27*, 5531-5542 10.1021/acs.chemmater.5b01627.

[33] G. M. Veith, M. Doucet, R. L. Sacci, B. Vacaliuc, J. K. Baldwin, J. F. Browning, *Scientific Reports* **2017**, *7*, 6326 10.1038/s41598-017-06555-8.

[34] A. Rezqita, M. Sauer, A. Foelske, H. Kronberger, A. Trifonova, *Electrochimica Acta* **2017**, *247*, 600-609 https://doi.org/10.1016/j.electacta.2017.06.128.

[35] A. L. Michan, B. S. Parimalam, M. Leskes, R. N. Kerber, T. Yoon, C. P. Grey, B. L. Lucht, *Chemistry of Materials* **2016**, *28*, 8149-8159 10.1021/acs.chemmater.6b02282.

[36] L. M. McGrath, J. Jones, E. Carey, J. F. Rohan, in *ChemistryOpen, Vol. 8*, **2019**, pp. 1429-1436.

[37] A. Lahiri, T. J. S. Schubert, B. Iliev, F. Endres, *Physical Chemistry Chemical Physics* **2015**, *17*, 11161-11164 10.1039/C5CP01337B.

[38] G.-H. Lee, S. Lee, C. W. Lee, C. Choi, D.-W. Kim, *Journal of Materials Chemistry A* **2016**, *4*, 1060-1067 10.1039/C5TA08806B.

[39] J.-K. Kim, L. Niedzicki, J. Scheers, C.-R. Shin, D.-H. Lim, W. Wieczorek, P. Johansson, J.-H. Ahn, A. Matic, P. Jacobsson, *Journal of Power Sources* **2013**, *224*, 93-98 https://doi.org/10.1016/j.jpowsour.2012.09.029.

Chapter 5:

Evaluation of the Crystallinity of Electrodeposited V_2O_5 as Li-ion Cathodes

5.1 Abstract

Microbattery literature primarily focuses on cobalt containing electrodes such as $LiCoO_2$ and NCM.[1] However, due to the fluctuating cost of Co, alternative materials such as vanadium oxide are being investigated. V_2O_5 is a promising cathode material with a high theoretical capacity (147 mAh g^{-1} per Li), and a variety of synthesis options. To date, V_2O_5 analysis for Li-ion applications has been reported in organic-based electrolytes,[2-7] but only one study describes the analysis with 1-propyl-1-methylpyrrolidinium bis(trifluoromethylsulfonyl)imide (C_3mpyrTFSI) ionic liquid electrolyte.[8] The results from that study showed an improved electrochemical performance of V_2O_5 in the IL when compared to a conventional organic electrolyte (1 M $LiPF_6$ in EC/DMC (1:1)).

This chapter highlights for the first time, the electrochemical performance of electrodeposited, binder-free V_2O_5 thin films with liquid and polymer gel electrolytes consisting of 1-butyl-1-methylpyrrolidinium bis(trifluoromethylsulfonyl)imide (C_4mpyrTFSI). The electrochemical performance of crystalline is shown to be superior to amorphous V_2O_5 thin films in both liquid and polymer gel electrolytes with higher coulombic efficiencies and electrode capacities obtained. The addition of vinylene carbonate (VC) facilitates the formation of a cathode electrolyte interface (CEI) layer, which stabilises the electrode/electrolyte interface, thus leading to enhanced electrochemical performances when compared to VC-free electrolytes, for example 110 mAh g^{-1} vs. 70 mAh g^{-1} at 2 C without adversely affecting the electrode kinetics.

Microbatteries typically utilise solid-state electrolytes to enable layer-by-layer fabrication, which is not possible with liquid electrolytes, therefore a polymer gel electrolyte was also investigated with the V_2O_5 electrodes. High electrode capacities of 110 mAh g^{-1} at 2 C are obtained, and these capacities are comparable with the VC-containing liquid electrolyte. Long-term cycling analysis (up to 400 cycles) was carried out both in the VC-containing and polymer gel electrolyte, whereby minimal capacity fade was demonstrated, for example 0.4% over 50 cycles at 5 C for the polymer gel electrolyte. The polymer gel option delivers the better long-term stability up to 400 cycles with lithium metal anodes with minimal capacity fade at elevated charge and discharge rates up to 5 C.

5.2 Introduction

The conceptualisation of the Internet of Things (IoT), has led to an increased demand for miniaturised IoT sensors.[9] In order to ensure autonomy, energy harvesters coupled with appropriate energy storage systems are necessary. Typical Li microbatteries utilise lithium cobalt oxide ($LiCoO_2$) cathode coupled with Li metal and a solid-state electrolyte. However, Cobalt (Co) is not an abundant material and can only be mined in a small number of global locations where the largest share (~50%) is found in the Democratic Republic of Congo.[10] This has led to price instability and a dramatic increase from ~$21,000 per metric tonne in January of 2016 to $95,307 in March of 2018, and more recently $34,500 in February 2020.[11] Therefore, researchers are investigating cathode materials that either have reduced Co content or are entirely Co-free.

Co-free materials such as vanadium pentoxide (V_2O_5), are of particular interest due to their lower cost, wider availability and higher energy density. V_2O_5 thin films can be prepared by various deposition techniques such as including sol-gel [12-14], spray pyrolysis[15-17], thermal evaporation[18-19], electron beam evaporation[20-21], pulsed laser deposition[20, 22-23], chemical vapour deposition[24-25], ion beam sputtering[26], electrodeposition[27-31] and D.C.[32-33] or R.F. sputtering.[33-40] Electrodeposition

is a well-established and relatively low cost option that is scalable to produce uniform deposits. Fabrication of thin films through electrodeposition can facilitate sequential layer build-up processes typically used in microbatteries.

To date, V_2O_5 analysis for Li-ion applications has been carried out in organic-based electrolytes,[2-7] however, the safety issues such as flammability and high volatility associated with organic based electrolytes hinder their use within microbatteries. Typical solid-state electrolytes such as LiPON have low ionic conductivities, typically 3 x10^{-3} mS cm^{-1},[41] which often result in low rate capabilities. Therefore, there is a need to assess the electrochemical performance of V_2O_5 with alternative electrolyte solutions such as ionic liquids, whose favourable properties such as high ionic conductivity and non-volatility offer a compromise between solid-state and organic electrolytes.

Chou *et al.*[8] described the electrochemical performance of different V_2O_5 morphologies with 1-propyl-1-methylpyrrolidinium bis(trifluoromethylsulfonyl)imide (C_3mpyrTFSI) ionic liquid electrolyte. The results from that study showed an improved electrochemical performance of V_2O_5 in the IL when compared to a conventional organic electrolyte (1 M $LiPF_6$ in EC/DMC (1:1)).

To the best of our knowledge there has been no V_2O_5 material research carried out using ionic liquid 1-butyl-1-methylpyrrolidinium bis(trifluoromethylsulfonyl)imide (C_4mpyrTFSI) based electrolytes. Therefore, in this study, the stability of the electrode material in the ionic liquid was investigated using CV, while galvanostatic cycling analysis was employed to determine the cycling efficiency and electrode capacity at different C-rates. The initial analysis is focused on determining whether crystalline or amorphous films are better suited for Li^+ cycling with C_4mpyrTFSI as some amorphous oxide materials have also been reported to have better electrochemical performance than their crystalline counterparts.[42] The use of a carbonate additive VC with the IL is investigated to determine if the electrochemical performance can be enhanced with the formation of a cathode electrolyte

interface (CEI) layer. The suitability of V_2O_5 electrodes in a quasi-solid-state microbattery was assessed using a polymer gel analogue. Finally, long-term cycling analysis is shown up to 400 cycles with increasing C-rates, such as 50 cycles at 5 C, with both the IL and polymer gel electrolytes to determine the long-term stability of the V_2O_5/Li metal cell.

5.3 Experimental

A stack of Ti (10 nm) and Au (100 nm) was deposited on a 1 μm thermal annealed SiO_2 layer on a 4" diameter silicon wafer using metal sputter targets (Kurt J. Lesker) in a D.C. magnetron (Quorum Q300T D) Dual sputter coating system. The Ti layer acted as an adhesion layer between the SiO_2 substrate and Au current collector. V_2O_5 was electrodeposited at room temperature using a CH Instruments 660B potentiostat. A constant potential of 2 V was applied to the Ti/Au working electrode in a three electrode setup with a saturated calomel electrode (SCE) and platinum (Pt) mesh as the reference and counter electrode, respectively. This resulted in V_2O_5 films of ~440 and ~220 nm for 20 s and 10 s deposition times respectively. The electrochemical bath was made up of a 0.25 M solution of $VOSO_4.xH_2O$, (assumed degree of hydration is 5) purchased from Sigma Aldrich, in a 1:1 (v/v) mixture of deionized water (DI) and ethanol. After deposition, some samples were heated to 325 °C for 7 hours to crystallise the V_2O_5 deposit (annealed), while other samples were dried using a N_2 gun (as-deposited).

The structure and the morphology of the samples were analysed with a Zeiss Supra 40 SEM coupled with an energy dispersive X-ray (EDX). For Raman spectroscopy a Renishaw Invia, 514 nm laser was utilised.

Electrochemical measurements of the Li^+ capacity were assessed by CV and galvanostatic cycling with potential limitation (GCPL) using a Bio-logic VSP potentiostat at various scan rates and discharge/charge currents, respectively. A three electrode pouch cell setup was utilised where 0.25

mm thick lithium foil (Sigma Aldrich) acted as counter and reference electrode. 1 cm^2 of the anode was exposed as the working electrode to the electrolyte solutions as mentioned in chapter 3. Cell assembly was carried out in an argon-filled glove box (M. Braun LABstar Glove Box) with O_2 and H_2O maintained below 0.1 ppm.

5.4 Results and discussion

The morphology of the electrodeposited V_2O_5 thin films were investigated to determine the influence of annealing at 325 °C for 7 hours to crystallise the V_2O_5 deposit (annealed), while other samples were deposited and dried using a N_2 gun (as-deposited). A low magnification (~220x and 500x) image of the annealed and as-deposited films are shown in figure 5.1(a and b). As shown, a film containing cracks is observed in both films. Utilisation of a higher magnification (~5,000x and 10,000x) (figure 5.1(c and d)) shows that the cracks are voids dispersed within the film. The voids are approximately 1.5 µm to 2 µm in width and are dispersed across the entire V_2O_5 film for both annealed and as-deposited samples. EDX analysis (figure 5.1(e and f)) confirmed that weight percentages of V and O within the in area/spectrum 1 (red box) are in agreement with theoretical weight percentages found in V_2O_5 films, where the V:O ratio is 5:2.[43] As shown in the SEM images, voids exist within the electrode, and therefore it can be considered a porous material as it has voids not occupied by the main framework of atoms[44] in this case V and O. The presence of voids within the film allows for a higher electroactive surface area, which would result in higher rate capabilities. Similar morphologies have been observed in the literature.[45]

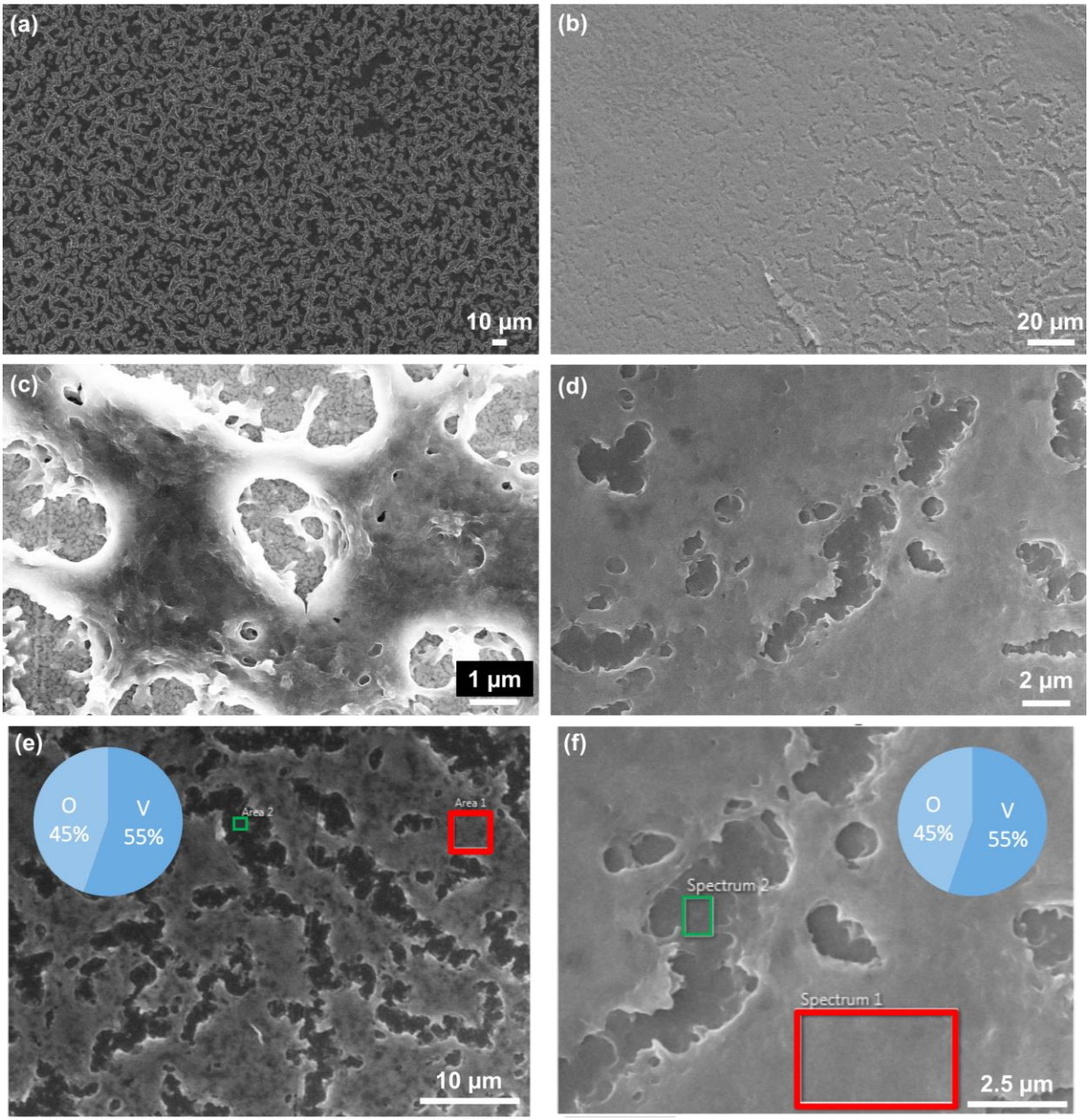

Figure 5.1: SEM micrographs of (a, c and d) annealed, and (b, d and f) as-deposited V_2O_5 thin films. EDX data obtained for (e) annealed and (f) as-deposited V_2O_5 films.

The crystallinity of the films due to annealing at 325 °C for 7 hours is confirmed by Raman spectroscopy. The as-deposited films shown in figure 5.2(c) yielded broad, low-intensity peaks, which is indicative of an amorphous film.[46-51] The peak assignments at 200 cm^{-1} and 450 cm^{-1} are attributed to the bending vibration modes of the V_3-O (triply co-ordinated oxygen), V_2-O (doubly co-

ordinated oxygen) and V=O (terminal) bonds in a disordered V-O-V framework, while the peak at 520 cm^{-1} is due to the stretching vibration modes of the V_3-O bonds in a disordered V-O-V framework.

The annealed films yielded intense, sharp well-defined peaks (figure 5.2(b)), which match the literature data for the orthorhombic phase of V_2O_5.[31, 46-47, 50] The crystal structures of V_2O_5 in the local environment and x-z projection, are shown in figure 5.2(e) and 5.2(f) respectively. The orthorhombic phase of V_2O_5 has a well-established spectrum with a space group *Pmmn* and D_{2h} point symmetry.[3, 52] There are 4 symmetry equivalent atomic positions per unit cell, and 12 symmetrical combinations can be built from the Cartesian displacement of the equivalent atoms. Six of the combinations are IR-active and six are Raman active. A_g and B_{2g} Raman modes are from the displacements of the x and z-axis while the B_{1g} and B_{3g} Raman modes come from displacement of the y-axis. In some symmetries, half the bond length is shortening and the other half is stretching so the bond stretching and shortening cancel each other out. The peaks for the annealed films correspond to in-phase stretching vibration of V=O1 bonds (993.40 cm^{-1}), anti-phase stretching of V-O2 bonds (700.90 cm^{-1}), x-axis displacements of stretching O2 atoms (524.9 cm^{-1}), bending of V-O3-V bridge angle (482.30 cm^{-1}), x-axis displacement of O1 atoms (403.70 cm^{-1}), z-axis displacements of $O2_1$ and $O2_2$ atoms (302.60 cm^{-1}), y-axis displacement of O1 atoms (283.20 cm^{-1}), x-axis displacement of V atoms (195.10 cm^{-1}), V atoms mixed signal of shear motion and rotation of the ladders, and O3-V-O2, in the y-axis (144.70 cm^{-1}), and V atom vibration in the O3-V-O2 bridge in the z-axis (103 cm^{-1}). The peaks at 195.10 cm^{-1} and 144.70 cm^{-1} correspond to the lattice vibration and are strongly associated with a layered structure.[49, 53-54] Based on the Raman spectra, the unannealed V_2O_5 thin films are amorphous with a disordered framework, while the annealed V_2O_5 thin films are crystalline with a layered structure as evidenced by the aforementioned peak assignments. In addition, Raman analysis did not detect peaks associated with VO_2 indicating that any tetravalent vanadium present is

a very small percentage which is in excellent agreement with other studies reported in the literature.[50, 55]

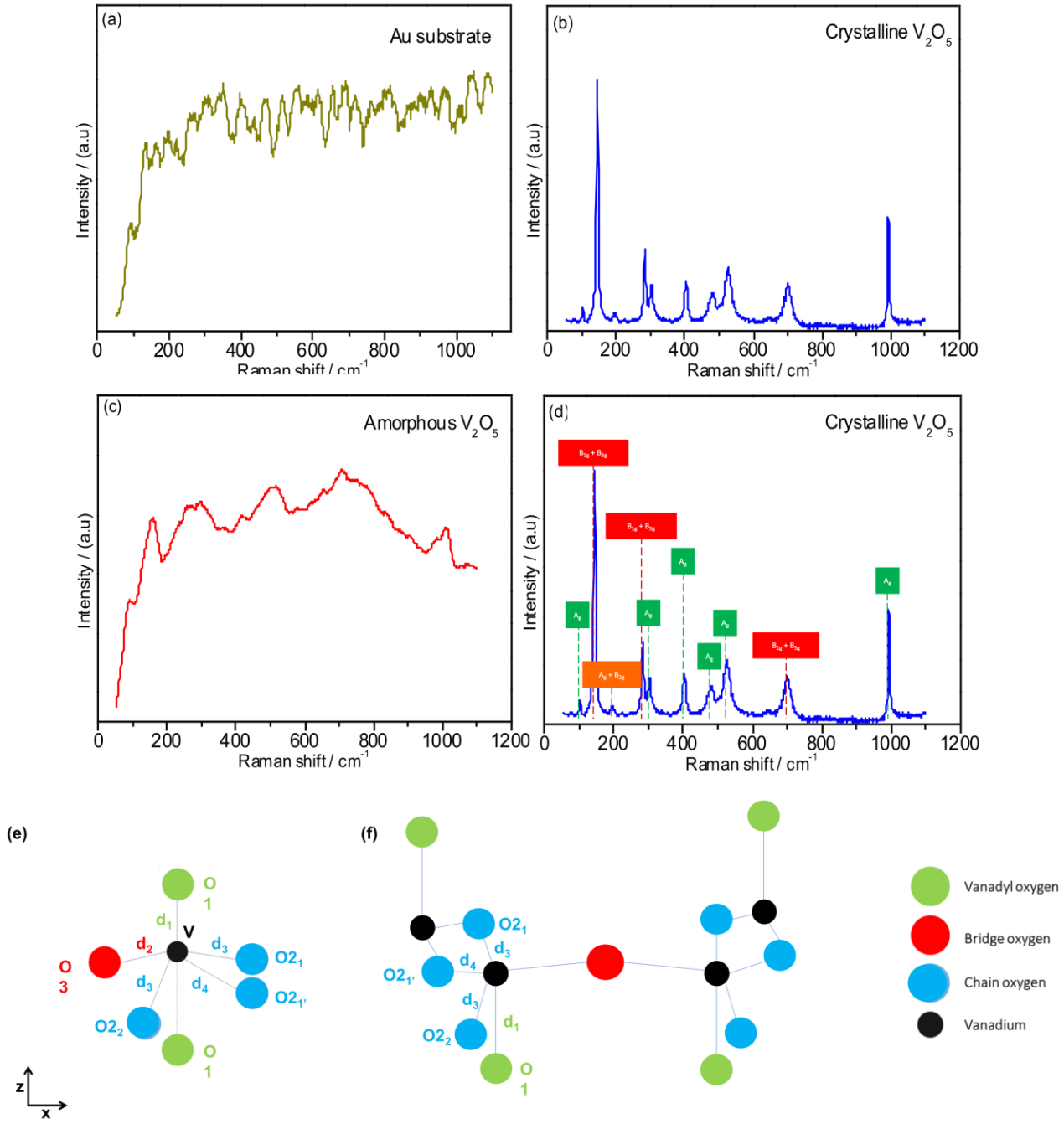

Figure 5.2: Raman spectra of (a) Au substrate, (b) crystalline V_2O_5, (c) amorphous V_2O_5 and (d) crystalline V_2O_5 with peak assignments. Crystal structure of V_2O_5 in the (e) local environment and (f) x-z projection, adapted with permission from Baddour-Hadjean et al.[3] Copyright 2020 American Chemical Society

The electrodeposition of V_2O_5 produces thin films compatible with microbattery fabrication processes. Distinct differences between the electrochemical performance of amorphous and crystalline V_2O_5 films have been previously observed for lithium based batteries in organic electrolytes.[46, 56-57] Amorphous films yielded higher electrode capacities (200 mAh g^{-1} vs. 150 mAh g^{-1} after 100 cycles at 0.1 C),[58] and thus outperformed the crystalline electrodes, however, they were more susceptible to dissolution in organic electrolytes.[59-60] Analysis of crystalline V_2O_5 electrodes in 1-propyl-1-methylpyrrolidinium bis(trifluoromethylsulfonyl)imide (C_3mpyrTFSI) yielded promising results as the IL electrolyte prevented dissolution of V_2O_5 as 50 cycles at 0.1 C were demonstrated with minimal capacity drop (0.3% per cycle).[8] Therefore, CV analysis for both amorphous and crystalline V_2O_5 electrodes was carried out to determine the stability of the V_2O_5 electrodes in ionic liquid electrolytes.

Due to the lack of long-range order in amorphous materials, no preferred ion diffusion channels exist, causing isotropic lithium diffusion.[59, 61] This results in the appearance of broad peaks, which are more indicative of pseudo-capacitive storage, where pseudo-capacitance occurs either at the particle surface or within the interlayer spacing of the material.[46, 57] Analysis of different film thicknesses (440 nm and 220 nm) yields similar CV data (figure 5.3), however, the thicker film offers a higher current density than for the thinner films (range: ~0.0075 mA cm^{-2} to -0.01 mA cm^{-2} vs. ~0.005 mA cm^{-2} to -0.006 mA cm^{-2} respectively), which is expected due to the higher material loading.

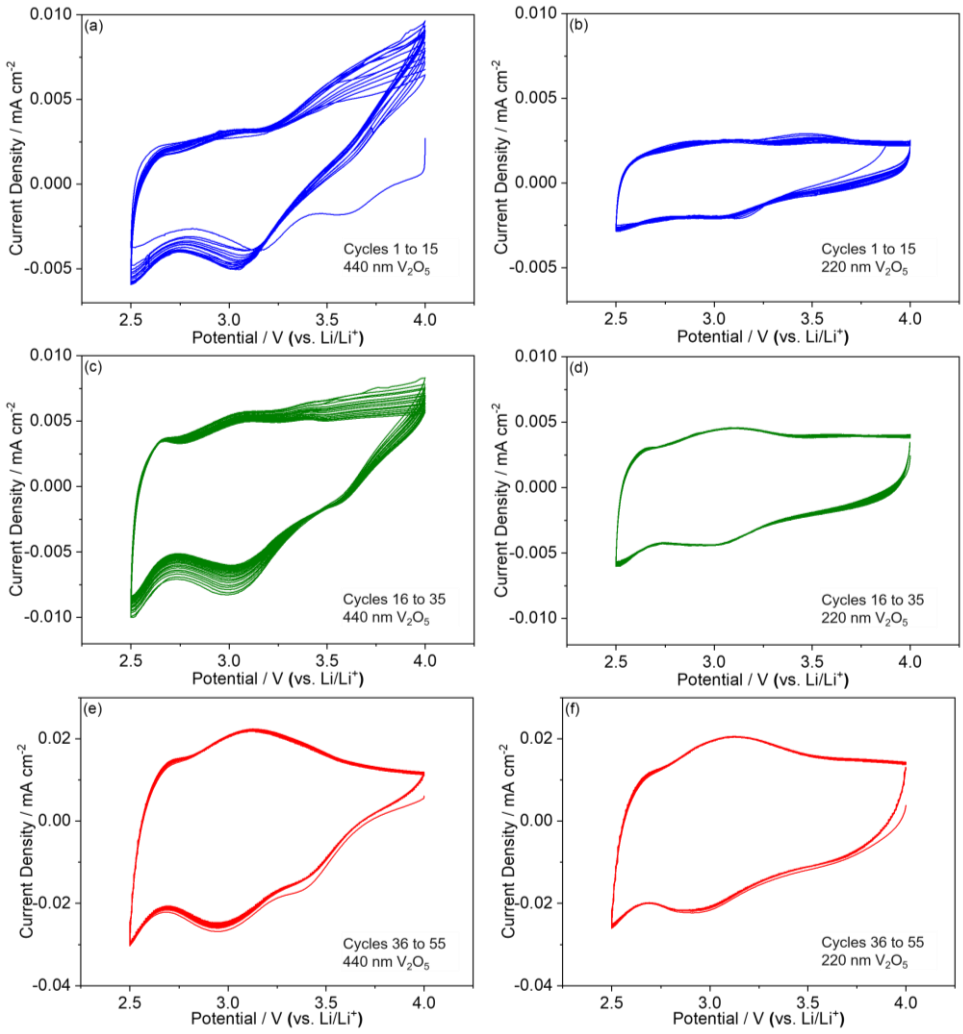

Figure 5.3: CV data for (a, c and e) ~ 440 nm and (b, d and f) ~ 220 nm amorphous V_2O_5 films where the scan rates utilised are (a and b) 0.05 mV s^{-1}, (c and d) 0.1 mV s^{-1} and (e and f) 0.5 mV s^{-1}.

In comparison, the crystalline data exhibits sharp, well-defined peaks for both film thicknesses. The peak definition is sharper in the thinner film, which is attributed to the shorter Li^+ diffusion pathways. As the scan rate is increased, the peaks broaden for both films (peak width: ~0.13 V at 0.05 mV s^{-1} to ~0.24 V at 0.5 mV s^{-1}), which suggest that the scan rate is increasingly becoming too fast to permit full Li^+ intercalation/deintercalation within the electrode, leading to lower capacity values when compared to the other scan rates. This effect is greater for the thicker film due to the longer Li^+ diffusion pathways. This is further evidenced by the peak positions as the peaks shift (50 mV to 70 mV) with increasing scan rate, thus demonstrating sluggish Li^+ intercalation/deintercalation. The

peak positions observed in figure 5.4 (intercalation peaks: 3.38 V and 3.18 V, deintercalation peaks: 3.23 V and 3.44 V) are similar to those obtained in organic electrolytes where such well-defined peaks are typically only seen for nanostructured cathode material (intercalation peaks: 3.35 V and 3.15 V, deintercalation peaks: 3.26 V and 3.47 V),[2] therefore demonstrating that the electrochemical performance of V_2O_5 with C_4mpyrTFSI electrolytes is comparable to that in organic electrolytes.

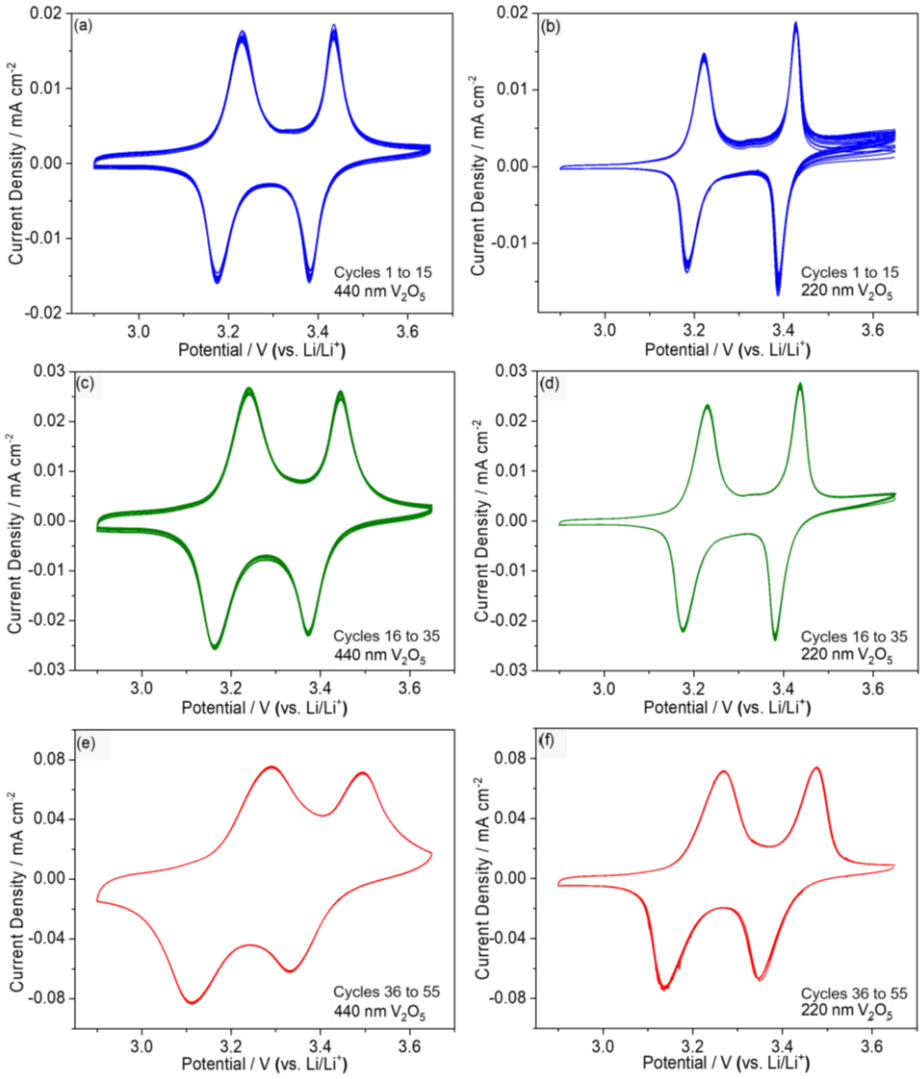

Figure 5.4: Comparison of V_2O_5 in 0.5 M LiTFSI in C_4mpyrTFSI CV data, where the scan rates utilised are (a and b) 0.05 mV s^{-1}, (c and d) 0.1 mV s^{-1} and (e and f) 0.5 mV s^{-1}.

As the 220 nm V_2O_5 films exhibited better Li diffusion than their 440 nm counterparts, only the 220 nm films were studied further. Comparing the CVs of the 220 nm V_2O_5 films, it is evident that the

current densities for the amorphous V_2O_5 are significantly lower than for the crystalline materials, which is also attributed to the isotropic Li^+ diffusion pathways.[59, 61]

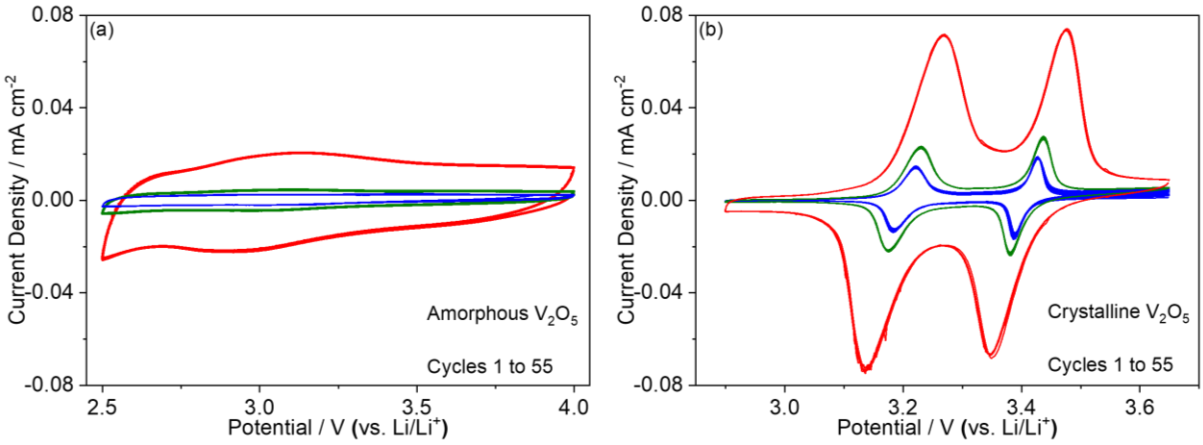

Figure 5.5: CV comparison of (a) amorphous and (b) crystalline V_2O_5 thin film electrodes in 0.5 M LiTFSI in C_4mpyrTFSI. Scan rates: 0.05 mV s^{-1} (blue), 0.1 mV s^{-1} (green) and 0.5 mV s^{-1} (red).

In addition, to get appreciable capacities cycling of amorphous films must be conducted over the potential range 2.5 to 4.0 V, while sharp very well defined peaks are observed for the crystalline material over a potential range of 2.9 to 3.6 V as shown in equations 1 to 3.[62-63]

$$V_2O_5 + xLi + xe^- \leftrightarrow \alpha Li_xV_2O_5 \quad (x < 0.13) \qquad \text{Equation 1}$$

$$V_2O_5 + xLi + xe^- \leftrightarrow \varepsilon Li_xV_2O_5 \quad (0.35 < x < 0.7) \qquad \text{Equation 2}$$

$$V_2O_5 + xLi + xe^- \leftrightarrow \delta Li_xV_2O_5 \quad (x = 1) \qquad \text{Equation 3}$$

Equations 1 and 2 refer to peaks that occur at ~3.3 V and ~3.4 V, as these peaks correspond to α/ε transitions, while ε/δ transition peaks at ~3.1 V and ~3.2 V are represented by equations 2 and 3. The peaks are identified in figure 5.6.

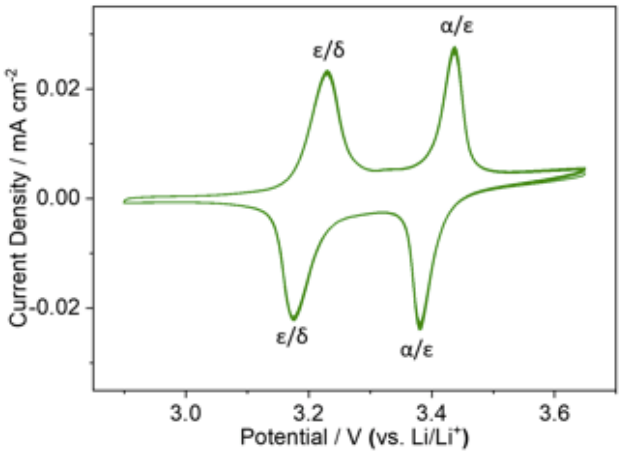

Figure 5.6: Peak identification for 220 nm V_2O_5 film.

The crystalline film exhibits greater capacity and cycling stability than the amorphous films during CV analysis as shown in the summary data of figure 5.7. The coulombic efficiencies for the crystalline material is close to 100% across all scan rates investigated up to 0.5 mV/s, which is due to high Li^+ intercalation/deintercalation reversibility as evidenced by the similar current densities in figure 5.5(b). The crystalline materials results in observed electrode capacities close to theoretical for both intercalation and deintercalation (~140 mAh g^{-1} at 0.05 mV s^{-1}, theoretical: 147 mAh g^{-1}). As shown in figure 5.7 the amorphous electrode exhibits low capacity and poor reversibility with significant capacity loss on cycling except at the slowest scan rate which still only achieved 80 mAh g^{-1}. The results indicate that the low electrical conductivity of the film (1.17 x10^{-3} S cm^{-1})[64] does not affect the electrochemical performance of the crystalline V_2O_5, as the average lithium ion diffusion coefficient calculated for the crystalline V_2O_5 was determined to be 7.83 x10^{-10} cm^2 s^{-1} for the 220 nm films which also compares very favourably with oxide materials typically utilised.[65] The sharp peaks in the voltammograms recorded at relatively high rates (0.5 mV s^{-1} over 600 mV) which approximates to a 3 C-rate further indicates the material is not complicated by low electronic conductivity.

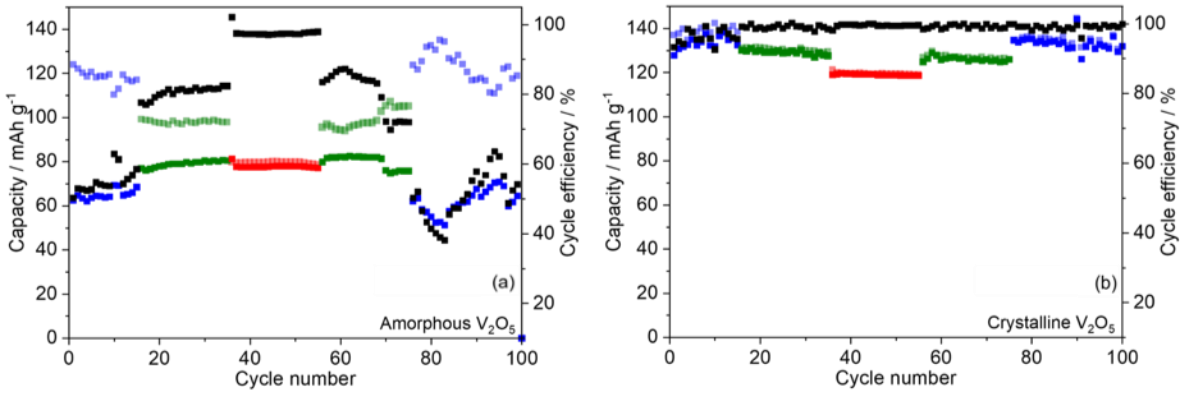

Figure 5.7: Comparison of electrode capacities and coulombic efficiencies (black) at various scan rates for (a) amorphous and (b) crystalline V_2O_5 thin film electrodes in 0.5 M LiTFSI in C_4mpyrTFSI. Scan rates: 0.05 mV s^{-1} (blue), 0.1 mV s^{-1} (green) and 0.5 mV s^{-1} (red).

The performance of the V_2O_5 films was analysed in electrolytes with additives (VC and FEC) and compared to its performance in 0.5 M LiTFSI in C_4mpyrTFSI. From the electrochemical data in figure 5.8, clearly defined peaks are observed for both VC and FEC additives in C_4mpyrTFSI, which, is similar to the 0.5 M LiTFSI in C_4mpyrTFSI data. Ordinarily, the peak positions for Li intercalation occur at ~3.35 V and 3.15 V in organic electrolytes,[2] and these peak positions have also been demonstrated within 0.5 M LiTFSI in C_4mpyrTFSI electrolytes (3.38 V and 3.18 V). The initial cycles for the V_2O_5 electrode cycled in VC additive electrolytes show a shift in the peak potentials (e.g. intercalation: from 3.33 V to 3.28 V, and from 3.14 V to 3.07 V) where the red line is the initial cycle, and the grey lines are the subsequent cycles before cell stabilisation. When 3 wt.% VC is added to the electrolyte (figure 5.8(b)), the Li intercalation occurs at 3.28 V and 3.07 V, which is 100 mV more negative than the additive free electrolyte. Once this potential is reached (blue data), stable cycling is observed as overlapping CV data is observed. The shift in the electrode potential may be attributed to the formation of an SEI layer on the surface of V_2O_5, as such a layer has been observed with other cathode materials such as $LiNi_{0.5}Mn_{0.3}Co_{0.2}O_2$ (NMC) when VC additives are utilised.[66] In contrast

the 3 wt.% FEC-containing electrolyte yield similar peak positions (intercalation peaks: 3.38 V and 3.18 V, deintercalation peaks: 3.23 V and 3.44 V) to those observed in the additive free electrolyte (intercalation peaks: 3.38 V and 3.18 V, deintercalation peaks: 3.23 V and 3.44 V), thus demonstrating that the addition of FEC does not affect the electrochemical performance of the electrode.

At higher scan rates, the 3 wt.% VC containing electrolyte yields peak currents which differ by 100 mV when compared to 3 wt.% FEC containing electrolytes for both Li^+ intercalation and deintercalation. This indicates that the addition of 3 wt.% VC leads to an increased resistance which leads to sluggish Li^+ diffusion, and therefore a later onset of Li^+ intercalation and deintercalation, which affects the peak separation (discussed below). However, despite this, the current densities achieved by the additive containing electrolytes are similar at each scan rate (FEC: 0.17 mA cm^{-2} vs. VC: 0.17 mA cm^{-2} at 0.1 mV s^{-1}). The current densities are lower than those obtained by the additive free electrolyte, at 0.5 mV s^{-1} the current density achieved by the additive containing electrolytes is approximately half that obtained in the additive free electrolyte (~0.045 mA cm^{-2} vs. ~0.08 mA cm^{-2}).

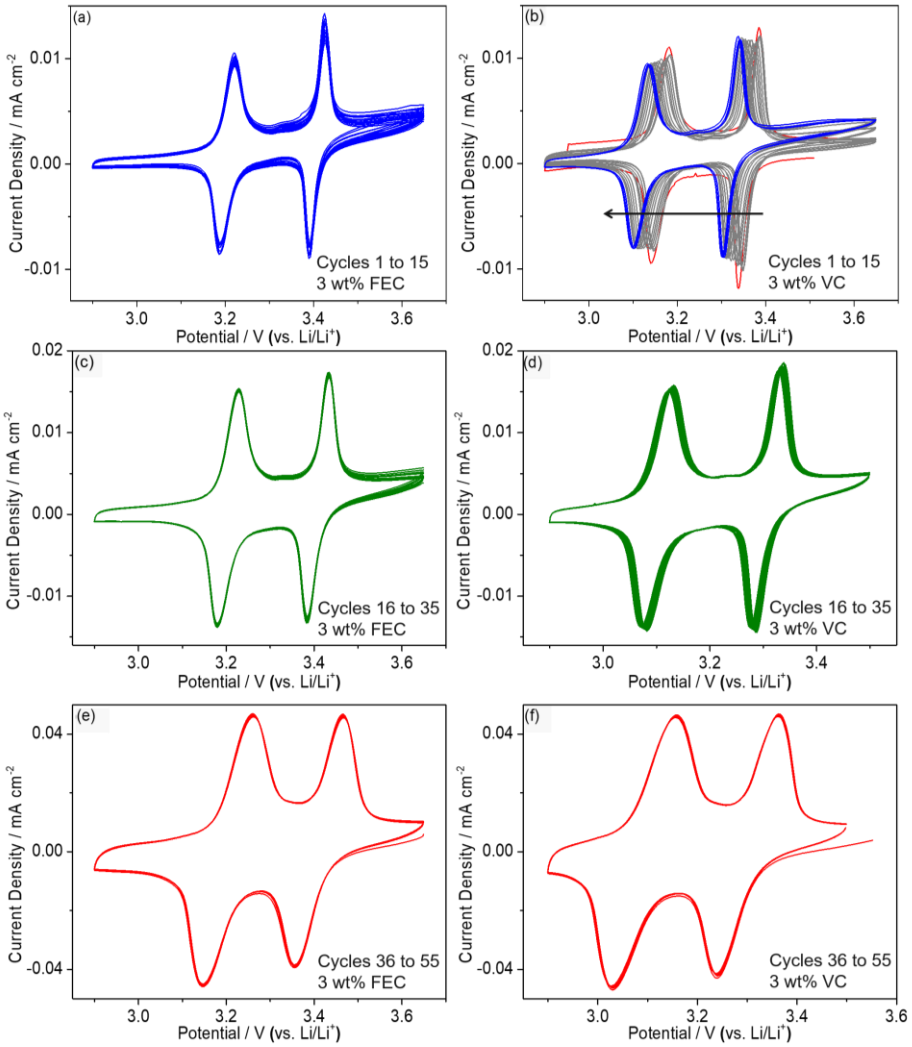

Figure 5.8: Comparison of 220 nm crystalline V_2O_5 in (a, c and e) 3 wt.% FEC in 0.5 M LiTFSI in C_4mpyrTFSI and (b, d and f) 3 wt.% VC in 0.5 M LiTFSI in C_4mpyrTFSI CV data, where the scan rates utilised are (a and b) 0.05 mV s^{-1}, (c and d) 0.1 mV s^{-1} and (e and f) 0.5 mV s^{-1}.

Lower electrode capacities were obtained for the V_2O_5 electrodes in the electrolytes with additives (FEC: 82 mAh g^{-1} and VC: 79 mAh g^{-1} at 0.5 mV s^{-1}), when compared to V_2O_5 in 0.5 M LiTFSI in C_4mpyrTFSI (119 mAh g^{-1} at 0.5 mV s^{-1}) as shown in figure 5.9. This is attributed to the lower current densities which were obtained when additives were added to the electrolyte, approximately half the current density obtained in the 0.5 M LiTFSI in C_4mpyrTFSI electrolyte, which would result in lower

capacities. High coulombic efficiencies of greater than 99% is noted in all three electrolytes which demonstrates the compatibility of the ionic liquid with V_2O_5 electrodes.

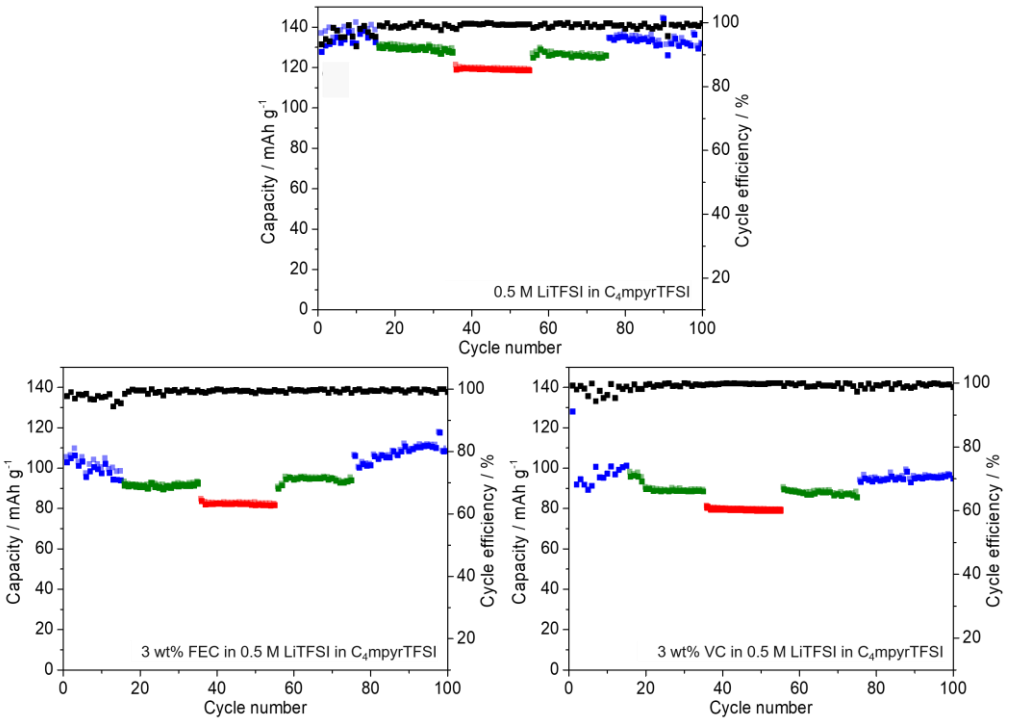

Figure 5.9: Comparison of the 220 nm crystalline V_2O_5 electrode capacities obtained during CV analysis. The scan rates used were 0.05 mV s^{-1} (blue), 0.1 mV s^{-1} (green) and 0.5 mV s^{-1} (red), where the coulombic efficiency is represented in black.

In order to determine the electrochemical performance of the V_2O_5 electrodes both in amorphous and crystalline forms at different C-rates, galvanostatic cycling was employed. This analysis will highlight their potential performance within a full cell, as their rate capabilities will be tested, in addition to their long term cyclability. The crystalline film exhibits the typical step profile as shown in figure 4 which is attributed to the various phase changes V_2O_5 undergoes during cycling with Li^+, while no plateau was observed in the amorphous films (figure 5.10). The linear curves without a clearly defined plateau is indicative of pseudo-capacitor behaviour,[67] which correlates well with the CV results.

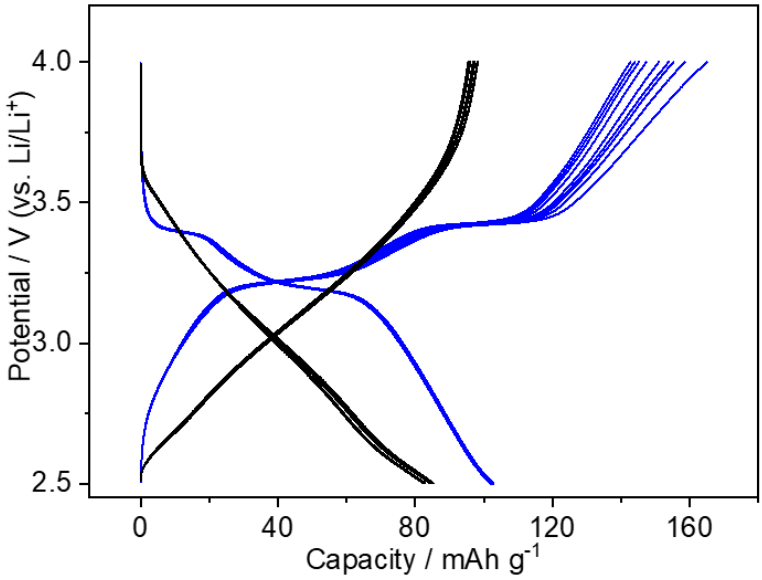

Figure 5.10: Galvanostatic profiles for cycles 1 to 10 for crystalline (blue) and amorphous (black) V_2O_5 thin films at 0.2 C in 0.5 M LiTFSI in C_4mpyrTFSI.

As demonstrated in figure 5.10, the crystalline V_2O_5 electrode exhibits excess capacity in the initial cycles due to the formation of a cathode electrolyte interface (CEI) layer. This results in low coulombic efficiencies in the initial scans. Coating cathode materials with ex-situ protective layers such as Al_2O_3 have yielded improved electrochemical performances in the literature.[68-69] An alternative to this coating is the utilisation of carbonate additives which form stable electrolyte interfaces in organic solvents early on in the cycling process. Despite the poor electrochemical performance during CV analysis, vinylene carbonate (VC) was investigated to determine its ability to form a stable electrode/electrolyte interface in this ionic liquid based electrolyte.

The electrode kinetics of the crystalline materials was investigated to determine if they change upon addition of VC within the electrolyte. Initially the peak separation for both the ε/δ and α/ε phases is investigated, and it was determined that the separations are similar in both electrolytes as shown in table 5.1. This indicates that the rates of Li^+ intercalation and deintercalation are similar. The diffusive and non-diffusive contributions (b-value) are compared for both electrolytes. The contribution from

the diffusion and non-diffusion controlled kinetics can be quantified as the measured current (i) at a fixed potential (V) where the current is a combination of the two kinetic regimes, equation 4. The equation is rearranged to a line equation (equation 5) where k_1 is equal to the slope and k_2 is equal to the intercept when $\frac{i}{\sqrt{v}}$ is plotted against $\sqrt{v}$. The percentage contribution of diffusion and non-diffusion controlled kinetics is calculated using equations 6 and 7, respectively.[65, 70]

$$i = k_1 v + k_2 v^{0.5} \quad \text{Equation 4}$$

$$\frac{i}{v^{0.5}} = k_1 v^{0.5} + k_2 \quad \text{Equation 5}$$

$$Diffusion\ controlled = \frac{k_2 v^{0.5}}{k_1 v + k_2 v^{0.5}} \quad \text{Equation 6}$$

$$Non-diffusion\ controlled = \frac{k_1 v}{k_1 v + k_2 v^{0.5}} \quad \text{Equation 7}$$

The corresponding b values for the VC-free electrolyte both the ε/δ and α/ε phases are ~0.75 and ~0.65 respectively. From this data it is evident that non-diffusion controlled kinetics is having an influence in the reaction as the value is higher than 0.5 which is attributed to diffusion controlled reactions solely. The non-diffusion controlled contribution increases from ~17% to ~62% as the scan rates increase from 0.05 mV s^{-1} to 0.5 mV s^{-1}. This increase is expected with phase changes as this can expose metal ions within the bulk to the outer surface and promote intercalation that is not diffusion controlled.[71] Similar b-values are obtained for the VC-containing electrolyte as shown in table 5.1, which indicates that the electrode kinetics are not significantly impacted by the addition of VC.

Scan rate (mV s^{-1})	0.5 M LiTFSI in C_4mpyrTFSI		3 wt.% VC in 0.5 M LiTFSI in C_4mpyrTFSI	
	Peak separation (mV)			
	ε/δ	α/ε	ε/δ	α/ε
0.05	36	39	37	42
0.1	54	55	50	50
0.5	132	132	131	125
b value	0.75	0.65	0.72	0.66

Table 5.1: Comparison of the peak separation between the ε/δ and α/ε phases, and b values in various electrolytes.

When the galvanostatic cycling performances are compared between the VC-free and VC-containing electrolytes, it is evident that the electrochemical performance of the crystalline material is enhanced as shown in figure 5.11. In figure 5.11(b), the electrode capacities are close to theoretical at 0.2 C, and more stable cycling is observed. This results in higher electrode capacities (VC-free: ~90 mAh g^{-1} vs. VC-containing: ~ 120 mAh g^{-1} at 0.75 C) and coulombic efficiencies (VC-free: ~93% vs. VC-containing ~97%) due to the reduced need for electrolyte breakdown, and thus a more stable interface.

As observed in figure 5.10, the amorphous electrodes yield lower electrode capacities than their crystalline counterparts in 0.5 M LiTFSI in C_4mpyrTFSI and a similar trend is observed when utilised in VC-containing electrolytes. At low C-rates such as 0.2 C, intercalation capacities exceed theoretical, whereby coulombic efficiencies are less than 60% which is in stark contrast with the values obtained in figure 5.11(b). At higher C-rates such as 3.5 C, the electrode capacities for the amorphous films are approximately 20 mAh g^{-1} lower than the crystalline materials (80 mAh g^{-1} vs. 100 mAh g^{-1}). Overall, the crystalline data shows greater electrode capacities in addition to better coulombic efficiencies across all C-rates when compared to the amorphous electrode in 3 wt.% VC

in 0.5 M LiTFSI in C_4mpyrTFSI. (5 C: 95 mAh g^{-1} and 99.7% vs. 73 mAh g^{-1} and 99%). The charge and discharge capacities of the crystalline data are 93% and 88% of the theoretical capacity at 0.2 C, even at 10 C the specific capacity is 52% of the theoretical (76 mAh g^{-1}), with a coulombic efficiency of 99.9%, which demonstrates the compatibility of the electrolyte with the crystalline V_2O_5.

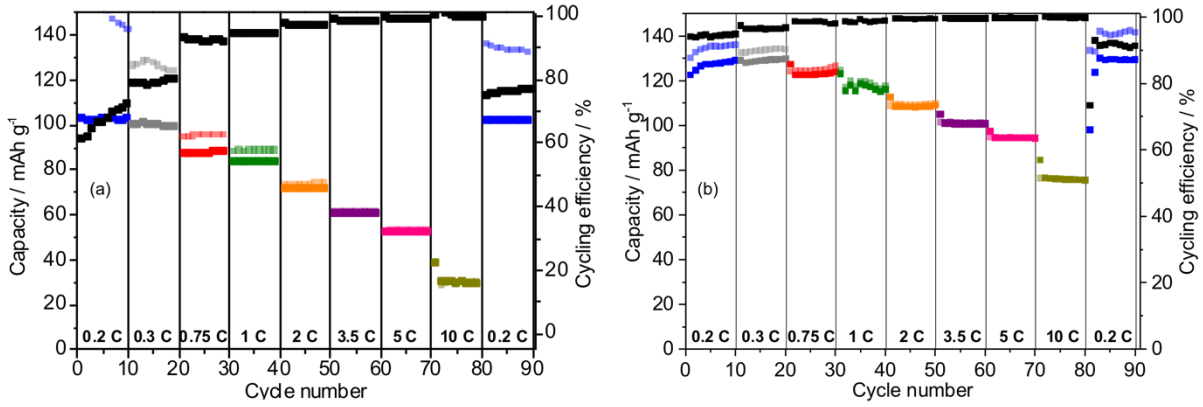

Figure 5.11: Comparison of crystalline electrode capacities and coulombic efficiencies (black) at various C-rates, where electrolytes used are (a) 0.5 M LiTFSI in C_4mpyrTFSI and (b) 3 wt.% VC in 0.5 M LiTFSI in C_4mpyrTFSI.

Microbatteries typically utilise a solid-state electrolyte which enables sequential layer build-up of thin film materials. Crystalline and amorphous V_2O_5 electrode were analysed with a quasi-solid-state polymer gel electrolyte containing the pyrrolidinium ionic liquid C_4mpyrTFSI, PVDF-HFP, and LiTFSI salt, where C_4mpyrTFSI accounted for 60% of the polymers weight. Once the solvent evaporated from the polymer film after solvent casting, no further post processing was required, unlike similar membranes in the literature where the polymer membrane required soaking in the electrolyte.[72] This thin film polymer gel has an ionic conductivity of 1.9 mS cm^{-1} which is higher than its liquid analogue: 0.5 M LiTFSI in C_4mpyrTFSI (1.5 mS cm^{-1}).[73] Figure 5.12 provides further evidence of crystalline V_2O_5 compatibility with ionic liquid electrolytes, particularly its polymer gel analogue. Similar to the liquid electrolytes the crystalline V_2O_5 exhibits higher electrode capacities when compared to amorphous V_2O_5 materials, 131 mAh g^{-1} versus 81 mAh g^{-1} at 0.3 C respectively.

The coulombic efficiencies were above 90% for all C-rates for both crystalline and amorphous materials. This is not observed in the liquid electrolytes, which highlights an improved electrode/electrolyte interface. The electrode capacities obtained for the crystalline V_2O_5 films are similar to those obtained with 3 wt.% VC in 0.5 M C_4mpyrTFSI. Again, the amorphous film exhibited poor performance with electrode capacity fading rapidly with less than half the capacity of the crystalline material at the 1 C rate.

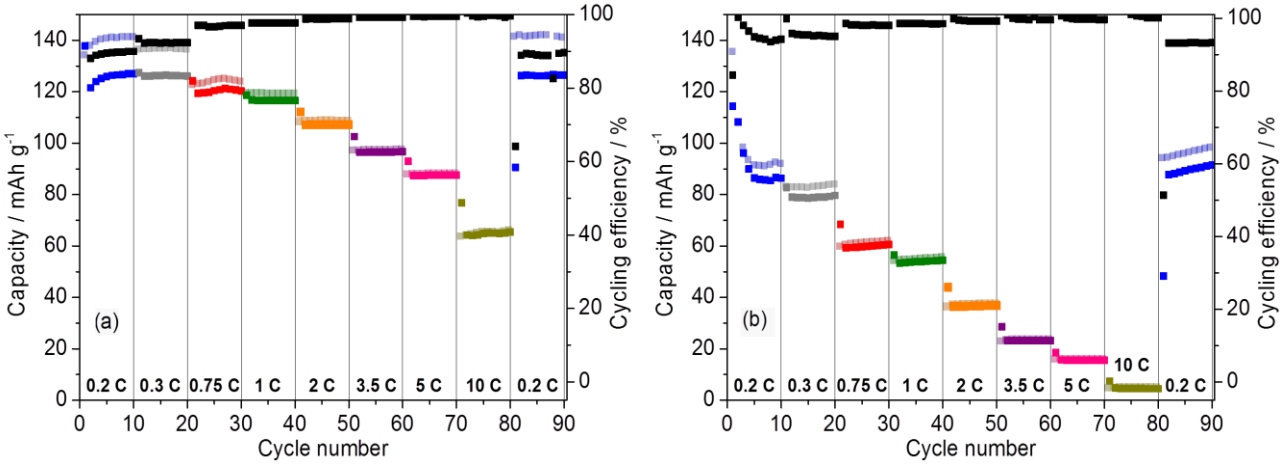

Figure 5.12: Comparison of electrode capacities and coulombic efficiencies (black) for (a) crystalline and (b) amorphous V_2O_5 thin films. Electrolyte: PG-60.

Due to the improved electrochemical performances of the crystalline V_2O_5 electrodes with the PG-60 electrolyte and 3 wt.% VC-containing electrolytes, long-term cycling was carried out. Both electrodes underwent the same C-rate analysis described above for figures 5.11 and 5.12, and then 50 cycles at various C-rates were analysed up to a total of 400 cycles as shown in figure 5.13. The crystalline V_2O_5 gave similar capacity values when cycled in the polymer gel and ionic liquid versions of the electrolyte, e.g. 110 mAh g^{-1} at 2 C. PG-60 exhibits the better long-term cycling as the electrode capacity had minimal fade (figure 5.13(b)), when compared to 3 wt.% VC in 0.5 M LiTFSI in C_4mpyrTFSI (0.4% vs. 2.9% over 50 cycles at 5 C). In addition, the final 0.2 C capacity is recovered in the PG-60 test to ~125 mAh g^{-1} after cycling at 5 C. This demonstrates that fast cycling does not lead to electrode deterioration as the final capacity matches the initial value at the 0.2 C rate. These

results demonstrate that the polymer gel is a good option for thin film semi-solid electrolytes without compromising on electrode performance. After cycling SEM, EDX and Raman analysis was carried out and compared to the results shown in figure 5.1. The SEM, EDX and Raman data acquired before and after cycling were identical, thus indicating no change in the films. It also indicates that lithium metal anodes can be used for long term cycling without capacity fade or short circuits developing in either the VC containing IL or the polymer gel analogue.

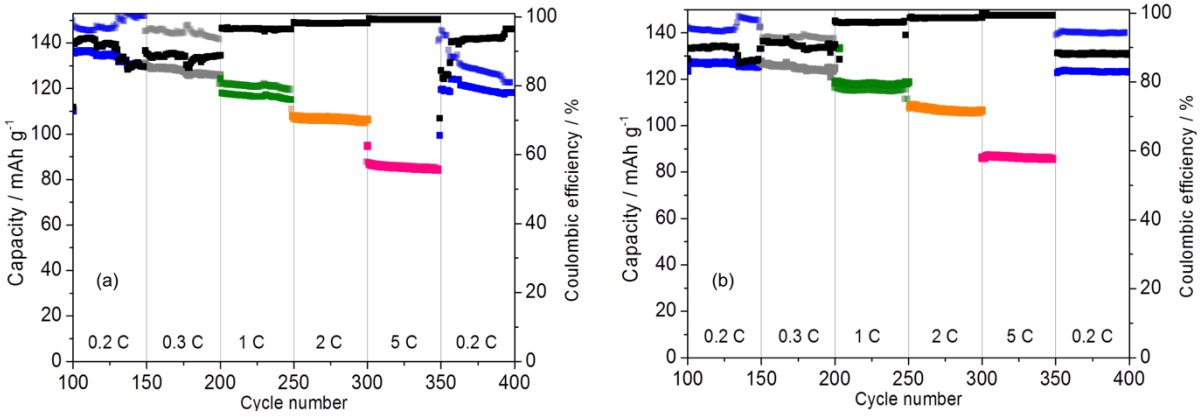

Figure 5.13: Comparison of electrode capacities and coulombic efficiencies (black) at various C-rates for crystalline V_2O_5 electrodes in (a) 3 wt.% VC in 0.5 M LiTFSI in C_4mpyrTFSI and (b) PG-60.

5.5 Conclusion

Cyclic voltammetry (CV) analysis of crystalline V_2O_5 yields coulombic efficiencies >99%, where high electrode capacities >120 mAh g^{-1} are obtained. This data has not been previously reported in the literature with C_4mpyrTFSI-based electrolytes. The electrodeposited V_2O_5 thin films produce sharp well-defined intercalation and deintercalation peaks in C_4mpyrTFSI, unlike the broad pseudo-capacitive-like peaks in C_3mpyrTFSI previously reported in the literature. In addition, the peak positions obtained in C_4mpyrTFSI are comparable with those obtained at nanostructured V_2O_5 in organic electrolytes demonstrating similar electrochemical performances. The formation of a cathode electrolyte interface (CEI) layer, facilitated by the introduction of VC additive, enabled higher electrode capacities during galvanostatic cycling than for the additive free electrolyte, for example ~ 120 mAh g^{-1} vs. ~90 mAh g^{-1} at 0.75 C. These results give insight into the electrochemical performance of V_2O_5 with liquid C_4mpyr-based IL electrolytes, whereby the utilisation of a suitable additive reduces the need to coat cathode materials with protective nanoscale layers such as Al_2O_3, which oftentimes are electrical insulators.

Crystalline V_2O_5 cycling with polymer gel electrolyte suited for layer-by-layer microbattery fabrication yields electrode capacities (110 mAh g^{-1} at 2 C) similar to those obtained in liquid electrolytes. Stable long-term cycling with minimal capacity fade at high C-rates is observed in the polymer gel electrolyte, for example 0.4% over 50 cycles at 5 C. In addition, the final 0.2 C capacity is recovered in the PG-60 test to ~125 mAh g^{-1} after cycling at 5 C. These results also indicate that lithium metal anodes can be used for long term cycling without capacity fade or short circuits developing in either the VC containing IL or the polymer gel analogue. The fabrication options described in this work for V_2O_5 with the polymer gel electrolyte and lithium metal anodes could realise all-solid-state Li microbatteries for long-life IoT sensors.

References

[1] S. Randau, D. A. Weber, O. Kötz, R. Koerver, P. Braun, A. Weber, E. Ivers-Tiffée, T. Adermann, J. Kulisch, W. G. Zeier, F. H. Richter, J. Janek, *Nature Energy* **2020**, *5*, 259-270 10.1038/s41560-020-0565-1.

[2] Y. L. Cheah, V. Aravindan, S. Madhavi, *ACS Applied Materials & Interfaces* **2013**, *5*, 3475-3480 10.1021/am400666n.

[3] R. Baddour-Hadjean, J. P. Pereira-Ramos, C. Navone, M. Smirnov, *Chemistry of Materials* **2008**, *20*, 1916-1923 10.1021/cm702979k.

[4] A. Benayad, H. Martinez, A. Gies, B. Pecquenard, A. Levasseur, D. Gonbeau, *Journal of Electron Spectroscopy and Related Phenomena* **2006**, *150*, 1-10 https://doi.org/10.1016/j.elspec.2005.09.001.

[5] J. Światowska-Mrowiecka, V. Maurice, S. Zanna, L. Klein, P. Marcus, *Electrochimica Acta* **2007**, *52*, 5644-5653 https://doi.org/10.1016/j.electacta.2006.12.050.

[6] H.-g. Wang, D.-l. Ma, Y. Huang, X.-b. Zhang, *Chemistry – A European Journal* **2012**, *18*, 8987-8993 10.1002/chem.201200434.

[7] B. Yan, X. Li, Z. Bai, Y. Zhao, L. Dong, X. Song, D. Li, C. Langford, X. Sun, *Nano Energy* **2016**, *24*, 32-44 https://doi.org/10.1016/j.nanoen.2016.04.002.

[8] S.-L. Chou, J.-Z. Wang, J.-Z. Sun, D. Wexler, M. Forsyth, H.-K. Liu, D. R. MacFarlane, S.-X. Dou, *Chemistry of Materials* **2008**, *20*, 7044-7051 10.1021/cm801468q.

[9] Statista, **2016,** https://www.statista.com/statistics/471264/iot-number-of-connected-devices-worldwide/.

[10] P. Barrera, **2019,** https://investingnews.com/daily/resource-investing/battery-metals-investing/cobalt-investing/cobalt-producer-cobalt-reserves/.

[11] T. Economics, **2020,** https://tradingeconomics.com/commodity/cobalt.

[12] D. Liu, Y. Liu, B. B. Garcia, Q. Zhang, A. Pan, Y. H. Jeong, G. Cao, *Journal of Materials Chemistry* **2009**, *19*, 8789-8795 10.1039/b914436f.

[13] D. Yu, C. Chen, S. Xie, Y. Liu, K. Park, X. Zhou, Q. Zhang, J. Li, G. Cao, *Energy and Environmental Science* **2011**, *4*, 858-861 10.1039/c0ee00313a.

[14] Y. Shimizu, K. Nagase, N. Miura, N. Yamazoe, *Solid State Ionics* **1992**, *53-56*, 490-495 https://doi.org/10.1016/0167-2738(92)90419-P.

[15] A. A. Akl, *Journal of Physics and Chemistry of Solids* **2010**, *71*, 223-229 10.1016/j.jpcs.2009.11.009.

[16] A. Bouzidi, N. Benramdane, A. Nakrela, C. Mathieu, B. Khelifa, R. Desfeux, A. Da Costa, *Materials Science and Engineering: B* **2002**, *95*, 141-147 https://doi.org/10.1016/S0921-5107(02)00224-6.

[17] L. Boudaoud, N. Benramdane, R. Desfeux, B. Khelifa, C. Mathieu, *Catalysis Today* **2006**, *113*, 230-234 https://doi.org/10.1016/j.cattod.2005.11.072.

[18] X. Wu, F. Lai, L. Lin, Y. Li, L. Lin, Y. Qu, Z. Huang, *Applied Surface Science* **2008**, *255*, 2840-2844 10.1016/j.apsusc.2008.08.048.

[19] K.-C. Cheng, F.-R. Chen, J.-J. Kai, *Solar Energy Materials and Solar Cells* **2006**, *90*, 1156-1165 https://doi.org/10.1016/j.solmat.2005.07.006.

[20] C. V. Ramana, O. M. Hussain, B. S. Naidu, C. Julien, M. Balkanski, *Materials Science and Engineering B* **1998**, *52*, 32-39 10.1016/S0921-5107(97)00273-0.

[21] C. V. Ramana, O. M. Hussain, B. S. Naidu, *Materials Chemistry and Physics* **1997**, *50*, 195-199 https://doi.org/10.1016/S0254-0584(97)01914-7.

[22] R. Teghil, L. D'Alessio, A. De Bonis, A. Galasso, N. Ibris, A. M. Salvi, A. Santagata, P. Villani, *Journal of Physical Chemistry A* **2009**, *113*, 14969-14974 10.1021/jp9050947.

[23] C. Julien, E. Haro-Poniatowski, M. A. Camacho-López, L. Escobar-Alarcón, J. Jímenez-Jarquín, *Materials Science and Engineering: B* **1999**, *65*, 170-176 https://doi.org/10.1016/S0921-5107(99)00187-7.

[24] H. Groult, K. Le Van, A. Mantoux, L. Perrigaud, P. Doppelt, *Journal of Power Sources* **2007**, *174*, 312-320 10.1016/j.jpowsour.2007.09.045.

[25] N. Thi Be Bay, P. M. Tien, S. Badilescu, Y. Djaoued, G. Bader, F. E. Girouard, V. v. Truong, L. q. Nguyen, *Journal of Applied Physics* **1996**, *80*, 7041-7045 10.1063/1.363777.

[26] T. Gallasch, T. Stockhoff, D. Baither, G. Schmitz, *Journal of Power Sources* **2011**, *196*, 428-435 https://doi.org/10.1016/j.jpowsour.2010.06.099.

[27] Y.-R. Lu, T.-Z. Wu, C.-L. Chen, D.-H. Wei, J.-L. Chen, W.-C. Chou, C.-L. Dong, *Nanoscale research letters* **2015**, *10*, 387-387 10.1186/s11671-015-1095-9.

[28] A. M. Engstrom, F. M. Doyle, *Journal of Power Sources* **2013**, *228*, 120-131 https://doi.org/10.1016/j.jpowsour.2012.11.075.

[29] D. Rehnlund, M. Valvo, K. Edström, L. Nyholm, *Journal of the Electrochemical Society* **2014**, *161*, D515-D521 10.1149/2.0511410jes.

[30] M. Rasoulis, D. Vernardou, *Coatings* **2017**, *7* 10.3390/coatings7070100.

[31] E. Armstrong, M. O'Sullivan, J. O'Connell, J. D. Holmes, C. O'Dwyer, *Journal of the Electrochemical Society* **2015**, *162*, D605-D612 10.1149/2.0541514jes.

[32] H. Poelman, H. Tomaszewski, D. Poelman, L. Fiermans, R. D. Gryse, M. F. Reyniers, G. B. Marin, *Surface and Interface Analysis* **2002**, *34*, 724-727 10.1002/sia.1397.

[33] Y. S. Yoon, J. S. Kim, S. H. Choi, *Thin Solid Films* **2004**, *460*, 41-47 https://doi.org/10.1016/j.tsf.2004.01.075.

[34] C. Delmas, H. Cognac-Auradou, J. M. Cocciantelli, M. Ménétrier, J. P. Doumerc, *Solid State Ionics* **1994**, *69*, 257-264 https://doi.org/10.1016/0167-2738(94)90414-6.

[35] D. Acosta, A. Perez, C. Magaña, F. Hernandez, *Journal of Materials Science and Engineering A* **2016**, *6* 10.17265/2161-6213/2016.3-4.007.

[36] C. R. Aita, L.-J. Liou, C.-K. Kwok, R. C. Lee, E. Kolawa, *Thin Solid Films* **1990**, *193-194*, 18-26 https://doi.org/10.1016/S0040-6090(05)80007-0.

[37] I. Quinzeni, S. Ferrari, E. Quartarone, P. Mustarelli, *Journal of Power Sources* **2011**, *196*, 10228-10233 https://doi.org/10.1016/j.jpowsour.2011.08.073.

[38] L. Ottaviano, A. Pennisi, F. Simone, A. M. Salvi, *Optical Materials* **2004**, *27*, 307-313 https://doi.org/10.1016/j.optmat.2004.04.001.

[39] H. M. R. Giannetta, C. Calaza, D. G. Lamas, L. Fonseca, L. Fraigi, *Thin Solid Films* **2015**, *589*, 730-734 https://doi.org/10.1016/j.tsf.2015.06.048.

[40] M. Panagopoulou, D. Vernardou, E. Koudoumas, D. Tsoukalas, Y. S. Raptis, *Electrochimica Acta* **2017**, *232*, 54-63 https://doi.org/10.1016/j.electacta.2017.02.128.

[41] J. F. M. Oudenhoven, L. Baggetto, P. H. L. Notten, *Advanced Energy Materials* **2011**, *1*, 10-33 10.1002/aenm.201000002.

[42] H.-T. Fang, M. Liu, D.-W. Wang, T. Sun, D.-S. Guan, F. Li, J. Zhou, T.-K. Sham, H.-M. Cheng, *Nanotechnology* **2009**, *20*, 225701 10.1088/0957-4484/20/22/225701.

[43] B. Pandit, D. P. Dubal, P. Gómez-Romero, B. B. Kale, B. R. Sankapal, *Scientific Reports* **2017**, *7*, 43430 10.1038/srep43430.

[44] J. T. Culp, in *Novel Materials for Carbon Dioxide Mitigation Technology* (Eds.: F. Shi, B. Morreale), Elsevier, Amsterdam, **2015**, pp. 149-176.

[45] Y.-R. Lu, T.-Z. Wu, C.-L. Chen, D.-H. Wei, J.-L. Chen, W.-C. Chou, C.-L. Dong, *Nanoscale Research Letters* **2015**, *10*, 387 10.1186/s11671-015-1095-9.

[46] S. Liu, Z. Tong, J. Zhao, X. Liu, J. wang, X. Ma, C. Chi, Y. Yang, X. Liu, Y. Li, *Physical Chemistry Chemical Physics* **2016**, *18*, 25645-25654 10.1039/C6CP04064K.

[47] C. Sanchez, J. Livage, G. Lucazeau, *Journal of Raman Spectroscopy* **1982**, *12*, 68-72 10.1002/jrs.1250120110.

[48] H. Drosos, A. Sapountzis, E. Koudoumas, N. Katsarakis, D. Vernardou, *Journal of the Electrochemical Society* **2012**, *159*, E145-E147 10.1149/2.017208jes.

[49] S.-H. Lee, H. M. Cheong, M. J. Seong, P. Liu, C. E. Tracy, A. Mascarenhas, J. R. Pitts, S. K. Deb, *Solid State Ionics* **2003**, *165*, 111-116 https://doi.org/10.1016/j.ssi.2003.08.022.

[50] P. Shvets, O. Dikaya, K. Maksimova, A. Goikhman, *Journal of Raman Spectroscopy* **2019**, *50*, 1226-1244 10.1002/jrs.5616.

[51] S.-H. Lee, H. M. Cheong, M. J. Seong, P. Liu, C. E. Tracy, A. Mascarenhas, J. R. Pitts, S. K. Deb, *Journal of Applied Physics* **2002**, *92*, 1893-1897 10.1063/1.1495074.

[52] R. Baddour-Hadjean, A. Marzouk, J. P. Pereira-Ramos, *Journal of Raman Spectroscopy* **2012**, *43*, 153-160 10.1002/jrs.2984.

[53] L. Abello, E. Husson, Y. Repelin, G. Lucazeau, *Spectrochimica Acta Part A: Molecular Spectroscopy* **1983**, *39*, 641-651 10.1016/0584-8539(83)80040-3.

[54] J. M. Jehng, F. D. Hardcastle, I. E. Wachs, *Solid State Ionics* **1989**, *32-33*, 904-910

[55] A. Ghosh, E. J. Ra, M. Jin, H.-K. Jeong, T. H. Kim, C. Biswas, Y. H. Lee, *Advanced Functional Materials* **2011**, *21*, 2541-2547 10.1002/adfm.201002603.

[56] J. B. Bates, N. J. Dudney, G. R. Gruzalski, R. A. Zuhr, A. Choudhury, C. F. Luck, J. D. Robertson, *Journal of Power Sources* **1993**, *43*, 103-110 https://doi.org/10.1016/0378-7753(93)80106-Y.

[57] E. Uchaker, Y. Z. Zheng, S. Li, S. L. Candelaria, S. Hu, G. Z. Cao, *Journal of Materials Chemistry A* **2014**, *2*, 18208-18214 10.1039/C4TA03788J.

[58] S. Petnikota, R. Chua, Y. Zhou, E. Edison, M. Srinivasan, *Nanoscale Research Letters* **2018**, *13*, 363-363 10.1186/s11671-018-2766-0.

[59] F. Mattelaer, K. Geryl, G. Rampelberg, J. Dendooven, C. Detavernier, *ACS Applied Materials & Interfaces* **2017**, *9*, 13121-13131 10.1021/acsami.6b16473.

[60] M. Arakawa, Y. Nemoto, S.-i. Tobishima, M. Ichimura, J.-i. Yamaki, *Journal of Power Sources* **1993**, *44*, 517-522 https://doi.org/10.1016/0378-7753(93)80197-W.

[61] C. Julien, G.-A. Nazri, in *Solid State Batteries: Materials Design and Optimization*, Springer US, Boston, MA, **1994**, pp. 1-96.

[62] X. Liu, J. Zeng, H. Yang, K. Zhou, D. Pan, *RSC Advances* **2018**, *8*, 4014-4031 10.1039/C7RA12523B.

[63] X. Zhang, J.-G. Wang, H. Liu, H. Liu, B. Wei, *Materials (Basel, Switzerland)* **2017**, *10*, 77 10.3390/ma10010077.

[64] J. C. Badot, A. Mantoux, N. Baffier, O. Dubrunfaut, D. Lincot, *Journal of Materials Chemistry* **2004**, *14*, 3411-3415 10.1039/B410324F.

[65] T. M. Clancy, J. F. Rohan, *ChemElectroChem* **2018**, *5*, 3273-3278 10.1002/celc.201800822.

[66] M. Hekmatfar, I. Hasa, R. Eghbal, D. V. Carvalho, A. Moretti, S. Passerini, *Advanced Materials Interfaces* **2020**, *7*, 1901500 10.1002/admi.201901500.

[67] E. Brown, S.-H. Park, A. Elangovan, Y. Yuan, J. Kim, X. S. Sun, X. Zhang, G. Wang, J. Li, *Electrochimica Acta* **2018**, *269*, 144-154 https://doi.org/10.1016/j.electacta.2018.02.167.

[68] T. Teranishi, Y. Yoshikawa, M. Yoneda, A. Kishimoto, J. Halpin, S. O'Brien, M. Modreanu, I. M. Povey, *ACS Applied Energy Materials* **2018**, *1*, 3277-3282 10.1021/acsaem.8b00496.

[69] P. Yan, J. Zheng, X. Zhang, R. Xu, K. Amine, J. Xiao, J.-G. Zhang, C.-M. Wang, *Chemistry of Materials* **2016**, *28*, 857-863 10.1021/acs.chemmater.5b04301.

[70] S. Gong, G. Zhao, P. Lyu, K. Sun, *Journal of Materials Chemistry A* **2019**, *7*, 1187-1195 10.1039/C8TA08120D.

[71] Y. Wang, Y. Song, Y. Xia, *Chemical Society Reviews* **2016**, *45*, 5925-5950 10.1039/C5CS00580A.

[72] J.-K. Kim, L. Niedzicki, J. Scheers, C.-R. Shin, D.-H. Lim, W. Wieczorek, P. Johansson, J.-H. Ahn, A. Matic, P. Jacobsson, *Journal of Power Sources* **2013**, *224*, 93-98 https://doi.org/10.1016/j.jpowsour.2012.09.029.

[73] L. M. McGrath, J. Jones, E. Carey, J. F. Rohan, *ChemistryOpen* **2019**, *8*, 1429-1436 10.1002/open.201900313.

Chapter 6:

Evaluation of Inverse Opal TiO_2 Anodes with Ionic Liquid Based Electrolytes

6.1 Abstract

To assess the potential use of C_4mpyrTFSI-based electrolytes with nanostructured electrodes, CV analysis was initially carried out with IO TiO_2 electrodes. The CV performance of the IO TiO_2 electrodes in 0.5 M LiTFSI in C_4mpyrTFSI is similar to a conventional organic electrolyte (1 M $LiPF_6$ in 1:1 v/v EC:DEC), whereby identical current densities (organic: -0.04 mA cm^{-2} vs. IL: ~ -0.04 mA cm^{-2} at 0.5 mV s^{-1}) and peak positions were achieved in both solutions. Without the use of additive, swelling of the TiO_2 is observed for both electrolytes as the thickness of the 12 nm TiO_2 interconnected lattice increased. However, the integrity of both electrodes was maintained despite the swelling.

The utilisation of additives such as FEC or VC minimises electrode swelling with organic electrolytes, however, they did not prevent significant electrode swelling with the ionic liquid (IL) electrolyte as the lattice increased from 12 to ~51 , ~48 and ~65 nm when 3 wt.% FEC, 3 wt.% VC and 10 wt.% VC were added to 0.5 M LiTFSI in C_4mpyrTFSI, respectively.

Polymer gel analysis yielded high coulombic efficiencies (>90%), however, electrode capacities (~ 56 mAh g- at 0.1 mV s^{-1}) are obtained due to the inability of the polymer gel to fully penetrate the IO structure. The combination of liquid and polymer gel electrolytes yielded marginal improvements

over the liquid only and polymer gel only data, however further work is required to optimise the IL/TiO_2 combination.

6.2 Introduction

With the ever advancing improvements in electronics and electrical engineering, there is a need to develop nanostructured Li-ion battery electrode materials which are able to meet the growing demands for miniaturised Li-based microbatteries. Consequently, there has been a tremendous amount of effort put into developing materials capable of long cycle-life with suitable stability in capacity, capacity retention, and voltage.[1-3] Currently, there is a growing need to identify eco-friendly, earth abundant materials which are capable of delivering stable capacities over a large number of cycles which will enable long-life IoT sensors, instead of materials that offer high initial capacities and then significantly fade over the course of a relatively low number of cycles.

Low-voltage intercalation materials such as TiO_2 have garnered attention due to their ability to yield fast Li^+ insertion/removal, in addition to having a low environmental impact and cost. TiO_2 exists in a variety of polymorphs including TiO_2(B), anatase, and rutile, where the rutile form is the most common natural form, as it is the most thermodynamically stable phase under standard conditions. Various rutile TiO_2 nanostructures have been reported for application as anode materials such as nanoparticles, nanowires, and nanorods.[4-6]

Inverse opal (IO) structures have proven effective as high-performance Li-ion cathode and anode materials due to advantageous properties such as high porosity, thin walls that allow short Li^+ diffusion path lengths, and large surface area.[7-11] The utilisation of a porous, highly-ordered 3D interconnected network such as an IO removes the necessity for conductive additives or binders within the electrode material which is advantageous for microbattery applications due to the decreased content of inactive materials. Full cell prototypes have been demonstrated in the literature

where Co_3O_4 IO anode and a V_2O_5 IO cathode were utilised with an organic based electrolyte consisting of EC in DMC and 3 wt.% VC.[12] The IO nanostructure can be applied to various materials which make it an attractive alternative to conventional nanowires, nanorods and core-shell structures.

In this chapter, the electrochemical performance of IO rutile TiO_2 electrodes is assessed to determine the compatibility of C_4mpyrTFSI-based electrolytes with the IO nanostructure. To the best of our knowledge, the utilisation of IO rutile TiO_2 electrodes with ionic liquid electrolytes has not previously been reported. This work was carried out in collaboration with the O'Dwyer research group in UCC.

6.3 Experimental

IO TiO_2 electrodes were obtained from the O'Dwyer group in UCC School of Chemistry. The mass of the electrode was determined from the weight of the stainless steel electrode before and after TiO_2 synthesis. Electrolyte analysis was carried out using the following electrolytes:

1. 1 M $LiPF_6$ in 1:1 v/v EC:DEC
2. 0.5 M LiTFSI in C_4mpyrTFSI
3. 3 wt.% FEC in 0.5 M LiTFSI in C_4mpyrTFSI
4. 3 wt.% VC in 0.5 M LiTFSI in C_4mpyrTFSI
5. 10 wt.% VC in 0.5 M LiTFSI in C_4mpyrTFSI
6. Ionic liquid-based polymer gel consisting of PVDF-HFP, LiTFSI and C_4mpyrTFSI, where C4mpyrTFSI content is 60% (PG-60)

CV analysis was carried out at various scan rates (0.05, 0.1 and 0.5 mV s^{-1}) over the potential window 3 V to 1 V using a Bio-Logic VSP multi-channel potentiostat. SEM images of the electrodes were obtained before and after cycling using a Carl Zeiss SEM.

The structure and the morphology of the samples were analysed using a Zeiss Supra 40 SEM coupled with an energy dispersive X-ray (EDX).

Electrochemical measurements of the Li^+ capacity were assessed by CV and galvanostatic cycling with potential limitation (GCPL) using a Bio-logic VSP potentiostat. A three electrode pouch cell setup was utilised where 0.25 mm thick lithium foil (Sigma Aldrich) acted as counter and reference electrode. 1 cm^2 of the anode was exposed as the working electrode to the electrolyte solutions as mentioned in chapter 3. Cell assembly was carried out in an argon-filled glove box (M. Braun LABstar Glove Box) with O_2 and H_2O maintained below 0.1 ppm

6.4 Results and discussion

To investigate both the liquid and polymer gel ionic liquid electrolytes compatibility with nanostructured electrode materials, they were tested with inverse opal (IO) TiO_2 electrodes and compared to results obtained with an organic electrolyte. The IO electrodes were prepared following the procedure described by McNulty *et al.*[11] via infilling of a PS sphere template. The templates were prepared by drop casting a solution of PS spheres (Polysciences Inc., diameter = 500 nm) in isopropanol (IPA) on to 1 cm^2 area of 2 cm x 1 cm pieces of stainless steel; the sphere templates were then infilled with a 0.1 m solution of titanium(IV) chloride tetrahydrofuran complex ($TiCl_4 \cdot 2THF$) in IPA. The infilled sphere templates were heated at 450 °C in air for 1 h, to remove the PS templates and to crystallize the samples. This results in voids of approximately 420 nm diameter, with a TiO_2 thickness of ~12 nm around the void as confirmed by SEM analysis. The overall thickness of the TiO_2 electrode is approximately 25 µm.

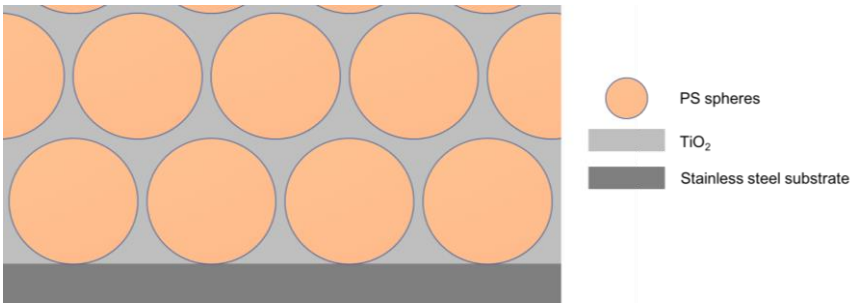

Figure 6.1: Cross-sectional image of TiO_2 electrodes deposited onto stainless steel electrodes with PS spheres.

SEM micrographs of the electrodes are shown in figure 6.2, and the clearly defined inverse opal structure can be seen. The TiO_2 does not cover the substrate uniformly but rather as islands on the substrate surface (figure 6.2(a)). As shown in figure 6.2(d) there are lower EDX signals observed for TiO_2 when focusing on the substrate by comparison with the TiO_2 island, therefore confirming that TiO_2 is concentrated to the islands only.

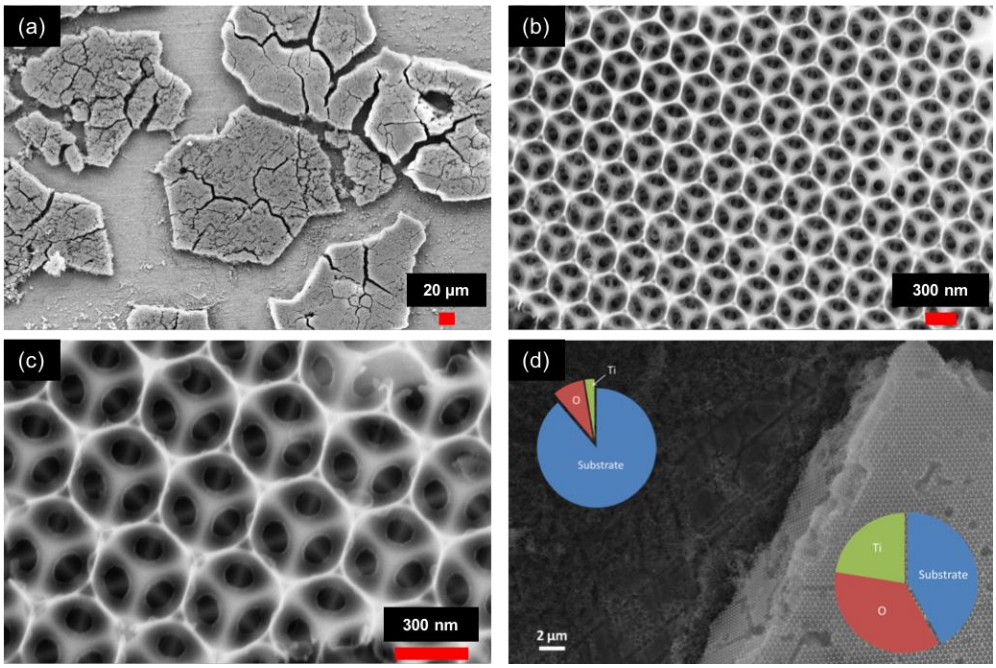

Figure 6.2: SEM micrographs of IO TiO_2 electrodes (a – c) at various magnifications and (d) EDX analysis of substrate and IO TiO_2.

The CV performance of the IO TiO_2 electrodes was determined using 0.5 M LiTFSI in C_4mpyrTFSI which was then compared to a conventional organic electrolyte (1 M $LiPF_6$ in 1:1 v/v EC:DEC). From figure 6.3, it can be seen that the current density for both solutions are similar which indicates compatibility of the ionic liquid electrolyte with nanostructured electrode materials. The current density was determined by assuming full coverage of the 1 cm^2 area. The mass loading of the TiO_2 electrodes were similar for each sample utilised in this study, therefore, the current densities would be comparable assuming the same area for each sample. In both instances the initial cycles yielded high current densities which then reduced and stabilised after 8 cycles. Stable cycling was further seen in subsequent cycles for both organic and ionic liquid electrolytes as evidenced by the overlapping CV data at 0.1 mV s^{-1} and 0.5 mV s^{-1}. The peak positions for Li^+ insertion and removal is comparable for both the organic and IL electrolyte (insertion: 1.42 V and 1.41 V, removal: 1.63 V and 1.60 V). As the peak positions are similar in both electrolytes, it indicates that Li-ion diffusivity is not hindered within the ionic liquid electrolyte, thus Li insertion/removal from the TiO_2 electrode

occurs at the same potential for both electrolytes. However, the peaks obtained in the organic electrolyte are much sharper than those in the IL and result in higher current densities. This indicates that higher electrode capacities would be expected for the organic electrolyte, which could be attributed to its lower viscosity (~13 cP vs. 100 cP) and higher ionic conductivity (7.9 mS cm^{-1} vs. 1.5 mS cm^{-1}).

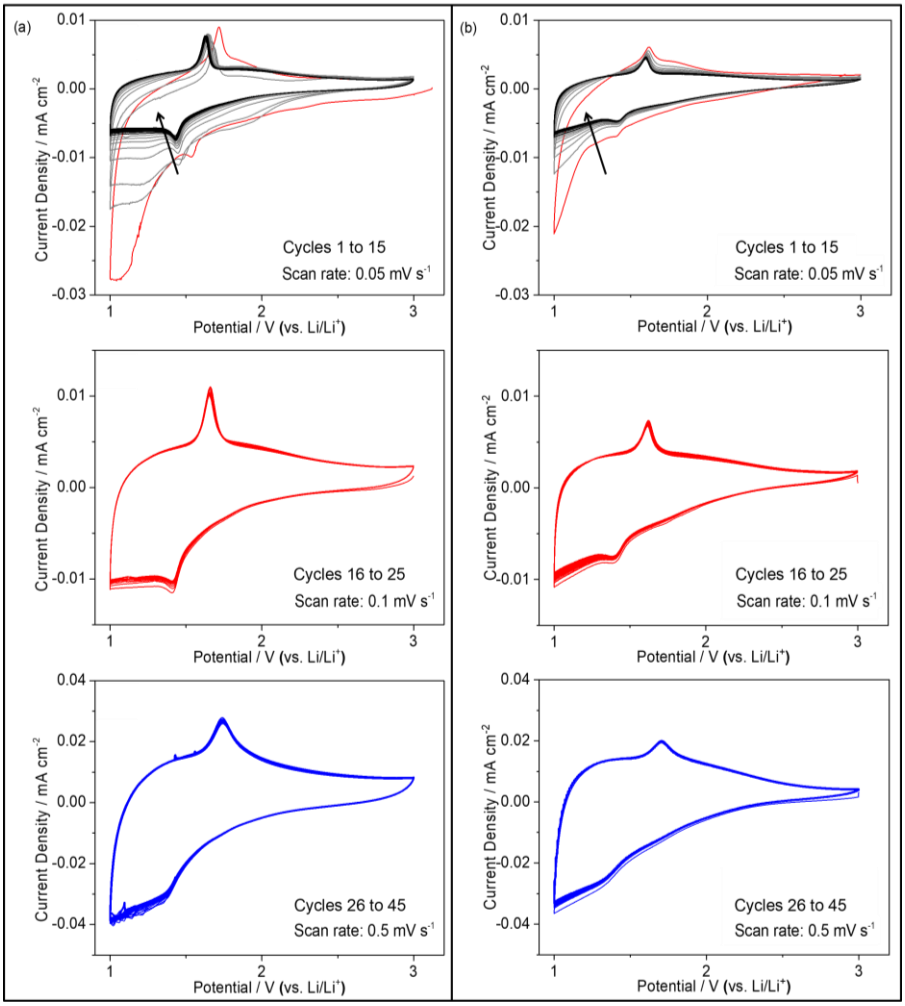

Figure 6.3: CV data for IO TiO_2 in (a) 1 M $LiPF_6$ in (1:1 v/v) EC:DEC and (b) 0.5 M LiTFSI in C_4mpyrTFSI. Scan rates outlined in graphs. Arrows indicate the decrease in current density from cycle 1 (red) to cycles 9 to 15 (black).

The theoretical capacity of TiO_2 is ~180 mAh g^{-1} when x is 0.5 in Li_xTiO_2. As shown in figure 6.4, the organic electrolyte 1 M $LiPF_6$ in 1:1 v/v EC:DEC, yields high electrode discharge capacities. At

0.05 mV s^{-1}, a discharge capacity of ~133 mAh g^{-1} is obtained which corresponds to 74% of theoretical. The discharge capacities obtained at 0.1 mV s^{-1} and 0.5 mV s^{-1} are 64% and 42% of theoretical, respectively. Comparing the average charge and discharge capacities for 0.1 mV s^{-1} (cycles 15 to 25 and 45 to 55), there is a capacity drop of 8% and 6% after cycling at 0.5 mV s^{-1} respectively. By comparison, the additive free ionic liquid-based electrolyte yields discharge capacities which are 47%, 36% and 25% of theoretical for the initial 0.05 mV s^{-1}, 0.1 mV s^{-1} and 0.5 mV s^{-1} scans respectively. The lower discharge capacities could be attributed to sluggish Li^+ diffusion caused by higher resistivity within the IL electrolyte (lower ionic conductivity), attributed to its higher viscosity (~100 cP vs. ~13 cP for 1 M LiPF6 in EC:DEC with VC[13]). Similarly, to the organic data, the final 0.1 mV s^{-1} charge and discharge capacity data is 8% less than the initial 0.1 mV s^{-1} capacity after cycling at 0.5 mV s^{-1}. This highlights the capacity drop experienced after cycling at 0.5 mV s^{-1} is attributed to the TiO_2 electrode rather than the electrolyte. A larger capacity drop (~30%) is observed for the 0.05 mV s^{-1} charge and discharge data.

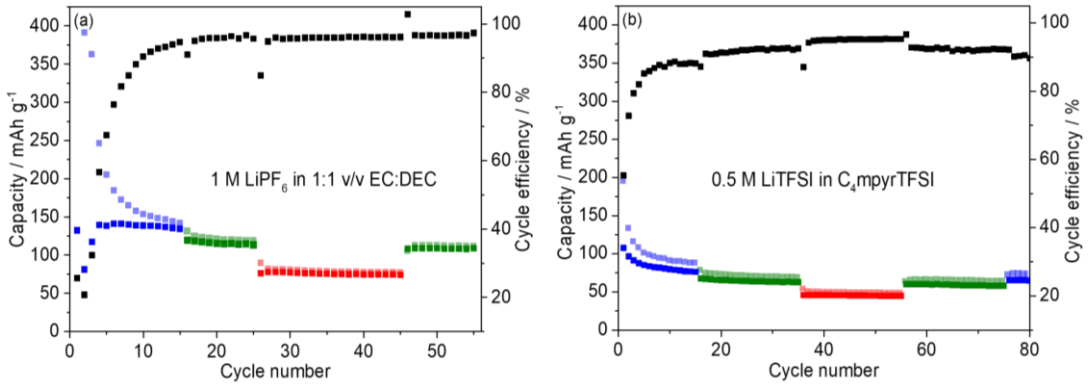

Figure 6.4: Comparison of the IO TiO_2 CV cycling data obtained in various electrolyte materials, where blue corresponds to 0.05 mV s^{-1}, green to 0.1 mV s^{-1} and red to 0.5 mV s^{-1}. The lighter colours refer to the lithiation process, while the darker colours refer to the delithiation processes. The black represents the cycle efficiency between the lithiation and delithiation processes.

In order to understand the large capacity drops in both organic and IL electrolytes, SEM analysis was carried out to determine if morphological changes have occurred, which could be attributed to the

capacity drops. From figure 6.5, it is evident that morphological changes have occurred during cycling in both organic and ionic liquid electrolytes. The pristine TiO_2 lattice is ~12 nm thick, while thicker lattice parameters are observed for the cycled electrodes. In particular, the electrode cycled in the organic electrolyte exhibits swelling of the lattice, which was observed in a similar study conducted by McNulty *et al.*[11]. However, in their study, swelling of the TiO_2 lattice was observed at the 1000th cycle. This mitigation of electrode swelling has been attributed to the addition of 3 wt.% VC to the electrolyte, as it enables the formation of stable SEI layers as observed in figure 6.5. Comparing the organic and ionic liquid cycled electrodes, it is evident that less swelling occurred within the ionic liquid electrolyte, however, the electrode looks less ordered, which may suggest that the TiO_2 lattice is breaking down, leading to the ~30% capacity drop between the initial and final 0.05 mV s^{-1} data.

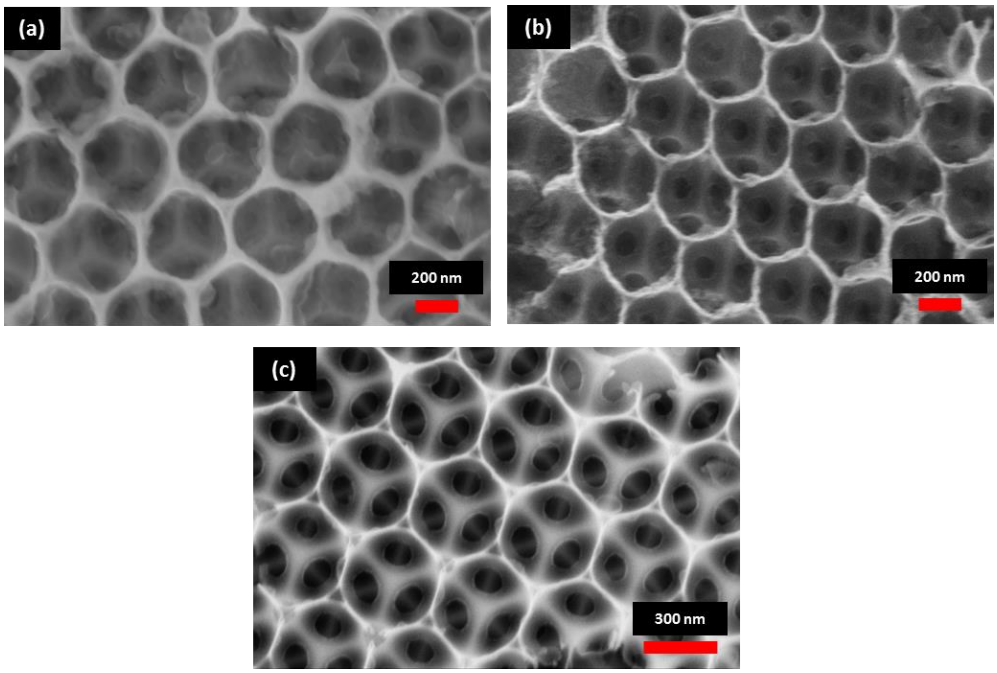

Figure 6.5: SEM micrographs of IO TiO_2 electrodes after cycling in (a) 1 M $LiPF_6$ in 1:1 v/v EC:DEC, (b) 0.5 M LiTFSI in C_4mpyrTFSI and (c) pristine IO TiO_2 for comparison.

As mentioned, McNulty *et al.*[11] utilise VC additive within their organic electrolyte which mitigates the effects of electrode swelling and allows for 1000 cycles to be obtained. The addition of additives such as VC and FEC in C_4mpyrTFSI-based IL electrolytes has previously shown to be beneficial in

chapters 4 and 5, whereby the formation of a stable SEI or CEI layer allowed for stable, long-term cycling of planar Ge and V_2O_5 electrodes. Both FEC and VC additives were investigated with IO TiO_2 electrodes to determine if positive effects in terms of cycle stability and capacity can be obtained. Initially, EIS data was obtained to determine if the presence of the additives changed the ionic conductivity of the ionic liquid electrolyte. Like the earlier ionic liquid EIS data shown in chapter 3, there was good agreement between the experimental EIS data and the fit for the chosen equivalent circuit. The ionic conductivities determined are shown in table 6.1. There is a marginal improvement when 10 wt.% VC is added to solution, however, the 3 wt.% VC and 3 wt.% FEC solutions are similar to the blank solution. This suggests that the addition of the additives does not affect the viscosity or the resistance of the solution.

	3 wt.% FEC	**3 wt.% VC**	**10 wt.% VC**
Conductivity ($mS\ cm^{-1}$)	1.45	1.54	1.60

Table 6.1: Ionic conductivity values for additives in 0.5 M LiTFSI in C_4mpyrTFSI as determined from EIS data.

Similar CV data is observed when FEC or VC is added to the ionic liquid as shown in figure 6.6. The CV data shape matches those observed in both the organic and additive-free ionic liquid electrolytes shown in figure 6.3. However, the peak positions for Li^+ insertion and removal have shifted to more positive potentials than for the organic or additive-free IL electrolyte (removal: ~2 V versus ~1.6 V respectively). This shift in the insertion and removal peak positions may suggest that an additional resistive process may be occurring, such as the formation of an SEI layer. Despite this shift, similar current densities are obtained in the additive free (~ -0.006 mA cm^{-2} at 0.05 mV s^{-1}) and additive containing electrolytes (~ -0.005 mA cm^{-2} to ~ -0.007 mA cm^{-2} at 0.05 mV s^{-1}). As observed in the additive-free electrolytes, the initial cycles produced large current densities which stabilises with

increasing cycle numbers thus demonstrating similar electrochemical performances with the additive-containing electrolytes. At low VC concentrations, a broad pseudocapacitive-like peak is observed, while sharp, clearly defined peaks are observed at higher VC concentrations (10 wt.%).

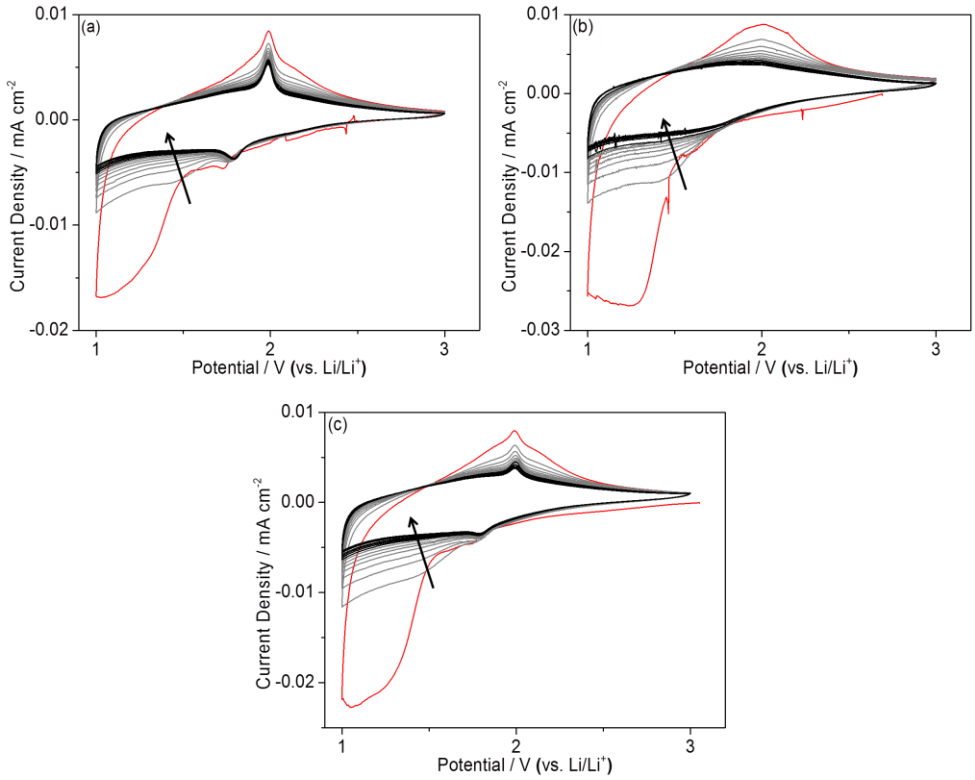

Figure 6.6: CV data for IO TiO_2 in C_4mpyrTFSI with (a) 3 wt.% FEC, (b) 3 wt.% VC and (c) 10 wt.% VC. Arrows indicate the decrease in current density from cycle 1 (red) to cycles 9 to 15 (black).

Comparing the electrochemical cycling data of the additive-containing electrolytes yields further insight into the effect of FEC and VC addition (figure 6.7). Stable cycling was achieved in all electrolytes, with the exception of the final 0.05 mV s^{-1} data obtained within 10 wt.% VC-containing electrolyte. The coulombic efficiencies obtained in figure 6.7, are similar to those obtained in the additive-free IL electrolyte shown in figure 6.4(b). Both the 3 wt.% FEC and 3 wt.% VC electrolyte solutions yield high coulombic efficiencies, in excess of 90% for all scan rates. By comparison, the 10 wt.% VC containing electrolyte, reached a maximum coulombic efficiency of 84% at 0.05 mV s^{-}

[1] with different coulombic efficiencies obtained at higher scan rates (~90% and ~95% at 0.1 mV s^{-1} and 0.5 mV s^{-1} respectively), which demonstrates that Li insertion and removal is scan rate dependent. This data is in stark contrast with the organic electrolyte data (figure 6.4(a)) whose coulombic efficiency is independent of the scan rate (~98% across all scan rates). This difference is attributed to the higher resistivity, and thus lower ionic conductivity of the ionic liquid-based electrolytes, as the organic electrolyte exhibits an ionic conductivity 5x greater than the IL as demonstrated in chapter 3 (7.9 mS cm^{-1} vs. ~1.5 mS cm^{-1}), thus achieves faster Li^+ diffusion.

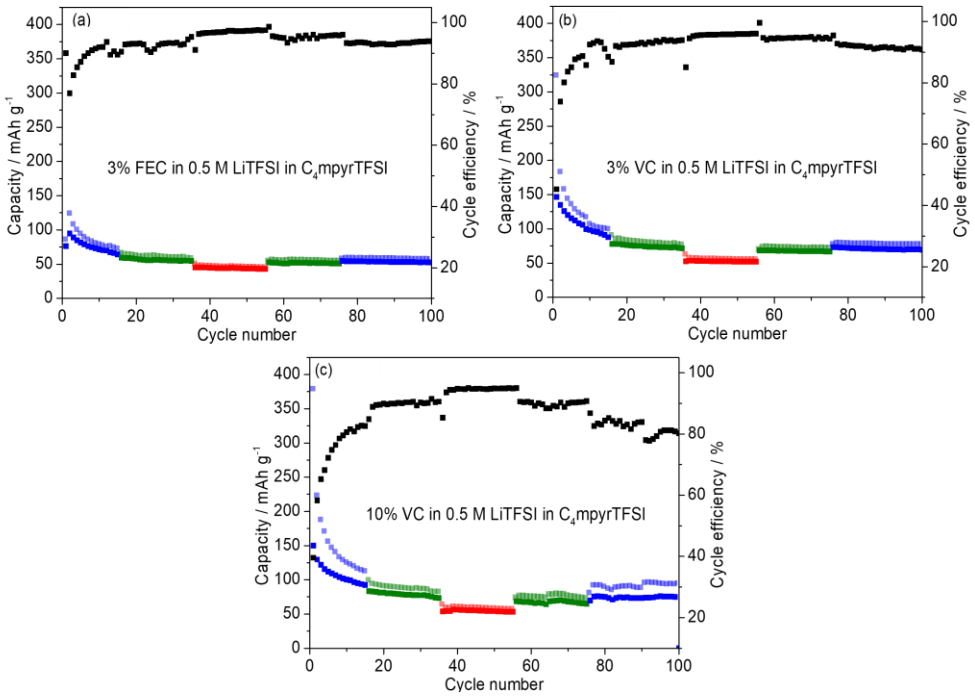

Figure 6.7: Comparison of the IO TiO_2 CV cycling data obtained in various electrolyte materials, where blue corresponds to 0.05 mV s^{-1}, green to 0.1 mV s^{-1} and red to 0.5 mV s^{-1}. The lighter colours refer to the lithiation process, while the darker colours refer to the delithiation processes. The black represents the cycle efficiency between the lithiation and delithiation processes.

The VC-containing electrolytes yielded higher initial capacity values than FEC-containing electrolytes as shown in table 6.2. However, comparing the two VC-containing electrolytes, it is evident that the electrode capacities obtained are similar, which demonstrates that VC contents above 3 wt.% do not yield higher electrode capacities over the course of 100 cycles. The capacity obtained

for the initial 0.05 mV s^{-1} cycle of the VC-containing electrolytes is ~83% of theoretical and is the highest electrode capacity obtained of all the ionic liquid electrolytes studied. By comparison, the FEC-containing electrolyte achieved only 43% in the initial 0.05 mV s^{-1} cycle. Despite demonstrating lower electrode capacities, the FEC-containing electrolyte exhibited the lowest capacity drop when comparing the average initial and final 0.1 mV s^{-1} discharge capacities (~7% vs. 9% and 15% for 3 wt.% VC and 10 wt.% VC respectively). This suggests that a marginally more stable system is obtained with the FEC-containing additive, however, lower electrode capacities are achieved. These values are similar to those obtained in the organic (~6%) and additive-free IL (~8%), which suggests that the addition of additives does not substantially improve the electrochemical performance of C_4mpyrTFSI with IO TiO_2 electrodes.

Scan rate ($mV\ s^{-1}$)	**10 wt.% VC**	**3 wt.% VC**	**3 wt.% FEC**
	Electrode capacity ($mAh\ g^{-1}$)		
0.05	149	147	77
0.1	83	78	59
0.5	54	53	45

Table 6.2: Comparison of the IO TiO_2 CV cycling data in the 0.5 M LiTFSI in C_4mpyrTFSI electrolyte containing either VC or FEC additives.

Post-mortem analysis of the electrodes cycled within the additive-containing electrolytes (figure 6.8) suggest that the use of additives in 0.5 M LiTFSI in C_4mpyrTFSI does not hamper or mitigate electrode swelling. The higher VC content (10 wt.%) seems to promote electrode swelling as the TiO_2 electrode dimensions increased from ~12 nm before cycling to ~65 nm after cycling. This may account for the unstable final 0.05 mV s^{-1} cycling data as shown in figure 6.7. When 3 wt.% FEC or VC is used, electrode swelling is noted, however to a lesser extent than for 10 wt.% VC as TiO_2 electrode dimensions were ~51 nm and ~48 nm respectively.

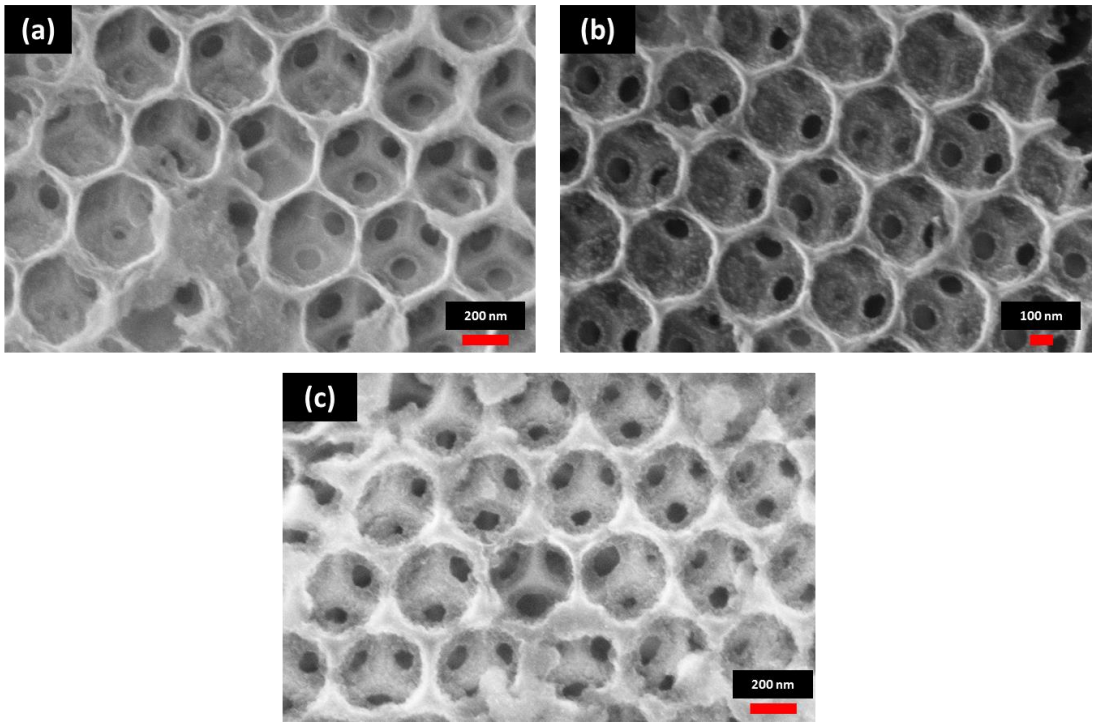

Figure 6.8: SEM micrographs of IO TiO_2 electrodes after cycling in (a) 3 wt.% FEC, (b) 3 wt.% VC and (c) 10 wt.% VC in 0.5 M LiTFSI in C_4mpyrTFSI.

The swelling of the electrodes may account for the lower than expected electrode capacity values, therefore the utilisation of a polymer gel electrolyte may prove beneficial as they can buffer expansion and contraction effects as shown in chapter 4. As the ionic liquid is encapsulated in the PVDF-HFP matrix, the ionic liquid should have minimal contact with the TiO_2 electrode, and therefore should not interfere with lattice structure of TiO_2. In addition, polymer gels have been reported to buffer the expansion effects of various electrode materials,[14-15] therefore, polymer gel based electrolytes should mitigate/dampen the TiO_2 swelling. Initially the polymer gel was solvent cast into the TiO_2 electrodes. From the CV in figure 6.9, sharp well-defined peaks were obtained for all cycles, whereby the peak positions match those previously observed for the organic and additive-free IL electrolyte. From the capacity data shown in figure 6.9(c), it is evident that the electrode capacity is lower with the polymer gel (~60 mAh g^{-1}) than for the additive-free IL electrolyte (~ 84 mAh g^{-1}) at 0.05 mV s^{-1}. Despite the lower electrode capacity, the coulombic efficiencies obtained in the polymer gel electrolyte (~97%)

are comparable to the organic electrolyte (~98%). In addition, there is less % capacity drop observed with PG-60 when the scan rate is increased from 0.05 mV s^{-1} to 0.1 mV s^{-1} than for the liquid electrolytes as shown in table 6.3. After 30 cycles another peak at ~1 V is observed as seen in figure 6.9(b). The presence of this peak has been observed in the literature and is attributed to the formation of an SEI layer and amorphous Li_2O formation.[16-18] After 30 cycles, the cycling behaviour deteriorates and cycling efficiencies greater than 100% were observed, indicative of additional complicating reactions during cycling (figure 6.9(c)). The cell stopped working after 40 cycles, and upon investigation with SEM, it is evident that the structure of the TiO_2 had changed, and the honeycomb structure was no longer observed. The incorporation of the polymer gel electrolyte within the TiO_2 matrix may have hampered the swelling of the lattice. By preventing the lattice from swelling, the polymer gel electrolyte may have caused the structure to breakdown more rapidly than was observed for the liquid-based electrolytes.

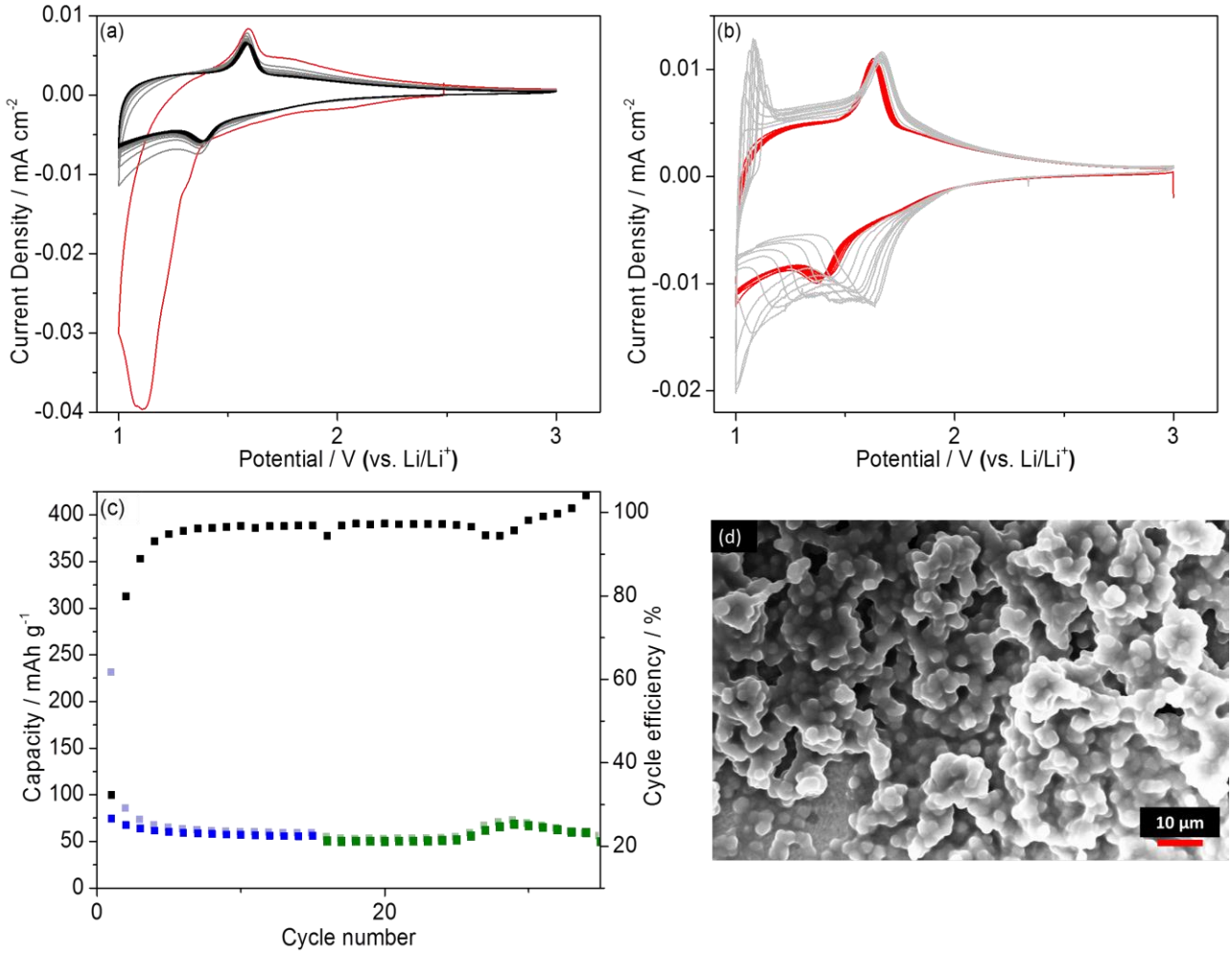

Figure 6.9: CV cycling data obtained at (a) 0.05 mV s^{-1} and (b) 0.1 m V s^{-1} with PG-60 as the electrolyte.

	PG-60	Organic	IL	3 wt.% FEC in IL	3 wt.% VC in IL	10 wt.% VC in IL
Capacity drop (%)	7	13	24	26	31	27

Table 6.3: Comparison of the % drop in the average discharge capacity when the scan rate is increased from 0.05 mV s^{-1} to 0.1 mV s^{-1}.

Despite the breakdown in the electrode structure, the coulombic efficiency and stable electrode capacities suggest that the use of polymer gel electrolytes with IO TiO_2 is promising but optimisation

is required. One method to circumvent total electrode breakdown is to utilise a hybrid electrolyte consisting of a liquid component and a polymer gel separator. Due to the enhanced performance when compared to the additive-free electrolyte, 3 wt.% VC in 0.5 M LiTFSI in C_4mpyrTFSI was chosen as the liquid electrolyte to be coupled with PG-60. This hybrid electrolyte yielded higher electrode capacities than PG-60 at 0.05 mV s^{-1}, discharge capacities: 76 mAh g^{-1} and 60 mAh g^{-1}, respectively (figure 6.10(a)). However, at faster scan rates (0.1 mV s^{-1}) similar electrode capacities are obtained (discharge: ~56 mAh g^{-1}). This increase in scan speed resulted in a 26% drop in the electrode capacity when compared to capacities obtained at 0.05 mV s^{-1}. This is a larger % drop when compared to PG-60 (7%), however, the use of the hybrid electrolyte led to an improvement in the % drop when compared to the liquid electrolyte only (31%). The coulombic efficiencies obtained for the hybrid electrolyte are comparable to PG-60 (94% vs. 97%), however, this drop in coulombic efficiency was expected due to the presence of the liquid electrolyte.

Comparing the hybrid electrolyte performance to the liquid 3 wt.% VC in 0.5 M LiTFSI in C_4mpyrTFSI cell which contains a glass fibre separator it is evident that the results are comparable as shown in figure 6.10(b). Similar coulombic efficiencies are obtained for the cells containing both polymer gel and glass fibre separators across the scan rates (~95%), however, the polymer gel electrolyte yields a higher coulombic efficiency for the final 0.05 mV s^{-1} scans (average: 94% vs. 92%). The electrode capacities obtained for the hybrid electrolyte are approximately 15 to 20 mAh g^{-1} less than its liquid counterpart, for example at 0.5 mV s^{-1} the discharge capacities are 38 mAh g^{-1} and 53 mAh g^{-1} respectively. However, in the final 0.05 mV s^{-1} analysis, the difference in the electrode capacities between the hybrid and liquid cells is reduced to 10 mAh g^{-1}. In addition, more stable cycling is obtained by the hybrid electrolyte as 0.09% capacity fade per cycle is observed versus 0.14% for the liquid electrolyte at 0.05 mV s^{-1} (cycles 75 to 100).

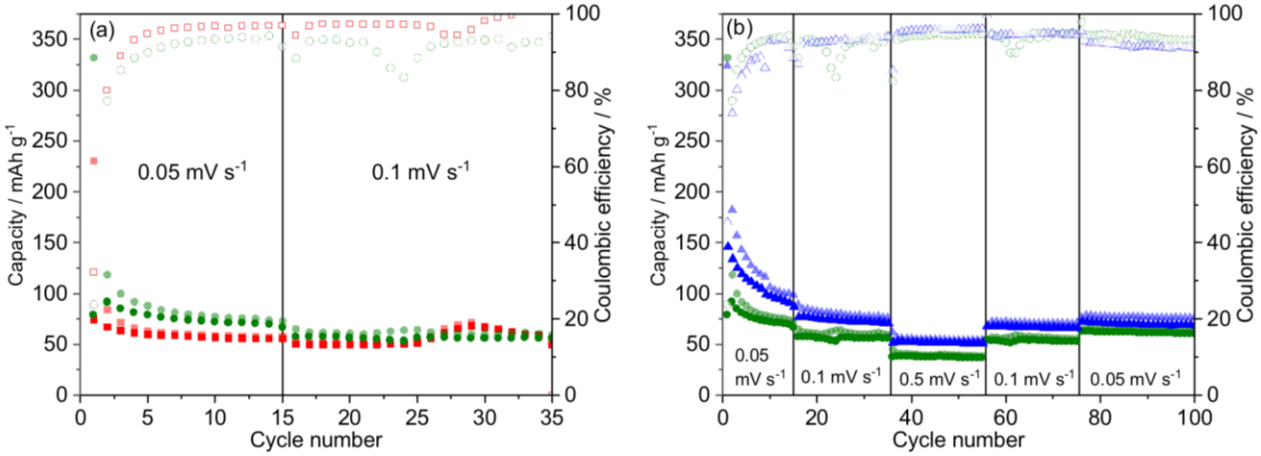

Figure 6.10: Comparison of TiO_2 electrochemical performances with (a) PG-60 (red) and PG-60 plus 3 wt.% VC in 0.5 M LiTFSI in C_4mpyrTFSI (green), and (b) 3 wt.% VC in 0.5 M LiTFSI in C_4mpyrTFSI (blue), and PG-60 with 3 wt.% VC in 0.5 M LiTFSI in C_4mpyrTFSI (green).

A comparison of the different electrolyte systems at 0.1 mV s^{-1} (cycles 15 to 35 or cycles 15 to 25 for organic) is shown in table 6.4. From this table it is evident that coulombic efficiencies greater than 90% are achieved by all the electrolytes. The PG-60 electrode capacities are similar to the FEC-containing electrolyte, however, the hybrid electrolyte offers higher charge capacities. The electrolyte systems containing PG-60 exhibit the lowest % drop in capacity, which further demonstrates their promise as an electrolyte material for IO TiO_2.

		Organic	IL	3 wt.% FEC in IL	3 wt.% VC in IL	10 wt.% VC in IL	PG-60	PG-60 and 3 wt.% VC in IL
Capacity (mAh g^{-1})	Charge	122	70	59	80	87	58	62
	Discharge	116	64	56	75	79	56	56
Coulombic efficiency (%)		95	91	95	94	91	97	90
Capacity fade per cycle (%)		0.59	0.25	0.23	0.31	0.49	.04	.08

Table 6.4: Comparison of the average charge and discharge capacities, coulombic efficiency and capacity fade per cycle (discharge data) obtained at 0.1 mV s^{-1} (cycles 15 to 35 or cycles 15 to 25 for organic).

These results highlight the compatibility of TiO_2 with PG-60-based electrolytes, as stable cycling was obtained over the course of 100 cycles, however, further work is required to obtain higher electrode capacities for the 25-micron thick deposits.

6.5 Conclusion

The electrochemical performance of IO TiO_2 electrodes demonstrate promise within C_4mpyrTFSI-based ionic liquids as the CV shape is similar to that obtained in organic electrolytes. In addition, the additive-free IL electrolyte yielded similar Li^+ insertion and removal peak positions (insertion: ~1.4 V, removal: ~1.6 V). This indicates that similar electrode kinetics are occurring within both electrolyte systems, however, the electrode capacities for the IL electrolyte were approximately 30 mAh g^{-1} to 40 mAh g^{-1} less than the organic cell. This is attributed to the sluggish Li^+ diffusion that occurs within the IL as it is a more resistive electrolyte than the organic as demonstrated by the differences in their ionic conductivities (1.5 mS cm^{-1} vs. 7.9 mS cm^{-1}). SEM analysis revealed that TiO_2 electrodes exhibit swelling upon cycling with Li. The electrode cycled in IL looks less ordered, which may suggest that the TiO_2 lattice is breaking down. The breakdown of the TiO_2 lattice would explain the large capacity drop (~30%) between the initial and final 0.05 mV s^{-1} data.

The addition of additives such as FEC and VC does not affect the ionic conductivity as values of ~1.5 mS cm^{-1} were obtained which match the value obtained for the additive-free electrolyte. A shift in the Li^+ insertion and removal peak positions is observed upon CV analysis, as the peaks are shifted approximately 300 mV more positive. The VC-containing electrolytes yielded higher initial capacity values than FEC-containing electrolytes (~147 mAh g^{-1} vs. 77 mAh g^{-1}), however, the 3 wt.% VC and 10 wt.% VC electrode capacities are comparable across all scan rates, thus demonstrating that VC contents above 3 wt.% do not yield higher TiO_2 electrode capacities over the course of 100 cycles. The capacity obtained for the initial 0.05 mV s^{-1} cycle of the VC-containing electrolytes is ~83% of theoretical and is the highest electrode capacity obtained of all the ionic liquid electrolytes studied. Post-mortem analysis of the electrodes cycled within the additive-containing electrolytes suggest that the use of additives in 0.5 M LiTFSI in C_4mpyrTFSI does not hamper or mitigate electrode swelling. The higher VC content (10 wt.%) seems to promote electrode swelling as the TiO_2 electrode

dimensions increased from ~12 nm before cycling to ~65 nm after cycling. When 3 wt.% FEC or VC is used, electrode swelling is noted, however to a lesser extent than for 10 wt.% VC as TiO_2 electrode dimensions were ~51 nm and ~48 nm respectively.

Polymer gel analysis was carried out due to the improved electrochemical performances noted in chapters 4 and 5. Sharp well-defined peaks were obtained for all cycles, whereby the peak positions match those previously observed for the organic and additive-free IL electrolyte. The electrode capacity is lower with the polymer gel (~60 mAh g^{-1}) than for the additive-free IL electrolyte (~ 84 mAh g^{-1}) at 0.05 mV s^{-1}, however, the coulombic efficiencies obtained in PG-60 (~97%) are comparable to the organic electrolyte (~98%). The cell stopped working after 40 cycles, and upon investigation with SEM, it is evident that the structure of the TiO_2 had changed, and the honeycomb structure was no longer observed.

Therefore, a hybrid electrolyte was investigated whereby, PG-60 acted as the separator, and 3 wt.% VC in 0.5 M LiTFSI in C4mpyrTFSI acted as the liquid electrolyte. This hybrid electrolyte yielded higher electrode capacities than PG-60 at 0.05 mV s^{-1}, discharge capacities: 76 mAh g^{-1} and 60 mAh g^{-1}, respectively. However, at faster scan rates (0.1 mV s^{-1}) similar electrode capacities are obtained (discharge: ~56 mAh g^{-1}). The coulombic efficiencies obtained for the hybrid electrolyte are comparable to PG-60 (94% vs. 97%), however, this drop in coulombic efficiency was expected due to the presence of the liquid electrolyte. Comparing the hybrid electrolyte performance to its liquid counterpart, the polymer gel electrolyte yielded a higher coulombic efficiency for the final 0.05 mV s^{-1} scans (average: 94% vs. 92%). In addition, more stable cycling is obtained by the hybrid electrolyte as 0.09% capacity fade per cycle is observed versus 0.14% for the liquid electrolyte at 0.05 mV s^{-1} (cycles 75 to 100).

Further analysis is required to optimise the compatibility of the TiO_2 electrodes with C_4mpyrTFSI-based electrolytes both in liquid and polymer gel form in order to obtain higher electrode capacities during cycling, with the mitigation of electrode swelling, however, the results obtained are promising for the use of C_4mpyrTFSI-based electrolytes with nanostructured electrodes.

References

[1] J. Luo, J. Liu, Z. Zeng, C. F. Ng, L. Ma, H. Zhang, J. Lin, Z. Shen, H. J. Fan, *Nano Letters* **2013**, *13*, 6136-6143 10.1021/nl403461n.

[2] Y.-K. Sun, S.-T. Myung, B.-C. Park, J. Prakash, I. Belharouak, K. Amine, *Nature Materials* **2009**, *8*, 320-324 10.1038/nmat2418.

[3] Y. Yao, M. T. McDowell, I. Ryu, H. Wu, N. Liu, L. Hu, W. D. Nix, Y. Cui, *Nano Letters* **2011**, *11*, 2949-2954 10.1021/nl201470j.

[4] Y. Gan, L. Zhu, H. Qin, Y. Xia, H. Xiao, L. Xu, L. Ruan, C. Liang, X. Tao, H. Huang, W. Zhang, *Solid State Ionics* **2015**, *269*, 44-50 https://doi.org/10.1016/j.ssi.2014.11.017.

[5] T. Lan, H. Qiu, F. Xie, J. Yang, M. Wei, *Scientific Reports* **2015**, *5*, 8498 10.1038/srep08498.

[6] H. Qiao, Y. Wang, L. Xiao, L. Zhang, *Electrochemistry Communications* **2008**, *10*, 1280-1283 https://doi.org/10.1016/j.elecom.2008.06.024.

[7] E. Armstrong, D. McNulty, H. Geaney, C. O'Dwyer, *ACS Applied Materials & Interfaces* **2015**, *7*, 27006-27015 10.1021/acsami.5b09511.

[8] J. H. Pikul, H. Gang Zhang, J. Cho, P. V. Braun, W. P. King, *Nature Communications* **2013**, *4*, 1732 10.1038/ncomms2747.

[9] A. Vu, Y. Qian, A. Stein, *Advanced Energy Materials* **2012**, *2*, 1056-1085 10.1002/aenm.201200320.

[10] H. Zhang, X. Yu, P. V. Braun, *Nature Nanotechnology* **2011**, *6*, 277-281 10.1038/nnano.2011.38.

[11] D. McNulty, E. Carroll, C. O'Dwyer, *Advanced Energy Materials* **2017**, *7*, 1602291 10.1002/aenm.201602291.

[12] D. McNulty, H. Geaney, E. Armstrong, C. O'Dwyer, *Journal of Materials Chemistry A* **2016**, *4*, 4448-4456 10.1039/C6TA00338A.

[13] K. Zaghib, J. Dubé, A. Dallaire, K. Galoustov, A. Guerfi, M. Ramanathan, A. Benmayza, J. Prakash, A. Mauger, C. Julien, **2014**, pp. 437-460.

[14] M. Le Thai, G. T. Chandran, R. K. Dutta, X. Li, R. M. Penner, *ACS Energy Letters* **2016**, *1*, 57-63 https://doi.org/10.1021/acsenergylett.6b00029.

[15] L. M. McGrath, J. Jones, E. Carey, J. F. Rohan, in *ChemistryOpen, Vol. 8*, **2019**, pp. 1429-1436.

[16] W. Luo, X. Hu, Y. Sun, Y. Huang, *Journal of Materials Chemistry* **2012**, *22*, 4910-4915 10.1039/C2JM15197A.

[17] H. Wang, D. Ma, X. Huang, Y. Huang, X. Zhang, *Scientific Reports* **2012**, *2*, 701 10.1038/srep00701.

[18] W. J. H. Borghols, D. Lützenkirchen-Hecht, U. Haake, W. Chan, U. Lafont, E. M. Kelder, E. R. H. van Eck, A. P. M. Kentgens, F. M. Mulder, M. Wagemaker, *Journal of The Electrochemical Society* **2010**, *157*, A582 10.1149/1.3332806.

Chapter 7:

Preliminary Full Cell Analysis

7.1 Abstract

Ionic liquid-based full cells are constructed using V_2O_5 cathodes and Ge anodes. Initial analysis demonstrates that VC-containing electrolytes require pre-lithiation steps as negligible capacities (<10 mAh g^{-1}) are obtained at higher C-rates, while the VC-free cell exhibits a capacity of ~20 mAh g^{-1} at 5 C. Pre-lithiating the cells yields a significant increase in the electrochemical performance of the VC-containing cell as the charge capacity at 0.15 C is ~135 mAh g^{-1} (~92% of theoretical), while the VC-free cell exhibits a drop in capacity, for example at 1 C the discharge capacity is ~20 mAh g^{-1} versus ~50 mAh g^{-1} for the non-pre-lithiated cell. Up to 400 cycles was demonstrated with both VC-free and VC-containing cells, where the maximum capacity fade noted across 50 cycles are 0.5 and 0.9 mAh g^{-1} respectively for cycles 100 to 150 (0.2 C) charge data, however, little capacity fade is observed for the higher C-rates.

A reduction in the separator thickness results in more stable cycling across the C-rates as minimal capacity drop is observed in the VC-containing 260 versus a 900 μm thick electrolyte cell (~0.3 vs. ~1 mAh g^{-1} per cycle at 0.5 C, respectively). Up to 700 cycles was achieved for both VC- and VC-free cells without significant capacity fade or cell failure. These cells are comparable to typical solid-state microbatteries, as capacities of 5.7 and 3.2 μAh at 0.2 C (cycles 11 to 20) and 1 C (cycles 41 to 50) respectively are demonstrated by the prototype, with an average discharge capacity of 1.3 μAh at 5 C for cycles 600 to 650 being attained after significant C-rate analysis.

7.2 Introduction

Various cathode and anode materials in the literature have demonstrated compatibility with C_4mpyr-based IL electrolytes as demonstrated in chapter 1. Several prototypes have been investigated by various research groups, where Li metal anode materials have been utilised. Balducci *et al.*[1] investigated Li metal batteries with a polymer gel electrolyte, in addition to a Li-ion batteries utilising LTP and LTO electrodes. Prototype cells were created by stacking 12 to 14 single bipolar cells to achieve a theoretical cell capacity of 0.7 Ah to 0.8 Ah. The electrolyte utilised with the Li-ion battery was a liquid electrolyte: C_4mpyrFSI with LiTFSI salt, while the Li metal battery contained a cross-linked PEO with C_4mpyr TFSI with LiTFSI salt. In both instances, long term cycling was attained as 1000 cycles were obtained for each C-rate, with minimal capacity fade observed. The cell capacity for both the Li metal and Li-ion batteries at C/20 is close to theoretical. Similarly, Kim *et al.*[2] utilised Li/LFP and LTO/LFP cells with C_4mpyrFSI-based electrolytes: PEO-LiTFSI-C_4mpyrFSI, and LiTFSI-C_4mpyrFSI electrolyte respectively. In both instances large scale batteries were utilised where electrode dimensions were ~8 or 10 cm x 5 cm.

Full cells incorporating group IV elements have been reported where Chaudoy *et al.*[3] constructed a battery prototype containing LCO cathode, microporous Si anode and a polymer gel electrolyte with PVDF-HFP, LiTFSI and C_4mpyrFSI. Thirty cycles were demonstrated, and the capacity obtained for it was 28% lower than that where Li metal is utilised. Therefore, further optimisation of the materials is required in order to ensure high cell capacities. Promising long-term results with group IV elements were obtained by Elia *et al.*[4] as more than 2000 cycles were demonstrated with coulombic efficiency close to 100% for a Sn-C/LFP cell. From the study, they determined that the C_4mpyrFSI-based IL allows for good high rate capabilities, as the cell capacity (w.r.t. LFP) was ~80 mAh g^{-1} at a current density of 500 mA g^{-1}. This was maintained over 2000 cycles, as a capacity retention of 98% was obtained after cycling. The exceptional cycling is due in part to the formation of an SEI layer after 10

cycles, in addition to low interfacial resistances. These results demonstrate that long-term cycling can be achieved with minimal capacity fade, or cell failure.

To the best of our knowledge, no full cells containing Ge anodes have been reported with C_4mpyr-based ionic liquids, however, literature is available for Ge-containing full cells with organic electrolytes.[5-7] In such studies either nanostructured[5, 7] or hybrid Ge electrodes[6] were employed. Li *et al.*[6] investigated full cells containing Ge/carbon hybrid nanoparticles as anodes, and $LiCoO_2$ cathodes. A 2016 coin cell format was utilised, where 1 M $LiPF_6$ in EC:DMC:DEC (1:1:1 v/v/v) was used as the electrolyte. Before full cell construction, the Ge anode underwent pre-lithiation treatment, and the full cells delivered a capacity of 712 mAh g^{-1} after 300 cycles, where the capacity drop per cycle was 0.018%. High C-rate capabilities were also determined, as stable discharge capacities of 606 mAh g^{-1} was attained at 5 C, where the voltage window utilised was 2.7 V to 4.4 V. Nanostructured Ge materials were investigated by Li *et al.*[7] whereby Ge was coated onto Co_3O_4 nanowires and placed into a 2032 coin cell with $LiCoO_2$ cathode and 1 M $LiPF_6$ in EC: DEC (1:1 v/v) electrolyte. In this instance a narrower electrochemical window (2.8 V to 3.9 V) was employed to prevent the Co_3O_4 from participating in the electrochemical reaction. High capacities have been reported at C-rates as high as 20 C (~1299 mAh g^{-1}), where the capacity corresponds to 98.5 % of capacities obtained at 0.5 C. Longer-term cycling at 5 C (150 cycles) have yielded final capacities above 1250 mAh g^{-1}. Mesoporous Ge electrodes with broad temperature ranges (-20 ºC to 60 ºC) have been utilised in full cells[5] with $LiFePO_4$ cathodes and 1.3 M $LiPF_6$ in EC: DEC (3:7 v/v) electrolyte with 10 wt.% FEC. These studies have highlighted that full cells containing Ge anodes can exhibit high electrode capacities at high C-rates, in addition to long cycle life (~300 cycles). However, full cells with dimensions less than those of coin cells have yet to be demonstrated.

Full cells incorporating V_2O_5 have been investigated in both organic and ionic liquid based electrolytes,[8-9] however, no full cell analysis has been demonstrated with C_4mpyr-based ionic liquids.

Cheah *et al.*[9] reported a full cell consisting of V_2O_5 nanofibres with $Li_4Ti_5O_{12}$ cathodes and 1 M $LiPF_6$ in EC: DMC electrolyte. A 2016 coin cell format was utilised, where a potential range of 1 V to 2.5 V was utilised to limit the Li^+ intercalation/deintercalation to 1 mol per Li per formula unit. Initial electrode capacities of ~120 mAh g^{-1} and ~110 mAh g^{-1} were attained at current densities of 20 mA g^{-1} and 100 mA g^{-1}, respectively. Higher electrode capacities can be obtained if Li^+ intercalation/deintercalation is not restricted to 1 mol per Li per formula unit, as each Li+ inserted yields a theoretical capacity of ~147 mAh g^{-1}. Lu *et al.*[8] utilised full cells consisting of vertically aligned carbon nanotubes (CNT) sheathed with V_2O_5 as the cathode, and without the V_2O_5 sheath as the anode. An ionic liquid electrolyte: N-ethyl-N,N-dimethyl-2-methoxyethylammonium bis(trifluoromethylsulfonyl)imide (EDMMEA TFSI) containing 1 M LiTFSI and 20% EC was utilised. In this instance, the potential range utilised allowed for the intercalation/deintercalation of three Li ions per unit formula. Capacities of 150 mAh g^{-1} were attained at 1 C within the potential range of ~3.7 V to 1 V. Comparing the two V_2O_5 containing full cells, maximum energy densities of ~215 Wh kg^{-1} and ~847 Wh kg^{-1} were obtained for the V_2O_5/ $Li_4Ti_5O_{12}$ and V_2O_5-CNT/CNT full cells respectively.

In this chapter, preliminary full cells containing D.C. sputtered Ge anodes, and electrodeposited V_2O_5 cathodes with C_4mpyr-based ionic liquids are constructed and tested to determine the feasibility of this particular material combination for use as a Li-ion battery.

7.3 Experimental

7.3.1 Ge fabrication

A stack of Ti (10 nm) and Cu (250 nm) was deposited on a 4" diameter silicon wafer using metal sputter targets (Kurt J. Lesker) in a D.C. magnetron (Quorum Q300T D) dual sputter coating system. The Ti layer acted as an adhesion layer between the SiO_2 substrate and Cu current collector. Planar Ge samples were created by direct current (D.C.) sputter deposition in an Ar environment using a 99.99% pure Ge target (Kurt J. Lesker) at a pressure and current of 1 $x10^{-2}$ mBar and 90 mA, respectively. A punched Cu foil template was placed over the samples during sputtering to control the size of the active electrode area (0.64 cm^2).

7.3.2 V_2O_5 fabrication

A stack of Ti (10 nm) and Au (100 nm) was deposited on a 1 μm thermal annealed SiO_2 layer on a 4" diameter silicon wafer using metal sputter targets (Kurt J. Lesker) in a D.C. magnetron (Quorum Q300T D) Dual sputter coating system. The Ti layer acted as an adhesion layer between the SiO_2 substrate and Au current collector. V_2O_5 was electrodeposited at room temperature using a CH Instruments 660B potentiostat. A constant potential of 2 V was applied for 10 s to the Ti/Au working electrode to achieve approximately 220 nm V_2O_5 in a three electrode setup with a saturated calomel electrode (SCE) and platinum (Pt) mesh as the reference and counter electrode, respectively. The electrochemical bath was made up of a 0.25 M solution of $VOSO_4.xH_2O$, (assumed degree of hydration is 5) purchased from Sigma Aldrich, in a 1:1 (v/v) mixture of deionized water (DI) and ethanol. After deposition, the samples were heated to 325 °C for 7 hours to crystallise the V_2O_5 deposit.

7.3.3 Cell construction and characterisation

A pouch cell was constructed as shown in figure 7.1, where the Ge and V_2O_5 electrode were placed opposite each other separated with either a glass fibre separator soaked with C_4mpyr-based ionic or by PG-60 (polymer gel electrolyte).

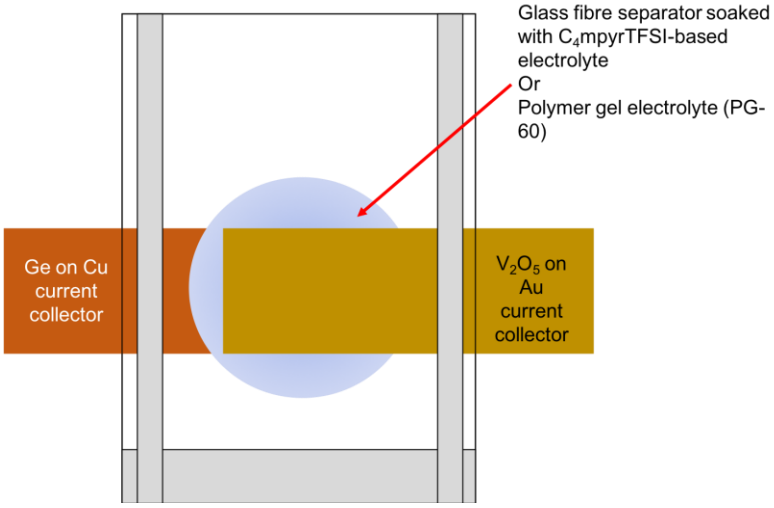

Figure 7.1: Schematic of pouch cell utilised for full cell tests.

Electrochemical measurements of the Li^+ capacity were assessed by CV and galvanostatic cycling with potential limitation (GCPL) using a Bio-logic VSP potentiostat at various scan rates and discharge/charge currents, respectively. A two electrode pouch cell setup was utilised where the D.C. sputtered Ge on Cu current collector acted as counter and reference electrode, with V_2O_5 on Au current collector acting as the working electrode. The electrodes were separated by either a glass fibre separator soaked in 0.5 M LiTFSI in C_4mpyrTFSI, or 3 wt.% VC in 0.5 M LiTFSI in C_4mpyrTFSI, or separated with a polymer gel electrolyte (PG-60). Cell assembly was carried out in an argon-filled glove box (M. Braun LABstar Glove Box) with O_2 and H_2O maintained below 0.1 ppm.

7.4 Results and discussion

CV analysis was carried out whereby the Ge anode acted as both the counter and reference electrode. Due to the multiple Li insertion phases observed for V_2O_5, only the voltage range which exhibited the ε/δ and α/ε intercalation peaks was considered. From the analysis, the appropriate voltage range was determined to be between 0.1 V and 3.3 V as the ε/δ and α/ε intercalation peaks are observed within this region. The initial tests carried out were on liquid-based cells which had not undergone pre-lithiation. These tests were utilised to determine the effects pre-lithiation would have on the cell's performance. As shown in figure 7.2, the coulombic efficiencies for both electrolytes is below 40% for the initial 30 cycles. This is indicative of SEI layer formation at both cathode and anode interfaces. The coulombic efficiency for the 3 wt.% VC increases incrementally over the following cycles until an efficiency of 99.9% is achieved at cycle 70. By comparison, the additive-free cell exhibited a jump in the coulombic efficiency from ~40% to >90% from cycle 40 onwards, with electrode capacities of ~50 mAh g^{-1} at 1 C. This shows that the additive-free cell is more capable of cell stabilisation the electrodes have not been pre-lithiated. The 3 wt.% VC cell does not perform as well as the electrode discharge capacity reaches a maximum of 40 mAh g^{-1} at 0.2 C, with negligible capacities (<10 mAh g^{-1}) being obtained at higher C-rates. This may suggest that the superior film forming abilities of VC hinders the lithiation of electrode materials as the SEI layer formation rapidly consumes the Li present in the electrolyte, thus resulting in the low electrode capacities. As evidenced in chapters 4 and 5, the additive-free electrolyte required greater than 30 cycles to achieve a stable cell with coulombic efficiencies in excess of 90%, therefore the sluggish SEI layer formation allowed for the electrodes to become sufficiently lithiated to yield electrode capacities in excess of 10 mAh g^{-1}.

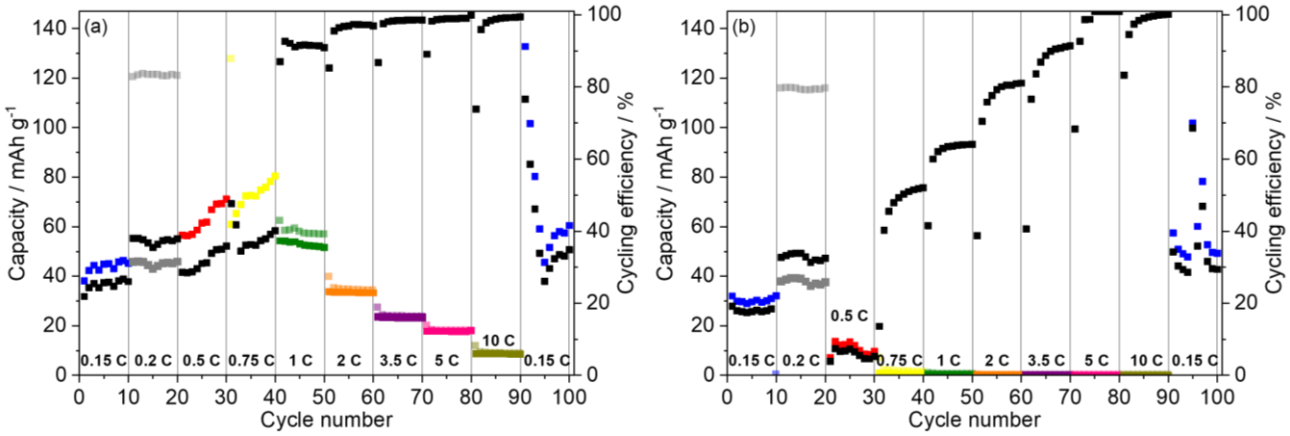

Figure 7.2: Full cell tests carried out in (a) 0.5 M LiTFSI in C_4mpyrTFSI and (b) 3 wt.% VC in 0.5 M LiTFSI in C_4mpyrTFSI.

When the electrodes are pre-lithiated, an enhanced electrochemical performance is observed for the additive-containing cell as shown in figure 7.3(b). In this instance, the charge capacity at 0.15 C is ~135 mAh g^{-1} (~92% of theoretical) with a coulombic efficiency >60% which suggests that a sufficient SEI layer was formed at both interfaces during pre-lithiation. The additive-free cell, however, still undergoes SEI layer formation as evidenced by the low coulombic efficiency (<50%) for the first 20 cycles. This is expected as only 10 pre-lithiation cycles were carried out, and at least 30 cycles are required for cell stabilisation. However, even after cell stabilisation, the capacities obtained are significantly lower than for the cell without pre-lithiation (figure 7.2(a)), for example at 1 C the discharge capacity is ~20 mAh g^{-1} versus ~50 mAh g^{-1}. This suggests that the Li consumption during the CV pre-lithiation stage is more extensive than for the galvanostatically charged cells, resulting in lower capacities. The VC-containing cell exhibited an improved electrochemical performance after pre-lithiation as higher electrode capacities are obtained, for example, at 1 C the average discharge capacity is ~50 mAh g^{-1} for the pre-lithiated cells, while the capacity was <10 mAh g^{-1} at 1 C for the non-lithiated cell (figure 7.2(b)). In addition, the coulombic efficiency of the pre-lithiated cell was above 60% for all C-rates, which is a significant improvement as 40 cycles was required to achieve a similar efficiency in the non-lithiated cell.

Comparing the performances of the lithiated cells it is clear that the VC-containing electrolyte yields an improved performance across the C-rates, particularly at lower C-rates. At 0.15 C, the VC-containing cell exhibited a discharge capacity of ~90 mAh g^{-1} (61% of theoretical), while ~75 mAh g^{-1} (51% of theoretical) was obtained for the additive-free cell. A similar trend is observed at 1 C. However, despite the increased capacity, a higher drop is noted across the 10 cycles for the VC-containing cell (~0.6 vs. ~0.05 mAh g^{-1} per cycle). At 10 C, similar capacities are obtained (~3% of theoretical), which demonstrates that the cell is incapable of sustaining practical capacities at high C-rates, regardless of the electrolyte utilised.

Long-term cycling analysis (up to 400 cycles) was carried with both cells to determine if the cell is capable of sustaining a cycle life beyond 100 cycles. As mentioned in chapter 4, Ge undergoes expansion and contraction during cycling with Li, leading to delamination of Ge from the current collector. As shown in figure 7.3, both full cells are capable of sustaining 400 cycles, with stable cycling being maintained across all C-rates. The maximum capacity fade noted across 50 cycles for the VC-free and VC-containing cells are 0.5 and 0.9 mAh g^{-1} respectively for cycles 100 to 150 (0.2 C) charge data, however, little capacity fade is observed for the higher C-rates. An improvement in the 0.5 C capacity is observed for the 0.5 M LiTFSI cell as cycles 150 to 200 yielded an average discharge capacity of 35 mAh g^{-1}, while cycles 20 to 30 exhibited 22 mAh g^{-1}. In addition, the coulombic efficiency is improved from 71% to 85%. At higher C-rates such as 5 C, the capacities obtained are similar to the initial values, ~9 mAh g^{-1}, which despite being low, demonstrate that electrode integrity is maintained up to 350 cycles. This is further compounded by the final 0.2 C data, ~52 mAh g^{-1}, which matches cycles 100 to 150.

The VC-containing cell experiences a decrease in its electrode capacity with increased cycle number as capacities less than 40 mAh g^{-1} are achieved across the C-rates. The capacities are similar or less than those for the additive-free cell as shown in table 7.1. The final 0.2 C data (cycles 350 to 400)

yield a capacity lower than cycles 100 to 150 which suggest that long diffusion pathways (thick separators) are not suited for VC-containing electrolytes.

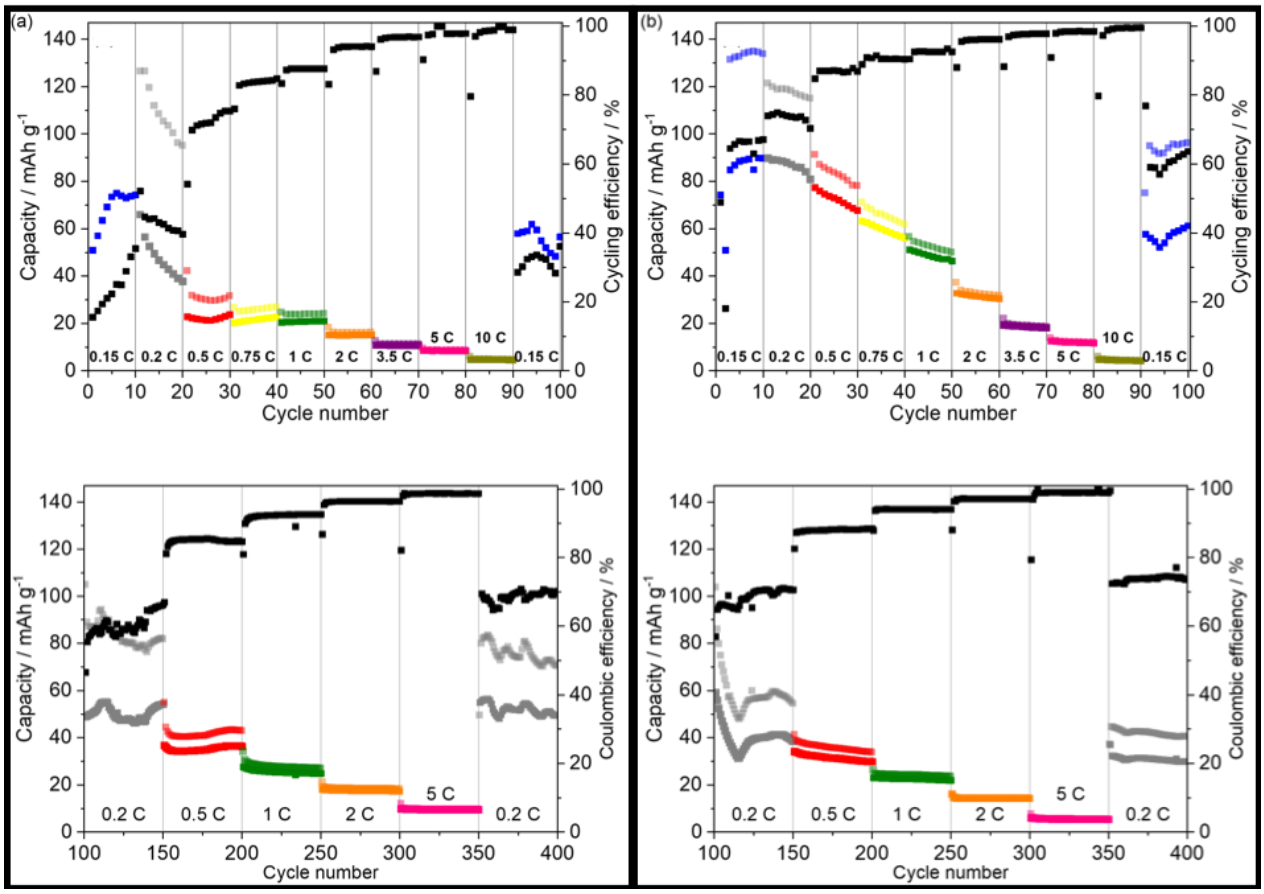

Figure 7.3: Full cell tests carried out in (a) 0.5 M LiTFSI in C_4mpyrTFSI and (b) 3 wt.% VC in 0.5 M LiTFSI in C_4mpyrTFSI. Separator: 900 μm glass fibre.

C-rate	Average discharge capacity (mAh g^{-1})	
	0.5 M LiTFSI in C_4mpyrTFSI	3 wt.% VC in 0.5 M LiTFSI in C_4mpyrTFSI
0.2	50	40
0.5	35	31
1	25	22
2	18	14
5	9	5
0.2 (final)	52	31

Table 7.1: Comparison of the average discharge capacities obtained during the long-term analysis of the full cells at different C-rates.

However, the need to miniaturise energy storage devices requires higher volumetric density, therefore the reduction of inactive components such as electrode binders and separators is required. The cells mentioned above utilised a 900 μm glass fibre separator, and a reduction in this thickness would allow for higher volumetric densities. A 260 μm separator was utilised in the cells, and they underwent the same pre-lithiation steps and analysis as above, with the results shown in figure 7.4. Higher capacities are obtained with the thinner separator are higher than those obtained for the 900 μm cell, particularly in the case of 0.5 M LiTFSI in C_4mpyrTFSI as shown in table 7.2. The capacity obtained for the 260 μm VC-containing cell is similar to those obtained with the 900 μm separator, as shown in table 7.2, however, more stable cycling is observed across the C-rates as minimal capacity drop is observed in the 260 μm cell versus the 900 μm cell (~0.3 vs. ~1 mAh g^{-1} per cycle at 0.5 C, respectively). Like the 900 μm cells, the 260 μm VC-containing cell outperformed the VC-free cell at low C-rates (<2 C) as shown in table 7.4, with similar capacities obtained at high C-rates (>2 C).

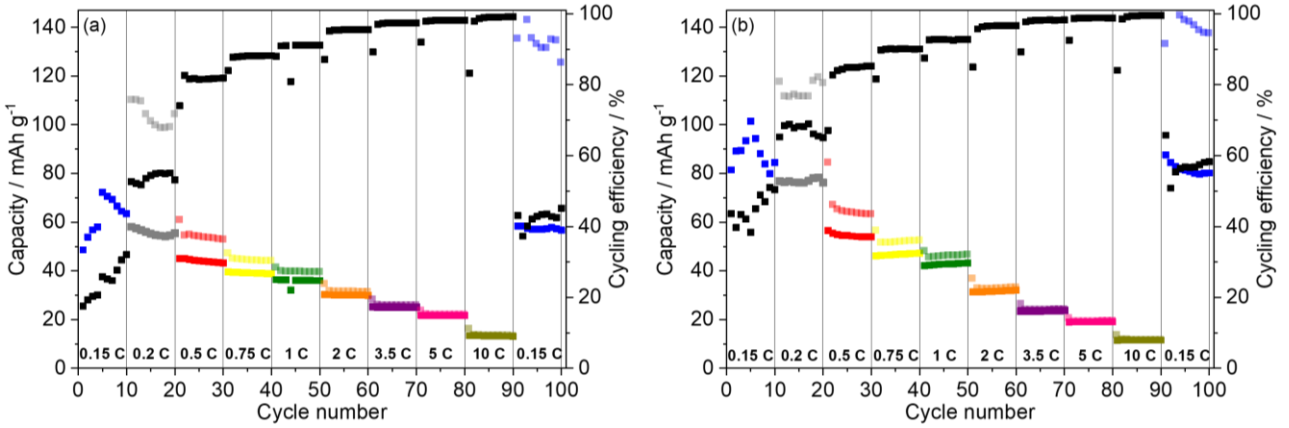

Figure 7.4: Full cell tests carried out in (a) 0.5 M LiTFSI in C_4mpyrTFSI and (b) 3 wt.% VC in 0.5 M LiTFSI in C_4mpyrTFSI. Separator: 260 μm glass fibre.

C-rate	Average discharge capacity (mAh g^{-1})			
	0.5 M LiTFSI in C_4mpyrTFSI		3 wt.% VC in 0.5 M LiTFSI in C_4mpyrTFSI	
	900 μm	260 μm	900 μm	260 μm
0.15	68	62	83	89
0.5	22	44	72	55
1	21	36	49	43
3.5	11	25	19	24
10	5	13	4	12
0.15 (final)	56	57	57	82

Table 7.2: Comparison of the average discharge capacities obtained for the 900 μm and 260 μm full cells at different C-rates.

The long-term performance of the 260 μm cells were investigated up to 700 cycles, with similar analysis being carried out for the initial 100 cycles as shown in figure 7.4. For the VC-free cell, there is a decrease in the capacity observed between the initial 100 cycles and the subsequent 300 cycles

as 15 to 20 mAh g^{-1} capacity drop is experienced for 0.5, 1, 2 and 5 C. In the following 300 cycles, the capacity is maintained which suggests that the cell has stabilised as 16 mAh g^{-1} was maintained at 1 C for cycles 201 to 250 and 501 to 550. Minimal capacity fade is observed for the cell even at cycles 601 to 650 (5 C), where a drop of only 0.001 mAh g^{-1} was noted per cycle. Unlike the VC-free cell, the VC-containing cell experienced minimal capacity drop between the initial 100 cycles and its subsequent 300 as a 1 to 6 mAh g^{-1} drop is observed for all investigated C-rates. This demonstrates the VC-cell's ability to stabilise the electrode/electrolyte interface, which ensures stable cycling. Overall, the VC-cell yields higher capacities across the C-rates than for the VC-free cell, however, a significant drop in the capacity (from ~96 to 56 mAh g^{-1}) is observed in the last number of cycles. This may be indicative of cell failure or could suggest that a significant event such as partial electrode delamination or cracking has occurred within the cell. Due to the current restrictions and equipment issues, the reason for this drop in capacity is currently unknown but will be investigated when appropriate.

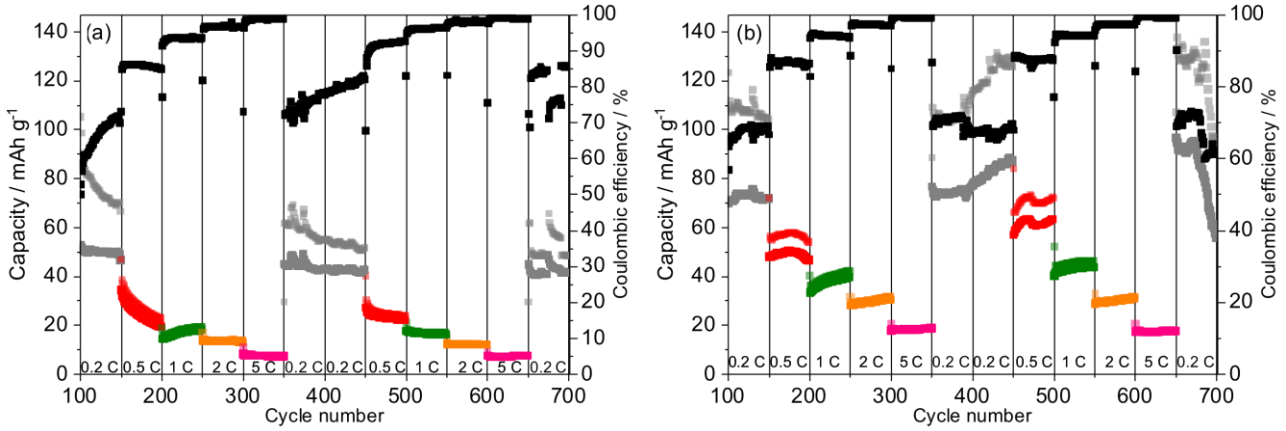

Figure 7.5: Long-term cycling tests carried out in (a) 0.5 M LiTFSI in C_4mpyrTFSI and (b) 3 wt.% VC in 0.5 M LiTFSI in C_4mpyrTFSI. Separator thickness: 260 µm.

The results obtained for the liquid IL electrolytes yield promising results as they demonstrate long-term stability (600 to 700 cycles) for binder-free planar Ge containing cells. The theoretical capacity of the full cells is 10.5 µAh. Figure 7.6 demonstrates the capability of the 260 µm full cells. For the

additive-free cell (figure 7.6(a)) capacities between 1 and 5 µAh are attained in the initial 100 cycles, whereby the average discharge capacity at 0.2 C was 4 µAh (~38% of theoretical). A similar trend is observed for the VC-containing cell, as the average capacity for the VC-cell is 5.7 and 3.2 µAh at 0.2 C (cycles 11 to 20) and 1 C (cycles 41 to 50) respectively. Even at a high C-rate of 10 C (cycles 81 to 90), 0.9 µAh is obtained. The VC-containing cell maintains an average discharge capacity of 1.3 µAh at 5 C for cycles 600 to 650, which show that the prototypes are competitive with commercial microbatteries provided further optimisation take place. In addition, the electrode thicknesses utilised within the full cells account for 300 nm (220 nm and 80 nm for V_2O_5 and Ge respectively), while typical microbatteries utilise micron scale electrodes.

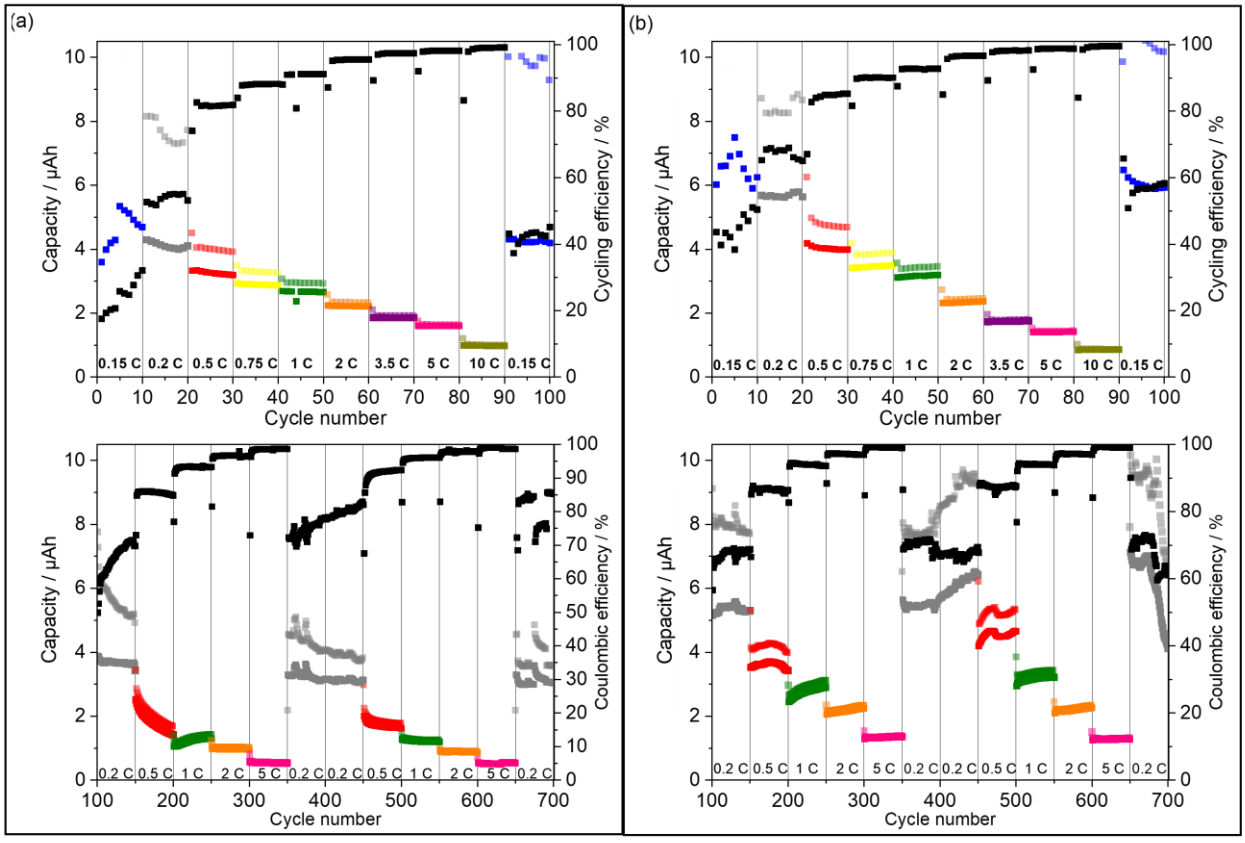

Figure 7.6: Full data demonstrating the capacity of the prototype batteries for (a) 0.5 M LiTFSI in C_4mpyrTFSI and (b) 3 wt.% VC in 0.5 M LiTFSI in C_4mpyrTFSI.

However, in order to be truly competitive with commercial microbatteries, a solid-state electrolyte must be utilised. A full cell test incorporating 312 µm PG-60 electrolyte was carried out. As the literature utilise slow C-rates such as C/20,[1-2] the analysis was carried out using 0.01 C to 0.1 C. The results are shown in figure 7.7. The galvanostatic profiles suggest that 0.01 C is too slow a scan rate to utilise for the cell as it appears that complicated side reactions occur which prevent the cell from charging. When 0.1 C is applied, the cell charges and discharges with no issues, hence careful consideration of the C-rate is required. From the capacity data, it is evident that low electrode capacities (< 14% of theoretical) are obtained at these slow C-rates. If faster rates are applied, then negligible capacities are obtained which may indicate that there is poor interfacial contact between the electrodes and the electrolyte or else the diffusion pathway for Li is too long, thus resulting in lower capacities.

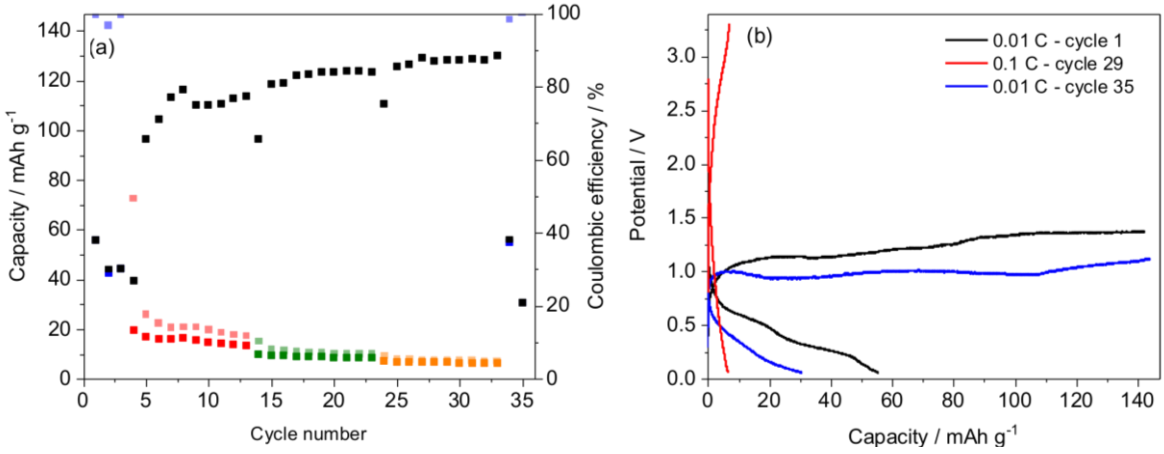

Figure 7.7: (a) Capacity versus cycle number at 0.01 C (blue), 0.05 C (red), 0.075 C (green) and 0.1 C (orange), where black refers to the coulombic efficiency and (b) galvanostatic profiles obtained for the full cell. Electrolyte: 312 µm PG-60

Further work is required to fully analyse the interfacial kinetics as good performances are expected with PG-60 as both Ge and V_2O_5 exhibited high electrode capacities and coulombic efficiencies in the half-cell tests. However, one method to try and improve the capacity per unit volume of the PG-60 cell is to reduce the electrolyte thickness. In order to reduce the thickness of PG-60, spin coating

is an option as it allows the electrolyte to be spun directly onto the electrode surface which ensures good interfacial contact. In order to optimise the parameters for spin coating, a variety of spin speeds were selected and analysed. The polymer was spin coated onto a 4 inch wafer, and the resultant thickness and corresponding ionic conductivities are shown in table 7.3. As the spin speed increases, the thickness decreases which is expected, however, the ionic conductivity also decreases with increased spin speed. As shown in table 7.3, high spin speeds such as 150 rpm yield ionic conductivities similar to the drop-cast PG-50, which consists of 50% ionic liquid. This decrease in conductivity could be attributed to the loss of ionic liquid and LiTFSI salt from the polymer when high spin speeds are utilised.

Spin speed (rpm)	Thickness (µm)	Ionic conductivity (mS cm^{-1})	Similar to drop cast polymer (chapter 3)
55	132	2.76	~0.3 to 0.8 mS cm^{-1} higher than PG-60
75	83	2.27	
100	91	1.39	~0.5 to 0.8 mS cm^{-1} less than PG-60
120	63	1.1	
150	55	0.61	PG-50

Table 7.3: Comparing the thickness and ionic conductivity of the polymer gels at different rpms.

A relationship between the spin speed and ionic conductivity was investigated and a linear relationship was identified as shown in figure 7.8. From the graph it was determined that spin speeds of ~89 rpm would yield a similar ionic conductivity as that observed for the drop casted polymer gel electrolyte PG-60. Both spin speeds were investigated and ionic conductivities of 1.5 and 1.7 mS cm^{-1} were obtained for 89 and 88 rpm, respectively. These results demonstrate that a prediction can be made from the spin speed to determine the ionic conductivity of PG-60, which will enable easy fabrication and tailoring of the electrolyte to suit any application.

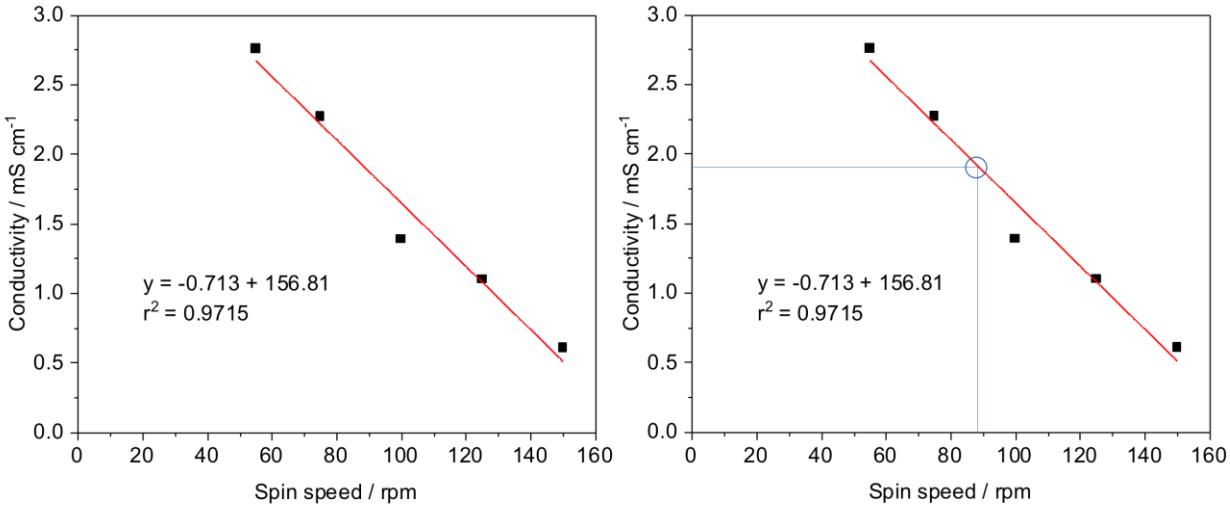

Figure 7.8: Relationship between spin speed and ionic conductivity of the polymer gel electrolytes, where the right image depicts the rpm which should produce film conductivities of ~1.9 mS cm^{-1}.

These results show the promise of V_2O_5/Ge cells, however, in order to realise their potential for IoT sensors, further optimisation is required, particularly with the polymer gel electrolyte in order to achieve a balanced cell with minimal loss of Ge active material. This may require the utilisation of thicker electrodes (µm-scale) which will compensate the loss of Ge during cycling. Due to the ongoing COVID-19 restrictions, the timescale for optimisation is longer than originally anticipated. Therefore, we have focused our research efforts on the alternative V_2O_5/Li full cell realised in chapter 5, where a 220 nm V_2O_5/Li cell exhibited over 400 cycles without the occurrence of short-circuiting, while maintaining high electrode capacities with minimal capacity fade (0.4% over 50 cycles at 5 C). Due to its compatibility with both liquid and polymer gel electrolytes, it is a suitable alternative to expedite the creation of a microbattery for IoT sensors. Comparing its performance with 0.5 M LiTFSI in C_4mpyrTFSI with the V_2O_5/Ge cell, it is evident that the 220 nm V_2O_5/Li cell performance is superior as capacities of ~6 µAh were obtained at 1 C (< 3 µAh for Ge-containing cell).

7.5 Conclusion

Pre-lithiation of V_2O_5/Ge cells is essential when utilising C_4mpyrTFSI-based electrolyte containing VC, while VC-free cells exhibit stable cycling after 40 cycles with capacities of ~60 μAh g^{-1} being obtained at 1 C. The performance of the VC-free cells is not greatly enhanced upon pre-lithiation as similar capacities are obtained when compared to its non-lithiated counterpart. However, a significant improvement occurs in the VC-cell as a capacity >30 mAh g^{-1} is obtained at 2 C, while the non-lithiated cell exhibited a capacity <1 mAh g^{-1}. Both the VC-free and VC-containing pre-lithiated cells exhibited long-term cycling capabilities as the maximum capacity fade noted across 50 cycles for the VC-free and VC-containing cells are 0.5 and 0.9 mAh g^{-1} respectively for cycles 100 to 150 (0.2 C) charge data, however, little capacity fade is observed for the higher C-rates.

The utilisation of a 260 μm separator leads to further improvements in the electrochemical performance of the cells as more stable cycling is observed across the C-rates as minimal capacity drop is observed in the VC-containing 260 μm cell versus the 900 μm cell (~0.3 vs. ~1 mAh g^{-1} per cycle at 0.5 C, respectively). This is further demonstrated with in the long-term cycling tests as minimal capacity fade is observed for the cell even at cycles 601 to 650 (5 C), where a drop of only 0.001 mAh g^{-1} was noted per cycle for the VC-free cell. The cells demonstrate long-term cyclability which has not been previously mentioned in the literature for a binder-free planar Ge thin film-containing battery.

It is evident to see that the prototype is a competitor to typical solid-state microbatteries as VC-cell exhibits 5.7 and 3.2 μAh at 0.2 C (cycles 11 to 20) and 1 C (cycles 41 to 50) respectively. Even at a high C-rate of 10 C (cycles 81 to 90), 0.9 μAh is obtained. Remarkably, the VC-containing cell manages to maintain an average discharge capacity of 1.3 μAh at 5 C for cycles 600 to 650, which show that the prototypes are capable of being competitive with commercial microbatteries provided

further optimisation take place. In addition, the electrode thickness utilised within the full cells account for 300 nm (220 nm and 80 nm for V_2O_5 and Ge respectively), while typical microbatteries utilise micron scale electrodes.

Solid-state prototype tests were carried out using slow C-rates, however, the capacities obtained are too low to be competitive with commercial cells. A method to reduce the thickness of the polymer is to spin coat the polymer gel. This would allow for greater interfacial contact to be attained, in addition to thinner electrolytes and higher volumetric energy density. A reliable fabrication method has been identified which utilises a relationship between spin speed and ionic conductivity, which can allow for tailored solutions to be obtained.

Due to COVID-19 lockdown and restrictions, further tests to optimise the full cells could not be carried out, however, the results shown demonstrate promise for ionic liquid-based batteries containing Ge and V_2O_5 electrodes.

References

[1] A. Balducci, S. S. Jeong, G. T. Kim, S. Passerini, M. Winter, M. Schmuck, G. B. Appetecchi, R. Marcilla, D. Mecerreyes, V. Barsukov, V. Khomenko, I. Cantero, I. De Meatza, M. Holzapfel, N. Tran, *Journal of Power Sources* **2011**, *196*, 9719-9730 https://doi.org/10.1016/j.jpowsour.2011.07.058.

[2] G. T. Kim, S. S. Jeong, M. Z. Xue, A. Balducci, M. Winter, S. Passerini, F. Alessandrini, G. B. Appetecchi, *Journal of Power Sources* **2012**, *199*, 239-246 https://doi.org/10.1016/j.jpowsour.2011.10.036.

[3] V. Chaudoy, E. Luais, F. Ghamouss, T. Defforge, S. Desplobain, G. Gautier, J. Wolfman, J.-C. Houdbert, F. Tran-Van, J. Sakai, *ECS Transactions* **2015**, *66*, 31-39 10.1149/06608.0031ecst.

[4] G. A. Elia, U. Ulissi, S. Jeong, S. Passerini, J. Hassoun, *Energy & Environmental Science* **2016**, *9*, 3210-3220 10.1039/C6EE01295G.

[5] S. Choi, Y.-G. Cho, J. Kim, N.-S. Choi, H.-K. Song, G. Wang, S. Park, *Small* **2017**, *13*, 1603045 10.1002/smll.201603045.

[6] X. Li, J. Liang, Z. Hou, W. Zhang, Y. Wang, Y. Zhu, Y. Qian, *Journal of Power Sources* **2015**, *293*, 868-875 https://doi.org/10.1016/j.jpowsour.2015.06.031.

[7] X. Li, Z. Yang, Y. Fu, L. Qiao, D. Li, H. Yue, D. He, *ACS Nano* **2015**, *9*, 1858-1867 10.1021/nn506760p.

[8] W. Lu, A. Goering, L. Qu, L. Dai, *Physical Chemistry Chemical Physics* **2012**, *14*, 12099-12104 10.1039/C2CP40726D.

[9] Y. L. Cheah, V. Aravindan, S. Madhavi, *ACS Applied Materials & Interfaces* **2013**, *5*, 3475-3480 10.1021/am400666n.

Summary, Conclusion and Future Work

Summary

General Introduction

A brief discussion of the Internet of Things (IoT), and the requirements required for its wide scale application is given. Various types of energy harvesters are discussed, where their typical power is outlined in addition to their requirements for operation. Their shortcomings are addressed, and the need for a combination of energy harvesters and microbatteries is outlined in order to ensure autonomy of IoT sensors.

The most recent advances in solid-state microbatteries is briefly mentioned, where references to microbatteries containing $LiCoO_2$ is initially addressed, followed by doped $LiCoO_2$ electrodes, and then Co-free electrodes such as $LiFePO_4$. The issues associated with solid-state electrolytes such as sluggish Li^+ are addressed as high temperatures are required in order to get enough power from the microbattery. As this reduces the applicability of the all-solid-state microbatteries, the need for an alternative material is highlighted.

Chapter 1: Literature Review

Ionic liquids (IL) are offered as an alternative electrolyte, and their advantages are outlined such as wide electrochemical windows, high ionic conductivity and negligible vapour pressure. The combination of the cation and anion can have a significant effect on the electrochemical and physiochemical properties of the IL.

A comprehensive discussion on pyrrolidinium-based ionic liquid electrolytes is carried out, where the electrolytes are separated based on their cations. In each section a thorough discussion of the recent advances are outlined. Different electrode materials are discussed where cathodes are thoroughly discussed initially focusing on cobalt containing electrodes ($LiCoO_2$, $Li(Ni_{0.8}Co_{0.15}Al_{0.05})O_2$, etc.) and transitioning into cobalt-free electrodes such as $LiFePO_4$, V_2O_5, etc. Finally, the anode materials are discussed where conventional materials such as graphite and Li metal are initially discussed, followed by various other anode materials such as Ge, Sn and Si. Polymer gel electrolytes and full cell tests were discussed in the relevant sections where applicable and in thorough detail which outline the feasibility of ionic liquid electrolytes for use in Li-ion batteries.

Chapter 2: Electrochemical and Physical Characterisation Techniques

A discussion of the fundamental principles of the electrochemical and physical characterisation techniques are discussed in this chapter, in addition to physical vapour deposition techniques. The electrochemical techniques discussed are cyclic voltammetry, chronopotentiometry, chronoamperometry and electrochemical impedance spectroscopy as they are typical techniques used in electrodeposition and battery studies. Physical characterisation techniques such as scanning electron microscopy (SEM) coupled with energy dispersive X-ray spectroscopy (EDX) are efficient instruments to study the surface morphology and microstructure changes during Li+ insertion and de-insertion and can yield quantitative material analysis. Techniques such as Raman spectroscopy and Fourier transform infrared spectroscopy (FT-IR) are common non-destructive techniques that give information on the chemical structure of the material, particularly useful for polymer gel materials. A profilometer was mostly used to measure the electrodeposited and direct current (D.C.) magnetron sputtered materials/thin film dimensions. Differential scanning calorimetry (DSC) and thermogravimetric analysis (TGA) techniques were discussed in order to characterise polymer gel electrolytes by determining the degree of crystallisation and decomposition temperatures respectively.

Finally, D.C. magnetron sputtering was discussed as the physical vapour deposition technique used to deposit substrates, current collectors and electrode materials utilised in this thesis.

Chapter 3: Ionic Liquid Analysis

In this chapter, an extensive analysis of ionic liquid electrolytes was carried out. CV analysis was initially utilised in order to determine the electrochemical window of both trihexyltetradecylphosphonium bis(trifluoromethylsulfonyl)imide ($P_{14,666}$TFSI) and 1-butyl-1-methylpyrrolidinium bis(trifluoromethylsulfonyl)imide (C_4mpyrTFSI) and compared to a standard organic electrolyte 1:1 v/v solution of ethylene carbonate (EC):diethyl carbonate (DEC). C_4mpyrTFSI yielded the largest electrochemical window of the three electrolytes and was the IL electrolyte chosen to be studied further. The effect of LiTFSI salt concentration was investigated to determine its compatibility, its Li-ion mobility within the ionic liquid and ultimately its optimum concentration. This was carried out in a two-fold investigation, CV and electrochemical impedance spectroscopy (EIS) to determine the optimum LiTFSI salt content for C_4mpyrTFSI electrolytes. Initially CV analysis was carried out to determine the lithium deposition and stripping mechanisms within the ionic liquid. Its performance was compared to 1 M $LiPF_6$ in a 1:1 v/v solution of EC:DEC to compare the efficiency of Li^+ mobility within the IL with conventional organic electrolytes. EIS analysis was utilised to determine the optimum LiTFSI salt concentration based on the ionic conductivity of the electrolyte. Initially the blank ionic liquid was investigated, and this was compared to the salt in ionic liquid data.

After a thorough investigation of the liquid ionic liquid, a polymer gel version was synthesised, which was comprised of LiTFSI salt, PVDF-HFP and C_4mpyrTFSI. A series of polymer gels were synthesized via drop casting, where the C_4mpyrTFSI content was varied between 10% and 60%. Flexible, free-standing films were obtained which demonstrated different surface morphologies

which was attributed to the C_4mpyrTFSI content. FT-IR and Raman spectroscopy was carried out to determine if the crystalline structure of the polymer gel is affected by increasing C_4mpyrTFSI concentrations. The crystalline structure was determined to be affected by the C_4mpyrTFSI concentration as high C_4mpyrTFSI concentrations (>40%) yielded more amorphous polymer gel films as evidenced by FT-IR and Raman spectroscopy analysis.

The effect of crystallinity on the melting point and thermal stability of the polymer gels were investigated by both DSC and TGA. Comparisons between the PVDF-HFP, PVDF-HFP with LiTFSI and PVDF-HFP with LiTFSI and various C_4mpyrTFSI concentrations were compared. The degree of crystallinity was affected upon addition of LiTFSI salt and C_4mpyrTFSI as determined by DSC analysis. TGA analysis in N_2 and air environments is discussed over temperature ranges of ~25 ºC to ~800 ºC, where different ramp rates were utilised, to determine the decomposition temperatures of the polymer gels. Comparing the results obtained for both N_2 and air environments demonstrate the effect the packaging environment of the battery could have on the operational temperature of the polymer gel.

EIS analysis of the polymer gel electrolytes was discussed as the ionic conductivities varied depending on the C_4mpyrTFSI concentration. The results were compared to solid-state electrolytes, to highlight the improved ionic conductivity when compared to solid-state electrolytes (23x to 600x greater). Ionic conductivities of similar magnitude were obtained when compared to conventional organic electrolyte, thus highlighting the feasibility of the polymer gel electrolytes.

Chapter 4: Evaluation of Ge Anodes with Ionic Liquid Based Electrolytes

Following on from chapter 3, further anode material analysis was discussed with D.C. magnetron sputtered Ge. The films were investigated initially using Raman analysis to determine if amorphous or crystalline films were obtained when sputter deposited onto a Si substrate. Characteristic

amorphous Ge Raman peaks were obtained. Investigation with SEM and EDX analysis yielded the expected results where Ge was detected in addition to the Cu current collector and Si substrate. Initially, CV analysis was carried out to determine the compatibility of Ge anodes with C_4mpyrTFSI-based electrolytes. Their performance was compared to Ge anodes within a conventional organic electrolyte (1 M $LiPF_6$ in 1:1 v/v EC:DEC). Solid-electrolyte interphase (SEI) layers formed more readily within the organic electrolyte due to its narrower electrochemical window as highlighted in chapter 3, thus demonstrating more stable cycling then the IL counterpart. Despite this, the capacities obtained at various scan rates were greater than 800 mAh g^{-1}.

EIS analysis was carried out to determine if the addition of additives has an effect on the ionic conductivity of the ionic liquid electrolyte. The ionic conductivities of the additives in 0.5 M LiTFSI in C_4mpyrTFSI are similar to the ionic conductivity of 0.5 M LiTFSI in C_4mpyrTFSI without additives (1.5 mS cm^{-1}). An investigation into VC and FEC additives was carried and discussed as the formation of an SEI layer within IL electrolytes is sluggish when compared to the organic carbonate containing electrolytes, therefore the utilisation of carbonate based additives whose breakdown occurs at potentials higher than 0 V vs. Li/Li^+, will allow for faster SEI layer formation within the IL electrolyte. Discharge capacities of ~1200 mAh g^{-1} were attained at 0.1 mV s^{-1} with 3 wt.% VC in 0.5 M LiTFSI in C_4mpyrTFSI which demonstrated higher capacities than the additive free electrolyte.

Post-mortem SEM analysis of the cycled Ge electrolytes was carried out after 100 cycles with various scan rates in the IL-based electrolytes to determine if a change in the morphological features occurred. All electrode exhibited delamination from the current collector as evidenced by the SEM and EDX data.

CV analysis of the Ge electrode with the polymer gel electrolyte PG-60 was carried out and comparisons between its performance and the liquid counterparts were drawn. A comparison of thick (~400 µm) versus thin (~42 µm) PG-60 was discussed. Despite the lower capacities exhibited by the 400 µm PG-60 film, the coulombic efficiencies were close to 100%, while lower coulombic efficiencies were obtained with the thinner film (~80%).

As galvanostatic cycling replicates the charging and discharging cycling that would occur in batteries, this analysis was carried out on the liquid and polymer gel electrolytes. Typical galvanostatic profiles were observed for the 3 wt.% VC in 0.5 M LiTFSI in C_4mpyrTFSI and PG-60 cells, where the 3 wt.% VC in 0.5 M LiTFSI in C_4mpyrTFSI results have demonstrated better electrochemical rate performances than those in literature where similar IL electrolytes were used: 1 M LiTFSI in C_4mpyrTFSI and 1 M LiTFSI in C_4mpyrFSI. The results are comparable to nanoarchitectured Ge-based anodes in organic electrolytes as capacities of <1200 mAh g^{-1} have been demonstrated at 1 C in 1 M $LiPF_6$ in 1:1:2 v/v/v of ethylene carbonate (EC):propylene carbonate (PC):diethyl carbonate (DEC) with 10 wt.% FEC. Galvanostatic cycling with PG-60 further demonstrated its compatibility with Ge, as coulombic efficiencies of >99% were obtained at various C-rates. Therefore, this polymer gel electrolyte is capable of buffering the expansion effects experienced by Ge and is suitable for use as a flexible, high conductivity, thermally stable electrolyte for application in Li-ion microbatteries.

Chapter 5: Evaluation of Electrodeposited V_2O_5 as Li-ion Cathodes with C_4mpyrTFSI ionic liquid electrolytes

In this chapter, the electrochemical analysis of an electrodeposited nanoscale film of V_2O_5 is reported. Current additive-free electrodes are typically deposited via physical vapour deposition. Utilisation of this line-of-sight technique is suitable for thin films, however, it makes it difficult to achieve uniform deposition onto micron tall 3D nanoarchitectures. To make the fabrication of 3D core-shell

nanoarchitectures a reality, electrode materials need to be easily deposited uniformly, which is achieved in this chapter as V_2O_5 is a cathode material that can be easily electrodeposited thus demonstrating its potential to be used to fabricate 3D core-shell nanoarchitectures.

V_2O_5 thin films were electrodeposited onto substrates, where some samples underwent annealing at 325 °C for 7 hours to crystallise the V_2O_5 deposit, while other samples were dried using a N_2 gun. Both films were investigated using SEM and EDX, where a porous structure was observed in both films. Raman analysis confirmed that the annealed V_2O_5 thin films exhibited a crystalline structure, while the unannealed films exhibited an amorphous structure.

CV analysis for the α/ε and ε/δ phases was carried out on the crystalline V_2O_5 films in 0.5 M LiTFSI in C_4mpyrTFSI, where CV cycling revealed the well-defined characteristics peaks for the crystal α/ε and ε/δ phases at scan rates 0.05 mV s^{-1}, 0.1 mV s^{-1} and 0.5 mV s^{-1}. The contributing kinetics were investigated and revealed that the α/ε phase is primarily diffusion controlled and that there is a significant intercalation pseudocapacitance (non-diffusion controlled) contribution in the ε/δ phases. A comparison of two different thicknesses (600 nm and 300 nm) was carried out, whereby faster electrode kinetics occurred in the thinner film as evidenced by the reduced peak separation and sharper peaks. Similar CV analysis was carried out on the amorphous films, however, due to the lack of long-range order in amorphous materials, no preferred ion diffusion channels exist, causing isotropic lithium diffusion. Unlike the crystalline material, no sharp peaks are observed, but rather broad peaks, which are more indicative of pseudo-capacitive storage, where pseudo-capacitance occurs either at the particle surface or within the interlayer spacing of the material. A comparison of the crystalline and amorphous data show that the crystalline V_2O_5 films offer higher electrode capacities and coulombic efficiencies than the amorphous electrodes.

As full cell prototypes were planned using Ge and V_2O_5 electrodes, investigations into the electrochemical performance of V_2O_5 electrodes with additive containing electrolytes were performed. Analysis of the electrode kinetics determined that the 3 wt.% VC containing electrolyte offered the highest peak separation of the additive containing electrolytes (ε/δ peaks VC: 131 vs. FEC: 110 at 0.5 mV s^{-1}), thus demonstrating that a higher resistance to electrolyte charge transport and transfer at the electrode/electrolyte interface is present. This could be indicative of the formation of an SEI layer, which would increase the resistance to charge transfer, however, the peak separation and b-value values are similar to the additive free electrolyte. All three electrolytes yielded coulombic efficiencies close to 100% which demonstrates the compatibility of the ionic liquid with V_2O_5 electrodes.

In order to determine the electrochemical performance of the V_2O_5 electrodes both in amorphous and crystalline forms at different C-rates, galvanostatic cycling was employed. Differences in the galvanostatic profiles were observed as the crystalline film exhibits the typical step profile indicative of the various phase changes V_2O_5 undergoes during cycling with Li^+, while no plateaus are observed in the amorphous films, indicative of the system behaving like a pseudo-capacitor. Various electrolytes were analysed including PG-60. The crystalline V_2O_5 films exhibited better galvanostatic performance than the amorphous counterparts in each electrolyte, for example ~131 mAh g^{-1} and ~81 mAh g^{-1} at 0.3 C with PG-60 electrolyte.

The addition of 3 wt.% VC to the electrolyte yielded better performances than for 0.5 M LiTFSI in C_4mpyrTFSI as higher electrode capacities were obtained at each C-rate (e.g. discharge capacity ~119 mAh g^{-1} vs. ~101 mAh g^{-1} at 1 C). In addition, the coulombic efficiencies were greater than 90% for all C-rates. A similar trend was observed for both crystalline and amorphous V_2O_5 films with PG-60 as an electrolyte. For all electrolytes, stable cycling was obtained for both amorphous and crystalline

films, however, at high C-rates a larger capacity drop is observed for the amorphous films (~5 mAh g^{-1} versus ~80 mAh g^{-1} at 10 C in PG-60).

Long-term cycling was carried out in three electrolytes, 0.5 M LiTFSI in C_4mpyrTFSI, 3 wt.% VC in 0.5 M LiTFSI in C_4mpyrTFSI and PG-60. All three electrode systems exhibited stable cycling over a further 300 cycles, and the electrode capacities were recovered after fast cycling (5 C) when 0.2 C was applied to the cell. The high coulombic efficiencies that were observed in the initial 100 cycles (>80%), were observed for the subsequent cycles which show the compatibility of the V_2O_5 electrodes with both Li^+ cycling and ionic liquid based electrolytes. The best performance was obtained for the PG-60 where minimal capacity drop was observed (0.4% over 50 cycles at 5 C)

Chapter 6: Evaluation of Inverse Opal TiO_2 Anodes with Ionic Liquid Based Electrolytes

Before investigating a prototype full cell, both the liquid and polymer gel ionic liquid electrolytes compatibility with nanostructured electrode materials was investigated with inverse opal (IO) TiO_2 electrodes which were prepared in collaboration with the Applied Nanoscience Group in University College Cork headed by Prof. Colm O'Dwyer. CV analysis of the TiO_2 electrodes were carried out with 1 M $LiPF_6$ in 1:1 v/v EC:DEC, and various C_4mpyrTFSI-based electrolytes. Swelling of the TiO_2 lattice was observed in both 1 M $LiPF_6$ in 1:1 v/v EC:DEC, and 0.5 M LiTFSI in C_4mpyrTFSI after 100 cycles, and in order to reduce this, electrolytes containing additives were discussed.

CV analysis determined that wt.% of VC additive should be less than 3 wt.% as contents above 3 wt.% do not yield higher electrode capacities over the course of 100 cycles. Polymer gel analysis was carried out with the TiO_2 electrodes to determine if the electrochemical performance can be enhanced. The polymer gel was drop casted into the TiO_2 electrode and did not penetrate the entirety of the TiO_2 porous network, therefore did not vastly improve the electrochemical performance.

Chapter 7: Preliminary Full Cell Analysis

Following on from the previous chapters, ionic liquid-based full cells are constructed using V_2O_5 cathodes and Ge anodes. Pre-lithiation of the electrode materials is desirable for VC-containing electrolytes (900 μm separator) as a significant increase in the electrochemical performance of the VC-containing cell. Up to 400 cycles was demonstrated with both VC-free and VC-containing cells, where the maximum capacity fade noted across 50 cycles are 0.5 and 0.9 mAh g^{-1} respectively for cycles 100 to 150 (0.2 C) charge data, however, little capacity fade is observed for the higher C-rates.

A reduction in the separator thickness results in more stable cycling across the C-rates as minimal capacity drop is observed in the VC-containing 260 versus a 900 μm thick electrolyte cell (~0.3 vs. ~1 mAh g^{-1} per cycle at 0.5 C, respectively). Up to 700 cycles was achieved for both VC- and VC-free cells without significant capacity fade or cell failure. These cells are comparable to typical solid-state microbatteries, as capacities of 5.7 and 3.2 μAh at 0.2 C (cycles 11 to 20) and 1 C (cycles 41 to 50) respectively are demonstrated by the prototype, with an average discharge capacity of 1.3 μAh at 5 C for cycles 600 to 650 being attained after significant C-rate analysis. Despite the promising results, the optimisation time-scale is severely impacted due to COVID-19 (much longer than originally anticipated), hence the research focus shifted to the alternative V_2O_5/Li full cell realised in chapter 5. Comparing its performance with 0.5 M LiTFSI in C_4mpyrTFSI with the V_2O_5/Ge cell, it is evident that the 220 nm V_2O_5/Li cell performance is superior as capacities of ~6 μAh were obtained at 1 C (< 3 μAh for Ge-containing cell). Therefore, demonstrating its promise as a prototype microbattery for IoT sensors.

Conclusion

In this thesis, the creation of new free-standing and flexible polymer gel electrolytes was demonstrated in chapter 3. They can be readily synthesised from ionic liquid precursors with no need for heat or vacuum during the drying process or no need for further processing once dry. The polymer gels exhibit ionic conductivities comparable to typical organic electrolytes, and 23x to 600x greater than for conventional solid-state electrolytes. The ionic liquid content affected the crystallinity of the polymer gel electrolyte, and thus differences in the physiochemical properties were observed. For liquid ionic liquids, the optimum salt concentration must be determined as increased salt concentrations led to increased viscosity and lower ionic conductivities, thus demonstrating the importance for optimisation. Chapters 4 demonstrated the need for thorough investigation of electrode materials with ionic liquid electrolytes as SEI layer formation within the IL is slower than for typical organic electrolytes, therefore the use of additives such as VC and FEC can enhance the SEI layer formation within the IL electrolyte, and improve the electrochemical performance of the Ge electrode. Chapter 5 demonstrated that the crystallinity of the electrode can affect its performance within ionic liquid-based electrolytes. In the case of V_2O_5, crystalline films exhibited better CV and galvanostatic cycling performances in both liquid and polymer gel electrolytes. Chapter 6 highlighted the electrochemical performance of the ionic-liquid based electrolytes with an inverse opal TiO_2 electrode. This analysis highlighted the importance of additive concentrations in addition to their combined use with polymer gel electrolytes. Finally, chapter 7 highlights promising V_2O_5/Ge preliminary full cell data, which is competitive with typical solid-state microbatteries, however, further optimisation of the cells are required.

Future Work

Future work based on these findings should focus on developing a deeper understanding of the materials and ionic liquid relationship and the development and optimisation of fabrication processes. Analysis of crystalline Ge materials could be investigated to determine if its crystalline form will perform better in C_4mpyrTFSI-based electrolytes as was observed for V_2O_5. Investigations into the use of C_4mpyrTFSI-based ILs as electrodeposition mediums can be carried out to realise nanostructured electrode materials which will enable higher electrode capacities to be obtained. In addition, its utilisation as the electrolyte for these nanostructured materials will ensure thorough wettability of the electrode material. Improving the understanding between the form and function of nanomaterials and their processing is a very important field, which undoubtedly will experience significant growth in the coming years, particularly where IL electrolytes are concerned.

In the course of this thesis, two full cell configurations have been identified and analysed: V_2O_5/Ge and V_2O_5/Li. Both offer promising results which are competitive with typical solid-state microbatteries. Currently further research is being carried out in our lab to utilise these full cells within implantable medical devices. In addition, the polymer gel synthesis outlined in both chapter 3 and chapter 7 are being utilised in various research projects in different fields such as gas sensing. The results offered within this thesis have created a steppingstone for further advancements in the field of energy storage, particularly when pyrrolidinium-based IL electrolytes are utilised.

Appendices

A1 Conferences

L. McGrath, A. O'Donoghue, T. Clancy, M. Burke and J.F. Rohan, Electrode, Electrolyte and Architecture Assessment for High Power Thin Film Microbatteries, Electrochemical Conference on Energy and the Environment, Glasgow, Scotland, July 21–26th, 2019

L.M. McGrath, T.M. Clancy J.F. Rohan, Ionic Liquid Based Flexible Polymer Gel Electrolytes for Nanoscale Germanium Anodes, 6th International Conference on Ionic Liquids for Electrochemical Devices (ILED-6) in Rome, Italy, September 9th – 11th 2018

L.M. McGrath, T.M. Clancy, J.F. Rohan, Nanoscale Germanium Li-ion Anodes in Ionic Liquid Electrolytes. 69th Annual Meeting of the International Society of Electrochemistry in Bologna, Italy, September 2nd to 7th 2018.

L.M. McGrath, T.M. Clancy, J.F. Rohan, High Energy Density Germanium as Lithium Battery Anodes in Organic and Ionic Liquid Electrolytes. IEEE Nano 2018, the 18th IEEE International Conference on Nanotechnology, July 23rd to 26th, 2018 Cork, Ireland.

T.M. Clancy, **L.M. McGrath**, J.F. Rohan, Nanoscale Cathode Materials for High Power Microbatteries, EnerHarv 2018, The Inaugural International Worksop of the Power Sources Manufacturing Association on Energy Harvesting for Smart Sensor Systems, Cork 26th to 28th May 2018

T. Clancy, **L. McGrath**, J.F. Rohan, High power thin film $LiCoO_2$ for wireless sensor applications, 68th Annual Meeting of the International Society of Electrochemistry in Providence, Rhode Island, 27th Aug to Sep 1st. 2017. USA.

A2 Peer Reviewed Publications

L. M. McGrath, J. Jones, E. Carey, J. F. Rohan, "Ionic Liquid Based Polymer Gel Electrolytes for Use with Germanium Thin Film Anodes in Lithium Ion Batteries" *ChemistryOpen,* **2019**, *8,* 1429.

L. M. McGrath, J. F. Rohan, "High rate lithium ion cycling in electrodeposited binder-free thin film vanadium oxide cathodes with lithium metal anodes in ionic liquid and polymer gel analogue electrolytes" *Batteries Supercaps* **2021,** *4* (3), 485-492

L. M. McGrath, J. F. Rohan, "Pyrrolidinium-based ionic liquid electrolytes as alternatives to solid-state electrolytes for Li-based batteries" *Molecules* **2020,** *25* (24), 6002

A3 Awards and Shortlists

1. Scientist of the Week, I'm a Scientist Stay at Home, May 2020

2. SFI CONNECT Education and Public Engagement Award 2019, February 2020

3. Finalist, Postgraduate Publication of the Year, "Ionic Liquid Based Polymer Gel Electrolytes for Use with Germanium Thin Film Anodes in Lithium Ion Batteries", February 2020

4. Second Place, Best Oral Presentation "Ionic Liquid Based Flexible Polymer Gel Electrolytes for Li-ion Batteries", ISE Satellite Student Regional Symposium on Electrochemistry, Trinity, November 2019

5. Finalist, ResearchFest, InspireFest Conference, May 2019

6. Top 50, Shortlisted, Student Entrepreneur Awards, Enterprise Ireland, 2017

7. Third Place, Student Poster Competition "Ionic Liquid based Electrolytes for Next Generation Li-ion Microbatteries", Postgraduate Research Day, Tyndall, December 2017

8. Third Place, STEM Demo Competition, Tyndall Internal Conference, Tyndall, March 2017

9. Finalist, Student Poster Competition "Ionic Liquid based Electrolytes for Next Generation Li-ion Microbatteries", Postgraduate Research Day, Tyndall, July 2016

A4 Innovation and Entrepreneurial Certificates and Programmes

A4.1 Certificate

Level 9 Certificate in Innovation, Commercialisation and Entrepreneurship, University College Cork, 2018

A4.2 Entrepreneurial Programmes

NDRC Pre-commercialisation Programme, NDRC, 2018

SPRINT Accelerator Programme, Gateway UCC, University College Cork, 2020

A5 Education and Public Engagement Events

2020

1. Acting SMART Edu STEM teacher/consulant
2. SMART Edu Science and Forensics Summer Camp Instructor
3. I'm a Scientist, Stay at Home! – Green Zone
4. Global Science Show, Twitter

2019

1. ResearchFest – Finalist (top 8)
2. iWish - Panellist
3. #InternationalDayofWomenandGirls, Twitter
4. Fota Mad Scientist Weekend
5. Carnival of Science
6. TY Work Placement
7. Silicon Republic Article on ResearchFest Finalists, "Meet 8 finalists set to dazzle the audience at Researchfest 2019"
8. Silicon Republic Researcher Profile, "I dived head-first into electrochemistry and I haven't looked back since!"
9. Silicon Republic Article, "25 bright sparks working to make our world a better place in 2020"

2018

1. Fota Mad Scientist Weekend
2. TeenTurn
3. #Imachemist, Twitter
4. CEIA TY Talks
5. 1st Year Engineering Tours

2017

1. Famelab
2. iWish

3. CEIA TY Talks
4. TY Student Shadowing
5. STEM Demo Creation and Exhibition
6. ResearchFest Entry
7. Three Minute CONNECT Video
8. Fota Mad Scientist Weekend
9. Culture Night
10. #ShowOffYourScience, Science Week, Twitter

2016

1. Famelab
2. CEIA TY Talks
3. MakerDojo Electronics Workshop
4. MakerDojo Energy Workshop
5. I'm a Scientist Get Me Out Of Here! – New Materials Zone
6. Vex Robotics
7. Science Week

2015

1. Micro Energy Day
2. Fota Mad Scientist Weekend
3. MakerDojo Launch Day
4. Science Week